The spectrum and charge-ratio of high energy cosmic rays

Peter J. Hayman

Hayman, Peter J. (1962) The spectrum and charge-ratio of high energy cosmic rays. Doctoral thesis, Durham University.

Frontispiece : The upper half of the Durham Cosmic Ray Spectrograph showing the flash-tube arrays.

The Spectrum and Charge-Ratio of High Energy Cosmic Rays

by Peter J. Hayman, B.Sc.

A thesis submitted to the University of Durham, on an application for the degree of Doctor of Philosophy.

June, 1962.

Contents

Abstract

The momentum spectrum and positive-negative ratio of cosmic ray μ-mesons, in the near vertical direction at sea-level, have been measured. The statistical accuracy and maximum detectable momentum are higher than have previously been attained by other workers using similar methods.

This has been made possible by the modification of a Geiger counter spectrograph and addition of flash-tube arrays. Fast particles have been selected electronically, and their trajectories recorded automatically by cameras which photograph the flash-tubes.

A precise differential μ-meson momentum spectrum has been derived in the momentum range 5 - 1000 GeV/c, after the usual instrumental corrections. In the lower momentum region, 5 - 10 GeV/c, there is good agreement with the spectrum determined with the Geiger counters alone. The measurements in the range 10 - 100 GeV/c are consistent with a π-meson production spectrum of constant exponent, $\gamma = 2.64 \pm 0.05$. More accurate methods of measurement of the flash-tube data at higher momenta lead to a maximum detectable momentum of the instrument, based on the probable error of deflection measurements, of 657 ± 112 GeV/c. In the momentum range 70 to 700 GeV/c these independent measurements lead to a value of $\gamma = 2.67 \pm 0.10$ and it must be concluded that there is little change in the exponent of the π-meson production spectrum in the whole

range of measurement.

The positive-negative ratio of μ-mesons at sea-level has been found to increase from about 1.25 at 5 GeV/c to about 1.5 at 250 GeV/c, where the results are the first measurement made at such high momenta.

The measurements have been used to study the energy loss processes of μ-mesons and also to study the production of π-mesons in the primary interactions.

Preface

This thesis describes work done by the author in the Cosmic Radiation Laboratory (Magnet Group) of the Physics Department of the Durham Colleges, under the supervision of Dr. A.W. Wolfendale.

Whilst the recipient of a studentship from D.S.I.R., the author was responsible for the assembly of the flash-tube section of the Durham Cosmic Ray Spectrograph, its alignment and electronic pulsing and control circuits.

The author has developed a method of film analysis which has enabled particle momenta up to several hundreds of GeV/c to be measured and investigated.

The flash-tube section of the spectrograph constructed by the author has been used to extend the measurement of the sea-level momentum spectrum of μ-mesons up to $\sim$1000 GeV/c using this method of film analysis. The preliminary results were published by the author and his colleagues in Nature, (Ashton et al, (1960)) and will not be given in this thesis.

An extension to this work has been made by the collection, solely by the author, of an extended set of data, involving some 18,000 particles. The author had the help of Mr. G. Brooke in the initial projection of the film data and its reduction by computer. An initial measurement of

Chapter 1

Introduction

The presence of an ionizing radiation in the atmosphere has been known since the early experiments of Hess, (1912, 1913), and Kolhorster, (1914-1919). The assumed origin led to the name 'cosmic radiation' which is now generally applied to the various forms it takes although it is now known that 'cosmic rays' are mainly particles.

The primary component of the cosmic radiation which is incident on the earth has been shown to consist mainly of protons, with about 20% of α-particles and heavier nuclei. The primary protons of the radiation interact with the oxygen and nitrogen nuclei, of which the atmosphere is mainly composed, in the first 100 $\mathrm{gm.cm^{-2}}$ or so. In these interactions, high energy nucleons, unstable mesons and hyperons are produced.

The primary particle loses only about 40% of its energy in the first collision and so it can continue and make further collisions until all of the energy is dissipated. The absorption length of the radiation is about 120 $\mathrm{gm.cm^{-2}}$. Since the total depth of the atmosphere is about 1000 $\mathrm{gm.cm^{-2}}$, the probability of a primary cosmic ray surviving to reach sea-level is thus very small.

The unstable mesons consist mainly of π-mesons, both charged and neutral, and a smaller proportion of heavier mesons. The π-mesons can further interact with nuclei or decay. The π-meson decays with a lifetime of 2.6 x 10^{-8} sec. into a μ-meson and a neutrino. In the absence of an interaction, the average distance traversed by the charged π-meson before decay, can be shown to be about 55 p_{π} metres, where p_{π} is the π-meson momentum in GeV/c. The probability of the competing process of interaction occurring depends on the height of production of the π-meson. Under the simplifying assumption that these mesons are produced 100 gm.cm^{-2} below the top of the atmosphere (15 km above sea-level), and taking the measured interaction length of about 70 gm.cm^{-2}, the mean free path before interaction is then about 2000 metres. Decay and interactions are therefore equally probable at a π-meson energy of about 40 GeV. Thus nearly all π-mesons with energies below about 40 GeV will decay while only a small fraction of those above 40 GeV will do so. The mesons travelling in the less dense higher regions of the atmosphere have a higher probability of decay than those of the same energy moving in denser regions lower in the atmosphere.

The heavy mesons and hyperons are removed by similar competing processes; the decay schemes of some K-mesons will contribute a few μ-mesons at very high energies, the proportion of the total μ-meson component derived from these sources depending on the fraction of the primary energy available for heavy meson production.

The neutral π-mesons produced in the primary interaction haveashort mean lifetime, about 10^{-16} sec, and decay into two photons which, if of sufficiently high energy, materialise in the presence of nuclei to form electron pairs. These can further lose energy by bremsstrahlung processes and the resultant cascade forms the electron-photon component of the large extensive air showers.

The π-mesons produced in the atmosphere by the primary protons, and which subsequently decay to produce μ-mesons or by electromagnetic interactions produce electron-photon cascades, form the two main types of the cosmic radiation at sea-level. The μ-mesons are weakly interacting and because of their ability to penetrate moderate thicknesses of matter (greater than about 10 cm of Pb), form the larger proportion of what it is customary to call the hard component of the sea-level cosmic radiation. The μ-mesons have comparatively long lifetimes, about 2.2×10^{-6}sec, and so can reach sea-level and also penetrate underground. The range of μ-mesons in air before decay is about 6000 p_{μ} metres, where p_{μ} is the μ-meson momentum in GeV/c,so that most μ-mesons, having momenta greater than about 3 GeV/c and derived from the decay of π-mesons produced in the first primary interaction, will survive to sea-level, but at lower momenta, decay, and the loss of energy in collision processes in the atmosphere, will result in a decrease in the sea-level intensity of μ-mesons.

Thus, at sea-level, the radiation with energies above 1 GeV consists mainly of μ-mesons together with a small flux of protons, about 1%, and smaller fluxes of π-mesons and electrons. Since the observed particles in the hard component are derived from primary collisions which take place far above sea-level, they will appear to be unaccompanied when observed over the dimensions of apparatus of moderate size, about 1m^2, at sea-level.

The hard component at sea-level has been the subject of many investigations. In particular, the momentum spectrum and the ratio of the number of positive to the number of negative μ-mesons in the near vertical direction, have been extensively measured in various energy ranges by many workers using different techniques. These quantities are of particular interest, since, by erecting the appropriate diffusion equations for the propagation of the particles in the atmosphere, it is possible to work back to the spectrum of π-mesons on production in the high energy collisions. Comparison of this spectrum with the primary spectrum then yields information on the nuclear processes at high energies. Further, the sea-level μ-meson spectrum can be compared with the measured intensity of particles as a function of depth underground. This comparison yields information on the energy loss processes of μ-mesons which can then be used to extend the knowledge of the spectrum of μ-mesons to higher energies using the underground intensities.

The present work increases the statistical accuracy and extends the measurement of the sea-level μ-meson spectrum and positive-negative ratio to higher momenta than previously attained. This has been made possible by the development of the neon flash-tube. This new technique can be used for the precise location of ionizing particle trajectories over large areas, thus enabling instruments of high collecting power to be constructed.

After a discussion of previous instruments and measurements, (chapter 2), a description is given of the design and construction of a magnetic spectrograph using flash-tubes, and having large solid angle of particle collection and high maximum detectable momentum, (chapter 3). The alignment of the instrument is considered, (chapter 4), and the momentum spectrum derived from the measured deflection spectrum, (chapter 5). The energy loss processes for μ-mesons are considered in the light of fluctuations in the various energy loss processes and a comparison of the sea-level integral spectrum with the underground intensities is made, (chapter 6). The positive-negative ratio is derived from the measured data and the various bias effects considered (chapter 7). Comparison of the π-meson production spectrum derived from the measured sea-level μ-meson spectrum and the predicted spectrum, is used to study nuclear processes at high energy, (chapter 8). The theoretical positive-negative ratio is derived and compared with the measured ratio at sea-level, (chapter 9). The implications of the various conclusions are finally considered in chapter 10.

Chapter 2

Cosmic Ray Spectrographs and the Measurement of μ-meson Spectra

2.1 Introduction

Most of the experiments to be described have been carried out in laboratories which are not far above sea-level (e.g. Durham, having geographic coordinates of latitude 54.5°N and longitude 1.3°W, is 200 feet above sea-level), and the measurements will be referred to loosely as 'sea-level measurements'. In fact significant differences in the measurements only appear at altitudes above a thousand feet or so.

Previous measurements of the sea-level energy spectrum of cosmic rays have been made by using two main methods: viz, determination of range and momentum.

The absolute flux of μ-mesons has been measured as a function of minimum range for various condensed materials. The range-energy relationship was then used to convert the range spectrum to the momentum spectrum. A rather low limiting momentum, ~ 5 GeV/c, is set by the maximum thickness of absorber available.

The determination of momentum, which at the relativistic region in question is numerically identical with energy, has been carried out by two techniques: viz, multiple scattering and magnetic deflection. The upper limit of momentum which has been measured by the study of multiple scattering in a multiplate cloud chamber is ~4 GeV/c. The limit is set by the gas movement which gives rise to distortion of the particle track. When nuclear emulsions are used, the limit is set a little higher, ~10 GeV/c; the distortions of the emulsion which take place during processing, setting the limit. The technique of magnetic deflection has been applied most widely to the determination of charged particle momenta and will be dealt with more fully in the next section.

2.2 The Magnetic Deflection and Determination of Particle Momenta

Previous measurements of the angular deflection of particles traversing a magnetic field have been carried out with Geiger counters and cloud-chambers, and more recently with nuclear emulsions, spark counters and flash-tube hodoscopes. The relation between momentum, p (in eV/c), magnetic field, H (in gauss), and radius of curvature, ρ (in cm.), for singly charged relativistic deflected particles, is given by

$$p = 300H\rho \qquad 2.1$$

If θ is the angular deflection then

$$p\theta = 300\int Hdl \qquad 2.2$$

where $\int Hdl$ is the line integral of magnetic field along the particle trajectory (in gauss-cm) for a particle travelling in the plane perpendicular to the magnetic field.

For a given value of $\int Hdl$, the maximum momentum that can be measured is set by the accuracy of measurement of θ. With detectors external to the magnetic field, the quantity usually measured, the linear deflection, Δ, is related to the angular deflection, θ, by the fixed separation of the measuring levels, y_1, (figure 3.12)

$$\theta = \frac{\Delta}{y_1} \qquad 2.2a$$

Hence $$p\Delta \simeq 300\, y_1 \int Hdl \qquad 2.2b$$

To set the limit of measurement of momentum and in order to compare the accuracy of measurement of various instruments, a quantity called the maximum detectable momentum (abbreviated to and subsequently referred to as m.d.m.) is defined as the momentum at which the probable error in a deflection measurement is equal to the magnetic deflection of a particle. In some work the standard deviation (r.m.s. error) is used to define the error in deflection, giving a m.d.m. lower by a factor 0.674 (if the error is Gaussian).

2.3 <u>The Previous Methods and Spectrographs Used to Measure μ-meson Spectra</u>

The early magnetic field methods used a cloud chamber between the poles of an electromagnet to measure the track curvature. However a low limit to the m.d.m. is set by track distortion and in addition only about 5% of the available magnetic field volume is used, (Hyams et al, (1950)).

Rossi, (1948), has reviewed the earlier work and combined it to give a spectrum to about 20 GeV/c. Most subsequent determinations of the spectrum have been associated with measuring the relative flux at different momenta and most work is normalised at 1 GeV/c to the flux given by Rossi.

In recent years the spectrum has been measured with magnetic spectrographs in which most of the detecting elements are external to the field. These are summarised in table 2.1. In most of these instruments, Geiger counters are used as the detecting elements, and in some cases when high momentum particles are detected, further apparatus is triggered which is able to define the particle position more precisely and enable higher momenta to be detected. For example, Hyams et al, (1950), have described an instrument with two electromagnets and hodoscoped Geiger counters as detectors having a m.d.m. of 31 GeV/c. This value was increased by Rodgers, (1957), Holmes et al, (1961a,b), to 356 GeV/c by placing flat cloud chambers at the three measuring levels and these were only triggered if a high momentum particle was detected. The location accuracy for the vertically expanded cloud chambers was about 1 mm at each of the three measuring levels. The efficiency

Table 2.1 : The Comparison of Spectrographs (post 1950)

	Geometry		Collecting power (st.cm^2)
*Glaser et al, (1950)		C.C. M C.C.	0.08
Caro et al, (1951)		G.C. G.C. M G.C.	0.69
Hyams et al, (1950) Owen and Wilson, (1955)	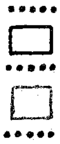	G.C. M G.C. M G.C.	0.93
*Rodgers, (1957) Holmes et al (1956, 1962a)	as Hyams et al, G.C.=C.C.		0.93
*Pine et al, (1960)		C.C. M, C.C. C.C.	7.9
*Roe et al, (1959) **Pak** et al, (1961)	as Pine et al, C.C.=F.T.		7.9
Allkofer, (1959, 1960)		3 x S.C. M. 3 x S.C.	-
Apostolakis et al, (1957a,b)	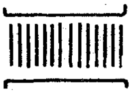	N.E., M.	-
*Ashton et al, (1960)		F.T.	8
Ashton et al, (1959)		F.T. M F.T.	-
Present work *Brooke et al, (1962b)			8
*Coates, (1961)		F.T.	-

*G.C. as detecting elements
G.C. = Geiger counter
C.C. = Cloud chamber
M = Magnet

S.C. = Spark chamber
N.E. = Nuclear Emulsion
F.T. = Flash-tube

with which the available magnetic field was used was 50%. However, the geometry of two magnets gives a small solid angle and consequently a low rate of collection of data.

Using a single magnet and three measuring levels, Pine et al, (1959), increased the solid angle by a suitable design of magnet, and high m.d.m. was obtained by using flat cloud chambers.

The development of spark discharge counters for the location of particle positions, has led to their application to magnetic spectrographs. Allkofer, (1959, 1960), has described their use to obtain a m.d.m. of 60 GeV/c with a very compact instrument (overall height 0.7 m). In 6 weeks, 1930 usable events were recorded. However, it is not clear whether the technique can be applied to large instruments with large collecting areas and high rates. Further developments in this field, and particularly the use of spark discharge chambers with scintillators as the detecting element, are to be expected.

An instrument described by Apostolakis et al, (1957), used 14 layers of nuclear emulsions accurately located between the poles of a magnet. Although the particle position is well known, a big disadvantage is the time taken in scanning the plates and the inability to use the particles for experiments other than perhaps the study of interactions in further emulsions, and the low rates involved.

The reliability of spectrographs has been improved by replacing the cloud chambers by neon flash-tube hodoscopes. The available solid angle for collection of particles can be increased because of the larger collecting areas possible. This dictates the use of a single deflecting magnet so that to achieve comparable momentum resolution, higher accuracy of track location is required. The geometry of the flash-tube array is fixed and the correction to be applied for the uncertainty in particle track location is well known, in contrast to the earlier cloud chamber spectrographs where the correction was uncertain. Ashton et al, (1959), described an instrument with a m.d.m. of 12 GeV/c. This was the prototype of the spectrograph used for the present work. The application of flash-tubes to spectrographs has also been reported by Roe et al, (1959), who modified a spectrograph, described by Pine et al, (1959), which formerly used flat cloud chambers. The m.d.m. of the modified spectrograph was 160 GeV/c. Coates, (1961), has also operated a small flash-tube spectrograph with m.d.m. 29 GeV/c.

2.4 The Results of the Determination of the μ-meson Sea-level Spectrum by Previous Methods

The work of Owen and Wilson, (1955), has been regarded as standard in the range, 0.5 - 20 GeV/c, because of its good statistical accuracy (~60,000 particles). These workers found that the μ-meson spectrum at production could be represented by a power law equation of the form

$$N(p_\mu) = K p_\mu^{-n} \qquad 2.3$$

where n = 2.85 and p_μ is in GeV/c. The corrections applied for μ-meson decay and energy loss were based on a simple model in which it was assumed that the μ-mesons were produced at a unique height.

The spectrum in the range 0.4 - 10 GeV/c, has recently been measured with greater statistical accuracy, (~190,000 particles), by Gardener et al, (1962), using the Geiger counter section of the Durham spectrograph, Brooke et al, (1962), Jones et al, (1962), which has been used in the present work, and it is found that there is good agreement with the work of Owen and Wilson.

Rodgers, (1957), and Holmes et al, (1961a,b), have extended the work of Owen and Wilson to higher momenta, using cloud chambers, the m.d.m. being 356 GeV/c. These workers concluded that the μ-meson production spectrum could be represented by a power law spectrum with the same form as equation 2.3, having n = 2.85, as before at low energy, and n = 2.75 ± 0.03 at high energy.

Pine et al, (1959), have measured the μ-meson spectrum, with an instrument having a m.d.m. of 260 GeV/c. These workers have concluded that the π-meson spectrum at production could be represented by

$$N(p_\pi) = c\,p_\pi^{-\gamma} \qquad 2.4$$

where $\gamma = 2.64$. Following the analysis of Barrett et al, (1952), the μ-meson production spectrum will involve an extra term,

$$N(p_\mu) = c'\,p_\mu^{-\gamma}\left(1 + \frac{p_\mu}{90}\right)^{-1} \qquad 2.5$$

to account for the probability of interaction of π-mesons before they can decay, the extra term being effective at π-meson momenta above about 20 GeV/c.

A preliminary measurement of the μ-meson spectrum, based on only ~600 particles having momenta above 20 GeV/c has been made by Ashton et al, (1960), using the flash-tube section of the spectrograph described in the present work. The value deduced for γ, the exponent of the π-meson production spectrum, from this work, was

$$\gamma = 2.55 \pm 0.2 \qquad 2.6$$

in good agreement with the value deduced by Pine et al.

Other estimates of the exponent of the π-meson production spectrum have been made by methods which do not involve the use of magnetic spectrographs; since these refer to energy ranges near the upper limit covered by the present work, their discussion is deferred until chapters 6 and 8.

2.5 The Results of the Determination of the Charge Ratio of μ-mesons at Sea-level by Previous Methods

The charge ratio of the number of positive μ-mesons, $N(\mu^+)$, to the number of negative μ-mesons, $N(\mu^-)$, at sea-level, has been defined differently by some authors. Thus the positive-negative ratio is given by

$$K = \frac{N(\mu^+)}{N(\mu^-)}$$

The positive excess is $N(\mu^+)-N(\mu^-)$. The relative positive excess is then

$$\eta = \frac{N(\mu^+)-N(\mu^-)}{N(\mu^+)+N(\mu^-)} = \frac{K-1}{K+1}$$

Some authors also give a percentage difference, $\delta = 2\eta$.

In order to accumulate data which will give sufficient statistical accuracy so that any real variation of the charge ratio with momentum can be studied, a lengthy period of collection of data must take place, during which strict control must be made of the many instrumental bias effects.

In the momentum range 1-20 GeV/c, the work of Owen and Wilson, (1951), has the most statistical weight. These authors have found that the positive-negative ratio increases with momentum, reaching a maximum value of about 1.25 at ~ 5 GeV/c but that at higher momenta a slow decrease in the ratio was indicated.

The positive-negative ratio has also been measured in the range 0.4-10 GeV/c with great accuracy using the

Geiger counters, for the data collected by Gardener et al, (1962), and there is good agreement with work of Owen and Wilson, (1951).

At higher momenta, $\geq$ 20 GeV/c, Pine et al, (1959), and Rodgers, (1957), and Holmes et al, (1962b), have measured the positive-negative ratio, but because of the small number of particles at these high momenta the accuracy is low. The percentage error for the positive-negative ratio, K, is a factor of two greater than for the equivalent spectrum error for a value of $K = \frac{5}{4}$. It is not possible to conclude from the work of these authors whether the slow decrease in the positive-negative ratio indicated by the values below 20 GeV/c continues at higher energies.

2.6 The Present Work

An extensive set of data, with 4520 particles above 20 GeV/c, was collected over an instrumental running time of 1800 hours, involving some 94 daily sets of records, from November 1959 to March 1960. In this time some 360,000 five-fold coincidences were recorded and 18,400 of these events were selected and recorded photographically with the flash-tube arrangement, leading to 14,556 useful particles.

The length of the period over which it was necessary to record data was determined by the accuracy required in the high momentum region. From the then known best estimate of the spectrum, it was estimated that in 100 days about 50 particles would be collected in the region above 500 GeV/c and at or about the maximum detectable momentum. Thus the statistical accuracy and correcting factors for uncertainty in deflection measurements would be of the same order.

The spectrograph with which these data were collected is described in the next chapter.

Chapter 3

The Durham High Energy Spectrograph

3.1 Introduction

From previous measurements in the high energy region of the μ-meson sea-level spectrum (e.g. Holmes et al, (1961b)) only preliminary conclusions have been able to be drawn and to substantiate these a more accurate measurement is necessary. A design study was carried out by Kisdnasamy, (1958), in which the use of neon flash-tubes at the detecting levels of the Durham magnetic spectrograph was considered. A small prototype was constructed, Ashton et al, (1959), to investigate the properties of flash-tubes under typical spectrograph operating conditions so that in a larger instrument the neon flash-tubes could be operated under their optimum conditions.

Preliminary results obtained at high energies by the author have been published in Nature, (Ashton et al, 1960)). Further details of the design of the instrument are given in this chapter: the work carried out by the author's colleagues will be indicated where appropriate in the text.

3.2 The Neon Flash-tube

3.2.1. The General Characteristics

The neon flash-tube was first developed by Conversi and Gozzini, (1955). Further developments were carried out by Gardener et al, (1957), with a view to producing a charged particle detector of high efficiency and low cost, and its application to the precise location of particle trajectories was considered by Ashton et al, (1958). The detector consists of a glass tube filled with neon gas and placed between parallel conducting electrodes. If a high voltage pulse is applied soon after the passage of an ionising particle there is a high probability of a visible glow discharge taking place, with such intensity that a photographic record can be made. Since in typical applications to spectrographs where precise location in one dimension only is required, large areas of detectors can be built up by placing long tubes of small diameter parallel to each other in arrays of many layers. A typical array used in the spectrograph is shown in figure 3.1a. Thus several such arrays can be used in a large geometrical configuration to give the trajectory of a charged particle. The passage of a charged particle through a typical array will then appear as a series of localised glow discharges, of the characteristic red colour given by neon. A typical particle traversal is shown in figure 3.2. This close-up of a single array has background illumination to render the unflashed tubes visible. Photoionisation of adjacent tubes is prevented by coating each tube with black paint, the discharge being

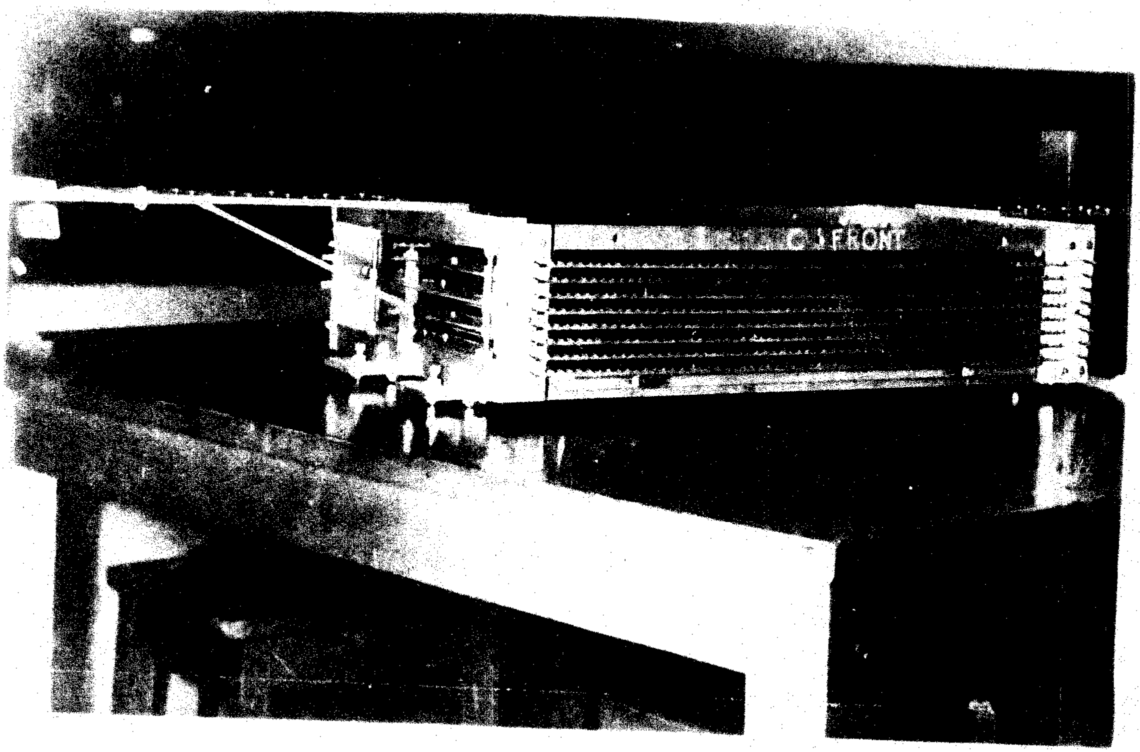

Figure 3.1a : A typical flash-tube array.

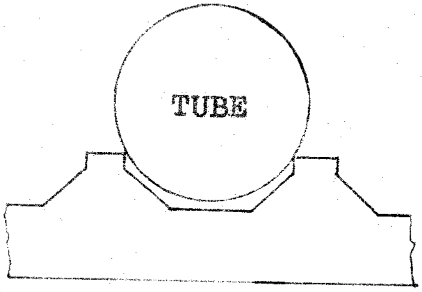

Figure 3.1b : The slots which support the flash-tubes.

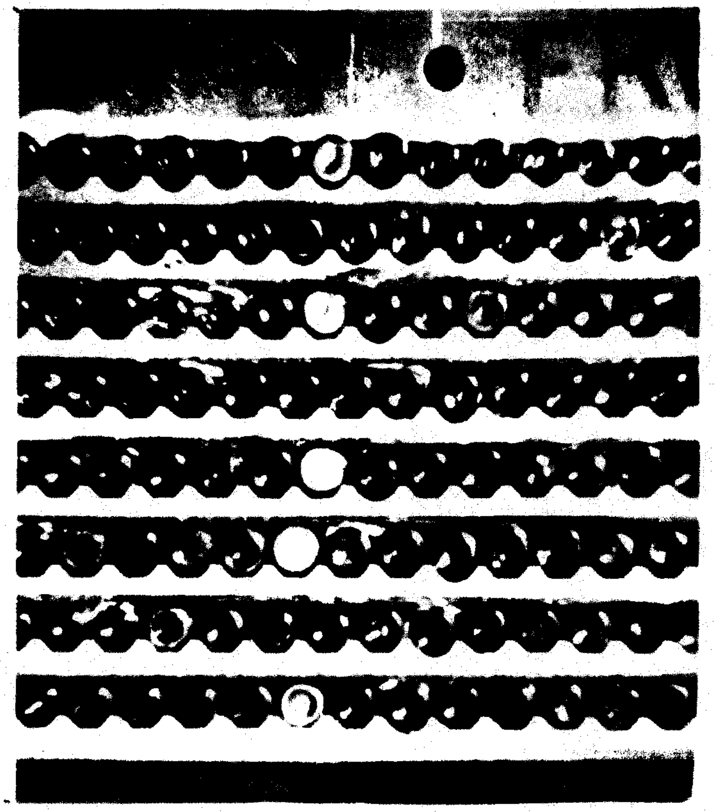

Figure 3.2 : A typical event.

viewed by a "window" in the flattened end of each tube.

The mechanism of operation of the flash-tubes is as follows. Of the ~10 ion pairs remaining after the passage of a relativistic charged particle through the gas, only electrons are useful in initiating break down of the gas and these are rapidly multiplied on the application of a pulsed electric field. In the period before the application of the electric field the electrons can diffuse to the glass walls of the tube and are lost. If there are no free electrons at the time of application of the electric field the tube will not "flash" since the neon ions never gain sufficient energy to reach the ionisation potential of neon. In practice it is found that the tubes have a high probability of flashing if an electric field of intensity ~8Kv/cm is applied within a few microseconds of the passage of a particle through the gas and the visible discharge takes place. A Geiger counter coincidence system is usually used to trigger the high voltage pulsing circuit which applies the electric field to the electrodes between the layers of flash-tubes.

3.2.2 The Efficiency

The layer efficiency for particle detection is defined as the ratio of the number of single flashes observed in a given layer to the total number of times that a single ionising particle passes through that layer. The layer efficiency will depend on the following factors:

1. The time delay, T_D, between the passage of the particle and the application of the pulse.
2. The rise time of the pulse, T_R.
3. The height of the pulse, E.
4. The gas filling.

The work of Gardener et al was extended by Coxell et al, (1960), in order to improve the characteristics of the tubes and in particular to obtain sufficient data to design tubes for particular applications. The particular application to cosmic ray spectrographs required certain characteristics, namely,

a) high efficiency for flashing after traversal by ionising particles

b) short sensitive time

c) low rate of spurious flashing

d) high spatial resolution

e) stability of operation over long periods

f) long life-time

g) inexpensive and easily reproducible by mass production methods

h) ability to operate over large areas, since large numbers of flash-tubes are required to cover large areas in extended telescopes.

It was shown that high efficiency results from short time delays ($\lesssim 10\ \mu$sec) and rise times ($\lesssim 0.5\ \mu$sec), and high electric fields (~ 8 Kv/cm).

These conditions together with ease of manufacture and cost have resulted in the choice of tubes, the details of which are summarised in table 3.1.

The form of the variation of absolute efficiency, defined as the ratio of the number of single flashes observed in a given layer to the total number of times that a single particle passed through the sensitive gas region of the tube with T_D, T_R and E is shown in figures 3.3a, b and c, and the probability of spurious flashing in figure 3.3d. This is the probability of a tube flashing which is not directly associated with an incident particle.

For investigations involving a number of layers of Geiger counters several meters apart and connected into coincidence or particle selection systems which control the operation of the flash-tube arrays, delays of several micro-seconds are likely to occur between the passage of the particle and the application of the electric field to the electrodes of the flash-tube array. Also, a relatively large value of the rise-time of the high voltage pulse is often dictated by the necessity of applying the high voltage pulse to a large array of tubes having considerable electrostatic capacity. In particular, values of

Table 3.1 : The details of the Neon Flash-tubes used in the spectrograph

Glass : soda (GEC, X8)

Internal diameter : 0.59 cm, external diameter 0.72 cm

Horizontal separation in a layer : 0.80 cm

Vertical separation of the layers : 1.15 cm

Length, levels A and D : 67 cm, levels B and C : 42 cm

Gas pressure : 2.3 atmospheres

Gas content : 98% Ne, 2% He, 10^{-4}% air

Average internal efficiency, 81%

Average layer efficiency, 60%

(both of the efficiencies refer to normal operating conditions of time delay of 10 μsec and rise-time of 0.5 μsec).

Table 3.2 : The dimensions of the constants of the spectrograph (see figure 3.12)

y_1 = 184.3 cm

y_2 = 61.4 cm

y_3 = 60.0 cm

y_4 = 189.5 cm

a_o = 9.38 cm

b_o = 36.54 cm

c_o = 36.52 cm

d_o = 10.97 cm

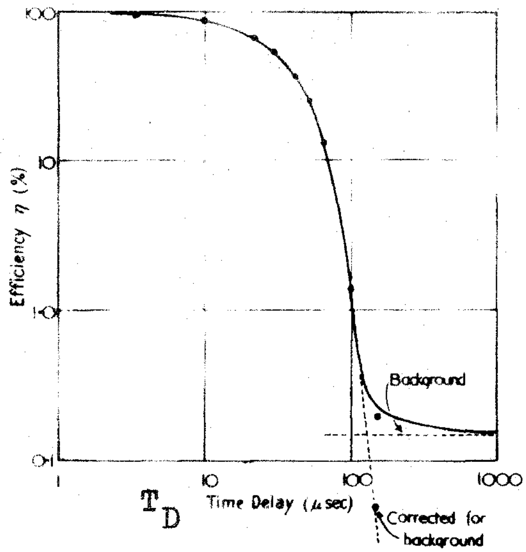

Figure 3.3a

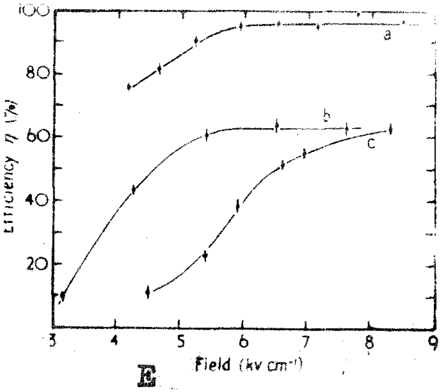

Figure 3.3c

Pulse length 3.5 μsec
a T_R=0.5μsec, T_D=3.4μsec
b T_R=0.5μsec, T_D=26μsec
c T_R=2.0μsec, T_D=4.0μsec.

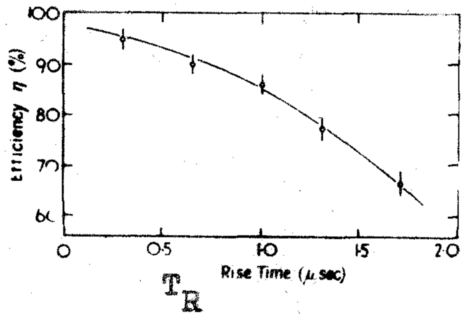

Figure 3.3b

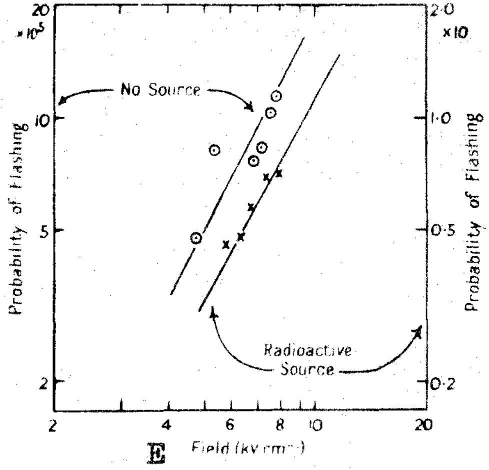

Figure 3.3d

Figure 3.3 : The variation of efficiency with parameters of the pulse, (after Coxell et al, (1960)).

time delays up to $\sim 12\,\mu$sec and rise-times up to $\sim 0.5\,\mu$sec are likely in the practical applications and the use of these values must not decrease the efficiency of the flash-tubes by more than a small amount.

3.2.3 The Spatial Resolution

The requirements of the arrays of flash-tubes were that they should be arranged to give the minimum positional uncertainty for the location of particle trajectories within the acceptance angle of the instrument which was ±13° to the vertical in the front plane. Eight rows of tubes were used - this being the number required to give the desired accuracy ($\sim$0.3 mm at each level).

The optimum arrangement to give the minimum possible value of the positional uncertainty was shown by Kisdnasamy, (1958), to be given by the geometry in figure 3.4. Assuming 100% internal (absolute) efficiency, an r.m.s. minimum value of positional uncertainty of 0.2 cm was found, which was very nearly constant for all angles of acceptance of the spectrograph, figure 3.5. It is not possible for a particle to pass through this configuration within ±13° to the vertical without producing at least four intersections with the sensitive gas volume of the flash-tubes. The variation for a purely random positioning is also shown in figure 3.5.

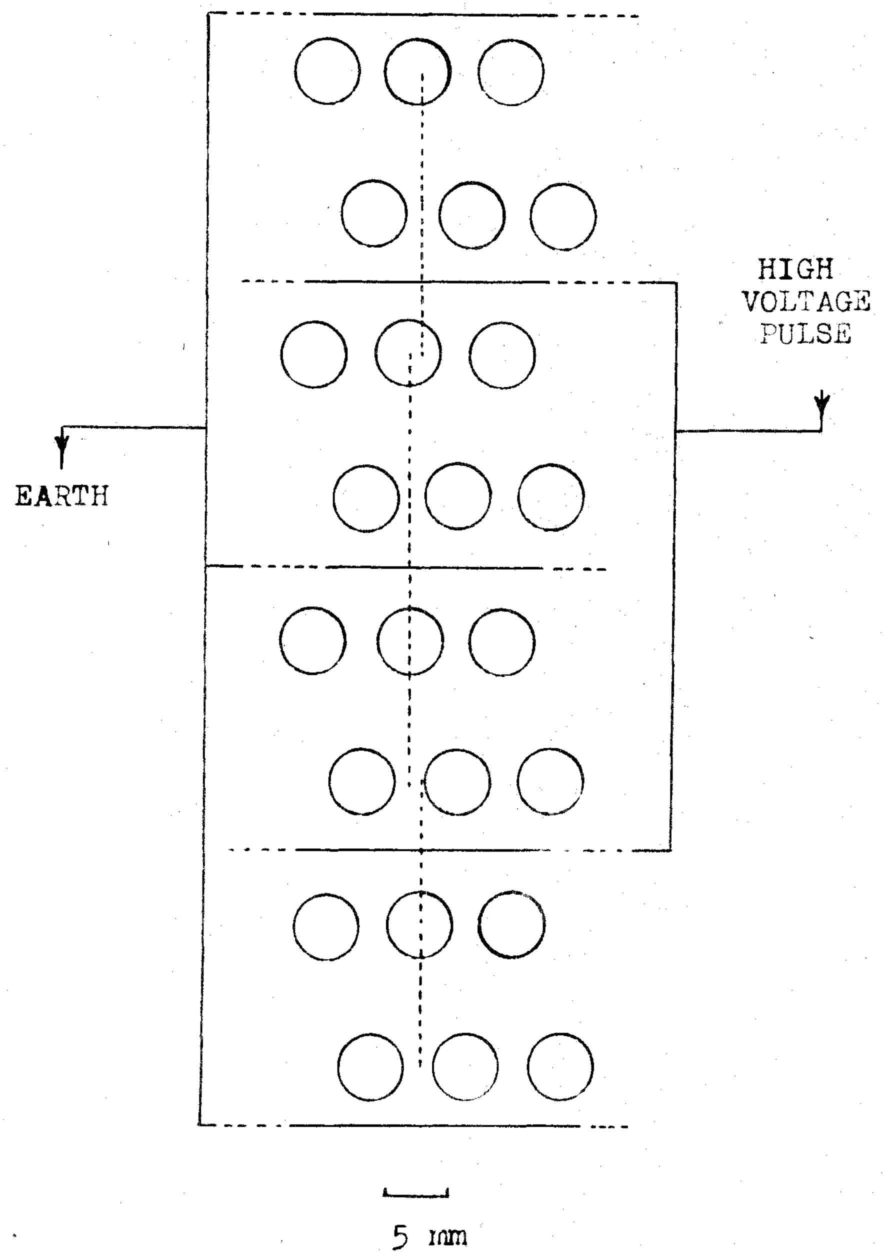

Figure 3.4 : The optimum arrangement of the flash-tubes (to scale) and the electrode system. The circles represent the internal circumferences of the tubes.

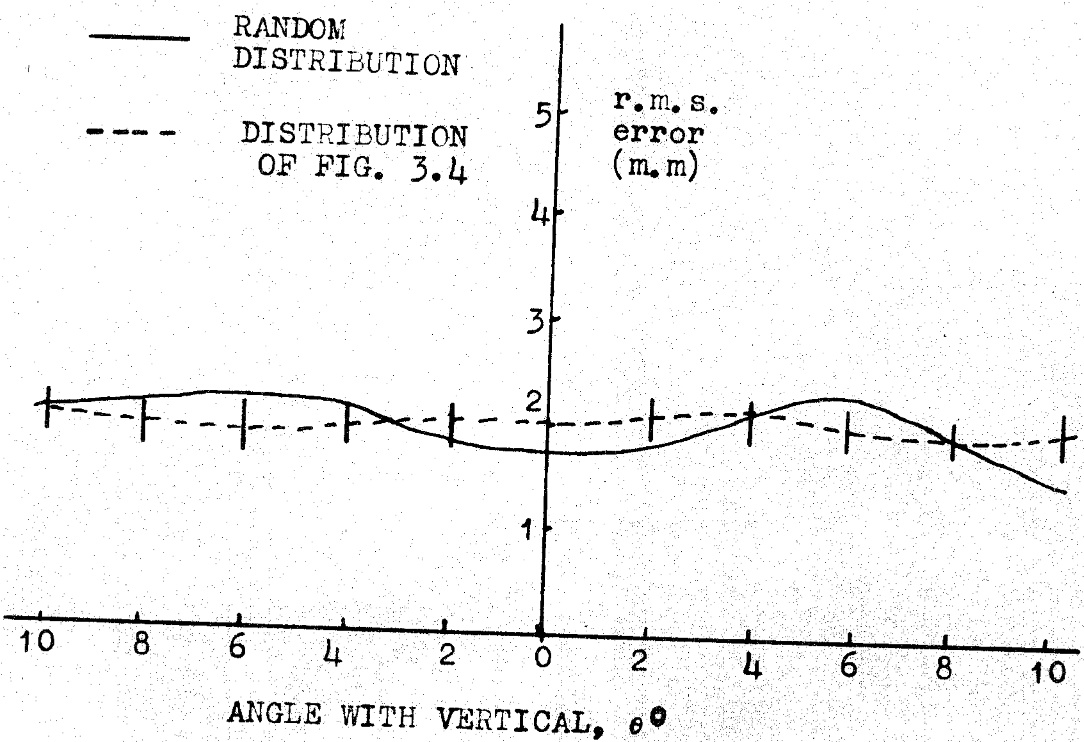

Figure 3.5 : Spatial resolution of a single flash-tube array (after Kisdnasamy, (1958)).

3.2.4 The Construction and Alignment of the Flash-tube Assemblies

There are four flash-tube assemblies or arrays, figure 3.6, those at A and D having about four times the horizontal area of B and C. The rectangular framework, figure 3.1 was constructed of aluminium angle. The slots which carried the tubes were milled in dural sheets which were subsequently cut into strips. The accuracy of milling was 0.1 mm (4 'thou') and the position of each tube was thus known to this accuracy. The profile of the slots, figure 3.1b, was such that selected tubes having external diameter between 7.85 mm and 7.15 mm rested on only two points of the slot.

Tubes were also selected for their straightness; the shorter ones were required to have a sagitta of less than 0.5 mm and the longer tubes about twice this value. Any curvature of the tubes was made to contribute least to the positional uncertainty of track location by positioning the tube so that the curvature was in a vertical plane. Two layers of tubes were contained between one pair of electrodes, figure 3.4.

It was essential that the tubes in the various levels of each tray were parallel to one another. A rectangle, two of the sides of which were accurately parallel to the tubes, was scribed on the top of the framework of the trays.

Circles of known radius were drawn with these corners as centre. The points of intersection of these circles, G_1 and G_2, have coordinates which are well known with respect to the tube centres, and also grids g_1 and g_2, which consist of lines scribed 0.05 cm apart. Holes of 2 mm diameter were drilled with G_1 and G_2 as centres. Two plumb lines forming a vertical plane perpendicular to the Geiger counters in the different levels, passed through the holes in the four frameworks (figure 4.1). Measurement of the vertical separation of the trays and their position with respect to the centre of the magnetic field then allows an accurately known coordinate system to be set up in which tube centres are well defined. The frames were kinematically located and clamped in their final position.

3.2.5 The Lifetime of Flash-tubes

This has been investigated by Coxell et al, (1960) and estimated to be $\sim$75 years. In the spectrograph, under operating conditions, only ten tubes out of 2672 were observed to become unusable either through not working, or giving spurious flashes. This was mostly due to fracture of glass seals. The few bad tubes were allowed for in the analysis of the data.

3.3 The Spectrograph

3.3.1 The Layout and Mode of Operation of Flash-tubes

The general layout of the flash-tubes in the spectrograph is shown in figure 3.6. The incident and emergent trajectories are located at four measuring levels, $G_A - A$, etc, two measuring levels above the magnet and two below. The magnet is a large electromagnet of the Blackett type and the spectrograph consists of Geiger counters as the detecting elements and hence defining the solid angle of acceptance of the instrument. Trajectories of particles through the central linear portion of the magnetic field is made certain by the Geiger counters near the centre of the field, and it is not possible for particles to be scattered in the pole pieces. The Geiger counters alone are used in studying the low momentum particles where the precision required in track location is less and the flash-tubes are used in conjunction with the Geiger counters to give a greater precision at high momentum.

3.3.2 The Geiger Counter System

The electronic circuits used with the Geiger counters have been fully described by Jones et al.,(1962), and only a brief description will be given here.

Passage of a particle through the spectrograph is registered by a five-fold Rossi coincidence from the Geiger counters G_A, G_B, G_G, G_C, G_D. The deflection is computed automatically by an electronic analogue computer referred to as a momentum analyser, (M.A.).

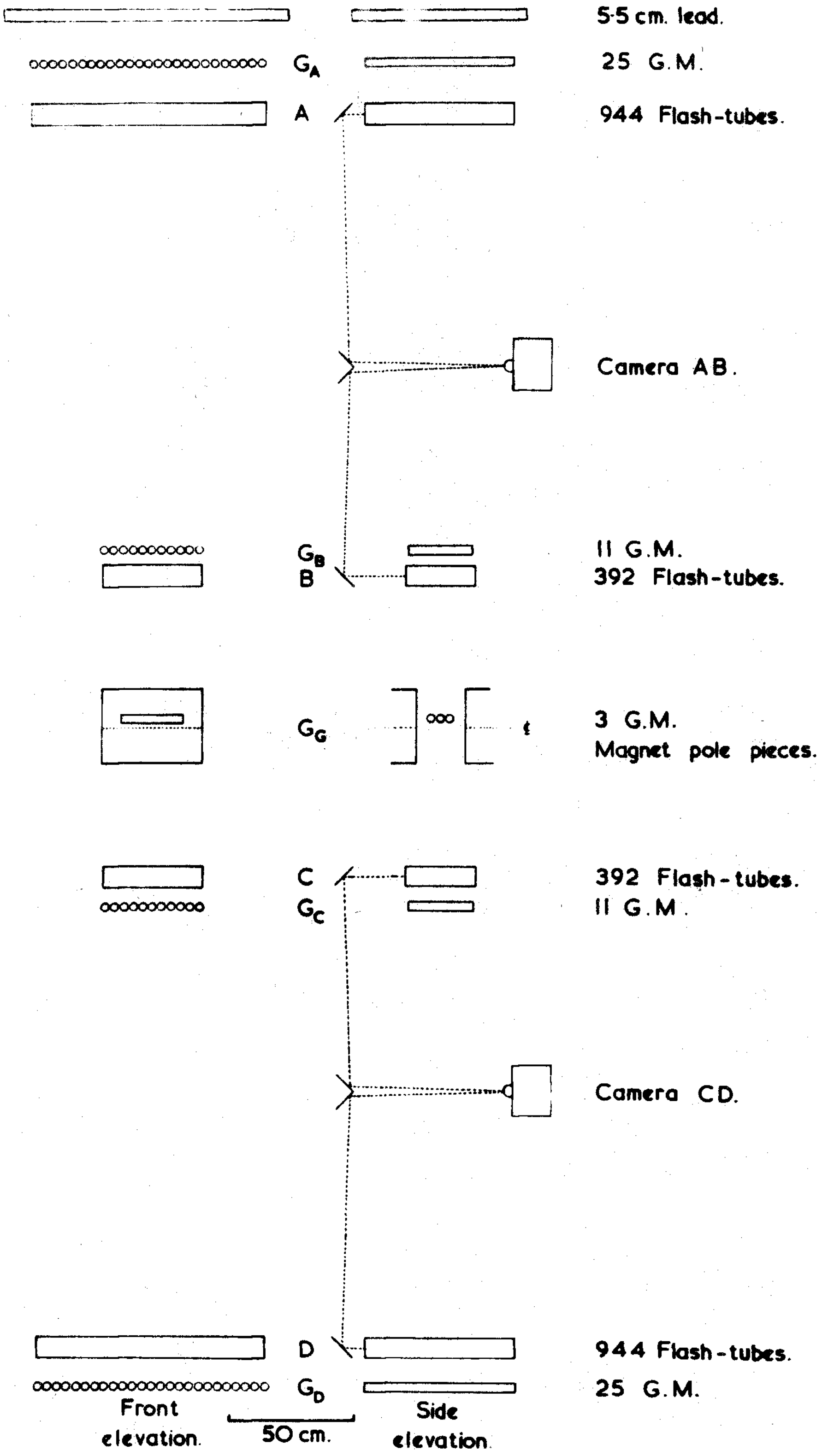

Figure 3.6 : The spectrograph.

From figure 3.7 it can be seen that the deflection of a particle is not determined uniquely by the Geiger counters - rather, because of the large relative size of the counters, deflections are assigned to groups whose mean magnitude differs by the distance by which Geiger counters are spaced at each level. The term, "Geiger counter categories", or "categories" is applied to these groups. Thus in the figure it can be seen that the nominal deflection in the Geiger counter system is

$$\begin{aligned} \Delta &= n_A - n_B - (n_C - n_D) \qquad 3.1 \\ &= (11+k) - (13+k) - (13+k) - (11+k) \\ &= n \times 3.8 \text{ cm} \end{aligned}$$

where in this case $n = -4$ and the distances are from an arbitrary reference line to the centre of the Geiger counter that has been discharged in G_A, etc. Each Geiger counter, through electronic circuits, gives a pulse which is characteristic of its position in that layer and by adding these pulses according to equation 3.1, a resultant pulse is obtained which is proportional to the deflection and is in fact the counter category number n. The final voltage pulse is displayed on an oscilloscope and can be photographed or can be fed into a pulse height analyser. On the oscilloscope there is allowance for 45 categories from -22 to +22. The normal rate at the highest magnetic

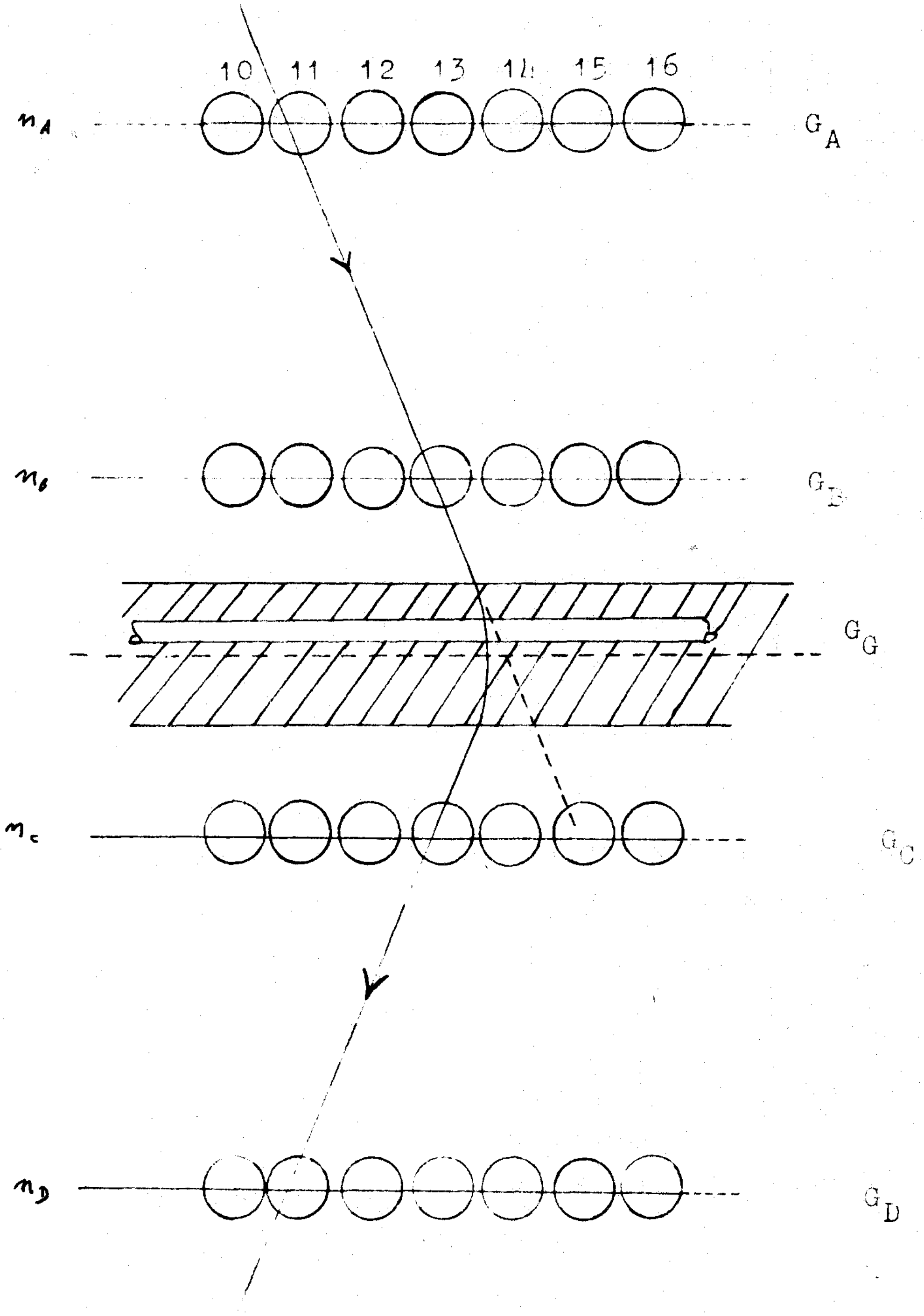

Figure 3.7 : The location of the particle trajectory with the Geiger counters.

field is ~200 particles per hour. The time taken between the passage of a particle through the four Geiger counter levels, and the rise of the fast leading edge of the Rossi coincidence pulse is 1.5 μsec. Further time delays are considered in subsequent sections.

3.3.3 The Momentum Selection System

The Geiger counter system is used in studying the momentum spectrum in the range 0.5 - 15 GeV/c at maximum field. To assist with the analysis of data at high energies and to more rapidly obtain higher statistical accuracy, particles corresponding to deflections of 0,±1,±2 Geiger counter categories are selected electronically and only these particles are allowed to trigger the high voltage pulse to the flash-tube arrays. This is done by using a pulse height selector (momentum selector, M.S.), D.G.Jones, (1961), figure 3.8. The characteristic of acceptance of pulse heights by this selector is biassed in favour of high energy particles (category 0). The time delay in this unit is ~7.5 μsec. This arises from the gating circuits which require a pulse from the Rossi coincidence circuits, where there is already a delay of 1.5 μsec and the resultant pulse from the M.A. circuits where a 5 μsec delay occurs, before the discriminator can operate and generate the triggering pulses for the flash-tubes. Thus

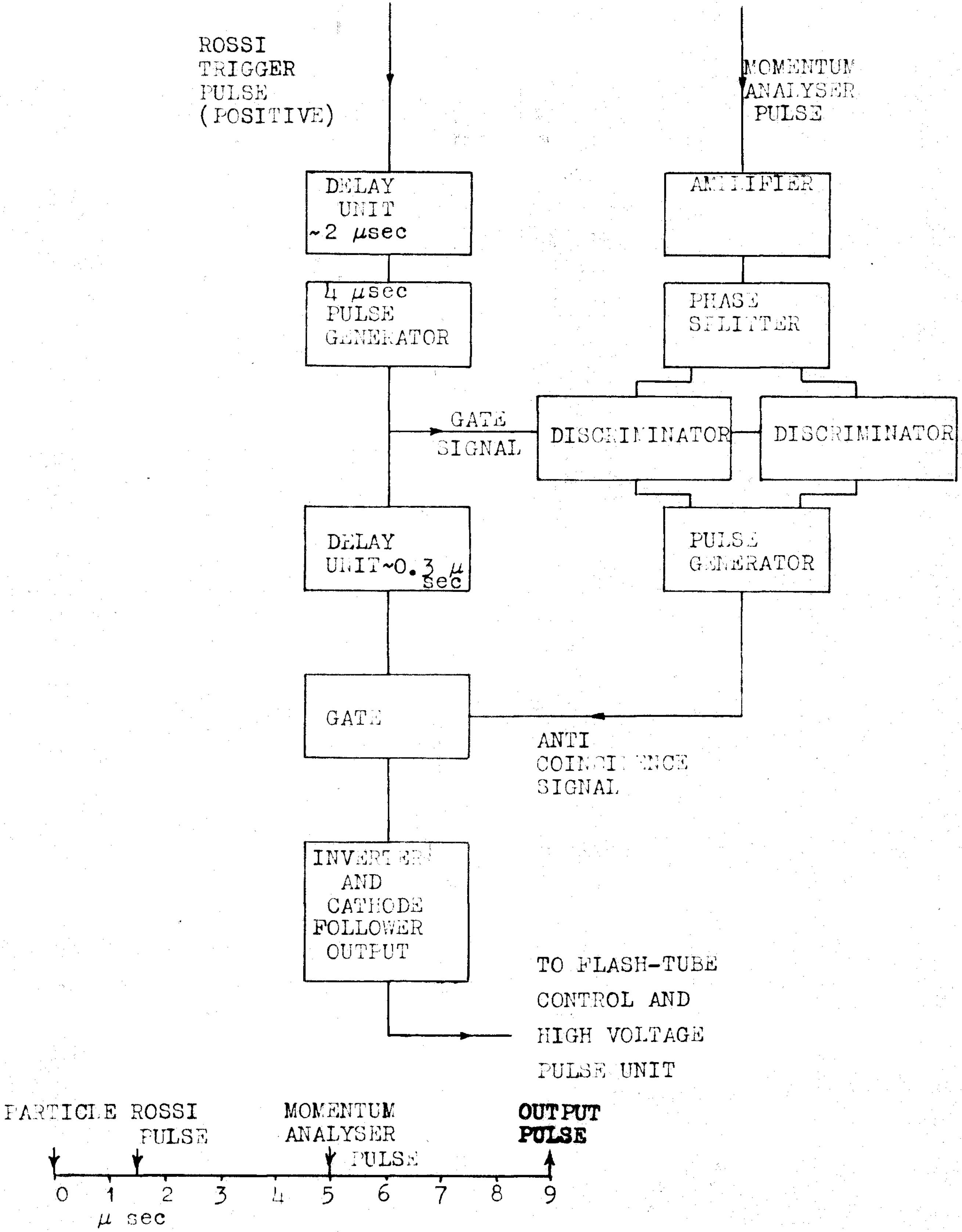

Figure 3.8 : The momentum selector.

the time delay between passage of a particle and the appearance of the fast leading edge of the M.S. pulse is 9.0 μsec.

In selecting category 0 pulses only, a fraction of these (~25%) are lost because of the variability of pulse heights created by the different combinations of Geiger counters which can give rise to a given pulse category (see Chapter 5). The rate of acceptance of particles in category 0 is ~ 8 - 10 per hour. The momentum selector demands only that the pulse height should be small. This condition can also occasionally be satisfied when more than one particle passes through the spectrograph, and can be recognised in the flash-tube photographic records (see section 3.5.1).

3.3.4 The Flash-tube Data Recording System

When a high momentum particle is detected, 3.3.2, 3.3.3, a high voltage pulse of rise time 0.5 μsec of length 6 μsec and height of 7.5 Kv/cm is applied across pairs of layers of flash-tubes, figure 3.4, after a further delay (already 9.0 μsec) of 1.0 μsec. The flashes in the four arrays of flash-tubes A, B, C, D, are then recorded by the two mirror-camera systems, figure 3.6. The whole of the flash-tube spectrograph is in a darkened enclosure. The cameras (Dallymeyer 2" focus lens at f 3.5) are shutterless and use 35 mm HPS (red sensitive) film. A typical

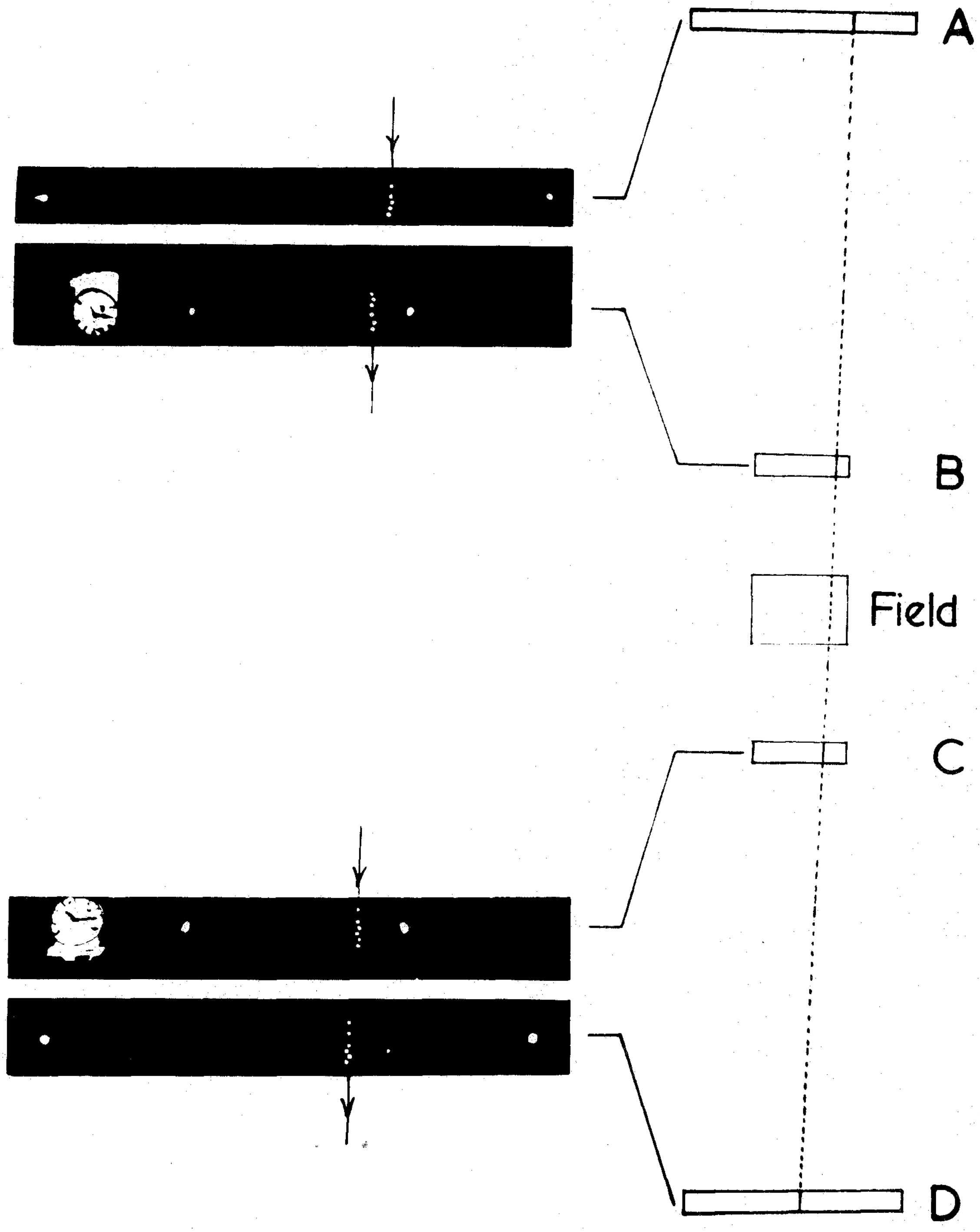

Figure 3.9 : A composite photograph showing the complete record of a fast particle.

record of a single particle is shown in figure 3.9. The large single images at the extremes of each record are electric lamps which are used to locate the record on a screen, (section 3.5.2). The clocks are used to correlate data from the two cameras. The nominal 'capacity' of the cameras is $\sim$3000 records.

3.4 The Electronic Circuits

3.4.1 The Flash-tube Circuits

A block diagram of the units generating the high voltage pulse for the flash-tubes is shown in figure 3.10. The input from the momentum selector is taken into a first stage (cathode follower) which then triggers a small hydrogen thyratron (CV 797). The output of this stage is then fed via a ferroxcube pulse tranformer to the grid of a high voltage hydrogen thyratron, (XH8-100), which discharges a 0.5 μsec delay line, charged to +8 Kv, through a pulse transformer. The output of this transformer is then used to trigger six switching valves, CV 85, each of which discharges a bank of condensers charged to -8 Kv through a U.H.V. step up voltage pulse transformer. Thus the capacitance of the flash-tube arrays, which differ because of their sizes, can be separated. The large arrays, A and D, have two output units each, whilst B and C, which have only about a quarter of the capacity of A or D have one output unit each. The final output pulse, of about 20 Kv,

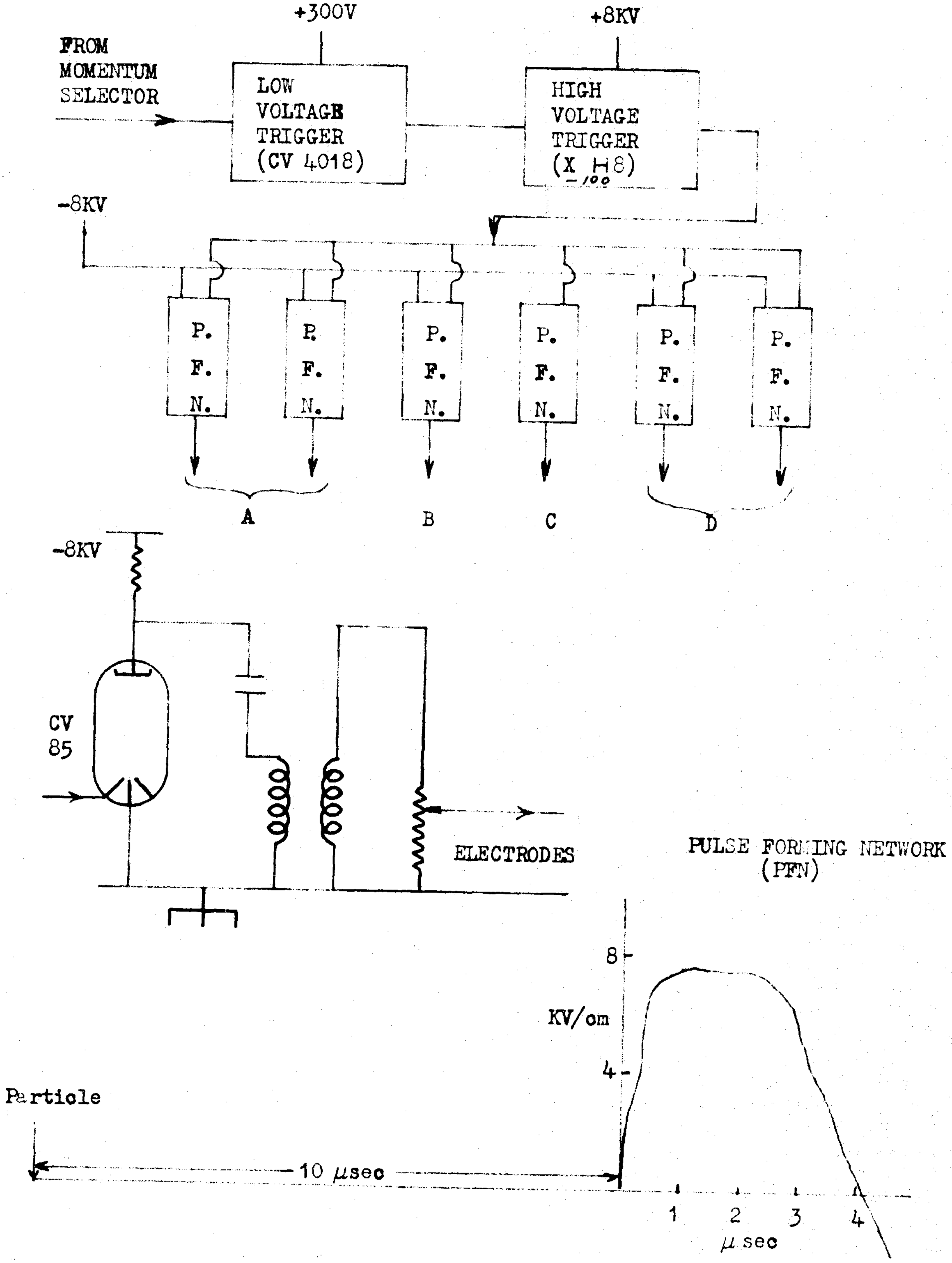

Typical high voltage pulse profile

Figure 3.10 : The high voltage pulse generator

rise time of 0.5 μsec and length 6 μsec can be matched to the individual electrode capacitance by feeding the pulse into a resistor chain, and taking the pulse to the electrode of the flash-tube arrays from a suitable tapping point. It was found that this resistor chain was very critical and it was necessary to use many resistors to prevent tracking and to obtain reliable operation over long periods.

3.4.2 The Control Circuits

The momentum selector output pulse is also used to set off the data recording apparatus, figure 3.11, which then successively performs the following operations.

1. Further trigger pulses are suppressed, by earthing one channel of the Rossi coincidence circuits (paralysis).

2. Reference bulbs on the faces of each flash-tube array are made to glow, and clocks, one in each camera system are illuminated so that the records can be correlated and the time of the event noted.

3. The cameras are wound on ready for the next event to be recorded.

4. The paralysis is removed.

3.5 The Experimental Measurements

3.5.1 The Selection of Events

The photographs were projected and events selected

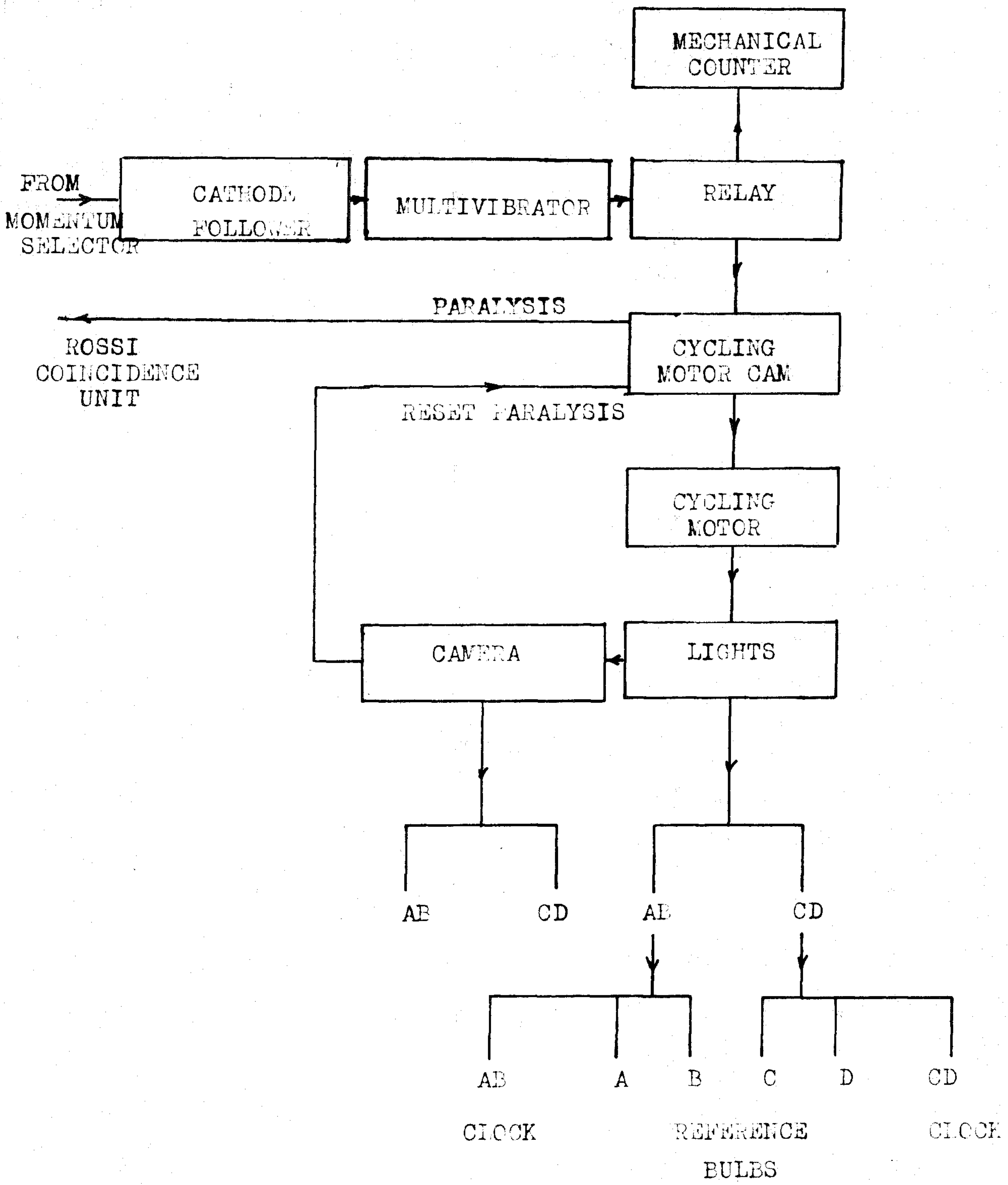

Figure 3.11 : The control circuits.

which corresponded to the passage through the instrument of either a single particle or a single particle accompanied by one other particle through one flash-tube array.

Of the latter events only those cases were accepted in which it was apparent from the photographic record (AB or CD) that the triggering particle and the accompanied particle could be distinguished. Since the events were in the first place selected electronically by the momentum selector, which demanded that the category number should be small, the majority of multiple events were rejected automatically. In practice, this meant that the only accompanied particles accepted were those few which generated "knock-on" electrons within the instrument, the electrons passing through gaps in the Geiger counters, and a few cases of widely separated μ-mesons. The accepted accompanied events amounted to 6% of the total.

3.5.2 Measurement of Films to give Particle Trajectories

A conventional projection system consisting of a single 35 mm film projector, set in a system of mirrors (not to be confused with the mirrors used in the spectrograph) is used so that the final image of the record for half of the spectrograph falls on to a moveable screen on a table. It is only possible to determine from the record, the projected distance of the trajectory from a fixed point on the front plane of the flash-tube array. Referring to figure 3.12, if a, b, c, d, are the distances of the trajectory to fixed points on the arrays (the reference bulbs on figure 3.9 are used to find these) and a_o, b_o, c_o, d_o are the distances of the fixed points to the arbitrary reference lines, figure 3.12, then the magnetic deflection is given by

$$\Delta = (a+a_o) - (b+b_o) - 0.972 \left[(c+c_o) - (d+d_o)\right] \qquad 3.2$$

$$= \Delta_o + (a-b) - 0.972\ (c-d)$$

$$\text{where}\ \Delta_o = (a_o-b_o) - 0.972\ (c_o-d_o) \qquad 3.3$$

The factor 0.972 reduces the measurements in the bottom half of the spectrograph to the same vertical distance as those measured in the top (see table 3.2). Only a, b, c, d will vary because of the particle positions in the trays.

Any errors introduced because of distortion produced by the (thin) mirrors in the spectrograph are reduced by projecting the films on to screens on which was drawn a complete diagram of the tube system for each array. These diagrams were drawn using photographs in which all the flash-tubes had flashed and the reference bulbs glowed and were obtained by irradiation of the arrays in turn by a γ-ray source during the application of a succession of several high voltage pulses. Thus the position of each photograph, and in particular the position of "flashed" tubes, could be related to the position of the reference

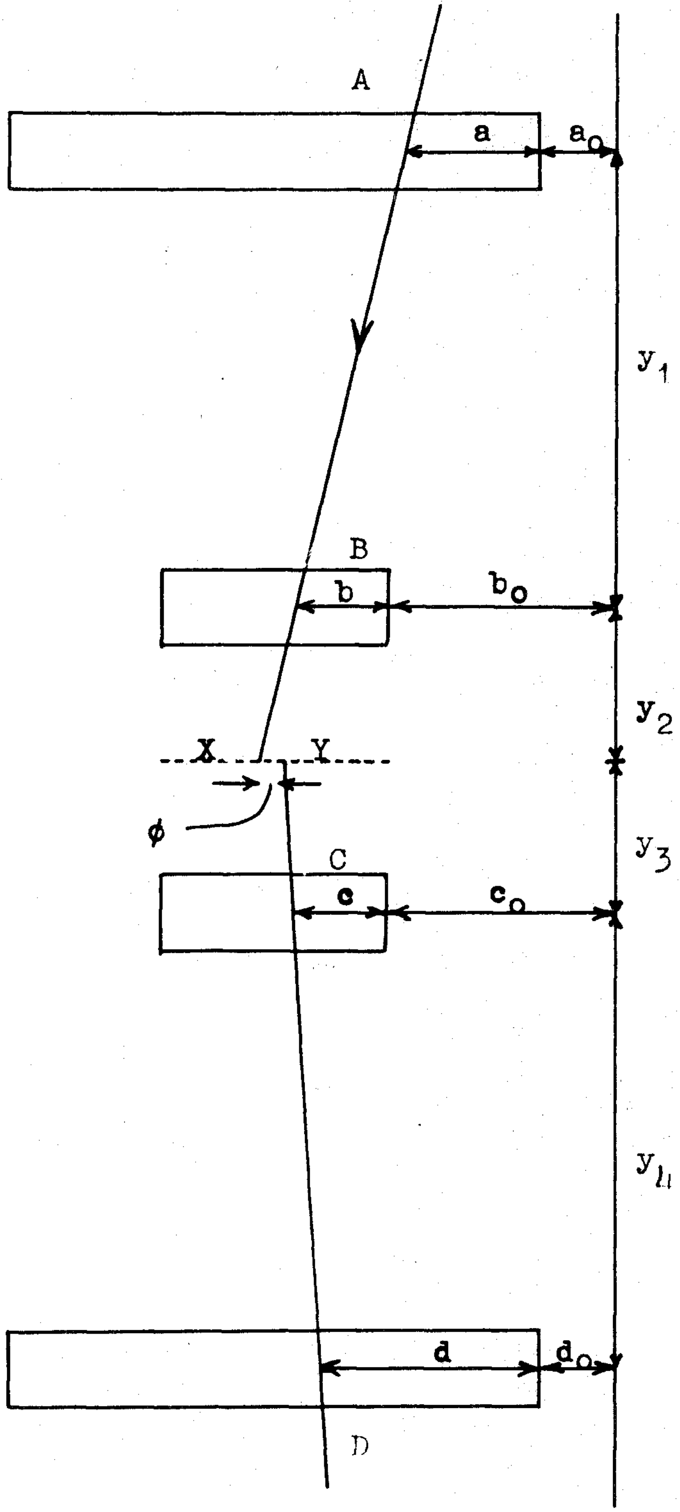

Figure 3.12. The dimensions to be measured in the flash-tube section of the spectrograph.

bulbs on the screens. The scale on which the distances a, b, c, d were read, was close to the centre of the array. The spacing of the tubes was used for the scale (units of 0.8cm or tube spacing, t.s.). The scale diagrams for the top and bottom halves of the spectrograph were drawn separately on screens, and the data analysed independently.

This method does not use the information given by the large separation of the levels for each half of the spectrograph (~1.8 m). Only a rough estimate of the parellelism of the set of flashes (figure 3.9) can be made. This sets a limit to the accuracy of measurements (see section 5.6).

This method of measurement will subsequently be referred to as the "projection method".

3.5.3 The Track Simulator

In order that all the information given by the flashes can be used, a scale model of a typical cross-section of the flash-tube array has been made. The cross-section has been enlarged by a factor of ten in the horizontal direction, where greater accuracy is required, and by three in the vertical direction, to make it of convenient size for comfortable manual operation. The measurements made by the method of 3.5.2 give the angle of the trajectory in each half of the spectrograph to quite high accuracy. The high momentum particles are selected for more accurate measurements, using the data given in the previous section so that there is a large overlap region to this data. These events are then re-projected and the position of individual flashes in each level recorded on data sheets.

The model is shown in figures 3.13 and 3.14. Slots represent the positions of the sensitive portions of the flash-tubes - accurately at the edges where the limits of possible tracks are determined and approximately in the intermediate positions. When illuminated from below the slots can be made to represent the exact geometrical configuration of flashes.

The establishment of criteria to be adopted for determining the best estimate of the trajectory is one of some difficulty, because the tubes do not have 100% internal efficiency and a particle may occasionally cross a tube without the tube flashing or a tube may sometimes flash when not traversed by the triggering particle but by a locally generated knock-on electron which is not recognised as such.

In principle, if the variation of efficiency across the radius of a tube is known, some form of maximum likelihood method can be used to estimate the position of the best trajectory. Bull et al, (1962), have recently developed a computer technique using a method of this

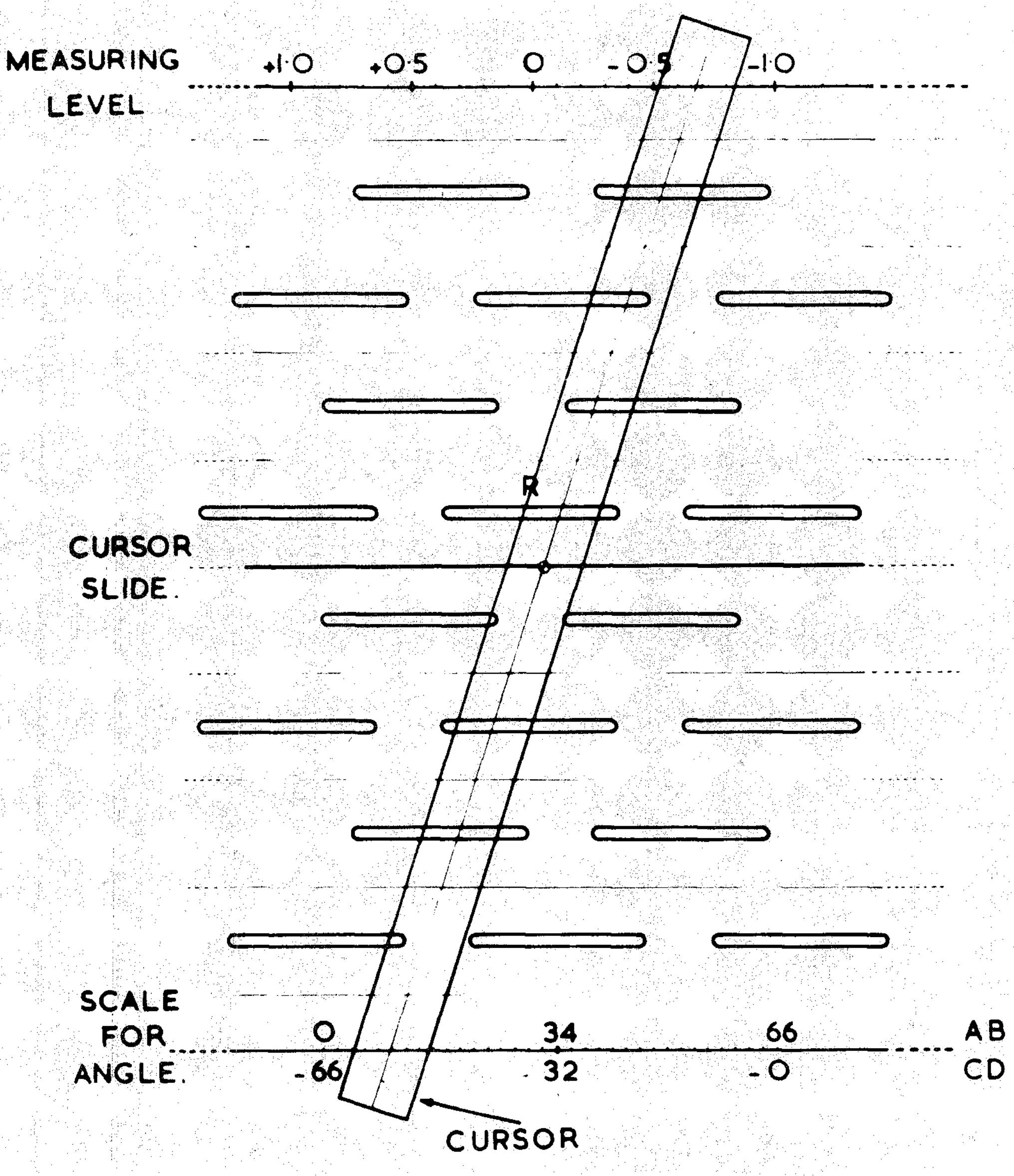

Figure 3.13 : The track simulator.

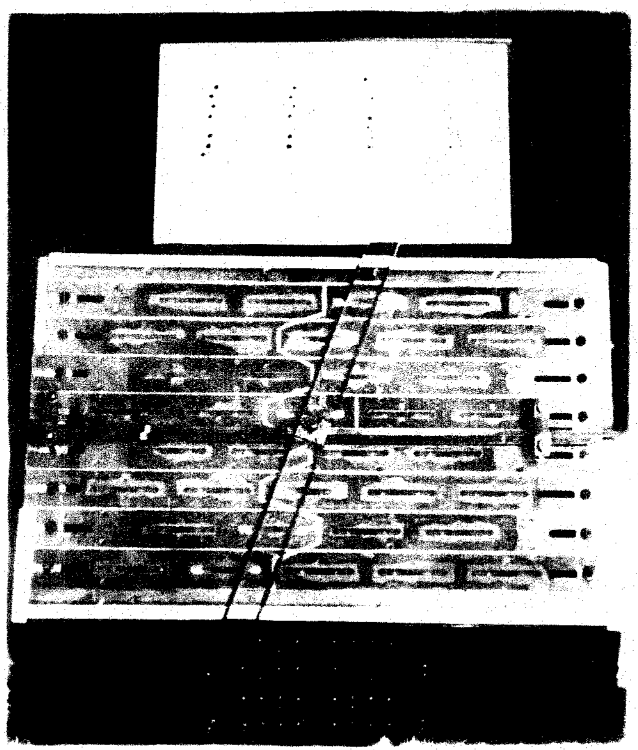

Figure 3.14 : A simulated event.

type. In the present work, however, it was felt that a computer method was unnecessary because of the small amount of data in the region where such high accuracy is necessary, and also because of the difficulty in allowing for the effect of the locally generated knock-on electrons which cannot be recognised by the computer, but which in many cases can be with the Track Simulator.

The cursor of the Track Simulator can be set to the correct angle given by the measurements in 3.5.2 (bottom scale) and using the edges of both "flashed" and "unflashed" slots the uncertainty in position or "corridor width" at each measuring level is obtained, such that the cursor only passes over illuminated slots and avoids other slots. The mean position in the corridor is taken as giving the best estimate of the particle position (top scale) and the particle deflection can be calculated as before.

Correction was made for the decrease in efficiency of the flash-tube as a function of their radius (figure A.4.3) by decreasing the radius slightly. This has the effect of increasing the corridor width slightly.

This method of measurement will subsequently be referred to as the "Track Simulator method".

3.5.4. The Calculation of the Data by Computer

The values of a, b, c, d (figure 3.12) obtained in 3.5.2 were punched out on computer tape and the values of deflection, Δ, and ϕ, (figure 3.12) have been evaluated using the Ferranti Pegasus Computer of the Durham University Computing Laboratory, by Mr. G. Brooke. The results are mostly presented in the form of histograms.

The computer also selects the particles which are remeasured by the method of 3.5.3.

In order that the number of histogram cells should be small, cut-off values of $|\Delta| = 6.5$ cm and $|\phi| = 0.8$ cm were selected, and all values greater than these values were rejected. Thus any combination of two particles, or more, which have simulated a fast particle and which have been measured because they satisfy the criteria for selection in 3.5.1 will almost certainly be rejected because of large values of ϕ.

Chapter 4

The Alignment Procedure and the Measurement of the Geometrical Constant

4.1 Introduction

In section 3.5.2 it was seen that measurement of the deflection of a particle involved the quantity

$$\Delta_o = a_o - b_o - 0.972\ (c_o - d_o)$$

which is a constant for all trajectories.

There are two methods of calculating this quantity. The values involved can each be measured directly on the spectrograph to a high degree of accuracy. This is a by-product of the alignment of the instrument during which the flash-tubes are made accurately parallel to each other.

Alternatively the spectrograph can be operated with zero magnet field. Then the "deflection" is composed of contributions due to multiple scattering in the spectrograph and errors of measurement. This distribution although it may not be purely Gaussian, would be expected to be symmetrical and the mean of the distribution gives

$$-\Delta_o = \bar{\Delta} = a - b - 0.972\ (c - d) \qquad 4.1$$

The method by which these two values are obtained will be outlined and the values compared. Ultimately the value of the m.d.m. depends on the accuracy of both the alignment and Δ_o.

4.2 The Alignment

4.2.1 The Calculation of Δ_o

The construction and alignment of the flash-tube assemblies described in 3.2.4 is extended here to cover the whole of the spectrograph. The alignment of the measuring levels within the spectrograph has been carried out by using a large template between the levels in each half of the spectrograph, figure 4.1. Fine mono-filament nylon ($\frac{1}{5}$ mm diameter) suspended above G_A, figure 3.6, and carrying weights below D, passed through holes in perspex plates at the north and south ends of each tray of flash-tubes. Similar temporary nylon filaments were used at the front, and rear in turn, of each tray to relate the position of a given milled slot to a grid on the template. Each level was rotated until the tubes were parallel. In this way the slots in each level were made parallel to an estimated accuracy of $\frac{1}{5}$ mm.

The value

$$\Delta_o = -65.01 \pm 0.05 \text{ units of } 0.8 \text{ cm} \qquad 4.2$$

was obtained.

The readings on the grids of the perspex plates at each level were checked periodically during the time the data were collected. No change greater than $\frac{1}{5}$ mm was detected.

4.2.2 The Staggering of the Arrays

This was remeasured with the trays in position and

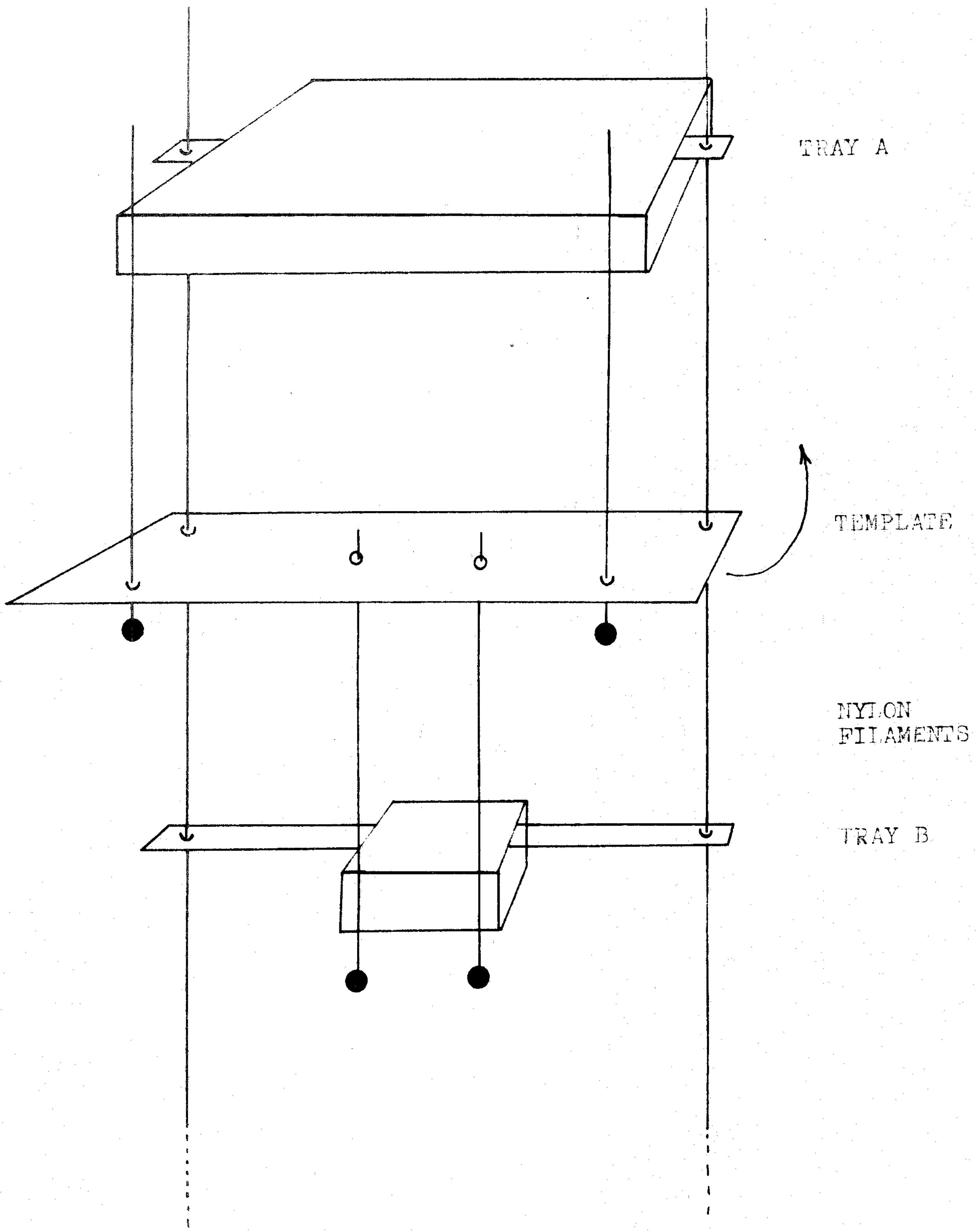

Figure 4.1 : The alignment of the flash-tube arrays.

full of tubes. This was an important measurement since distortion of the arrays could occur, especially the larger ones which held over 900 flash-tubes weighing over 100 lbs. No deviation of the staggering at the ends of each array greater than $\frac{1}{5}$ mm was detected.

4.2.3 The Accuracy of the Milling of the Slots

A strip was taken as standard and compared with an accurately engraved steel metre rule. Deviations of the strips used in the arrays, from the standard, measured at intervals of 5 tube slots, could thus be related to a true scale. No systematic deviation greater than $\frac{1}{5}$ mm was found. A map of the deviations was prepared which could be used in conjunction with the track simulator on the highest momentum particles, but in fact it was not found necessary to use it.

4.3 The Zero Field Measurements

The frequency distribution of Δ_o, equation 4.1, was obtained from flash-tube data on zero field both before and after the main set of data was collected, in order to see if there was any systematic movement of the flash-tube arrays. The histograms of these distributions are shown in figure 4.2 where they are compared with Gaussian distributions of the same standard deviation. The difference between the two distributions is due to multiple scattering of particles in the spectrograph. The mean values of Δ_o, are shown in table 4.1, together with the

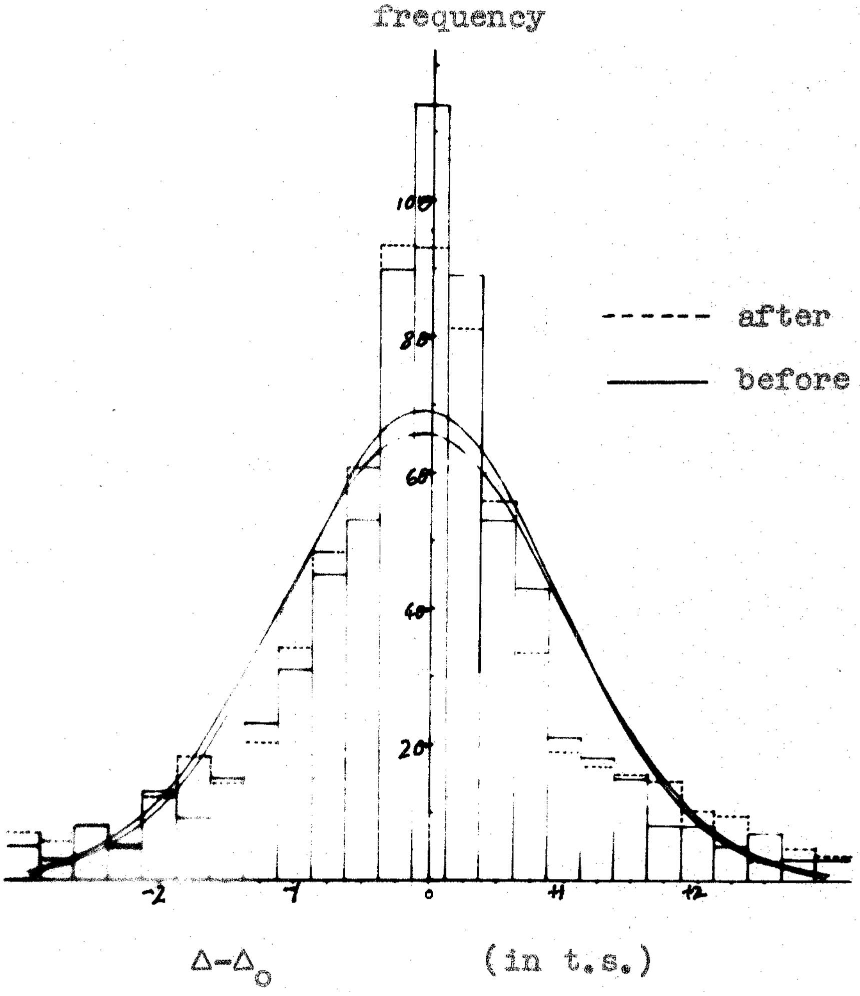

Figure 4.2 : The zero field distribution of Δ_o.

Table 4.1 : Comparison of measurements before and after run.

	Before	After	Combined	Measured value (4.2.1)
Δ_o	-64.94 ± 0.04	-64.93 ± 0.03	-64.94 ± 0.03	-65.01 ± 0.05
$\bar{K}$	-68.66 ± 0.05	-68.81 ± 0.04	-68.77 ± 0.03	$\underline{-68.77 \pm 0.04}$
$\bar{\phi}$	$+0.04 \pm 0.01$	-0.02 ± 0.01	0.00 ± 0.01	$+0.01 \pm 0.01$ (corrected for d_o)
no. of events	687	1579	2266	

All dimensions are in units of (0.8 cm).

values for other quantities derived from the same data.

There is good agreement between the values of Δ_o before and after the main run and also of the combined result with the measured value.

It is also possible to check the values of a_o, b_o, c_o, d_o individually by calculation of the geometrical constant for any three measuring levels at a time. When this is done all values containing d_o differ by a small amount from the values obtained from the frequency distributions involving the same measuring levels. However, when d_o is omitted, as in the geometrical constant $(\bar{K})$ for the three measuring levels, A, B, C, then there is good agreement with the frequency distribution calculated using the data from those levels. It is thus concluded that the value of d_o may have some slight systematic error and calculation shows this to be +0.04 cm, comparable with the accuracy of measurement attempted.

Another quantity which is used in later calculations ϕ, defined in figure 3.12, is given by

$$\phi = 0.985 + \left\{1.333\ b - 0.333\ a - (1.317\ c - 0.317\ d)\right\}\ \text{cm} \qquad 4.3$$

for the projection measurements of section 3.5.2.

The frequency distribution of this value is almost symmetrical about zero and the mean value is shown in the table. However the correction to the value of d_o affects the constant term in 4.3, but the change is only small; the corrected value of $\bar{\phi}$ is also shown in the table, (4·1).

The discrepancy in d_o is not unexpected in view of the methods adopted in its measurement. It must be remembered that the mono-filaments are effectively pendulums of length ~5 metres, and the weights of the bobs were limited by the available dimensions in which they were to hang.

4.4 Conclusions

It is concluded from the above measurements, that the geometry of the spectrograph is known to a high degree of accuracy - several times better than the overall uncertainty in the locational accuracy of tracks given by the most accurate method of measurement with the flash-tubes and that the best value of Δ_o, the geometrical constant of the spectrograph is given by

$$\Delta_o = -64.94 \pm 0.03 \text{ units of } 0.8 \text{ cm.}$$

Chapter 5

The Measurement of the μ-meson Momentum Spectrum at Sea-level

5.1 Introduction

The method of analysis in which the momentum spectrum is derived from the basic data involves the application of certain corrections to the basic data. Besides the normal corrections for the finite lateral extent of the Geiger counter system and magnetic field, which results in an increasing loss of particles as the deflection increases, and errors in the location of the particle trajectories, there is another correction introduced by the momentum selector.

The absolute intensity of particles is not itself calculated but in order to normalize the spectrum it was necessary to select some events from categories one and two, in addition to the highest momentum group in category zero, and before the μ-meson spectrum can be evaluated the relative acceptance of each of the categories must be accurately known.

In evaluating the μ-meson spectrum it is convenient to use an incident comparison spectrum, and to derive from this, using the instrumental corrections, the deflection spectrum that would have been observed in the experiment.

The various corrections will now be considered and the momentum spectrum derived in three overlapping bands, each of which has its own particular technique of track measurement and uncertainty for the deflection estimate. Finally, a best estimate of the differential μ-meson spectrum will be obtained and compared with previous results.

5.2 The Magnetic Field.

In the running of an extensive piece of apparatus many sources of errors, which can lead to bias in the data, can arise. To reduce these to a minimum the following procedures were adopted.

The greatest source of bias lies in the determination of magnetic deflection. To reduce this bias to a minimum, the direction of the magnetic field was frequently changed, normally daily, and its value was kept nearly constant during the period of collection of data. The mean value, $\bar{I}$, is given by

$$\bar{I} = 57.48 \text{ Amperes (r.m.s. deviation 0.87A)},$$

giving a value for the line integral of the magnetic field, figure 5.1, of,

$$\int H dl = 6.025 \times 10^5 \text{ gauss-cm}$$

The mean current and the mean, weighted for the numbers of particles accepted during each "run" of varying period, were not found to differ.

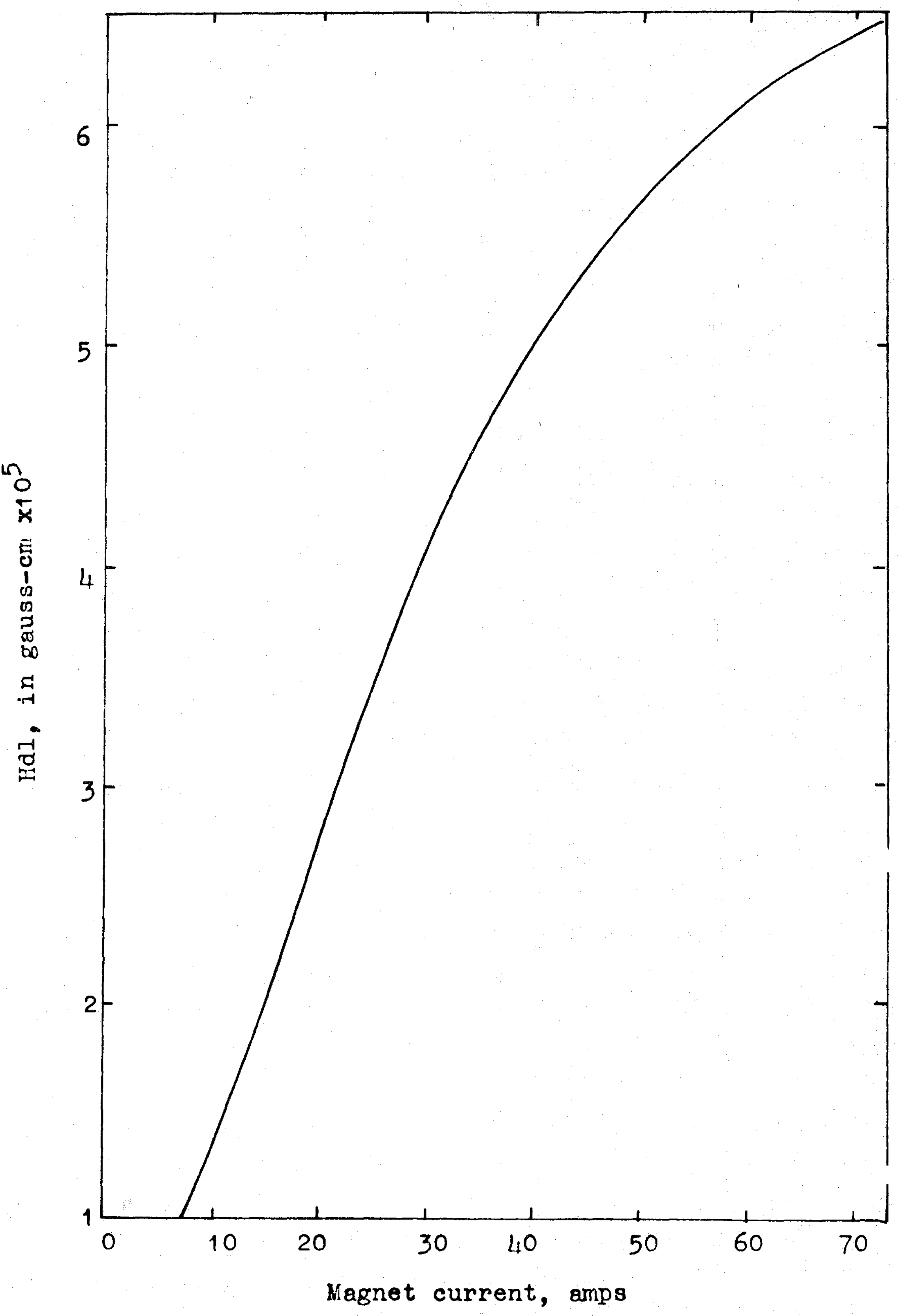

Figure 5.1 : The variation of the line integral of the magnetic field with the magnet current (after Brooke et al, (1962b)).

In terms of the separation of the layers A and B, the relation between magnetic deflection, Δ, and momentum, p, is given by (see equation 2.2b)

$$p\Delta = 41.64 \pm 0.08 \text{ GeV/c. t.s.} \qquad 5.1$$

$$= 33.31 \pm 0.06 \text{ GeV/c. cm.} \qquad 5.1a$$

By frequently reversing the field, bias, due to variations in the efficiency of the Geiger counter acceptance system or small amounts of assymmetry in the geometry of this system are largely removed. This is the case also for the momentum analyser where periodic changes in bias voltages are likely to occur. These forms of bias should not be confused with the magnetic bias imposed by the overall geometry of the counter acceptance system (section 5.4) which can be corrected for in the data.

The difference in running time for the two field directions amounted to 5 hours (more for negative field) but this was counteracted by accepting more particles (2%) for the opposite direction of field. This is especially important in regard to the determination of the positive-negative ratio of the μ-mesons at sea-level.

5.3 The Calibration of the Momentum Selector.

Before the selector can be used as described in section 3.3.3, it is necessary to know accurately the relative probability of selection of voltage pulses of different size since this will otherwise introduce bias into the measurements. The acceptance characteristic of pulses fed into the momentum selector i.e. the relative numbers allowed to pass through it, was obtained at the beginning and termination of each daily run. A mean characteristic of these two measurements was obtained.

The calibration was obtained by feeding in artificial pulses at a constant rate whose height could be varied to simulate the different pulse heights from the momentum analyser. The rate at which pulses were transmitted by the selector was then obtained. Typical curves are shown in figure 5.2, for acceptance of two different category groups. It can be seen that whereas nearly all pulses corresponding to category number 0 are passed for the larger acceptance curve, only 75% are accepted for the smaller curve. However the ratio of acceptance is far larger for pulse categories ±1. In order to more rapidly accumulate data in the high energy region, the smaller curve which is more biassed against the lower energy particles was used.

The relative numbers of particles in the categories passed by the selector, can be obtained if the distribution of pulse heights about the mean value for each category, is known. This distribution arises from the various combinations of Geiger counter geometries (and therefore

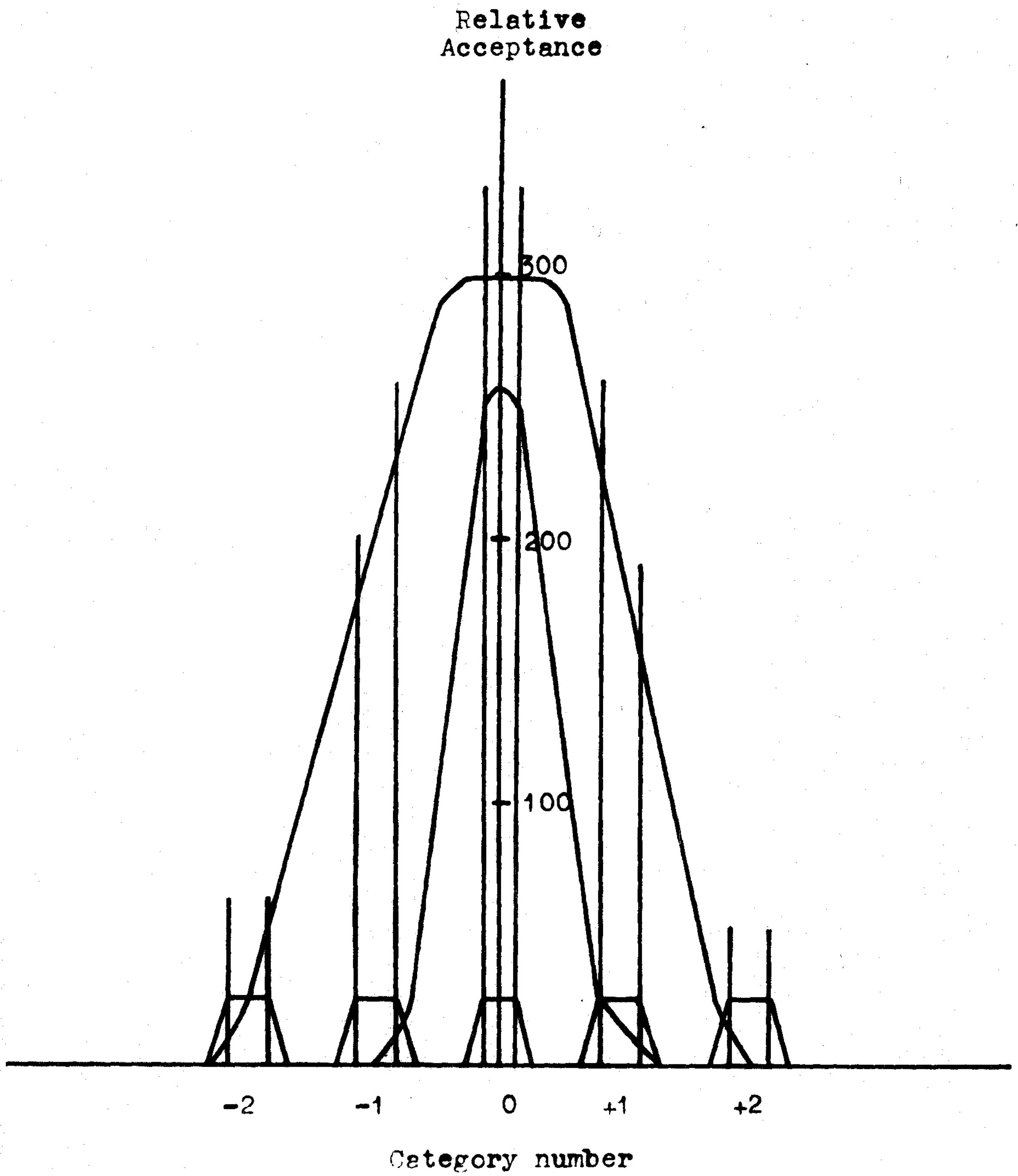

Figure 5.2 : The momentum selector characteristics for category 0 only, and categories 0, ±1 only.

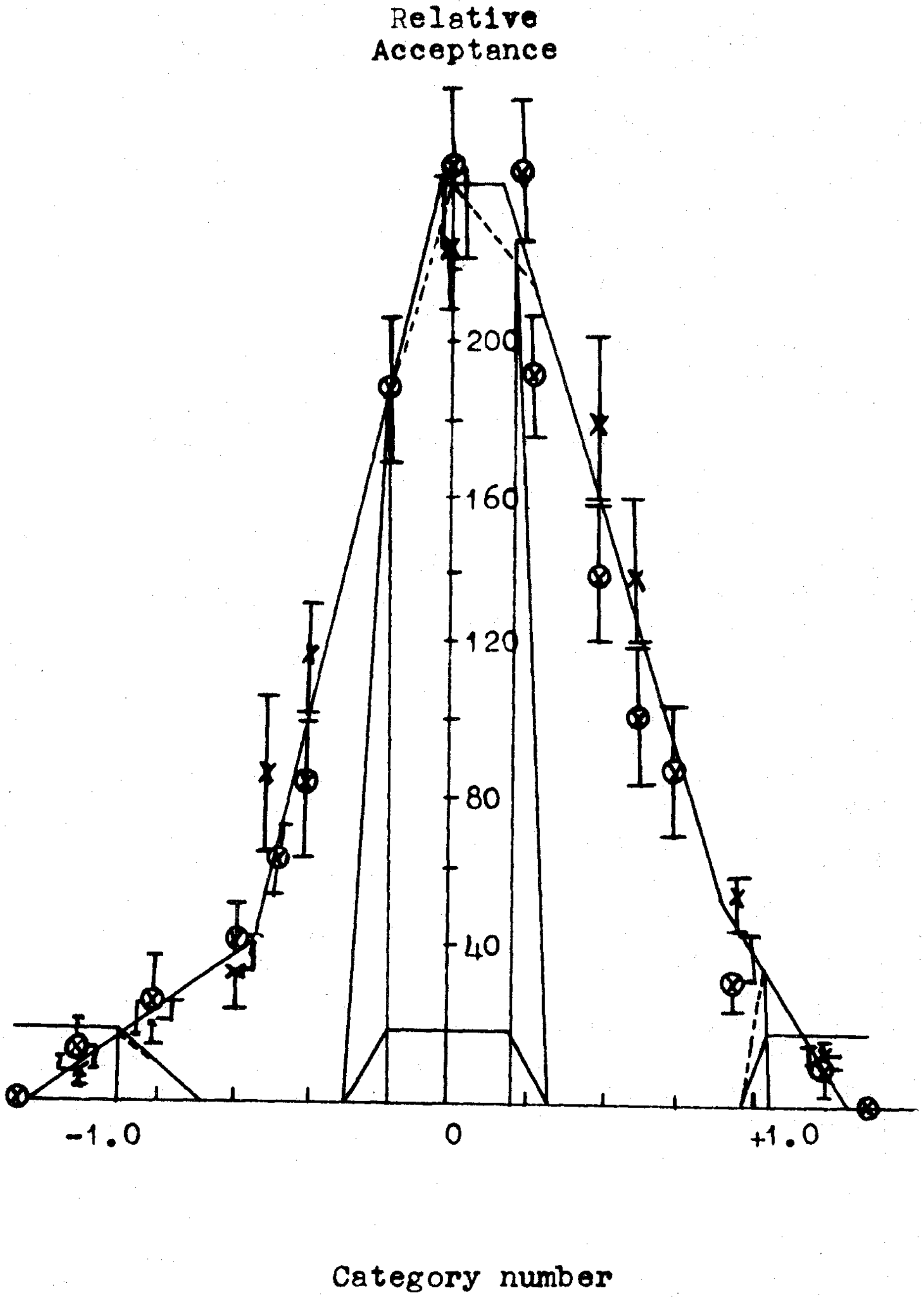

Figure 5.3 : A typical momentum selector characteristic.

voltages) which give rise to a given category, and the inherent inaccuracy of the voltages gives rise to a distribution of pulse heights about the ideal or mean value. This distribution can be represented by a function which is flat to a distance 0.15 categories from the ideal value and then falls linearly to zero at 0.25 categories (D.G.Jones, 1961). These functions will be centred about the means of the categories as shown in figure 5.2.

The relative probability of categories +1, 0, -1 being passed by the momentum selector will then be given by the product of the ordinates of the calibration curve and the distribution within a category and taking the ratio of the areas under the new curves so formed. A typical momentum selector characteristic is shown in figure 5.3.

The calibration data on positive and negative magnetic field were kept separate. Final separate sets of data were obtained which were representative of the total number of events gathered in the 94 "runs". These are given in Table 5.1. It can be seen that there is a small bias in favour of negative categories and negative particles.

5.4 <u>The Magnetic Bias</u>

The magnetic bias is determined by the overall geometry of the Geiger counter telescope as well as by the finite size of the Geiger counters alone. Both of these factors have been considered by Brooke et al, (1962b). The probability of a particle of deflection Δ being recorded in

Table 5.1 : The percentage of particles in the categories from the momentum selector calibration.

Magnetic field	Mainly positive particles*	pulse category	Mainly negative particles*		No. of films
	+1	0	-1		
positive	4.69	91.68	3.63	%	49
	-1	0	+1		
negative	4.67	92.42	2.92	%	45
Total	3.84	92.04	4.12	%	94

* due to overlapping of acceptance characteristics of Geiger counters.

Table 5.2 : The percentage of particles in the categories from a representative sample of particles.

Magnetic field	Mainly positive particles		Spectrograph counter category	Mainly negative particles			Total Number
	-2	-1	0	+1	+2		
positive	1.0	24.44	65.8	8.3	0.5	%	970
	+2	+1	0	-1	-2		
negative	0.8	11.5	68.2	18.5	1.0	%	1004
	-2	-1	0	+1	+2		
Total	1.0	21.6	67.0	9.8	0.6	%	1974

Table 5.2 : The comparison of the computer and drawing methods.

Method/Spectro. cat.no.	-2	-1	0	+1	+2	
Drawing	1.0	21.6	67.0	9.8	0.6	%
Computer	0.86	20.8	67.3	10.04	0.69	%

a given category, (conveniently taken to be category zero), called the elementary function $G(\Delta)$ is given in figure 5.4a. The overall acceptance function $A(\Delta)$ which arises from the finite lateral extent of the magnetic field and Geiger counter trays, is given in figure 5.4b. To obtain the acceptance function for a category number n the mean of the elementary function curve is moved by 3.8 x n cm and multiplied by $A(\Delta)$. Correction has been made for the shorter separation of the flash-tube measuring levels, A, B.

5.5 The Alternative Derivation of the Relative Numbers of Particles in the Categories

It was felt that an independent check on the momentum selector characteristic was desirable. A representative sample of films was selected, comprising some 1974 particles on both field directions. A scale drawing of the spectrograph was made giving the flash-tube measuring level scale position and also the Geiger counter positions. Using a perspex cursor, the position of the trajectory of the particle was reconstructed with the values a, b, c, d, figure 3.12, and the particular Geiger counter intersected at each level was noted. Thus it was possible to obtain the numbers of particles occurring in the categories.

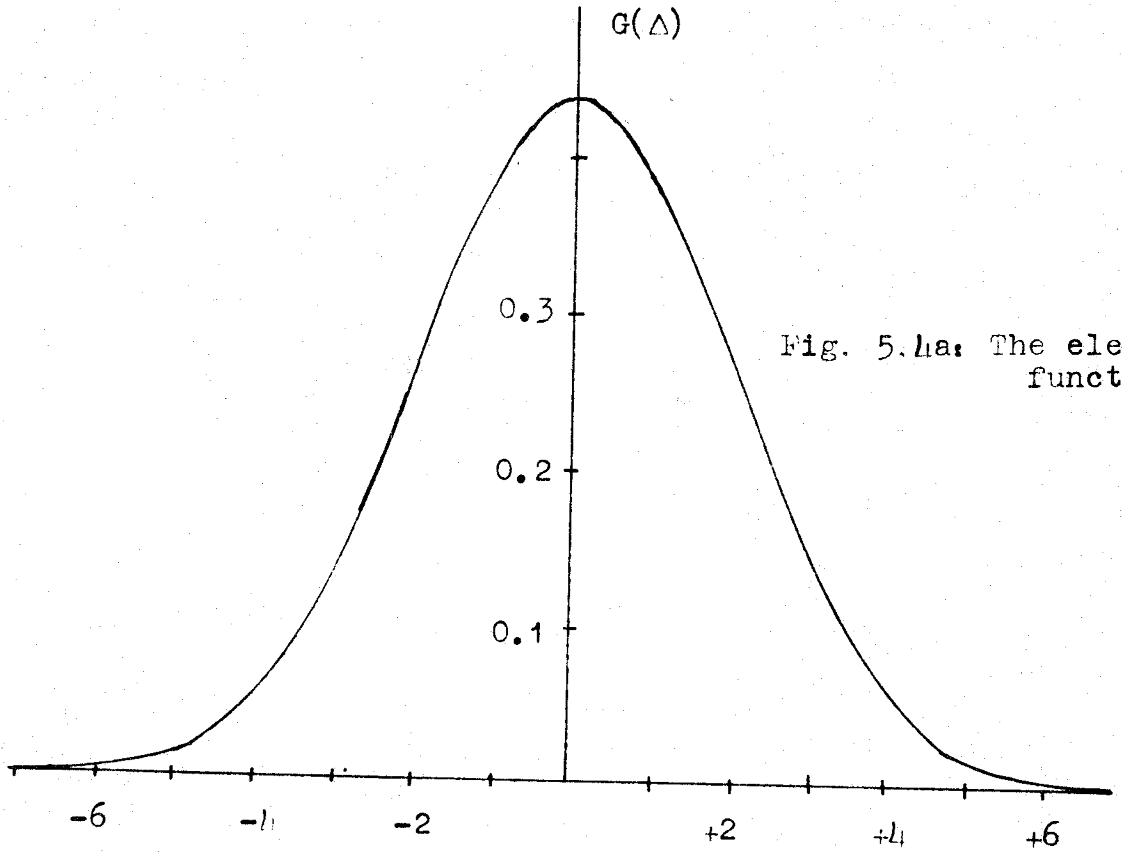

Fig. 5.4a: The elementary function.

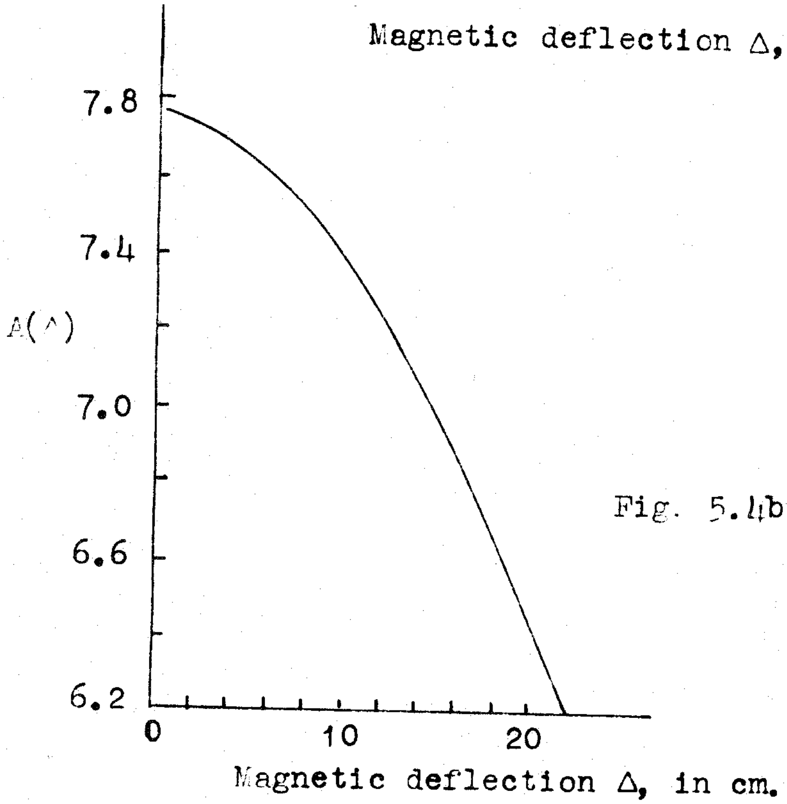

Fig. 5.4b: The acceptance function

(after Brooke et al, 1962b)).

Since the data used in the spectrum determination (section 3.5.4) only had deflections in the range $-6.5 \leqslant \Delta \leqslant +6.5$ cm in order to simplify the calculation and storage in the computer calculation programme, then only fractional parts of the categories with values of deflection in this range will be required. The deflection spectra of the various categories was calculated using the momentum spectrum previously determined, Ashton et al, (1960). Applying this correction for the spectrum, then the relative numbers in the categories is obtained, table 5.2. The effect of the positive-negative ratio on the bias was subtracted out by the addition of the data for both field directions for a given category. Equal numbers of particles were considered on each field direction.

The conclusions to be drawn from comparison of tables 5.1 and 5.2 are that some unknown source of error is present in the calibration procedure of the selector. This may be due to the relatively large rate at which pulses are fed into it, ~ 360/min, compared with the experimental rate ~ 3/min. Since using the particles themselves obviously gives a more reliable category distribution this data has been used in the derivation of the spectrum carried out in this chapter. The form of the variation of the momentum selector bias over two ranges of Δ is shown in figures 5.5a and 5.5b. It is

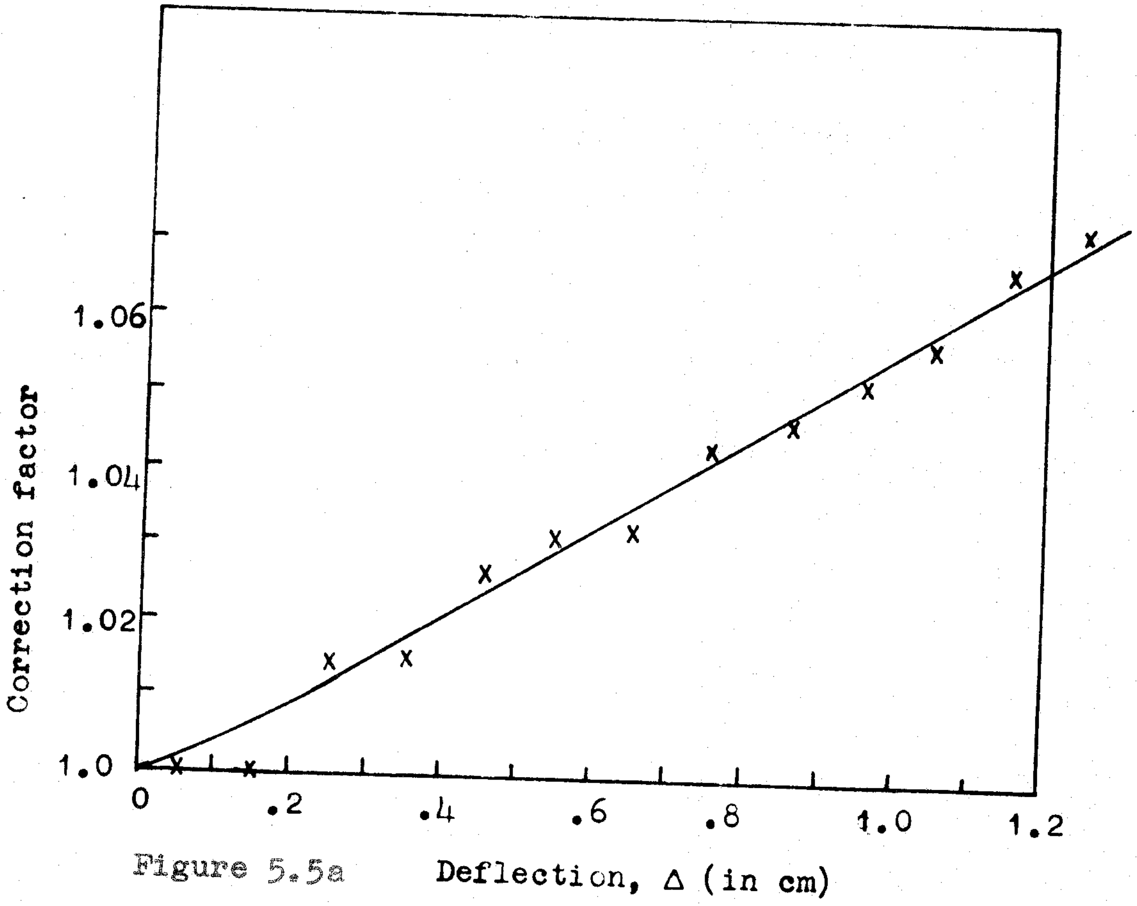

Figure 5.5a

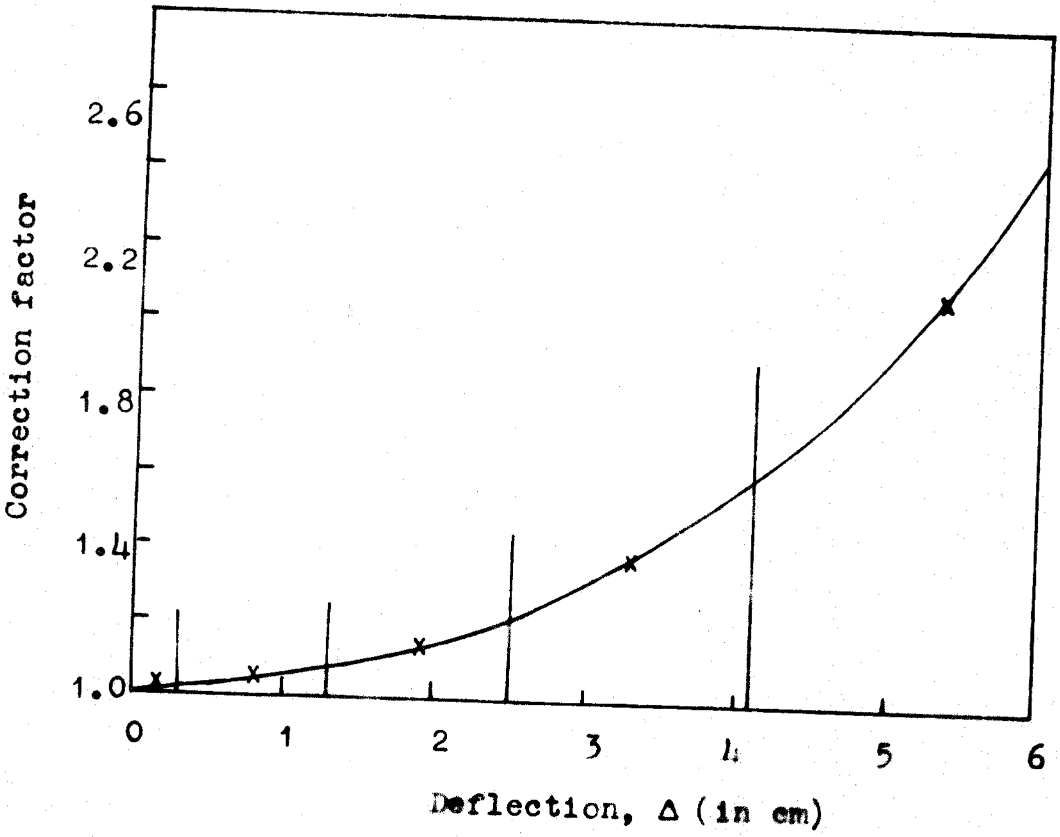

Figure 5.5b: The momentum selector bias.

seen that the number of positive particles accepted exceeded the number of negative particles accepted. This will be further considered in section 7.3.

A further check was afforded independent of any assumed spectrum, with a direct calculation by a computer programme of the distribution of particles in the categories using the data accepted by the computer. In this programme the procedure previously adopted using the scale drawing was carried out by algebra. The result of the computer programme and the drawing method are compared in table 5.3. In the drawing technique corrections were made for the inaccuracy of track location with the flash-tubes, measured by the projection method. This amounted to a 6% loss of particles.

In both techniques also, a certain fraction of the data gave trajectories which passed through the gap between Geiger counters. These are attributed to particles which produce "knock-on" electrons which trigger the Geiger counters or to two particles or small local showers or parts thereof, passing through the apparatus. These later events can also be recognised by the incoherence of their trajectories at the centre of the magnetic field (ϕ, figure 3.12). The percentage of particles rejected in this way was 12%, in good agreement with the expected value for "knock-on" electrons of 4%, for each of the four measuring levels, e.g. (Lloyd and Wolfendale, (1959)).

5.6 The Errors in the Deflection Measurements by the Projection Method

The measured deflection derived from the position of the flashes in each level is not the true magnetic deflection, but a combination of magnetic deflection, scattering deflection, and a component due to the location error, arising from the geometry of the flash-tubes. The dependence of these quantities on each other is derived in Appendix 1. Thus if $\bar{\phi}^2$, equation A1.4, is plotted against Δ^2, the slope of the graph will give K and the intercept, δ_q.

The calculation was carried out in two parts. In order to get the intercept $\bar{\phi}_0^2$ accurately, 958 particles were used, having Δ in the range

$$-1.2 \leq \Delta \leq +1.2 \text{ cm} \quad (\beta \simeq 1)$$

The relation between $(\bar{\phi})^2$ and $(\Delta)^2$ is shown in figure 5.6a. Using the expected value of K' (equation A1.3), the r.m.s. error at a single measuring level δ_a can be derived from the intercept,

$$\delta_a = 0.091 \pm 0.003 \text{ cm} \qquad 5.2$$

This corresponds to a total r.m.s. error for four measuring levels

$$\delta_T = 0.181 \pm 0.006 \text{ cm} \qquad 5.3$$

or a median value of

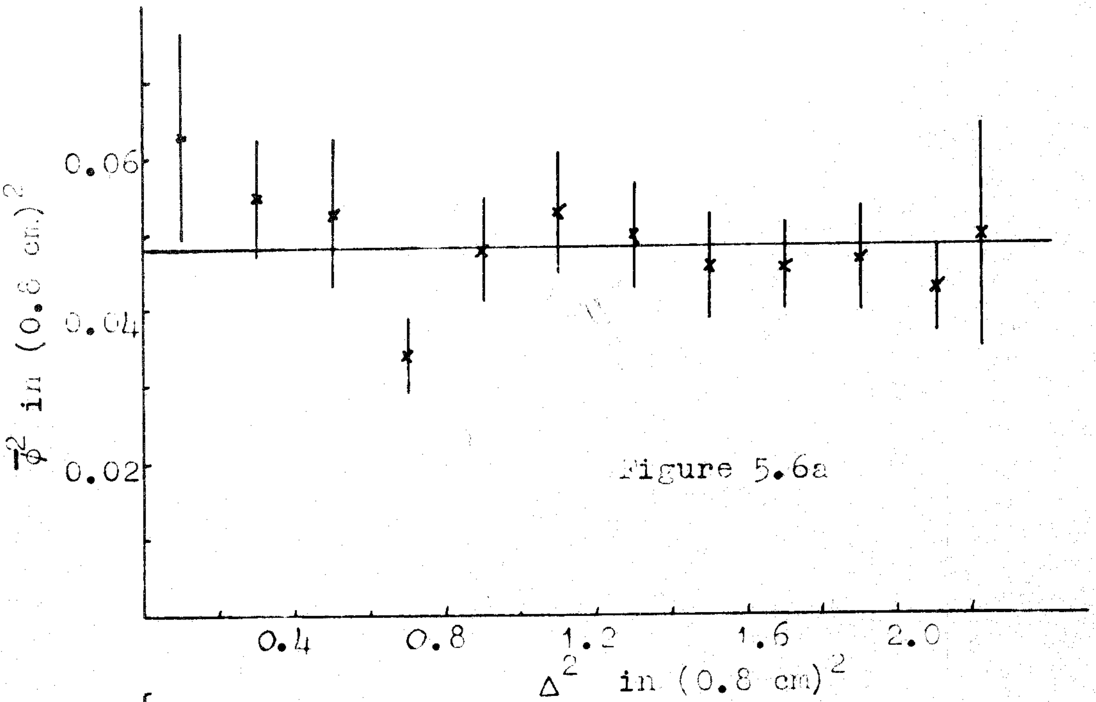

Figure 5.6a

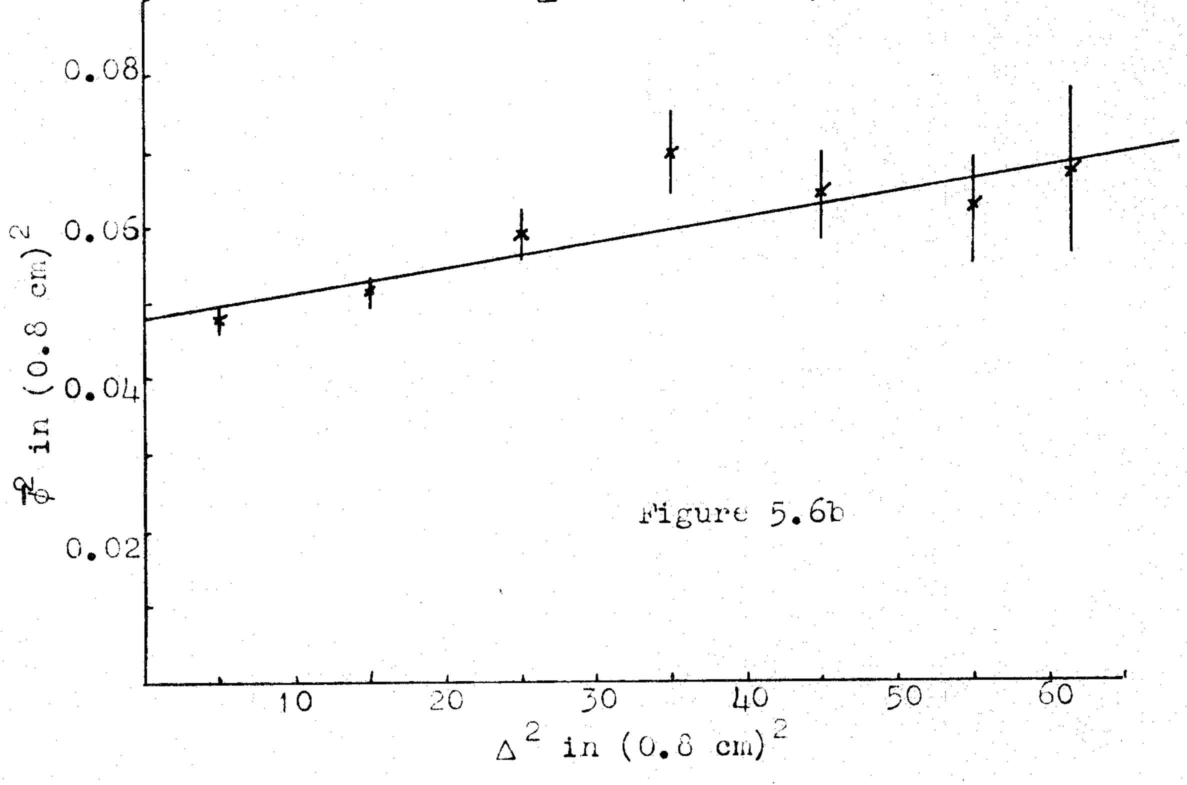

Figure 5.6b

Figure 5.6. a and b : Variation of $(\bar{\phi})^2$ with Δ^2

$$(\delta_T)_{med} = 0.120 \pm 0.004 \text{ cm} \qquad 5.3a$$

From equation 5.1a, this leads to a maximum detectable momentum based on the probable error (see section 2.2) of

$$p_{m.d.m.} \simeq 273 \pm 8 \text{ GeV/c} \qquad 5.4$$

Since even in the range $-6.5 \lesssim \Delta \lesssim +6.5$ cm, the increase in Φ^2 with scattering is small, then a frequency distribution of ϕ can be plotted. This is shown in figure 5.7 for 680 of the particles used in the above calculation. The r.m.s. standard deviation of this distribution leads to $\delta_T = 0.180$ cm. The distribution is compared with a Gaussian distribution having the same standard deviation and it is apparent that they are very similar.

It is possible for the Geiger counter telescope to be triggered by two unassociated particles or parts of small showers e.g. one through G_A and G_B and the other through G_G, G_C and G_D, (figure 3.6), within the resolving time of the Rossi coincidence circuits. These events can be recognised by predicting the position of intersection of level M from records of the flashes in A, B, C and D layers of flash-tubes. Genuine 5-fold coincidences will have a small value for the separation . For ease of accumulation of data for the $\Phi^2 - \Delta^2$ distributions, figures 5.6a and 5.6b, within the computer programme, limits have to be imposed on ϕ. The limits imposed, $-0.8 \lesssim \phi \lesssim +0.8$ cm, are such that few spurious events can be recorded and the

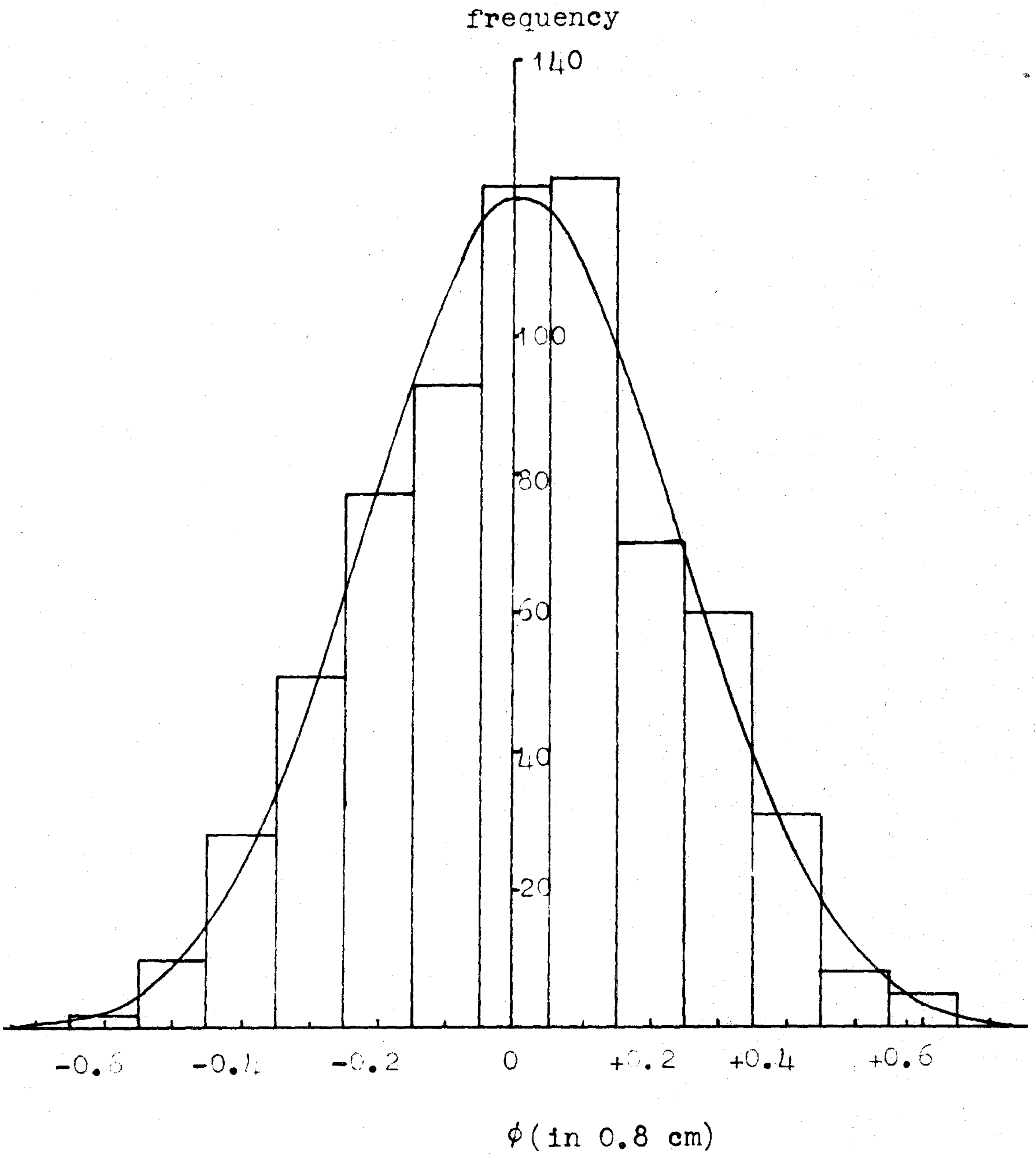

Figure 5.7 : The frequency distribution of ϕ by the Projector method.

assumption of a Gaussian distribution without a cut-off affecting the r.m.s. value of ϕ^2 implies that the correct location error has been obtained.

Having obtained $\bar{\Phi}_0$ accurately, a similar calculation with particles having Δ in the range $-6.5 \leq \Delta \leq +6.5$ cm (momentum $\gtrsim 5$ GeV/c) yields the value of K (equation A1.4). This result is shown in figure 5.6b which is based on 4390 particles. Using the previously found value of $\bar{\Phi}_0$, a least squares calculation was performed to find the best slope. The best line is shown in figure 5.6b and yields a value of

$$K = 0.0534 \pm 0.008 \qquad 5.5$$

in good agreement with the value found from knowledge of the material in the spectrograph beam (equation A1.3).

5.7 The Correction Factors for the Error in Track Location

It is convenient to divide the momentum range under investigation into three overlapping bands, each of which corresponds to a particular technique of particle track measurement and uncertainty for the deflection estimate. Since most of the particles fall in the lowest momentum band because of the steep slope of the spectrum, it is necessary to adopt a method of measurement which is both quick and sufficiently accurate and here the measurements made with the projection method are used. In the higher momentum bands more involved techniques involving the use of the Track Simulator method of measurement are used.

In a given momentum band, it is possible to extend the spectrum to momenta above the m.d.m. by applying corrections to the computed intensities at the upper end of the band. This problem is considered in Appendix 2 where a relation is derived for the correction to the ordinate of the deflection spectrum in terms of the r.m.s. error in deflection. The variation of the correction factor is shown in figure 5.8 as a function of Δ/δ_T. At the maximum detectable momentum ($\Delta/\delta_T = 0.674$) the apparent intensity exceeds the true intensity by 44%.

Since it is desired to extend the spectrum measurements to the highest possible momenta, even above the m.d.m. in the highest momentum band, it is necessary to check the validity of the correction factors. This can be done by comparing the intensities measured in the region of overlap between two momentum bands, where significant corrections will have been applied to the intensities in the lower band, but not in the higher band. Consistency in the data will then support the validity of the corrections to the highest momentum point.

If the error distribution were known with very great accuracy, it would in principle be possible to determine the momentum spectrum to momenta many times the m.d.m. by applying the appropriate corrections to the observed

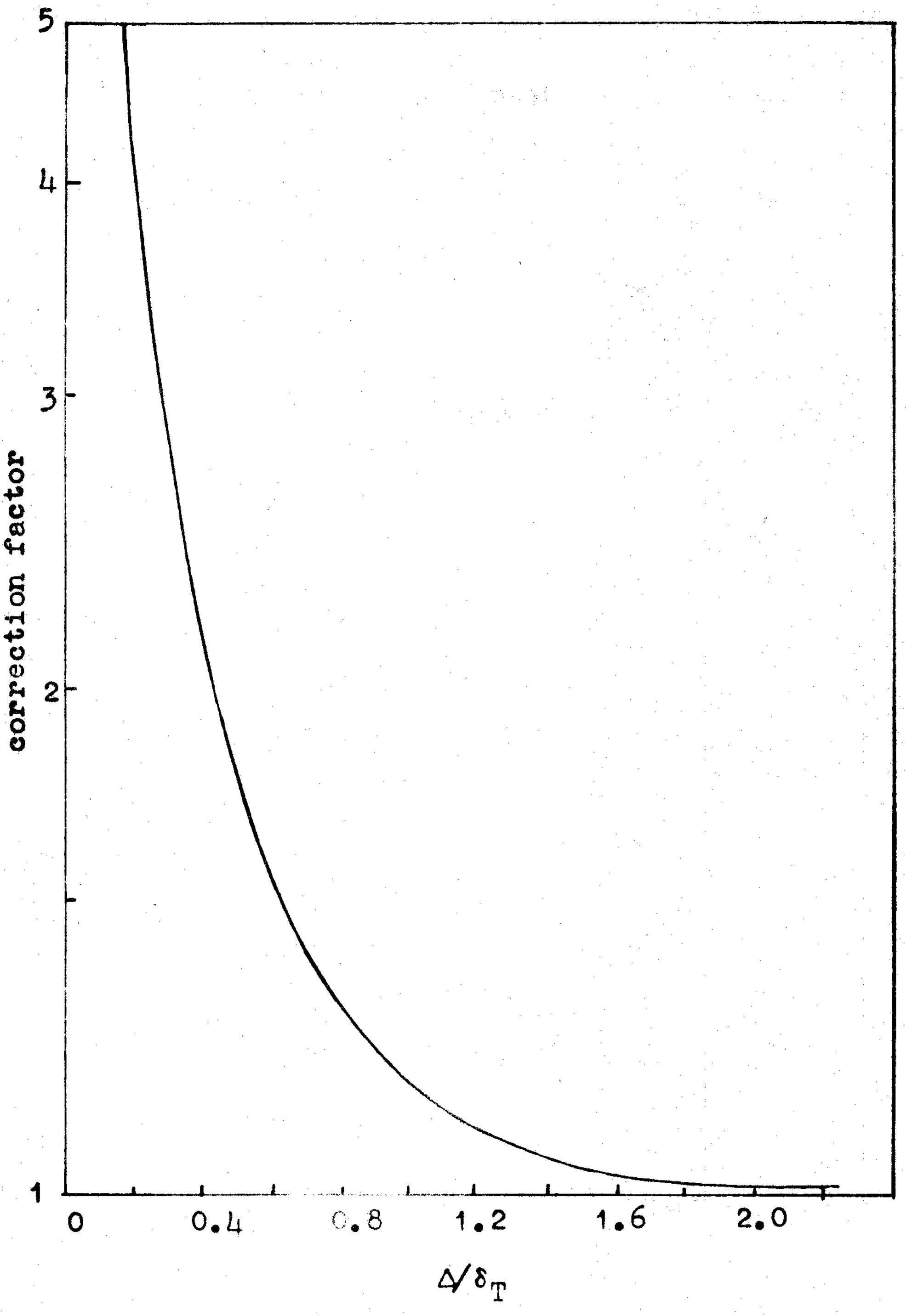

Figure 5.8 : The correction factor for the error in track location.

data (Appendix 2). In the present case however it is felt that the distribution is only known to sufficient accuracy to permit a determination to a momentum of about twice the m.d.m.

5.8 The Comparison Spectra

In evaluating the μ-meson spectrum it is convenient to use an incident comparison spectrum and to derive from this using the instrumental corrections, a deflection spectrum which is of the form of the expected measured spectrum and then vary some parameter until a good fit with the measured data is obtained. As mentioned in Chapter 1, several processes contribute to the resultant flux of particles.

At momenta less than about 10 GeV/c the processes of the ionisation loss and decay of μ-mesons predominate in removing μ-mesons from the sea-level flux but above this figure interaction of π-mesons takes place, resulting in a loss to the μ-meson beam and other processes have smaller contributions.

The data collected with the selector have momenta above $\sim$5 GeV/c. In the region 5 to 10 GeV/c the data are compared with the μ-meson momentum spectrum obtained using the Geiger counters, Gardener et al, (1962), which has high statistical accuracy, ($\sim$0.8% error), and the whole of the data collected in the present experiment is effectively normalised in this region. Above 20 GeV/c, the form of the comparison spectrum is based on the analysis of Barrett et al, (1952). It is shown in Appendix 3 that the sea-level differential μ-meson spectrum in the vertical direction can be evaluated from assumed π-meson production spectra which can be represented by

$$N(p_\pi)\,dp_\pi = A\,p_\pi^{-\gamma}\,dp_\pi\,, \qquad (E \sim pc) \qquad 5.6$$

where p_π is the π-meson momentum at production. Since the momentum spectrum of the parent π-mesons is of such interest, the μ-meson comparison spectra at sea-level have been evaluated from this assumed spectrum by varying γ until the best fit with the measured data is obtained, and by using a simple model for the propagation through the atmosphere. The contributions to the measured intensities by protons and π-mesons above 5 GeV/c are negligible, Mylroi and Wilson, (1951) and Brooke et al, (1962a).

The extrapolated measured Geiger counter spectrum, Gardener et al, (1962) and the spectrum of equation A3.9 agree in the predicted rates at about 20 GeV/c.

5.9 The Momentum Spectrum in the Range 5.1 - 333 GeV/c by the Projection Method

The first band of momentum refers to deflections between 6.5 and 0.1 cm. The momenta corresponding to these limits are 5.1 and 333 GeV/c and the effective mean values of momentum, p_m, in the cells are given by

$$p_m^{-\gamma_{1,2}} = \frac{\int_{p_1}^{p_2} p^{-\gamma_{1,2}}\,dp}{p_2 - p_1} \qquad 5.7$$

where $\gamma_{1,2}$ is the mean slope of the differential μ-meson spectrum between the limits of momentum p_1, p_2, corresponding to the limits of the deflection cell.

The accepted measurements of deflection using the projection method are given in tables 5.4 and 5.5. Positive and negative deflections have been taken together so that the results refer to all particles, irrespective of sign.

For μ-meson momenta in the range $5.1 \leqslant p \leqslant 20$ GeV/c, the Geiger counter momentum spectrum and its extrapolation was converted to a deflection spectrum using equation 5.1. For higher momenta the theoretical comparison spectra were similarly converted. Correction was made for magnetic bias, section 5.4. The deflection spectrum of each category was then derived; normalisation of the two parts of the spectrum was carried out at a deflection corresponding to 20 GeV/c. Correction was made for the momentum selector bias, figure 5.5. Summation was then carried out over all the categories and correction made for errors in track location, section 5.7 and equation 5.3. The observed and expected deflection distributions were then normalised to each other over the whole range of deflection for measurements carried out by the projection method.

The results for $5.1 \leq p \leq 10.1$ GeV/c are shown in table 5.4. The χ^2 test was used to study the goodness of fit of the observed data and the predicted values from the Geiger counter spectrum and it was found that there was a 15% level of significance. It can therefore be concluded that the agreement between the experimental data and the predicted values is satisfactory. The observed intensities shown in table 5.4 are calculated for the observed number of particles normalised to the Geiger counter spectrum in this region, and it is concluded that the accuracy of normalisation is within the statistical accuracy, ±1.6% of the number of particles observed. Bearing in mind the relevant errors it is considered that the additional error introduced into the higher momenta data by the normalisation procedure is ~±2%. The Geiger counter spectrum was itself normalised at 1 GeV/c to the Rossi, (1948) value and any systematic error in this intensity will be carried forward (such an error has, in fact, been suggested by York, (1952)).

In the range of μ-meson momentum unaffected by normalisation, 10.1 - 333 GeV/c, the observed deflection distribution and the expected deflection distribution

Table 5.4 : The basic data below 10.1 GeV/c.

Deflection Interval (cm)	Mean Momentum (GeV/c)	Observed no. of particles	Expected no. of particles	Observed Intensity at $\bar{p}$ *	S.D. %
6.5-5.7	5.45	545	563	$3.21\mathrm{x}10^{-4}$	4.2
5.7-4.9	6.3	789	814	$2.44\mathrm{x}10^{-4}$	3.5
4.9-4.1	7.45	1252	1181	$1.95\mathrm{x}10^{-4}$	2.8
4.1-3.3	9.15	1770	1718.	$1.28\mathrm{x}10^{-4}$	2.4
		4356	4276		

The expected number of particles is calculated from the Geiger counter spectrum, Gardener et al, (1962). The observed rates are those normalised to the Geiger counter spectrum.

* $(\mathrm{cm}^{-2}\mathrm{sec}^{-1}\mathrm{st}^{-1}(\mathrm{GeV/c})^{-1})$

Table 5.5 : The basic data above 10.1 GeV/c.

Deflection Interval (cm)	Mean Momentum (GeV/c)	Observed no. of particles	Expected no. of particles	Observed Intensity at $\bar{p}$ *	S.D. %	x
3.3-2.9	10.8	1167	1118	$8.51\mathrm{x}10^{-5}$	3.0	
2.9-2.5	12.4	1347	1314	$6.14\mathrm{x}10^{-5}$	2.7	
2.5-2.1	14.6	1492	1481	$4.35\mathrm{x}10^{-5}$	2.6	
2.1-1.7	17.8	1520	1600	$2.52\mathrm{x}10^{-5}$	2.6	
1.7-1.3	22.6	1550	1607	$1.39\mathrm{x}10^{-5}$	2.6	
1.3-0.9	31.3	1410	1467	$5.85\mathrm{x}10^{-6}$	2.6	
0.9-0.7	42.3	635	619	$2.88\mathrm{x}10^{-6}$	3.9	
0.7-0.5	56.1	498	502	$1.22\mathrm{x}10^{-6}$	4.5	
0.5-0.3	85.0	329	354	$3.53\mathrm{x}10^{-7}$	5.4	1.01
0.3-0.1	181	192	181	$3.63\mathrm{x}10^{-8}$	7.1	1.15
<0.1	-	60	37	-	12.8	2.66

x Average correction factor for uncertainty in track location where different from unity. The expected column is calculated from equation A3.9 with $\gamma = 2.64$ and from the Geiger counter spectrum. The observed rate is normalised to that predicted by the Geiger counter spectrum, table 5.4.

* $(\mathrm{cm}^{-2}\mathrm{sec}^{-1}\mathrm{st}^{-1}(\mathrm{GeV/c})^{-1})$.

based on equation A3.9 were again compared using the χ^2 test. The comparison was carried out by taking different values of γ in this equation and calculating χ^2 for each value. The values of χ^2 are plotted as a function of γ in figure 5.9. From this curve it can be seen that the best fit is given by

$$\gamma = 2.64 \pm 0.05 \qquad 5.8$$

where the best fit has a 50% level of significance, the error corresponding to 16% probability of γ being outside the limits.

Although the exponent refers to the range 10.1 - 333 GeV/c, the highest momentum is at 181 GeV/c and the bulk of the statistical weight comes from 10 - 100 GeV/c. Gardener et al, (1962) have shown that the best fit value of γ over the range 5 - 10 GeV/c is 2.65, so that the measurements do not suggest a significant change in γ over the range 5 - 100 GeV/c. The intensities found from the projection method of analysis are given in figure 5.10, (circles), where they are shown above 20 GeV/c as a percentage difference from the expected intensities derived from a π-meson production spectrum having constant exponent, $\gamma = 2.64$, and below 20 GeV/c as a percentage difference from the Geiger counter spectrum and its extrapolation. This figure serves to check on the consistency of the intensity measurements from the

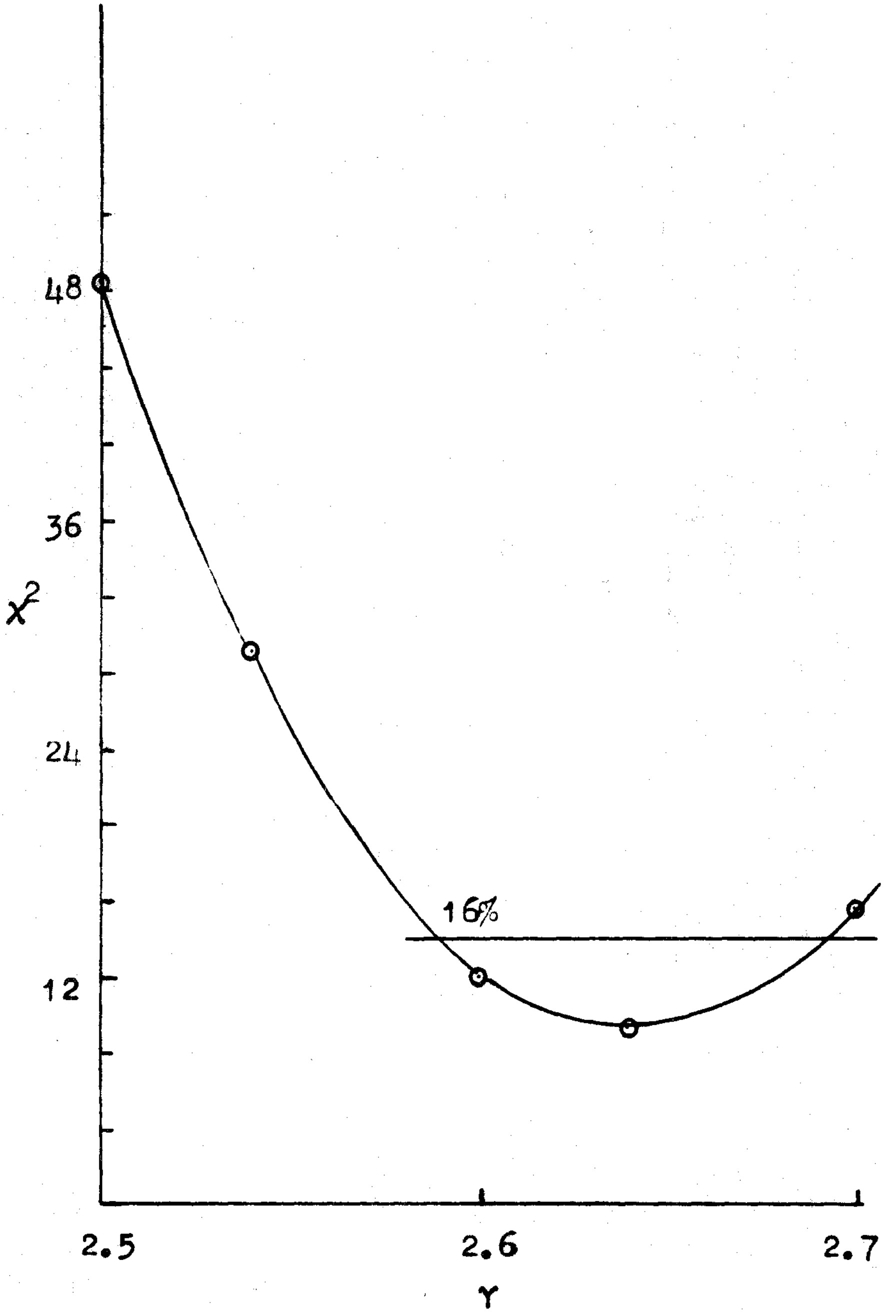

Figure 5.9 . The variation of χ^2 with γ for the momentum region 10.1-333 GeV/c.

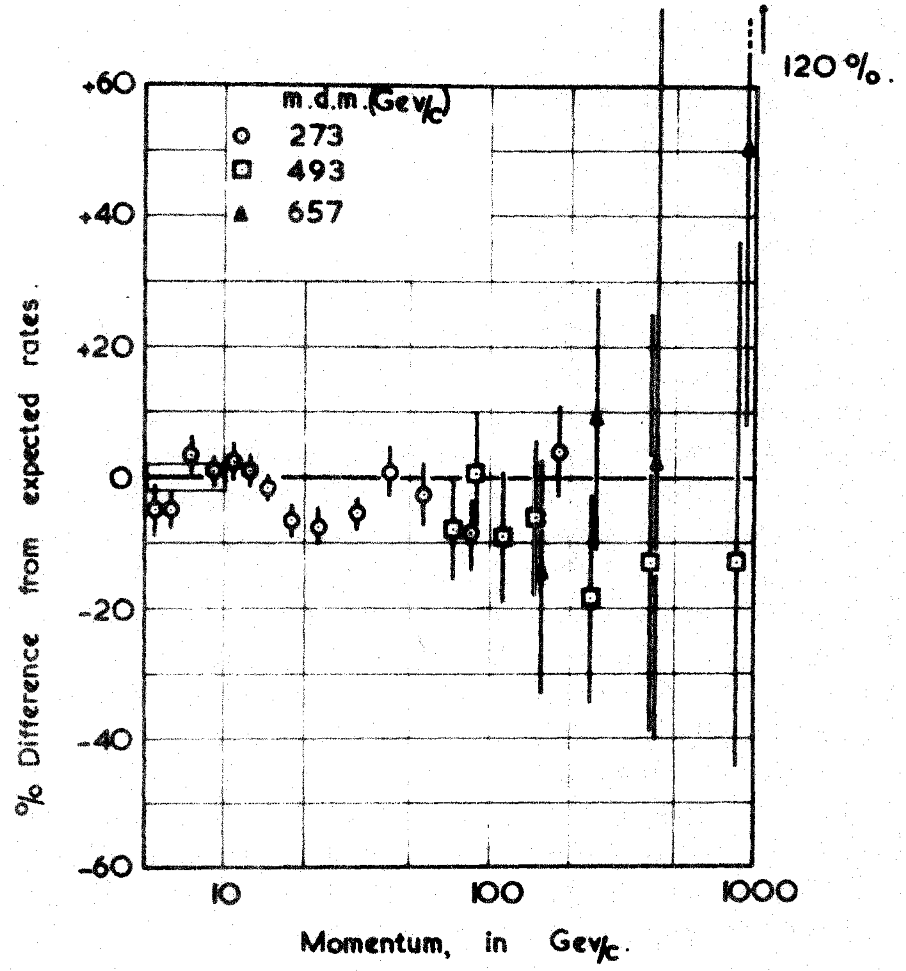

Figure 5.10 : The percentage difference of the measured intensities from the expected intensities calculated for $\gamma = 2.64$.

different methods of analysis in the overlap regions.

5.10 The Momentum Spectrum in the Range 66.6 - 1640 GeV/c by the Track Simulator Method

The level of accuracy with which flash-tube data is analysed is set by the amount of data which has to be analysed and the time available.

The relatively simple projection method of analysis in which a best estimate is chosen by eye is satisfactory from the point of view of accuracy for a large fraction of the flash-tube data. Reference to table 5.5 shows that the correction factor to be applied for uncertainty in track location rises rapidly at small deflections and the data cannot be quoted reliably much above the maximum detectable momentum because of the limited statistics. It can be seen that the percentage correction applied to the expected spectrum for the cell of mean momentum approaching the m.d.m. is 15%, where the statistical accuracy is about half this value.

In order to determine the deflection spectrum more accurately at higher momenta, the Track Simulator method can be applied to those cells where the correction for noise is appreciable by the projection method of analysis. Because of the longer time taken for this more accurate method of analysis of the flash-tube data, the region over which it can be usefully and efficiently applied is limi-

Table 5.6 : The correction to the selected remeasured data because of errors in track location by the projection method of analysis.

Cell (cm)	No. of Particles	S.D. %	"Expected" no. of particles	Corrected "Expected" no.	% Correction
0.26-0.34	95	10	105	104	0.95
0.34-0.42	131	9	133	130	2.2
0.42-0.50	140	8	161	151	6.3

The expected number of particles is calculated for a value of $\gamma = 2.64$ in the comparison spectrum A3.9.

Table 5.7 : The basic data in the range 66.6 - 1640 GeV/c.

Deflection Interval (cm)	Mean Momentum (GeV/c)	Observed no. of particles	Expected no. of particles	Observed Rate at $\bar{p}$ *	S.D.^{o} %	X
0.5-0.42	72.5	140	151	5.75×10^{-7}	8	
0.42-0.34	88.1	131	130	3.27×10^{-7}	9	
0.34-0.26	112	95	104	1.36×10^{-7}	10	
0.26-0.18	153	70	73.2	5.44×10^{-8}	12	1.007
0.18-0.10	244	39	45.4	9.78×10^{-9}	16	1.08
0.10-0.06	413	12	13.5	1.83×10^{-9}	$^{+38}/_{-26}$	1.36
0.06-0.02	894	8	8.7	1.34×10^{-10}	$^{+50}/_{-31}$	2.64

X Average correction factor for noise where different from unity. The expected column is calculated from equation A3.9 with $\gamma = 2.64$. The observed rate is normalised to that predicted by the Geiger counter spectrum, (1951).

o, Regener, (1951).

Table 5.8 : The basic data in the range 128 - 1640 GeV/c.

Deflection Interval (cm)	Mean Momentum (GeV/c)	Observed no. of particles	Expected^{x} no. of particles	Observed Rate at $\bar{p}$ *	S.D.^{o} %	X
0.26-0.18	153	31	35.9	4.93×10^{-8}	18	1
0.18-0.10	244	24	21.0	1.31×10^{-8}	20	1.02
0.10-0.06	413	6	5.75	2.14×10^{-9}	$^{+60}/_{-37}$	1.18
0.06-0.02	894	5	3.25	2.32×10^{-10}	$^{+70}/_{-42}$	2.16
< 0.02	-	1	0.85	-	$^{+230}/_{-83}$	5.1

X, ^{o}, ^{x}, see table 5.7. * $(cm^{-2}sec^{-1}st^{-1}(GeV/c)^{-1})$

ted. To apply this further method of analysis the original data, having deflection less than 0.8 cm, was selected. On re-analysis a cut-off for the new deflection spectrum was made at 0.5 cm. Because of the original cut-off at 0.8 cm some particles which on re-analysis would have had deflection within the new cut-off will be excluded, figure5.11, and this will depend on the magnitudes of the deflection and the uncertainty in track location, section 5.6. The correction to the expected spectrum for this reason is shown in table 5.6 where it can be seen that they do not exceed the statistical errors.

In order to study the accuracy of this method of analysis the value of ϕ , figure 3.12, was calculated for 217 particles with new deflections less than ~0.3 cm. The frequency distribution of ϕ is shown in figure 5.12. The median value of this distribution is

$$\phi_{\text{median}} = 0.066 \pm 0.01 \text{ cm} \qquad 5.9$$

and the m.d.m. derived from this value, corresponding to the probable error in track location is

$$p_{\text{m.d.m.}} = 493 \pm 84 \text{ GeV/c} \qquad 5.9\text{a}$$

If the distribution is Gaussian then the r.m.s. value will be

$$(\phi_{\text{r.m.s.}})_{\text{Gaussian}} = \frac{0.066}{0.674} = 0.0984 \pm 0.0056 \text{ cm} \qquad 5.10$$

or

$$\delta_a = 0.050 \pm 0.003 \text{ cm} \qquad 5.10\text{a}$$

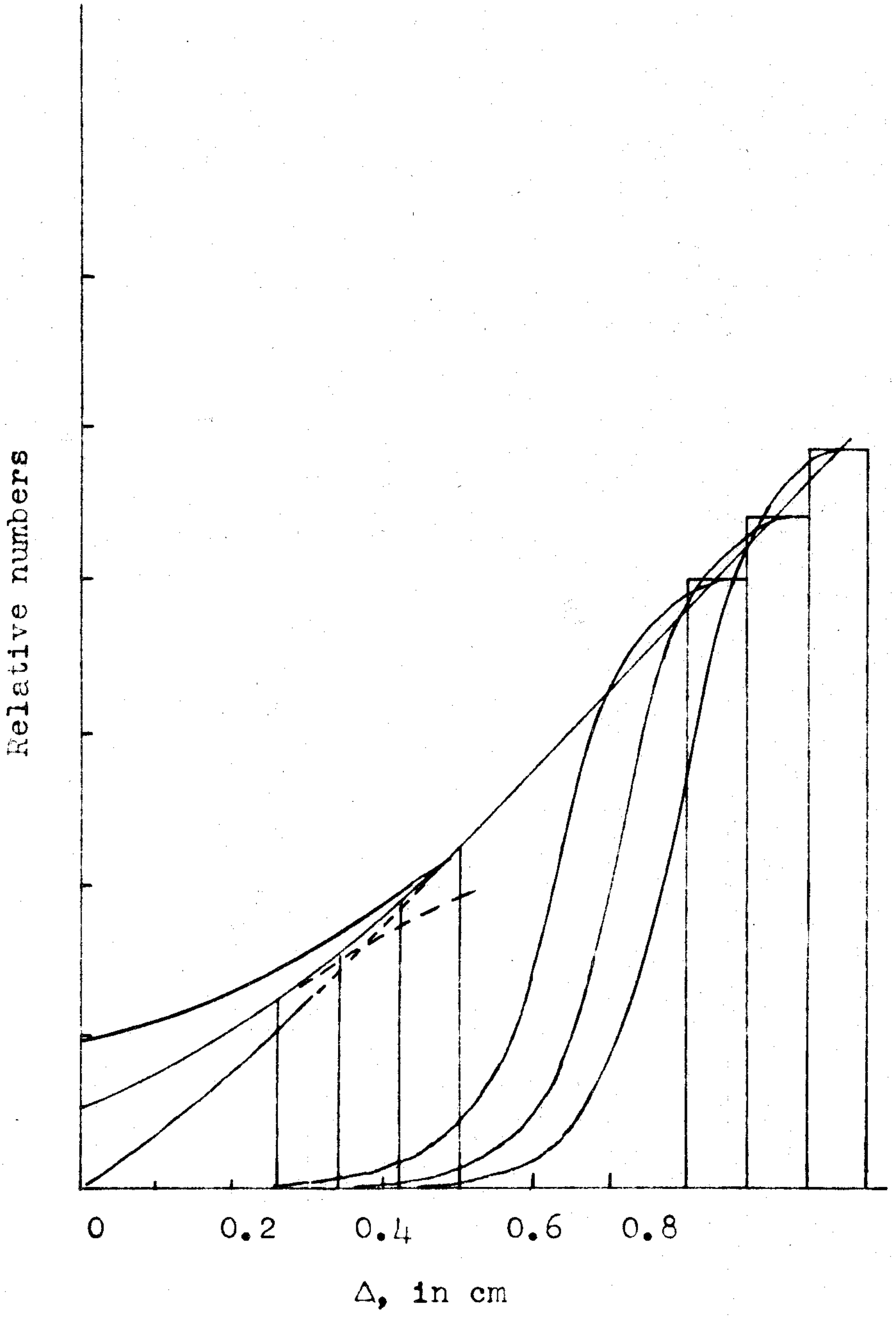

Figure 5.11 : The correction to be applied to the selected remeasured data because of errors in track location by the projection method of analysis.

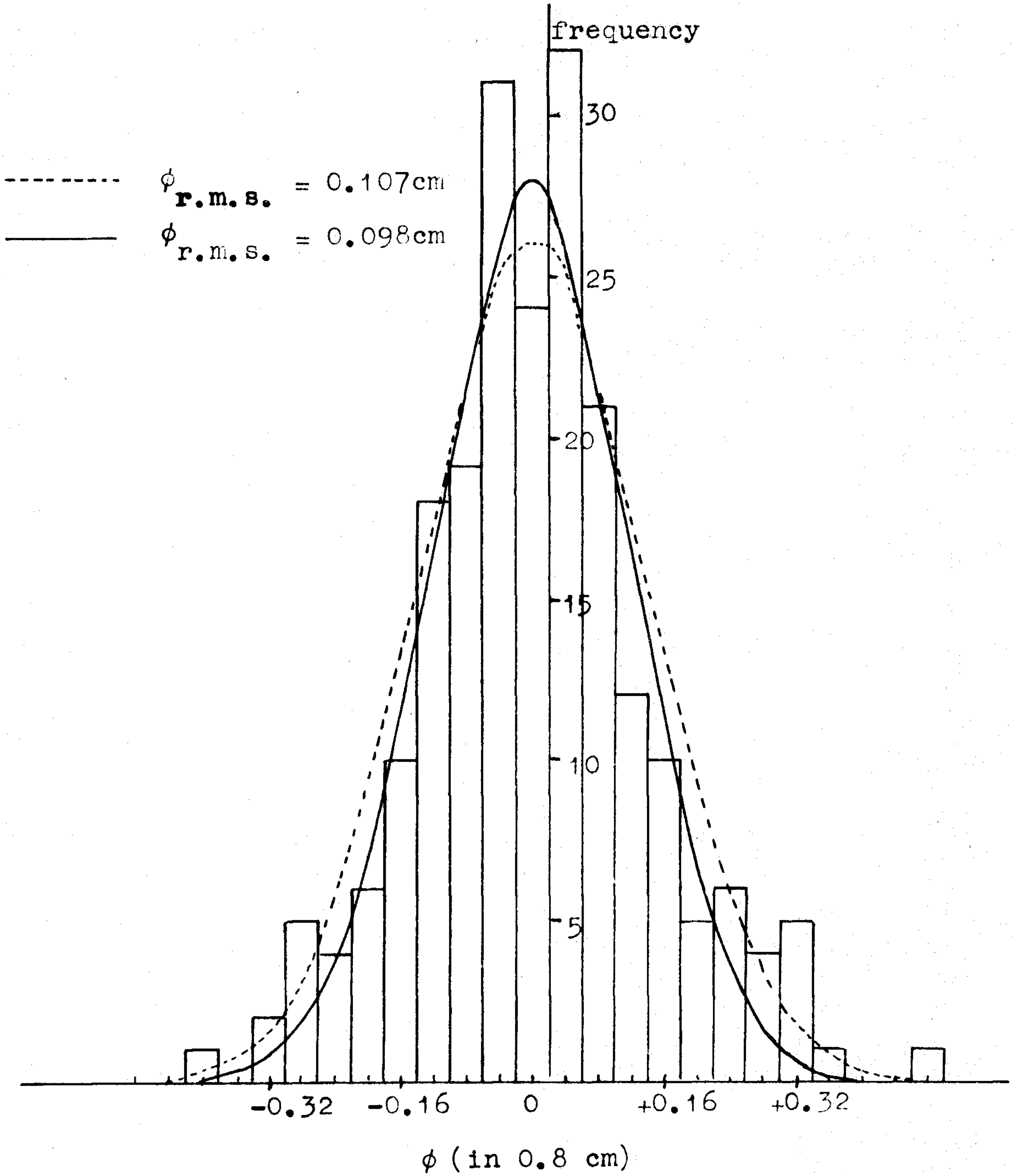

Figure 5.12: The frequency distribution of ϕ by the Track Simulator Method.

The actual r.m.s. value is

$$\phi_{r.m.s.} = 0.107 \pm 0.005 \text{ cm} \qquad 5.11$$

or

$$\delta_q = 0.055 \pm 0.002 \text{ cm} \qquad 5.11a$$

showing that the distribution is not quite Gaussian, and the method of correction for errors of location of particle trajectory calculated on the basis of a Gaussian distribution Appendix 1, cannot be directly applied. It can be seen that if the correction factor, figure 5.8, is applied to the trial spectrum assuming the larger value of error of track location, equation 5.11, then the trial spectrum will be over-corrected for noise, while if the smaller value is used, equation 5.10, the effect of noise is underestimated. The best estimate of the correction factor is given by some intermediate value and this was obtained by taking the mean value of those values given by the limits, equation 5.10, 5.11. This resultant correction factor is shown in figure 5.13.

The value of the m.d.m. can be compared with the values estimated by Bull et al, (1962), for the present instrument. These authors show that an upper limit to the m.d.m. should be 681 ± 24 GeV/c and estimate that a realistic value would be about 520 GeV/c, in good agreement with the measured value, equation 5.9a.

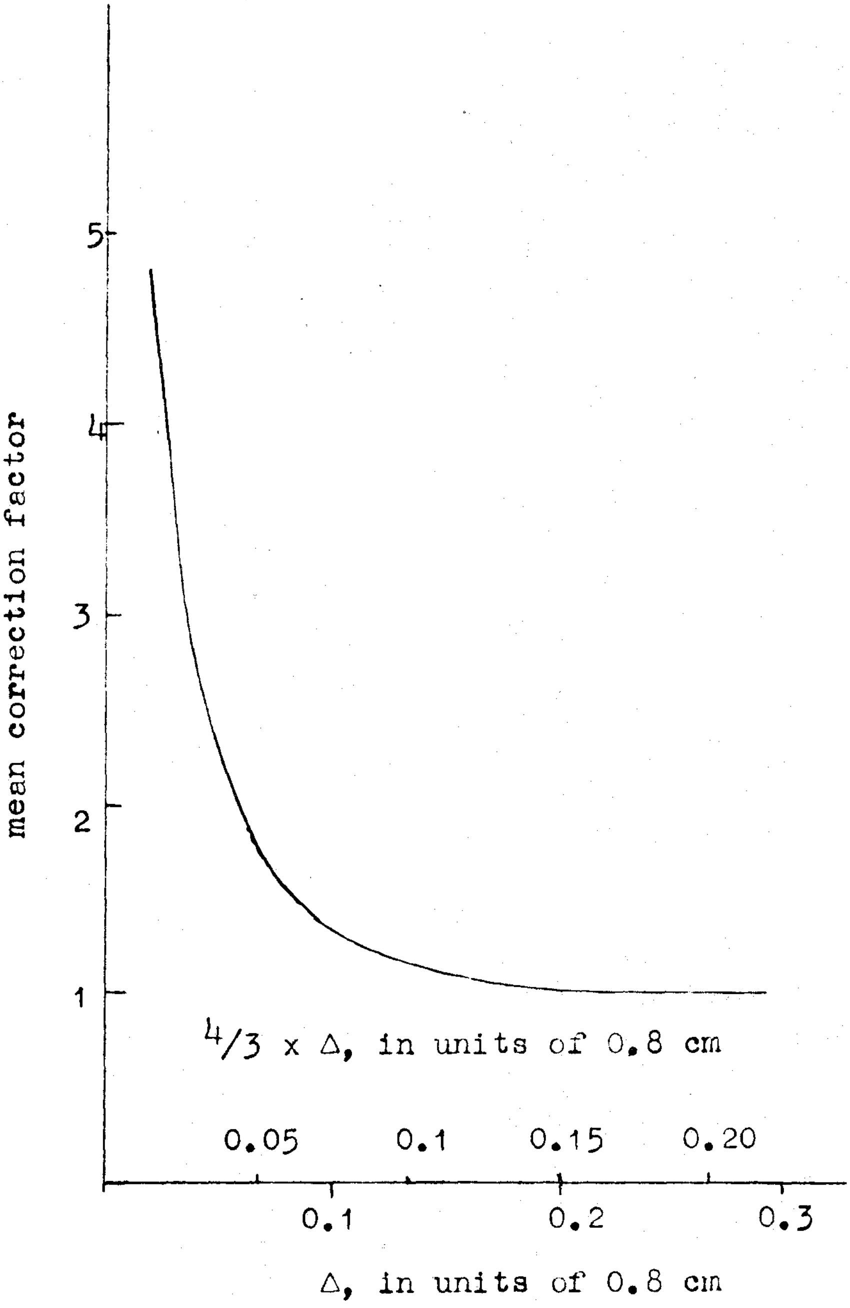

Figure 5.13 : The mean correction factor for the error in track location for the two ranges of momentum covered by the track simulator measurements.

As in the previous section the observed and expected deflection spectra were compared using the χ^2 test, for different values of γ and in the range of momentum from 66.6 GeV/c to 1640 GeV/c. The result is shown in figure 5.14, where χ^2 is plotted as a function of γ. The value of γ giving the best fit is

$$\gamma = 2.67 \pm 0.10$$

at the 90% level of significance, the error corresponding to the 16% probability of γ being outside the limits. The high level of significance is due to the very small departure of the results and the theoretically predicted deflection spectrum from linearity. It is therefore concluded that the value of γ giving best fit to the data in the range 66.6 - 1640 GeV/c is not significantly different from the value deduced over the lower momentum range 10.1 - 333 GeV/c. In order to compare the results over the whole range of momentum from 10.1 GeV/c to the maximum detectable momentum, the data in the present range are compared with a trial spectrum with $\gamma = 2.64$, in table 5.7.

The data from the present momentum range are shown in figure 5.10, (squares), where they are given as a percentage difference from the expected spectrum calculated as before with $\gamma = 2.64$. At the lower end of the range where there is an overlap with the previous range it is seen that there is good agreement confirming the validity of the method of correction.

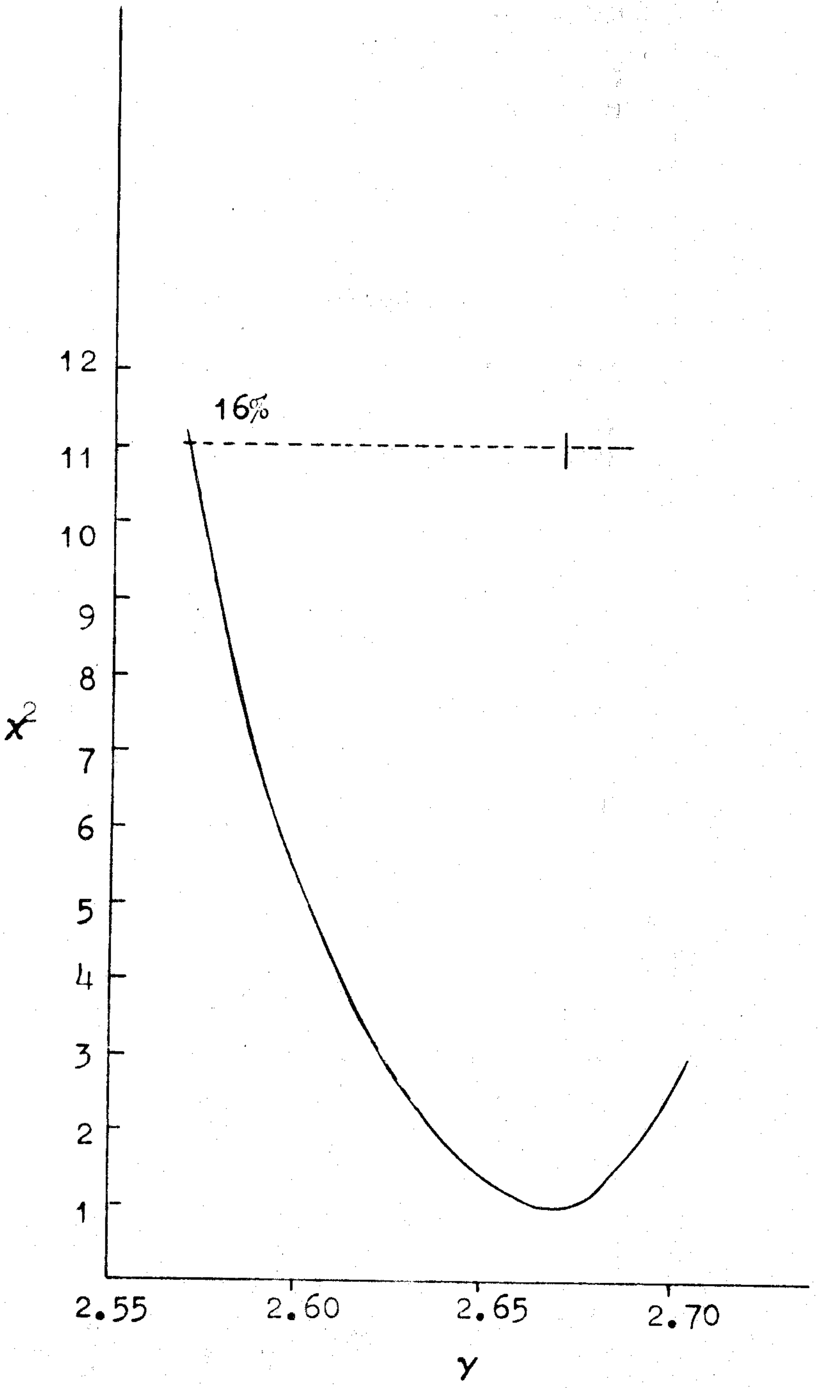

Figure 5.14 : The variation of χ^2 with γ for the momentum region 66.6–1640 GeV/c.

The possibility of extending the accuracy of the particle trajectory location by various methods was investigated and the results are shown in Appendix 4. Using the conclusions drawn from this appendix the results in table 5.7 above 128 GeV/c were re-analysed and all events where

$$\phi > \phi_{\text{median}} \qquad \text{(see equation 5.9)}$$

were rejected. The new correction factor for errors in track location, figure 5.13, was determined by taking the resulting factor by which the accuracy of determination of particle trajectory was improved and finding the new smaller value of deflection at which this occurred. The resulting new correction factor will then be given by the upper abscissa scale, figure 5.13. The data are shown in table 5.8, where they are again compared with a trial spectrum with $\gamma = 2.64$. The application of this method results in an increase in the m.d.m., the new value being 657 ± 112 GeV/c. The data in the higher momentum range, above 128 GeV/c, are shown in figure 5.10, (triangles), where they are given as before, and it is seen that there is good agreement in the overlap region at the low momentum end.

Comparison of the measurements made by the different methods shows no evidence for inconsistency outside the statistical errors and it is concluded that there is no significant inconsistency over the whole momentum range.

5.11 The Best Estimate of the Spectrum and its Comparison with other Work

Not all the data of figure 5.10 can be used for the final spectrum because in the overlap regions the points are not statistically independent. Instead, independent points have been chosen from the separate momentum bands in the range 5.1 - 128 GeV/c (tables 5.4, 5.5, and 5.7) and are given in table 5.9. Above 128 GeV/c observed intensities given in tables 5.7 and 5.8 were combined to obtain a mean value, the error on this mean value being taken as that of the more accurate method of measurement, (table 5.8). The justification of taking a straight mean and not a weighted one lies in the relative accuracy of the measurements. Although the results in table 5.7 are less accurate because of the large correction factor for uncertainty in track location, they are based on better statistics.

The best estimate of the measured intensities above 128 GeV/c is given in table 5.9. Thus table 5.9 forms the best estimate of the measured intensities with the

Table 5.9 : The measured intensity of near-vertical cosmic ray muons as a function of momentum above 5.1 GeV/c.

Method of measurement	Momentum (GeV/c)	Differential Intensity $cm^{-2}sec^{-1}st.^{-1}(GeV/c)^{-1}$	Statistical error, (standard deviation) %
I	(5.45	3.21×10^{-4}	4.2
	(6.3	2.44×10^{-4}	3.5
	* (7.45	1.95×10^{-4}	2.8
	(9.15	1.28×10^{-4}	2.4
	10.8	8.51×10^{-5}	3.0
	12.4	6.14×10^{-5}	2.7
	14.6	4.35×10^{-5}	2.6
	17.8	2.52×10^{-5}	2.6
	22.6	1.39×10^{-5}	2.6
	31.3	5.88×10^{-6}	2.6
	42.3	2.88×10^{-6}	3.9
	56.1	1.22×10^{-6}	4.5
II	72.5	5.75×10^{-7}	8
	88.1	3.27×10^{-7}	9
	112	1.36×10^{-7}	10
II, III	153	5.18×10^{-8}	18
	244	1.14×10^{-8}	20
	413	1.98×10^{-9}	+60/−37
	894	1.84×10^{-10}	+70/−42

* Region of normalisation to Geiger counter spectrum

I Projection method; m.d.m. = 273 ± 8 GeV/c

II Track simulator method; m.d.m. = 493 ± 84 GeV/c

III Track simulator method; m.d.m. = 657 ± 112 GeV/c.

present apparatus. The intensities given in this table and which are plotted in figure 5.15 have been calculated in two parts: conversion of the deflection spectrum to a relative momentum spectrum, and the normalisation of the intensity. The relative intensities have been determined by drawing the continuous momentum spectrum having the best fit value of γ, and plotting the experimental points at the mean momentum (equation 5.7) corresponding to the limits of the deflection cell with an intensity which bears the same relationship to the ordinate of the continuous momentum spectrum as the frequency of events in the deflection cell bears to the expected number.

The intensities given in table 5.9 and figure 5.15 are absolute in that they have been determined by the normalisation of the flash-tube data to the low momentum Geiger counter spectrum in the common range, 5.1 - 10.1 GeV/c. It is shown in section 5.9 that the error introduced by this procedure is ± 2%. The full line in figure 5.15 above 20 GeV/c is calculated from equation A3.9 with $\gamma = 2.64$. It can be seen that there is close agreement of the measured intensities with the predicted values above 20 GeV/c. Below 20 GeV/c, the full line is the best estimate of the Geiger counter spectrum and its extrapolation, Gardener et al, (1962), which is normalised at 1 GeV/c

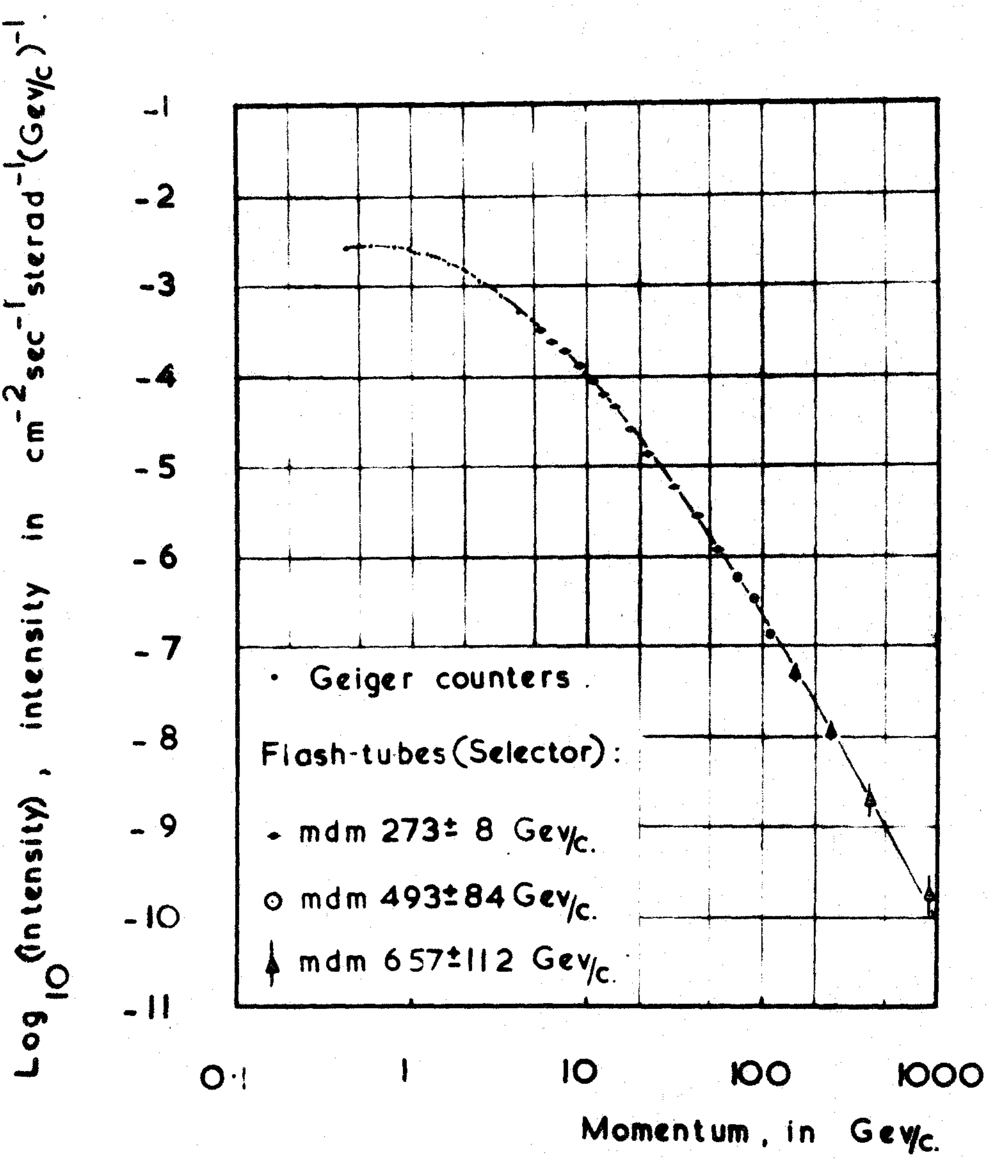

Figure 5.15 . The differential momentum spectrum of μ-mesons in the vertical direction at Durham.

to the value given by Rossi, (1948),

$$I_v = 2.45 \times 10^{-3} \mathrm{cm}^{-2} \mathrm{sec}^{-1} \mathrm{st}^{-1} (\mathrm{GeV/c})^{-1}$$

The intensities read from the curve giving the best fit to the experimental points are given in Appendix 5, table A5.1, together with the exponent of this spectrum (i.e. the slope of the curve) at each of the stated momenta. The spectrum refers essentially to single particles which pass unaccompanied through the instrument, the number of events involving accompanied particles being very small (3.5.1).

Before comparing the present results with those obtained by other workers, it is relevant to compare the results with the earlier measurements obtained with the same instrument given by Ashton et al, (1960). Although that work gave the low momentum spectrum measured with the Geiger counters (which is identical with that shown in figure 5.15 - 'Geiger counters') the results obtained at high momenta with the flash-tubes were only preliminary. The present intensities are consistently below the best line through the earlier data at momenta above 10 GeV/c, figure 5.16. The reduction in intensity increases from about 20% at 100 GeV/c to 50% at 1000 GeV/c. The reason for this discrepancy is partly statistical (the present work is based on some seven times as many particles) and partly due to an overestimate of the maximum detectable

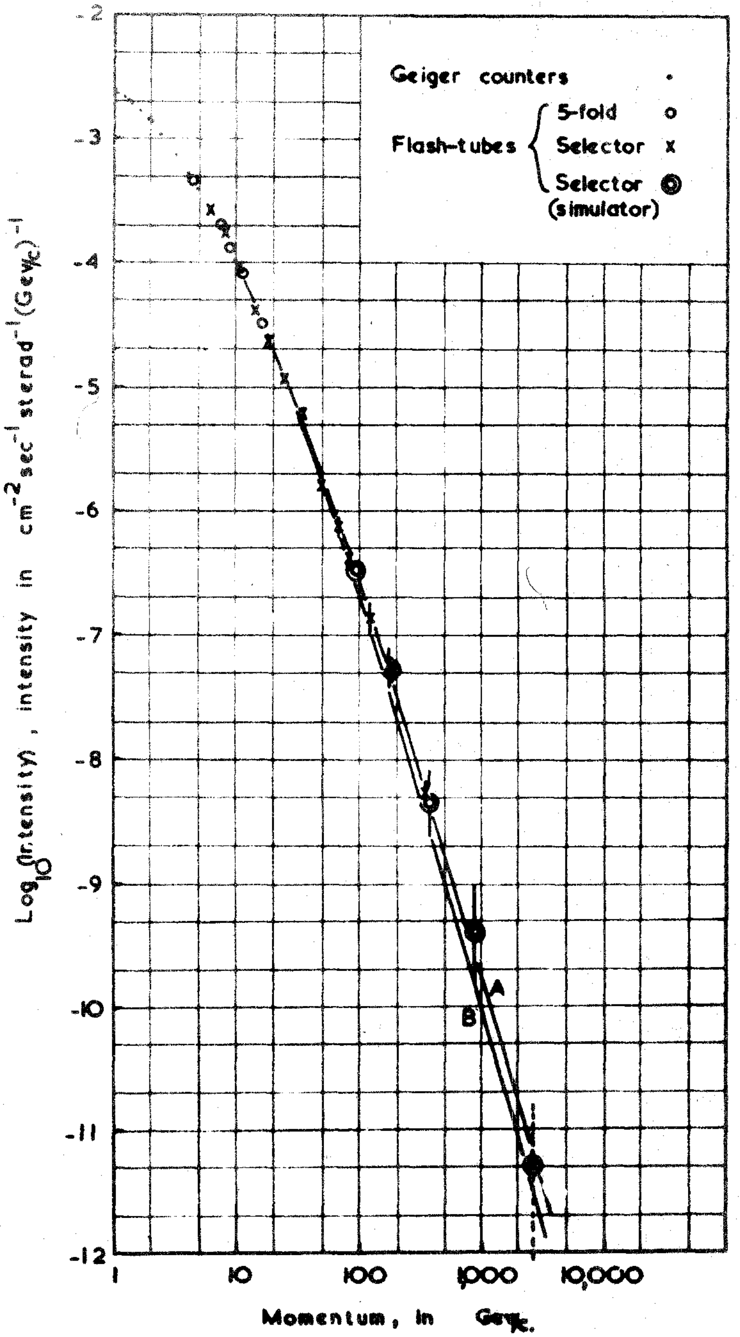

Figure 5.16 : The comparison of the best estimate from the present work, curve B, with the preliminary results, curve A, obtained by the author at high momenta, Ashton et al, (1960).

momentum in the earlier work arising from the paucity of data on which the estimate was based. A further improvement in the present work has been in the investigation of the momentum selector characteristics which are now known more accurately. In the previous work, a π-meson production spectrum was deduced having an exponent $\gamma = 2.55 \pm 0.2$, which is not in significant disagreement with the present work.

The data in figure 5.15 are plotted in figure 5.17, "D", as a percentage difference from the theoretical best estimate of the spectrum (with $\gamma = 2.64$) for $p > 20$ GeV/c and the Geiger counter spectrum and its extrapolation for $5 < p < 20$ GeV/c. The data between 5.1 and 10.1 GeV/c are shown together with the accuracy of normalisation.

The present work is also compared with the measurements with other spectrographs in figure 5.17. Only those spectrographs having an m.d.m. above 100 GeV/c are considered, namely Pine et al, (1959) (triangles), and Pak et al, (1961), (crosses), with the Cornell spectrograph and Rodgers, (1957), and Holmes et al, (1961a,b), (squares) with the Manchester spectrograph.

It is convenient for the purposes of comparison to consider two ranges, 5 - 100 GeV/c and 100 - 1000 GeV/c. In the lower momentum range there is excellent agreement between the results of the present experiment and the Cornell data to within about 10%. The agreement with the

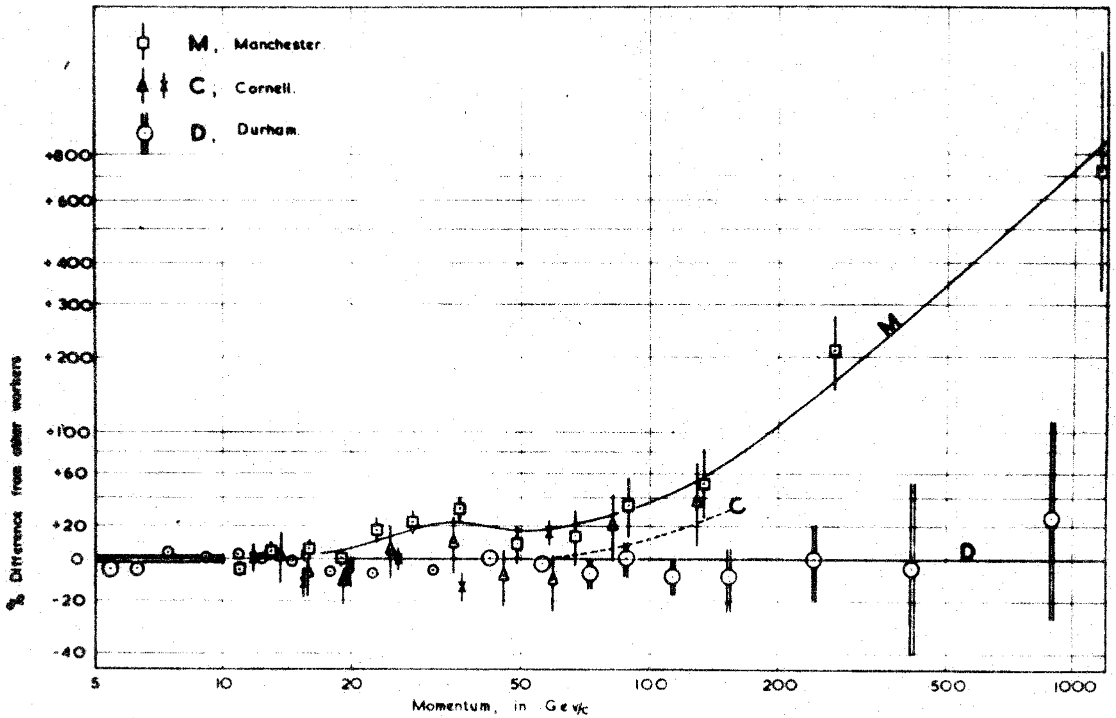

Figure 5.17 : The comparison with previous results. The radius of the circles gives the standard deviation, where no error is indicated.

Manchester data is not as good, since the Manchester points appear to be significantly higher above about 30 GeV/c. In the higher momentum range 100 - 1000 GeV/c, the divergence of the Manchester and Durham data increases and near 1000 GeV/c the Manchester intensity is some seven times the Durham intensity. There is also indication of an increase in the Cornell intensity but this is based on their final point which is of low statistical accuracy so that there is no real inconsistency over the common momentum range.

It should be noted that the highest point of the Manchester data is over three times their m.d.m., (356 GeV/c) whereas the highest Durham point is only higher than the m.d.m. by a factor of 1.4. Some difference might therefore be expected since the accuracy of the corrections applied for errors of measurement diminishes progressively as the m.d.m. is exceeded. The Manchester point at 250 GeV/c is higher than the present value by a factor of three. The Manchester data were collected using a momentum selecting device similar to the one used in the present work. This was calibrated electronically and it has been shown that errors can arise on this account (section 5.5). Further, the difficulty of determination of the appropriate correction factors for uncertainty in track location arises and their magnitude might possibly have been underestimated for the cloud chambers used in the Manchester work. The effect of turbulence in the cloud chambers has a variable effect in trajectory location which is difficult to estimate. The work on the sea-level spectrum mentioned above, together with other similar work is compared in table 5.10.

5.12 Conclusions

It is concluded that the measured differential intensities in figure 5.15 are well represented above 20 GeV/c by an equation of the form given by equation A3.9, with $\gamma = 2.64 \pm 0.05$ and below 20 GeV/c by the Geiger counter spectrum and its extrapolation. There is some slight evidence for an increase in the exponent of the π-meson production spectrum between 70 and 700 GeV/c, to $\gamma = 2.67 \pm 0.10$. It is felt that the correction factors for uncertainty in track location are known well enough for the intensities to be quoted up to a momentum of about twice the ultimate m.d.m. which is 657 ± 112.

It is concluded that the present measurements represent the most accurate measurement of the sea-level μ-meson spectrum in the vertical direction, in the interval 10 - 1000 GeV/c, table 5.10. Because of the fixed geometry of the flash-tube hodoscopes, the correction for uncertainty in track location is well known, for the different methods used. The m.d.m. for the methods used are collected and compared in table 5.11.

Table 5.10 : The comparison of the present work with other similar work.

Workers		Ultimate detecting element	Ultimate m.d.m. (probable error) (GeV/c)	r.m.s. error in track location (One level)	No. of events $p > 20$ GeV/c
Caro et al,	(1951)	S.G.C.	90	± 3.1 mm	167
Rodgers,	(1957)	C.C.	356	± 1 mm	905
Pine et al,	(1959)	C.C.	260	± 0.75mm	230
Pak et al,	(1961)	F.T.	160	± 1 mm	895
Coates,	(1961)		43	± 0.55mm	60
Ashton et al,	(1960)		1000 ± 200	± 0.32mm	600
Present work,	(1962)		657 ± 112	± 0.55mm	4520

S.G.C.	Staggered Geiger Counters.
C.C.	Cloud chambers.
F.T.	Flash-tube hodoscopes.

Table 5.11 : The Comparison of the accuracy of the present measurements.

Method of Measurement	Total Probable error in track location	m.d.m. (GeV/c)
Projection	0.12 cm	273 ± 8
Track Simulator	0.068cm (no selection)	493 ± 84
	< 0.068cm (with selection)	657 ± 112

Chapter 6

The Integral Spectrum at High Energies

6.1 Introduction

It seems likely that the results obtained in Chapter 5 are near the upper limit in the accuracy of determination of the sea-level spectrum, both from the point of view of particle trajectory location and statistical accuracy, using the present technique.

In order to improve the spatial resolution by an order of magnitude, more sophisticated detectors are required and the deflecting power of magnets must be increased for the larger field volume necessary for higher collecting rates of particles which will then enable higher statistical accuracy.

Any attempt to extend the knowledge of the sea-level μ-meson spectrum to higher energies, at the present time, must therefore be based on some indirect method. Since the high energy μ-mesons at sea-level have great penetrating powers, measurements at great depths underground yield data which, by assuming a form for their rate of energy loss in the passage through rock to the underground stations, can be interpreted in terms of the integral sea-level μ-meson spectrum.

The intensity of particles underground has been reviewed by George, (1952) and Barrett et al, (1952). The form of the energy loss relation for μ-mesons has also been considered by these authors, and more recently by Ashton, (1961) and Ozaki, (1962). Since the reviews in 1952 the great importance of measurements underground and their interpretation has been realised.

In this chapter the intensity data from the underground experiments obtained since the above reviews are collected together. The various expressions for the rate of energy loss used by different authors are considered, and the best relation between the range of μ-mesons in rock and their sea-level energy is calculated. The integral spectrum derived from the present results is then compared with the measured intensities underground, to a depth corresponding to the highest momentum measured by the present technique which corresponds to a depth of about 2000 m.w.e. This method of comparison will therefore indicate whether the expression for the rate of energy loss is correct. Up to about 300 GeV, the form of the rate of energy loss deduced by different authors does not vary substantially, so that the best estimate of the rate of energy loss from the present work can only be compared in the narrow region of intensity measurements between depths of ~1000 - 2000 m.w.e. The effect of fluctuations in the rate of energy loss will be briefly considered. At depths greater than 2000 m.w.e., an extrapolated form of the rate of energy loss deduced from the previous comparison, together with a correction for the effect of fluctuations in the rate of energy loss, will be used to predict intensities at these great depths, using different forms for the sea-level spectrum at energies beyond that covered in the present work.

6.2 The Integral Spectrum of μ-mesons from the Present Experiment

Since all the measurements underground refer to total rates of particles, that is the integral spectrum, this quantity must first be derived, using the data of figure 5.15, so that direct comparison can be carried out. The integral intensity above momentum p_0 is defined by

$$N(>p_0) = \int_{p_0}^{\infty} N(p)\,dp \qquad 6.1$$

where $N(p)$ is the differential intensity at momentum p. For large values of momentum the differential intensity can be represented, assuming γ to be constant, by

$$N(p) = K\,p^{-\gamma} \qquad 6.2$$

that is, a power law of constant slope $-\gamma$. For the spectrum of figure 5.15, this would be almost true for p $\gtrsim$ 8000 GeV/c for the smooth curve. Thus

$$N(>p_0) = \frac{K}{\gamma-1}\,p_0^{-(\gamma-1)} = \frac{p_0\,N(p_0)}{\gamma-1} \qquad 6.3$$

If small cells of momentum ($<p_0$) are taken then

$$N(>p_1) = \int_{p_1}^{p_0} K p^{-\gamma}\,dp + \int_{p_0}^{\infty} K p^{-\gamma}\,dp$$

$$= \frac{1}{{}_{p_1}\gamma_{p_0} - 1}\left[p_1 N(p_1) - p_0 N(p_0)\right] + \frac{p_0 N(p_0)}{\gamma - 1} \qquad 6.4$$

where ${}_{p_1}\gamma_{p_0}$ is the slope at the arithmetic mean of the limits of momentum, and assuming that the spectrum can be represented by a power law between the limits, which is true if the cells are small. Having evaluated $N(>p_1)$, then successive integration for momenta less than p_1 can be carried out in a similar manner. The result is shown in figure 6.1.

The point at 1640 GeV/c has been included in this figure although omitted from figure 5.15 as it is closer to the m.d.m. on the integral scale than on the differential scale. The measured points are plotted at the minimum momenta corresponding to the maximum deflection of the corresponding deflection cells and they bear the same relationship to the expected integral curve as do the frequencies of the measured deflection spectrum. Integration of the deflection cells has been carried out by straightforward addition. The measured integral intensities are given in Table 6.1 for momenta above 5.1 GeV/c. Integral intensities have also been found for momenta $>$ 0.4 GeV/c using the best estimates of the spectrum of Gardener

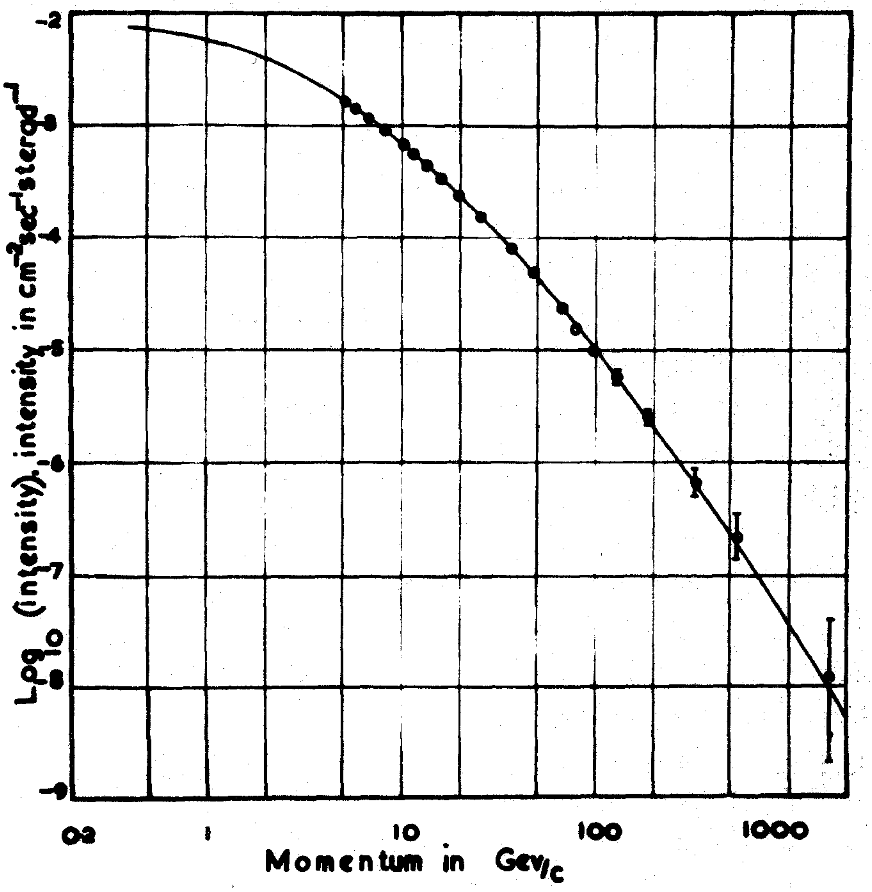

Figure 6.1 : The integral momentum spectrum of μ-mesons in the vertical direction at Durham.

Table 6.1 : The Measured Integral Intensity of near-vertical cosmic ray muons as a function of momentum above 5.1 GeV/c.

p_{min}(GeV/c)	Statistical error (standard deviation) %	Integral Intensity cm^{-2}sec^{-1}sterad^{-1}
5.1	0.8	1.69×10^{-3}
5.8	0.8	1.44×10^{-3}
6.8	0.9	1.19×10^{-3}
8.1	0.9	9.45×10^{-4}
10.1	1.0	6.87×10^{-4}
11.5	1.1	5.55×10^{-4}
13.3	1.2	4.49×10^{-4}
15.9	1.3	3.38×10^{-4}
19.6	1.5	2.38×10^{-4}
25.6	1.9	1.52×10^{-4}
37.0	2.5	8.14×10^{-5}
47.6	3.3	4.91×10^{-5}
66.6	4.7	2.35×10^{-5}
79.5	5.7	1.57×10^{-5}
97.5	7.8	9.88×10^{-6}
128	12	5.76×10^{-6}
184	17	2.54×10^{-6}
330	+30/-26	6.68×10^{-7}
550	+60/-37	2.09×10^{-7}
1640*	+230/-87	1.18×10^{-8}

* In addition to the large statistical error there is uncertainty in the magnitude of the correction factor at momenta so far above the m.d.m.

et al, (1962), and the present work and these are given in Appendix 5, Table A5.2, both as absolute values and as percentages of the total μ-meson flux above 0.4 GeV/c. The values have been calculated from the smooth curve through the differential spectrum, figure 5.15. The value of 0.4 GeV/c at the lower end has been chosen as being for most purposes the minimum cosmic ray μ-meson momentum which is used in experimental work, and corresponds to a range of μ-mesons in lead of about 250 gm.cm^{-2}.

6.3 The Total Rate of Energy Loss of μ-mesons in Rock

The processes by which high energy μ-mesons are known to lose energy can be listed as follows:

a. Collision

b. Pair Production

c. Bremsstrahlung

d. Nuclear Interaction.

The contributions of the above processes to the total energy loss, obtained by George, G, and Barrett et al, B, are given in table 6.2 using the approximate forms given by these authors.

The exact theoretical form of the various energy loss processes are now considered in turn for rock with $Z = 11$, $A = 22$, $\rho = 2.65$ gm.cm^{-3}.

Table 6.2 : The rate of energy loss derived by different authors compared with the best value estimated from the present work.

μ-meson energy (GeV)	Author	Rate of Energy Loss in MeV/gm.cm^{-2}				
		Collision	Pair production	Bremsstrahlung	Nuclear Interaction	Total
10	G	2.43	0.016	0.010	0.025	2.94
	B	2.17	0.013	0.015	0.007	2.205
	O		0.0075	0.010	0.005	2.19
	6.9	2.08				
	PJH	2.13	0.009	0.0076	0.006	2.15
100	G	2.66	0.16	0.10	0.25	3.17
	B	2.4	0.13	0.15	0.07	2.75
	O		0.075	0.105	0.05	2.63
	6.9	2.32				
	PJH	2.39	0.0132	0.116	0.107	2.74
1000	G	2.89	1.6	1.0	2.5	7.99
	B	2.58	1.3	1.5	0.7	6.08
	O		0.75	1.05	0.5	4.88
	6.9	2.50				
	PJH	2.61	1.52	1.58	1.5	7.21
10000	G	3.12	16	10	25	54.12
	B	2.71	13	15	7	37.71
	O		7.5	10.5	5	25.71
	6.9	2.68				
	PJH	2.72	16.3	21.3	19.3	59.62
100000	6.9	3.09				

G George, (1952)
B Barrett et al†(1952) ($\sigma_w = 2 \times 10^{-28}$)
O Ozaki, (1962)† ($\sigma_w = 2 \times 10^{-28}$)
6.9 equation 6.9 of this work
PJH best estimate of the present work ($\sigma_w = 10^{-28}$ cm^{-2})

† It has been pointed out by Greisen (p.c.) that the total average rate of energy loss derived by Ozaki is only empirical in that it has been obtained by comparison of the integral μ-meson spectrum at sea-level with the underground intensity measurements and neglects the effect of fluctuations in energy loss, thus giving a result which is too low.

6.3.1 Collision

When μ-mesons pass through matter, they lose energy to the electrons of the medium via the coupling of the electric fields of the μ-meson and the electron. If the energy given to the electron is high enough then it can escape from the atom. The transfer of energy can be considered in two stages; that of high energy transfer, greater than some value η, and also for values less than η.

For large energy transfers, (close collisions) the electrons of the medium can be considered to be free. The differential collision probability for μ-mesons, (mass, m, spin $\frac{1}{2}$) for energy transfers $> \eta$ have been given by Bhabha, (1938), and Massey and Corben, (1939). They give the probability per gm.cm^{-2} for μ-mesons of energy E, mass m, of producing an electron in the interval E' to E' + dE' as

$$\Phi_{col}(E,E')\,dE' = \frac{2Cm_ec^2}{\beta^2}\frac{dE'}{(E')^2}\left[1-\beta^2\frac{E'}{E'_m}+\frac{1}{2}\left[\frac{E'}{E+mc^2}\right]^2\right] \qquad 6.5$$

where

$$C = \pi N\frac{Z}{A}r_e^2 = 0{\cdot}15\frac{Z}{A}\ \text{gm}^{-1}\,\text{cm}^2,$$

$$E'_m = \frac{E^2}{E+\frac{m^2c^4}{2m_ec^2}} = \frac{E^2}{E+1{\cdot}13\times10^4}\ \text{Mev}$$

is the maximum energy transferable to the electron, r_e its classical radius, and N is Avogadro's number. The average rate of energy loss is obtained by integration over E', giving

$$-\left(\frac{dE}{dx}\right)_{col>\eta} = \int_{\eta}^{E'_m} E' \cdot \Phi_{col}(E, E')\, dE'$$

$$= 0.0766\left[\log \frac{E'_m}{\eta} - 1 + \frac{1}{4}\left(\frac{E'_m}{E + mc^2}\right)^2\right] \qquad 6.6$$

(in MeV. $(\mathrm{gm.cm}^{-2})^{-1}$)

for $\beta \sim 1$ and $E \ll \frac{(mc^2)^2}{m_e c^2}$

For energy transfers $E' < \eta$, the collision can be considered as distant. If η is sufficiently small ($\sim 10^4$-10^5 eV) then the average rate of energy loss per $\mathrm{gm.cm}^{-2}$ is as given by Bethe, (1930), (1932),

$$-\left(\frac{dE}{dx}\right)_{col<\eta} = \frac{2Cm_e c^2}{\beta^2}\left[\log \frac{2m_e c^2 \beta^2 \eta}{(1-\beta^2)[I(Z)]^2} - \beta^2\right] \qquad 6.7$$

where $I(Z) = 13.5.\ Z$ eV.

Thus in both equations the rate of energy loss increases logarithmically, partly due to the increase in the maximum energy which can be transferred, and partly due to the enhanced relativistic effects of the electric field of the particle perpendicular to its path which causes it to be effective at larger distances.

The above equations are derived for atoms which are independent of each other. However, for distant collisions, the atoms of the medium screen the electric field of the fast particle and reduce the interaction and therefore the energy loss, the effect increasing with the energy of the incident particle. The reduction in the rate of energy loss (density correction) has been considered by Fermi, (1939), Halpern and Hall, (1940), (1948), and Wick, (1941), (1943). The reduction in the average rate of energy loss is given by

$$\Delta_1 = \frac{2C_{m_e c^2}}{\beta^2}\left[\log \frac{\eta'}{1-\beta^2} - 1\right] \qquad 6.8$$

where

$$\eta' = \frac{N Z \rho h^2 e^2}{\pi A [I(Z)]^2 m_e}$$

The total average rate of energy loss can be expressed as

$$-\left(\frac{dE}{dx}\right)_{col} = -\left(\frac{dE}{dx}\right)_{col<\eta} - \Delta_1 + \left(\frac{dE}{dx}\right)_{col>\eta}$$

$$-\left(\frac{dE}{dx}\right)_{col} = 0.0766\left[\log \frac{2 m_e^2 c^4 \pi A m}{N Z \rho e^2 h^2} - 2\right] + 0.0766\left[\log \frac{E'_m}{mc^2} + \frac{1}{4}\left(\frac{E'_m}{E+mc^2}\right)^2\right]$$

$$= 1.43 + 0.0766\left[\log \frac{E'_m}{mc^2} + \frac{1}{4}\left(\frac{E'_m}{E+mc^2}\right)^2\right] \qquad 6.9$$

(in MeV. $(\text{gm.cm}^{-2})^{-1}$)

This expression is in good agreement with the results of Sternheimer, (1952), who has calculated the energy loss for aluminium ($Z = 13$, $A = 26$, $\rho = 2.7$, where $\frac{\rho}{ZA} = 0.8$ compared with rock, $\frac{\rho}{ZA} = 1.11$, this occurring only in the log term of the density correction term). More recent values of I(Z), equation 6.8 and other smaller terms have been used by Sternheimer, (1959), but with little change in the result, and his 1952 values will be assumed as being the best estimate of the collision loss. These values are shown in figure 6.2 and table 6.2 (P.J.H.).

The theoretical values of energy loss are in good agreement with the measured values, reviewed by Cousins, (1960) at low energies, $\lesssim$100 GeV. At higher energies any small deviations have negligible effect on the total energy loss relation because of the larger contribution of other processes, (sections 6.32 - 6.34).

Bohr, (1948), first pointed out that part of the energy dissipated by high energy particles appears as Cerenkov radiation. Since this results from interaction of the electric fields of the particle and atoms of the medium for distant collisions, it has already been included in equations 6.7 and 6.9.

6.3.2 Pair Production

A high energy μ-meson can lose energy by the creation of an electron pair in a nuclear Coulomb field. The theoretical cross-section for pair production has been given by Bhabha, (1935), and Racah, (1937). The cross-sections given by Bhabha are about twice those calculated by Racah. Mando and Ronchi, (1952) have calculated the average rate of energy loss using the cross-sections given by Racah, neglecting the screening effect of the

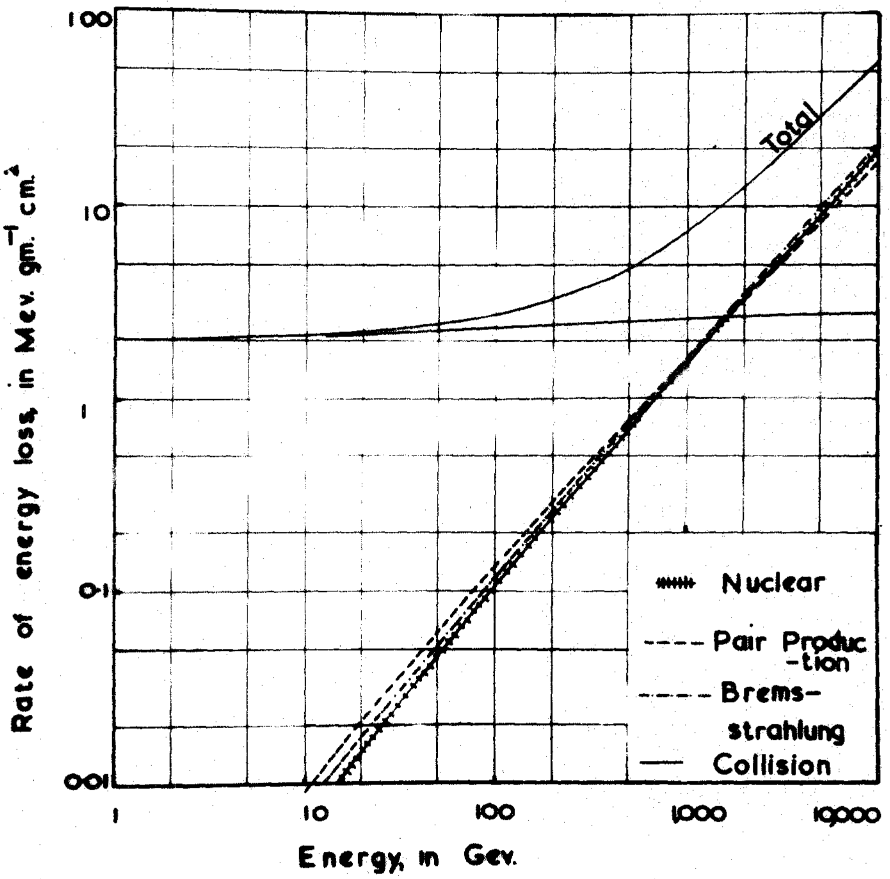

Figure 6.2 : The various contributions to the best estimate of the total average energy loss.

orbital electrons,

$$-\left(\frac{dE}{dx}\right)_{pair} = \frac{N}{A}\frac{m_e}{m}\left(\frac{\alpha Z r_e}{\pi}\right)^2 \cdot E\left(19.3 \log\frac{E}{mc^2} - 53.7\right) \qquad 6.10$$

where $\alpha = \frac{1}{137}$, and r_e is the classical electron radius. Hayakawa and Tomonaga, (1949), have considered the energy losses including and excluding screening, and Mando and Ronchi have concluded the ratio to be

$$\frac{-\left(\frac{dE}{dx}\right)_{screening}}{-\frac{dE}{dx}_{\text{no screening}}} = \frac{\frac{16}{9}\log a + 1}{\frac{16}{9}\log\frac{E}{mc^2} - \frac{14}{9} + \log 2} \qquad 6.11$$

where $a = 183\ Z^{-1/3}$.

The equation for the average rate of energy loss, corrected for the effect of screening is obtained by the multiplication of equation 6.10 by equation 6.11.

Block et al, (1954), have reconsidered the work of Bhabha and have shown that with more careful mathematical treatment the cross sections of Bhabha are consistent with those given by Racah. However Murota et al, (1956), have calculated cross-sections for pair production by μ-mesons. Their results give values which are approximately three times the cross-sections given by Block et al.

The results of Avan and Avan, (1957) who have studied pair production underground (580 m.w.e.) using emulsions, are in good agreement with the predicted cross-sections of Block et al, and up to the mean energies of 120 GeV corresponding to their depth, the maximum error is 10%. More recently Roe et al, (1959), and Gaebler et al, (1961), have studied pair production and find good agreement if the Murota et al cross-section is reduced to half its value. Under these conditions Gaebler et al specifically find better agreement with the Murota et al cross-section than with the corrected Bhabha cross-sections. The measured cross-sections have been found for lead, and Roe et al have measured the momenta of the primaries (μ-mesons) up to 120 GeV/c.

All the theories have arbitrary parameters known to be equal to unity only approximately, and neglect the finite size of the nucleus. The effect of finite nuclear size has been considered by Davies et al, (1954), and shown not to be significant.

The cross-section for pair production including correction for complete screening is given approximately by

$$f(E,v) \sim \frac{1}{Ev^3} \qquad 6.12$$

where v is the fractional energy loss.

This will be considered in section 6.6.

6.3.3 Bremsstrahlung

When a μ-meson is accelerated or decelerated in its passage through matter, electromagnetic radiation or bremsstrahlung is produced. The differential cross-section for the production of photons by μ-mesons has been given by Christy and Kusaka, (1941),

$$f(E,v)\,dv = \frac{16}{3}\alpha N r_e^2 \frac{Z_1^2}{A}\left(\frac{m_e}{m}\right)^2\left(\frac{3v}{4}+\frac{1-v}{v}\right)\left[\log\frac{12(1-v)E}{5vZ_1^{1/3}mc^2}-\frac{1}{2}\right]dv \qquad 6.13$$

where E is the energy of the μ-meson and v the fractional energy loss. The average rate of energy loss is then

$$-\left(\frac{dE}{dx}\right)_{\text{brems}} = \int_0^1 E\cdot v\cdot f(E,v)\,dv$$

$$= 4\alpha N r_e^2 \frac{Z_1^2}{A}\left(\frac{m_e}{m}\right)^2 E\left[\log\frac{12E}{5mc^2 Z_1^{1/3}} - \frac{1}{3}\right] \qquad 6.14$$

It has been pointed out by Marshak, (1952) that equation 6.13 is not true at high energies because it neglects atomic electron screening effects. Rossi, (1952), has rewritten the argument of the log term of equation 6.13 to include the maximum and minimum impact parameters,

$$\frac{b_{max}}{b_{min}} = \left(\frac{E}{mc^2}\right)^2 \cdot \frac{ch\,(1-v)}{v\;E\,r_n} \qquad 6.15$$

where $r_n = 1.38.10^{-13}\,A^{\frac{1}{3}}$ cm is the nuclear radius. The constant factor of E in the argument of the log term of equation 6.14 has a value 1.07, compared to a value of 0.97 for the constant term in equation 6.15. Photons can only be produced for values of $b < b_{max}$. Thus when $b_{max} > r_a$, (the atomic radius) the atomic electrons shield the particle from the electric field of the nucleus. This atomic electron screening effect is effective for energies

E, exceeding values given by

$$b_{max} = \frac{ch}{vE}\left(\frac{E}{mc^2}\right)^2 = r_a$$

The Fermi-Thomas model of the atom gives

$$r_a = \frac{1}{\alpha^2} r_e Z^{-\frac{1}{3}}$$

or,

$$E = 137\, Z^{-\frac{1}{3}} \cdot 2\pi v \frac{m^2c^2}{m_e}$$

$$= 4300 \text{ Gev.} \quad \text{for } v = \frac{1}{2}$$

For values of E greater than this, the cross-section has been considered by Rozental et al, (1959), who give, following Bethe and Heitler, (1934)

$$f(E,v)dv = 4\alpha N r_e^2 \frac{Z^2}{A}\left(\frac{m_e}{m}\right)^2 \left\{\left[1+(1-v)^2-\frac{2}{3}(1-v)\right]\log\frac{m}{m_e}\cdot 183 Z^{-\frac{1}{3}} + \frac{1}{9}(1-v)\right\}\frac{dv}{v} \qquad 6.15a$$

giving

$$-\left(\frac{dE}{dx}\right)_{brems} = 4\alpha N r_e^2 \frac{Z^2}{A}\left(\frac{m_e}{m}\right)^2 E\left\{\log\frac{m}{m_e}\cdot 183 Z^{-\frac{1}{3}} + \frac{1}{18}\right\} \qquad 6.16$$

$$= 2\cdot 13 \times 10^{-6} E \quad \text{Mev.} \left(\text{gm.cm}^{-2}\right)^{-1} \quad \text{for } E \gtrsim 4300 \text{ Gev}$$

The energy loss given by equations 6.14 and 6.16, is shown in figure 6.2 and table 6.2, where it is compared with approximate values deduced by other workers. The values of dE/dx at 10^{13} eV, is 20.3 MeV $gm^{-1}cm^2$ from equation 6.14, compared with 21.3 MeV $gm^{-1}cm^2$ from equation 6.16. There is no experimental evidence which is inconsistent with the energy loss expressed by equation

6.14, if it is assumed that the spin of the μ-meson is $\frac{1}{2}$ and it has zero anomalous magnetic moment, Peaslee, (1952), Driggers, (1952), Walker, (1953), Hirokawa et al, (1956).

6.3.4 Nuclear Interactions

It has been observed from experiments using nuclear emulsions exposed underground that μ-mesons produce stars. George and Evans, (1950) and Marshak, (1952), have suggested that the differential cross section for a μ-meson of energy E to transfer a fraction v of its energy, can be expressed using the virtual photon flux given by the Williams-Weizsäker (W.W) method, as

$$\sigma(E,v)\,dv = \sigma_w \cdot \frac{2\alpha}{\pi} \cdot \frac{1}{v} \cdot \log\frac{1}{v} \cdot dv \qquad 6.17$$

where $vE = \hbar w$, the photon energy and σ_w is the photonuclear cross-section, assumed constant.

The average rate of energy loss is thus

$$-\left(\frac{dE}{dx}\right)_{nuc} = \int^{1} N.\sigma_w \cdot \frac{2\alpha}{\pi} \cdot \frac{1}{v} \log\frac{1}{v} . dv$$

$$= \frac{2N\alpha}{\pi} . \sigma_w . E = 2.8 \times 10^{21} . \sigma_w . E \quad \text{Mev}(\text{gm cm}^{-2})^{-1}$$

Kessler and Kessler, (1956), and Kessler, (1959), have considered the interaction dynamics and have shown inconsistencies with the earlier work of George, (1952), (1956). The argument of the logarithm term in 6.17 can be rewritten

$$\frac{1}{v} = \frac{E\hbar c}{mc^2 q R} \qquad 6.18$$

where R is the radius over which the electromagnetic interaction is strong and q is the photon energy.

If $R \simeq \hbar/p \simeq hc/E$ then

$$\frac{1}{V} = \frac{E^2}{mq} = \left(\frac{E}{m}\right)_T \left(\frac{E}{q}\right)_L \qquad 6.19$$

Kessler and Kessler have calculated only the transverse, T, term in 6.19, and neglected the longitudinal term, L. At high energies where the probability of large energy transfers is still relatively high, the logitudinal term will not be so important. This assumes that the minimum impact parameter has no finite size,in contrast to the treatment of equation 6.17, (R is the Compton wavelength $R \simeq \hbar/mc$).

The differential cross-section given by Kessler and Kessler is

$$\sigma(E,q)dq = \frac{2\alpha}{\pi}\sigma_w(q)\frac{dq}{q}\left[\frac{2E^2-2Eq+q^2}{2E^2}\log\frac{E-q}{m} - \frac{E-q}{2E}\right] \qquad 6.20$$

where q is the photon energy transferred by the μ-meson, and $\sigma_W(q)$ is the photo-nuclear cross-section. The average rate of energy loss is then

$$-\left(\frac{dE}{dx}\right)_{nuc} = \int_{0 \text{ or } m_\pi c^2}^{E} N.q.\sigma(E,q)dq$$

$$= \frac{2N\alpha\sigma_w(q)}{\pi}\left[\frac{2}{3}\log\frac{E}{m} - \frac{29}{36}\right] \qquad 6.21$$

where $\sigma_W(q)$ is assumed constant, $\sigma_W = 10^{-28}\text{cm}^{-2}$/nucleon.

This energy loss is shown in figure 6.2 and given in table 6.2.

The energy loss by nuclear interaction of μ-mesons has been deduced by Barrett et al. They have subtracted the expected amount of all other types of energy loss using their approximate relations, from the total energy loss deduced from their intensity measurements,

$$-\left(\frac{dE}{dx}\right)_{nuc} < 2.10^{-6} E . \ \mathrm{Mev} \ (\mathrm{gm\ cm}^{-2})^{-1} \qquad 6.22$$

Using equation 6.17, they obtain $\sigma_W < 0.7 \times 10^{-27} \mathrm{cm}^2/$ nucleon. However they recognize that the treatment given by equation 6.17 is inaccurate for large values of photon energy. Using equation 6.21, then at $E = 10^{12}$ eV from table 6.2, $\sigma_W \lesssim 1.3 \times 10^{-28} \mathrm{cm}^2$/nucleon. If the values of energy loss for pair production and bremsstrahlung from equations 6.10 (and 6.11) and 6.14 are used in the subtractions mentioned above then

$$\sigma_W \lesssim 0 \cdot 9 \times 10^{-28} \ \mathrm{cm}^2/\mathrm{nucleon} \qquad 6.23$$

There is thus little error introduced if σ_W is assumed to be constant, and having the value $\sigma_W = 10^{-28} \mathrm{cm}^2$/nucleon.

Measurements made by Meyer et al, (1962), show that the Kessler and Kessler modification of the W.W. method is in better agreement with the measured data on neutron production by μ-mesons, assuming both (γ,n) reactions, and direct interaction between the charge of the μ-meson and the nucleons than with the unmodified W.W. method up to μ-meson energies of 100 GeV/c. There is some indication therefore that the Kessler and Kessler modification of the W.W. method gives a better description of the nuclear interaction of μ-mesons.

6.3.5 The Total Average Rate of Energy Loss

The contributions from the various energy loss processes shown in figure 6.2 and table 6.2 are added to give a total rate of energy loss expression which is also shown in the figure and table.

It is concluded that the average rate of loss of energy indicated by the present work is substantially greater than that assumed by Barrett et al, and deduced by Ozaki, above about 300 GeV. The form of the average rate of energy loss given in figure 6.2 is concluded to be the best theoretical estimate available.

6.4 The Range-Energy Relation of μ-mesons in Rock

The mean range of μ-mesons in rock is derived from the total average rate of energy loss, figure 6.2 and is given by

$$R = R(E_0) + \int_{E_0}^{E} \frac{1}{\left(\frac{dE}{dx}\right)} dE$$

For ranges up to the lower limit of integration the most accurate values are given by Sternheimer, (1959). Thus for $E_0 \doteq 1$ GeV, $R(E_0) = 545$ gm cm^{-2} and

$$R = 545 + \int_{1}^{E} \frac{1}{\left(\frac{dE}{dx}\right)} \cdot dE \ \mathrm{gm.cm}^{-2} \qquad 6.24$$

Above 1 GeV, the energy loss relation, figure 6.2, can be integrated numerically. The resulting range-energy relation is given in figure 6.3. The usual units of range have been taken, that is metres water equivalent, m.w.e., (1 m.w.e. = 100 $\mathrm{gm.cm}^{-2}$, measured from sea level).

6.5 The Intensity of Cosmic Rays Underground

Using the integral sea-level μ-meson spectrum and the range-energy relation derived above, the intensity of μ-mesons which penetrate to given depths underground can be derived and compared directly with the measured intensities up to depths corresponding to the maximum detectable momentum of the sea-level spectrum.

Most of the data obtained have been relative, that is, measurements have been taken of the rates at various depths and then the rate at the least depth has been normalised to an intensity value predicted from a sea-level integral spectrum and a range-energy relation, usually at depths between 10 and 100 m.w.e. As the measurements on the sea-level μ-meson spectrum have become more accurate the values of the intensity taken for normalisation have changed. Thus Barrett et al, have used the integral spectrum derived by Rossi, and also a range-energy relation of his, to normalise the data of V.C. Wilson, (1938), and others.

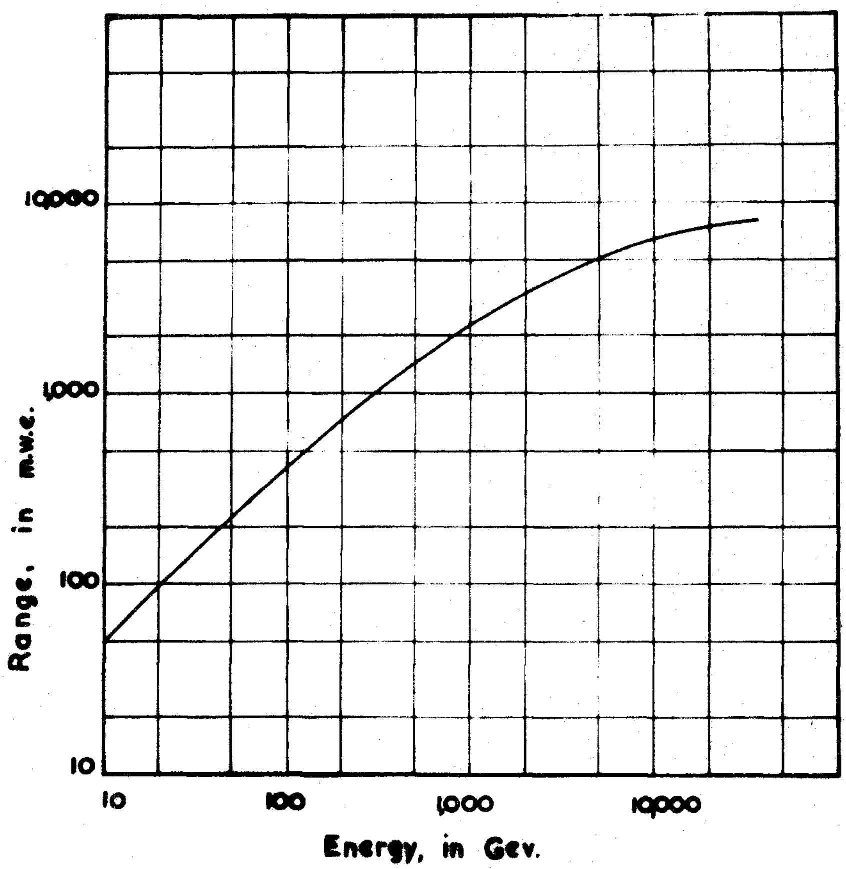

Figure 6.3 : The mean range of μ-mesons in rock as a function of their energy at sea-level. (derived from figure 6.2)

Another factor which influenced the early results, and conclusions on the intensity at various depths, has been the geometry of the apparatus and the use of lead to screen it and thus cut down the spurious rate of counting, arising from local radio-activity or locally produced soft radiation. This has been considered in detail by Clay, (1939). The use of lead in various quantities in some experiments, to separate the Geiger counters in telescopes, has added to the complexity in comparison of the results obtained by different workers.

The normalisation is comparatively unaffected by the various forms of energy loss which have been adopted. From table 6.2 it can be seen that there is little difference in the rate of energy loss deduced by various authors up to energies $\sim$100 GeV or $\sim$400 m.w.e.

There is very little data below 2000 m.w.e. This is partly due to the small numbers of mines of sufficient depth which have surrounding rock of low radio active content, and partly because of the extremely low rates and technical problems involved at such depths, (heat, humidity, etc.).

Accordingly, the measured intensities underground will be compared with the predicted intensities in two ranges of depth, that is 100 - 2000 m.w.e. and at depths greater than 2000 m.w.e.

6.5.1 The Measured Intensity at Depths in the Range 100 - 2000 m.w.e.

In this section only data in the vertical direction will be considered. All the data have been taken under rock except that of Ehmert which was taken under water and has been corrected for this. The measured intensities are not all absolute values. The relative intensities have been normalised to rates predicted from the sea-level integral spectrum and the mean range energy relation figure 6.3. The most extensive data are those of V.C. Wilson, (1938). These data were obtained without the use of lead within the Geiger counter telescope so that the intensities at the greatest depths will be in excess because of the contribution of the soft component to the total intensity, which increases with depth as the mean energy of the penetrating component increases. These data will not be included for comparison purposes. Most of the data of Clay and Van Gemert, (1939), were obtained using 5 cm of lead between the Geiger counter trays and also lead shielding. The corrected data taken from Barrett et al have also been normalised. Clay,(1939) has also obtained data under similar conditions with 10 cm Pb.

The values are given in table 6.3 for the normalised data, together with absolute intensities by different authors. The data of Randall and Hazen, (1951), who have measured the absolute intensity, were obtained using a two-fold Geiger counter telescope which would be sensitive to showers, even though there was some lead in the apparatus. Avan and Avan, (1955), have measured the absolute intensity using emulsions where, quite possibly, electrons will have been included in the total intensity. These measured intensities are compared with the predicted values in figure 6.4. The upper full curve is the best estimate of the depth-intensity variation from the measured data. The lower full curve is the predicted intensity calculated from the sea-level integral spectrum of μ-mesons (figure 6.1) and the mean range-energy relation (figure 6.3) calculated from the best estimate of the average rate of energy loss of the present work. The conclusions to be drawn from the comparison of these two full curves are deferred until after the effect of fluctuations in the rate of energy loss have been considered (section 6.6). For the present however it can be seen from figure 6.4 that the measured intensities obtained by different authors have quite wide limits of variation. In particular the absolute measurements seem to have consistently higher intensities than the normalised values. Pine et al, (1959), have also renormalised the data in table 6.3 using their integral spectrum. However their integral spectrum is itself calculated on the assumption that the slope of the differential spectrum has a value

Table 6.3. Intensities at various depths by different authors

All depths in m.w.e. below sea-level in the vertical direction : all intensities in (cm^{-2} sec^{-1} st^{-1}).

Randall and Hazen, (1951)

Depth	Intensity
850	2.17 .02x10^{-6}

Bollinger, (1951)

Depth	Intensity	Error
1500	3.9 x10^{-7}	2%
1840	1.91x10^{-7}	2%

Barrett et al, (1952)

Depth	Intensity
1574	3.25 .05x10^{-7}

Sreekantan et al, (1952, 1956)

Depth	Intensity
90	2.56x10^{-4}
371	1.34x10^{-5}
465	9.7 x10^{-6}
674	4.32x10^{-6}
875	1.99x10^{-6}

Clay and van Gemert, (1939)

Depth	Intensity
90	2.56x10^{-4}*
253	3.97x10^{-5}
362	1.70x10^{-5}
503	6.92x10^{-6}
664	2.84x10^{-6}
990	9.40x10^{-7}
1304	4.48x10^{-7}
1635	1.82x10^{-7}

Ehmert° (1937) taken from Pine et al, (1959)

Depth	Intensity
93	2.45x10^{-4}*
111	1.51x10^{-4}
159	9.9 x10^{-5}
280	3.68x10^{-5}

Clay, (1939)

Depth	Intensity
75	3.5 x10^{-4}*
209	5.61x10^{-5}
301	2.43x10^{-5}
417	9.69x10^{-6}
553	3.95x10^{-6}
1097	6.49x10^{-7}

Avan and Avan, (1955)≠

Depth	Intensity
300	3.8x10^{-5}
580	7.3x10^{-6}
1280	8.0x10^{-7}

*normalised to this value

°under water

≠emulsion work.

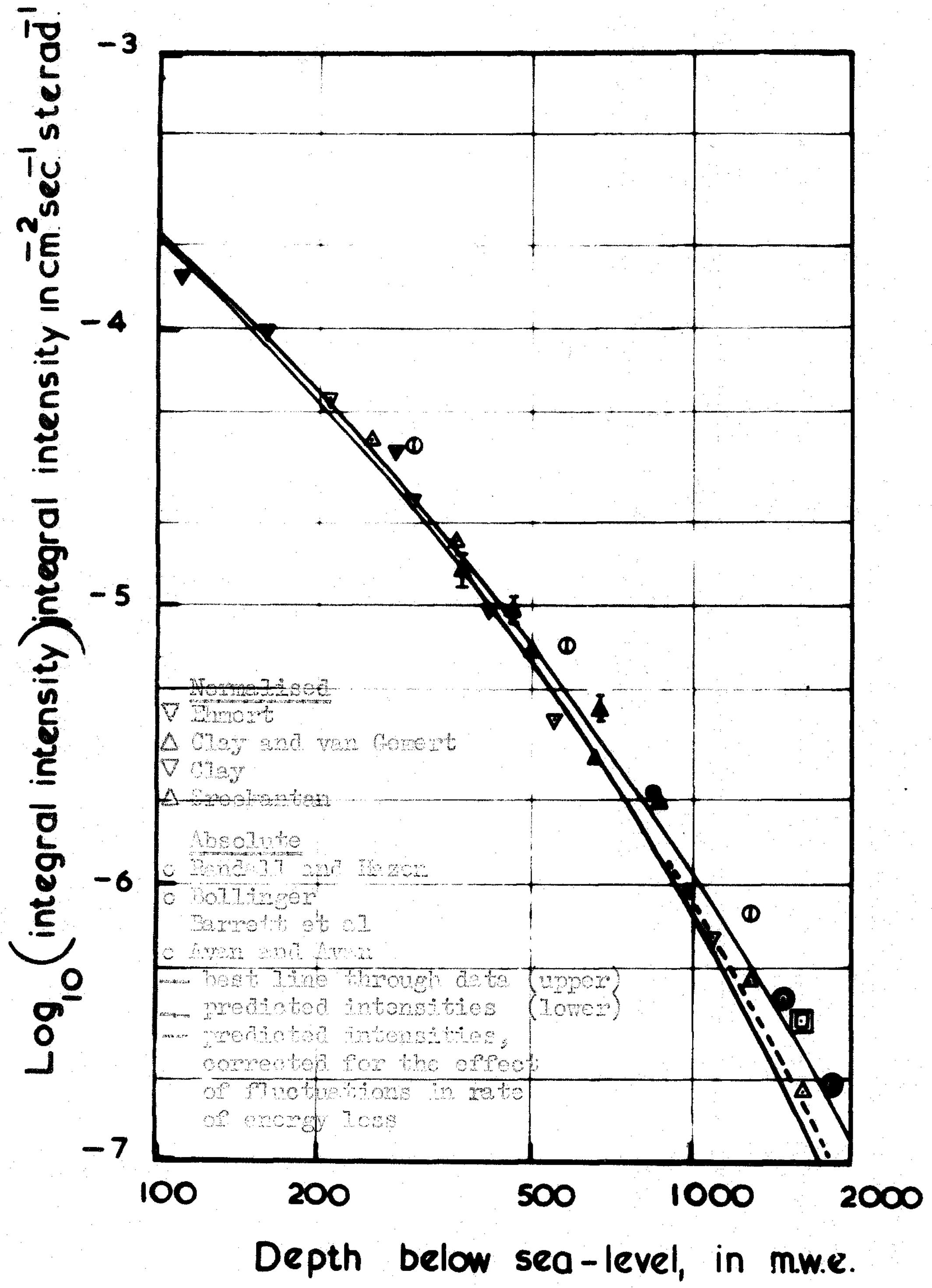

Figure 6.4 : The comparison of the measured intensities with the predicted values at depths 100 - 2000 m.w.e.

2.81 for momenta above 50 GeV/c and this leads to an integral spectrum having an intensity which is ~ 36% too high at 100 GeV/c.

6.5.2 The Measured Intensity Below Depths of 2000 m.w.e.

The first measurements made at depths below 2000 m.w.e. were made by Miyazaki, (1949). However, doubt has been cast on these data because of technical and measurement imperfections, (Meisowicz and Massalski, (1950)), and these will not be considered further. The only other measurements are those of Barton, (1961), Miyake et al, (1962 and p.c.) and Bollinger, (1951), (also given by Pine et al, (1960)). Of these, the first two are in the vertical direction, only the work of Barton being absolute. The work of Bollinger was made at various zenith angles and refers to absolute rates and therefore does not need normalisation. Bollinger's work was carried out at only 1500, and 1840 m.w.e. and because of the large zenith angles used extend to effective depths far greater because of the greater path of the particles through rock at inclined angles. However these measurements cannot be applied here directly because of the enhanced intensities of μ-mesons at inclined angles in the sea-level radiation which gives rise to the underground intensities.

The enhanced intensities of μ-mesons at inclined angles at sea-level havebeen shown by Jakeman, (1956), Smith and Duller, (1959), to be important only at high energies, where although the total intensity is very much reduced by the increased depth of the atmosphere, an increase by a factor of 3 or 4 in the differential spectrum is possible at 1000 GeV/c for zenith angles approaching 90°.

The analysis of Barrett et al, (1952), and Appendix 3 for the case of inclined angles gives

$$M(E) = \frac{F(E/r)}{r} \cdot \frac{b}{E\cos\theta} \left\{ 1 + \frac{b}{E\cos\theta} \right\}^{-1} \qquad 6.25$$

where the symbols have the same meaning as in the Appendix. At high energies, $E \sim 10^{13}$ eV, this reduces to

$$M(E) = 8.9\, E^{-3.64} \left(\frac{x}{\rho}\right)_\theta \Big/ H \qquad (E \text{ in GeV}) \qquad 6.26$$

assuming that the value of γ, the exponent of the π-meson production spectrum derived in the previous chapter, can be extrapolated to these energies. Allen and Apostolakis, (1961), have shown that uncertainties of more than 4% are not introduced if a unique height of production of π-mesons is assumed and this is taken to be 120 gm.cm^{-2}. Using their values of $(x/\rho)_\theta$, shown in figure 6.5a as $(x/\rho)_\theta \frac{1}{H}$, the intensities for 5° intervals $>60°$ have been calculated for an energy of 10^{13} eV. The intensities at 1000 GeV for the angles given by Allen et al have been corrected in the light of the present more accurate sea-level μ-meson spectrum in the vertical direction (these authors used the preliminary spectrum obtained by using the flash-tubes, Ashton et al, (1960)). The resulting differential spectra have been

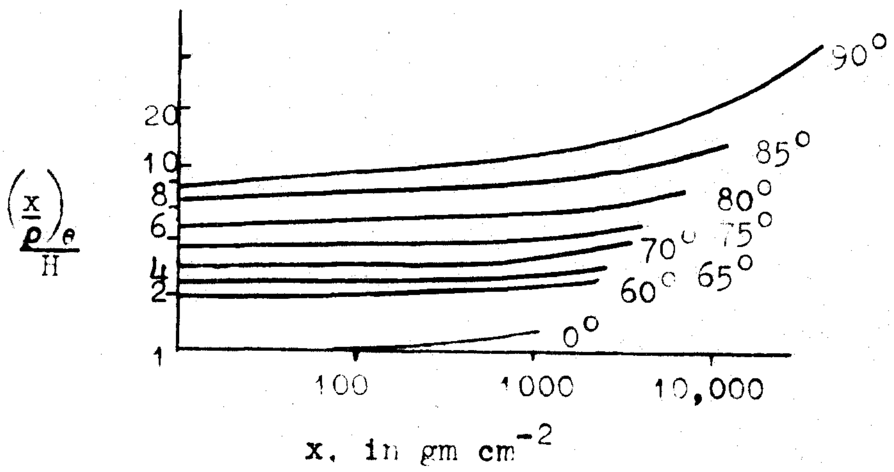

Figure 6.5a :
The variation of $(x/p)\theta/H$ with x for various zenith angles θ

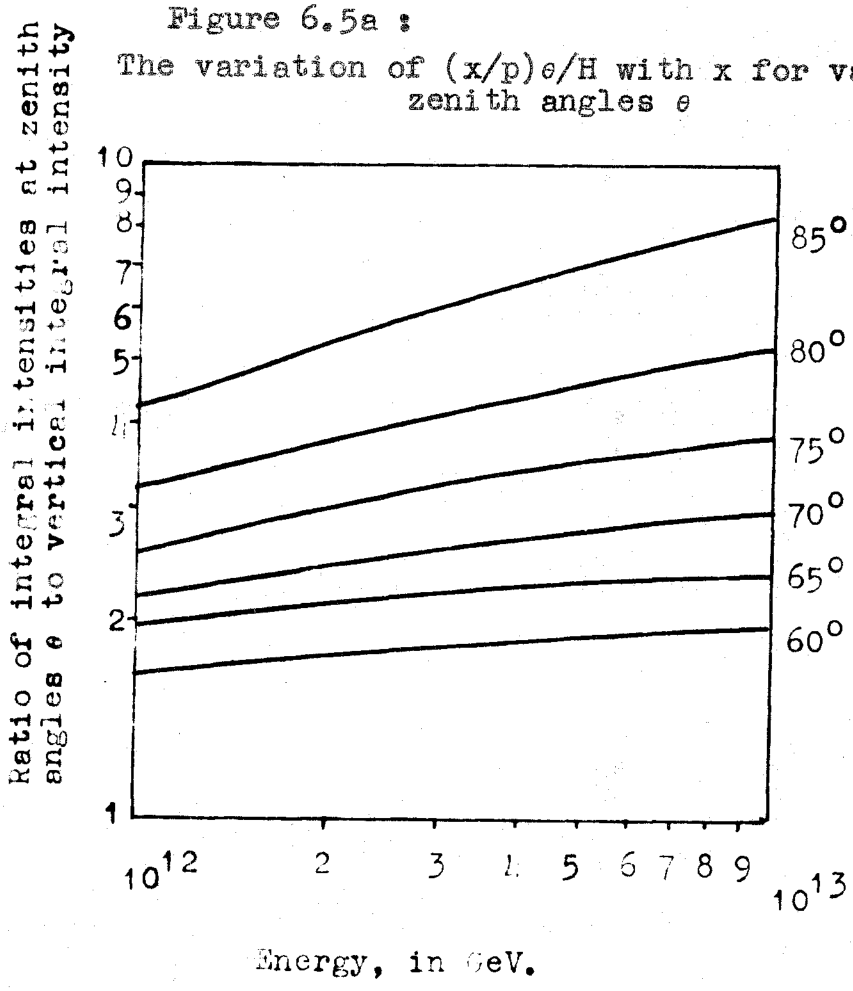

Figure 6.5b : The variation of the ratio of the integral intensity at various zenith angles θ, to that in the vertical direction, with energy at sea-level.

integrated for energies above 1000 GeV. The ratios by which the integral intensities are increased over the vertical integral intensity

$$I(>E)_\theta \Big/ I(>E)_0$$

were derived, figure 6.5b. Any changes in the value of γ (equation A3.9) at higher energies are reduced by taking this ratio.

Taking the effective depths of Bollinger's results, table 6.4, the minimum energy was derived from the range-energy relation, figure 6.3. The correction factor derived using figure 6.5b is shown in table 6.4 together with the corrected intensities.

The data of Bollinger have also been considered by Miyake et al. However it seems that these authors use a sec θ correction factor which is only approximate at large zenith angles since it neglects the curvature of the earth. The two correction factors are compared in figure 6.6.

The effect of scattering of μ-mesons in the rock above Bollinger's apparatus must also be allowed for. Allen et al have shown that the scattering of μ-mesons in the atmosphere increases the intensity by a small amount at low energies and large zenith angles, because of the greater intensity of particles in the vertical direction at low energies. A similar effect will be inherent in Bollinger's results. If the last ~ 900 gm.cm^{-2} of rock is considered, the approximate magnitude of the

Table 6.4 : The Corrected Data of Bollinger, (1951)

	Intensity ($cm^{-2}sec^{-1}st^{-1}$)	No. of counts	Zenith angle	Effective Depth m.w.e.	Energy (GeV)	Corrn. factor	Corrected Intensity
I	$7.04x10^{-10}$	1	$77\frac{1}{4}$	8330	25500	5.05	$1.38x10^{-10}$
	$3.52x10^{-9}$	5	$70\frac{3}{4}$	5560	6000	2.9 (3.05)	$1.22x10^{-9}$
	$7.39x10^{-9}$	10.5	$65\frac{1}{8}$	4370	3200	2.35 (2.35)	$3.15x10^{-9}$
	$1.44x10^{-8}$	20.5	$59\frac{1}{8}$	3580	2080	1.72	$8.35x10^{-9}$
	$3.10x10^{-8}$	44	$53\frac{1}{2}$	3094	1570	1.4	$2.22x10^{-8}$
II	$3.52x10^{-10}$	0.5	$81\frac{3}{8}$	12300	-	9-10	-
	$1.24x10^{-9}$	1	$76\frac{3}{8}$	6350	9000	4.15 (4.23)	$3.00x10^{-10}$
	$8.67x10^{-9}$	7	$71\frac{1}{2}$	4730	4000	2.9 (3.15)	$3.00x10^{-9}$
	$1.73x10^{-8}$	14	$66\frac{1}{2}$	3760	2250	2.3	$7.50x10^{-9}$
	$3.10x10^{-8}$	25	$60\frac{1}{4}$	3020	1450	1.75	$1.77x10^{-8}$

I location I , 1840 m.w.e.
II location II , 1500 m.w.e.

The correction factors in brackets are those obtained from Miyake et al, (1962) and included for comparison.

Table 6.5 : The above data corrected for scattering.

Zenith angle	Correction %	Corrected Intensity ($cm^{-2}sec^{-1}st^{-1}$)
$77\frac{1}{4}$	-6.4	$1.28x10^{-10}$
$70\frac{3}{4}$	-3.0	$1.19x10^{-9}$
$65\frac{1}{8}$	-1.7	$3.09x10^{-9}$
$59\frac{1}{8}$	-1.4	$8.25x10^{-9}$
$53\frac{1}{2}$	-1.0	$2.20x10^{-8}$
$81\frac{3}{8}$	-12.1	-
$76\frac{3}{8}$	-5.8	$2.83x10^{-10}$
$71\frac{1}{2}$	-3.3	$2.90x10^{-9}$
$66\frac{1}{2}$	-2.0	$7.35x10^{-9}$
$60\frac{1}{4}$	-1.4	$1.75x10^{-8}$

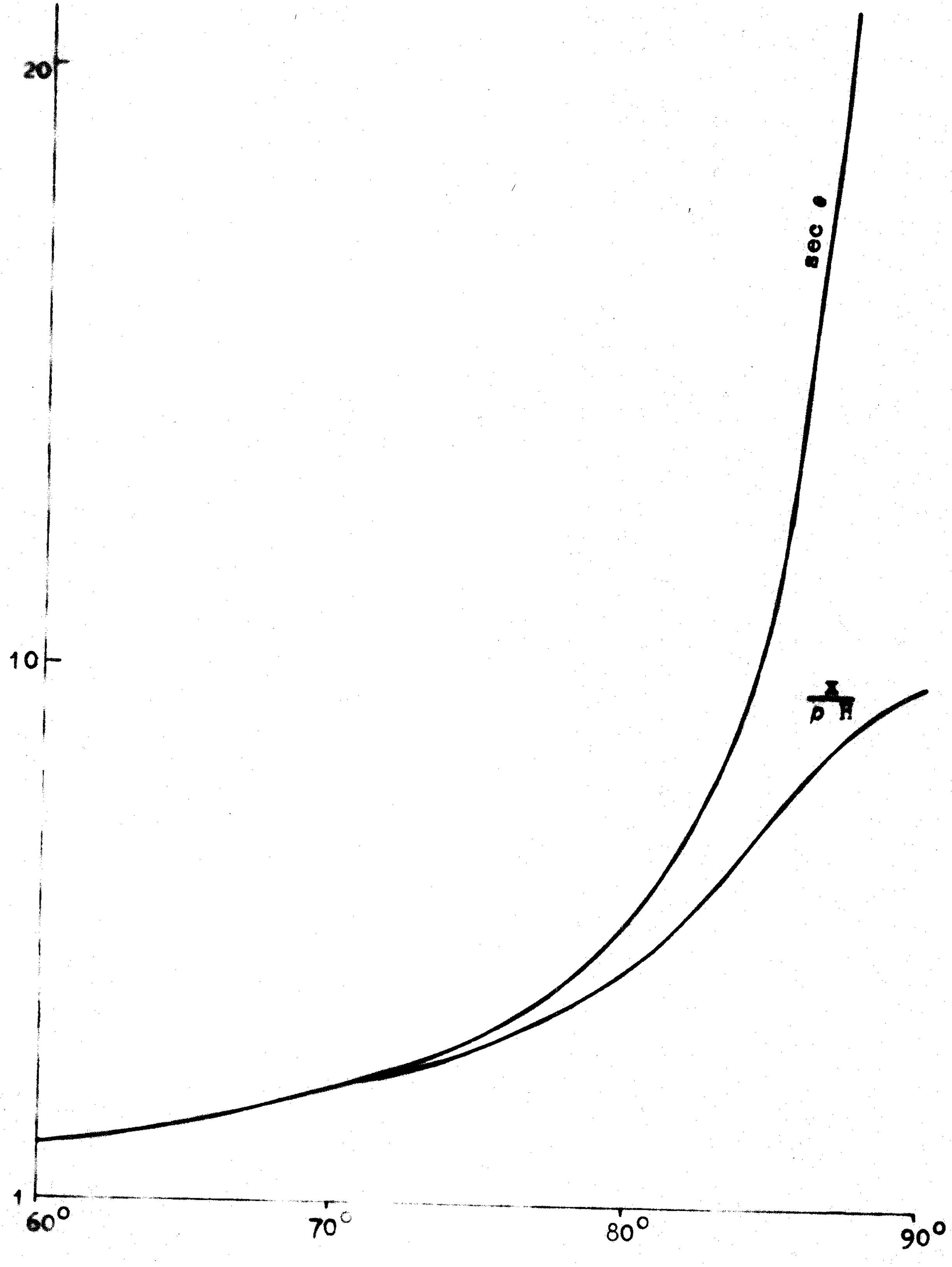

Figure 6.6 : The comparison of x/pH and sec θ with zenith angle, θ.

effect can be determined. The μ-mesons will lose an average of about 2 GeV in this thickness of rock, so that nearly all of the scattering will take place in this region above the apparatus. The previously corrected differential spectra of Allen et al have been integrated above 0.4 GeV, corresponding approximately to the minimum energy of μ-mesons able to penetrate Bollinger's apparatus. The increase in the intensity, because of scattering, at various angles is shown in figure 6.7, where the maximum increase in the intensity is seen to be less than 12%. Bollinger's results have been corrected further and the final corrected intensities are given in table 6.5. The other data of Bollinger have been corrected by the factor

$$\frac{B+E}{E\cos + B}$$

where $B = 89.26$ GeV, which is accurate at the angles where it is applied and these corrected intensities are given in table 6.6. The measured intensities in tables 6.5 and 6.6 are shown in figure 6.8. It is not clear from the results of Miyake et al, whether they have applied a correction for the zenith angle variation to their results, which will be considerable because of the large angular acceptance of their apparatus. This important correction has been considered by Barton.

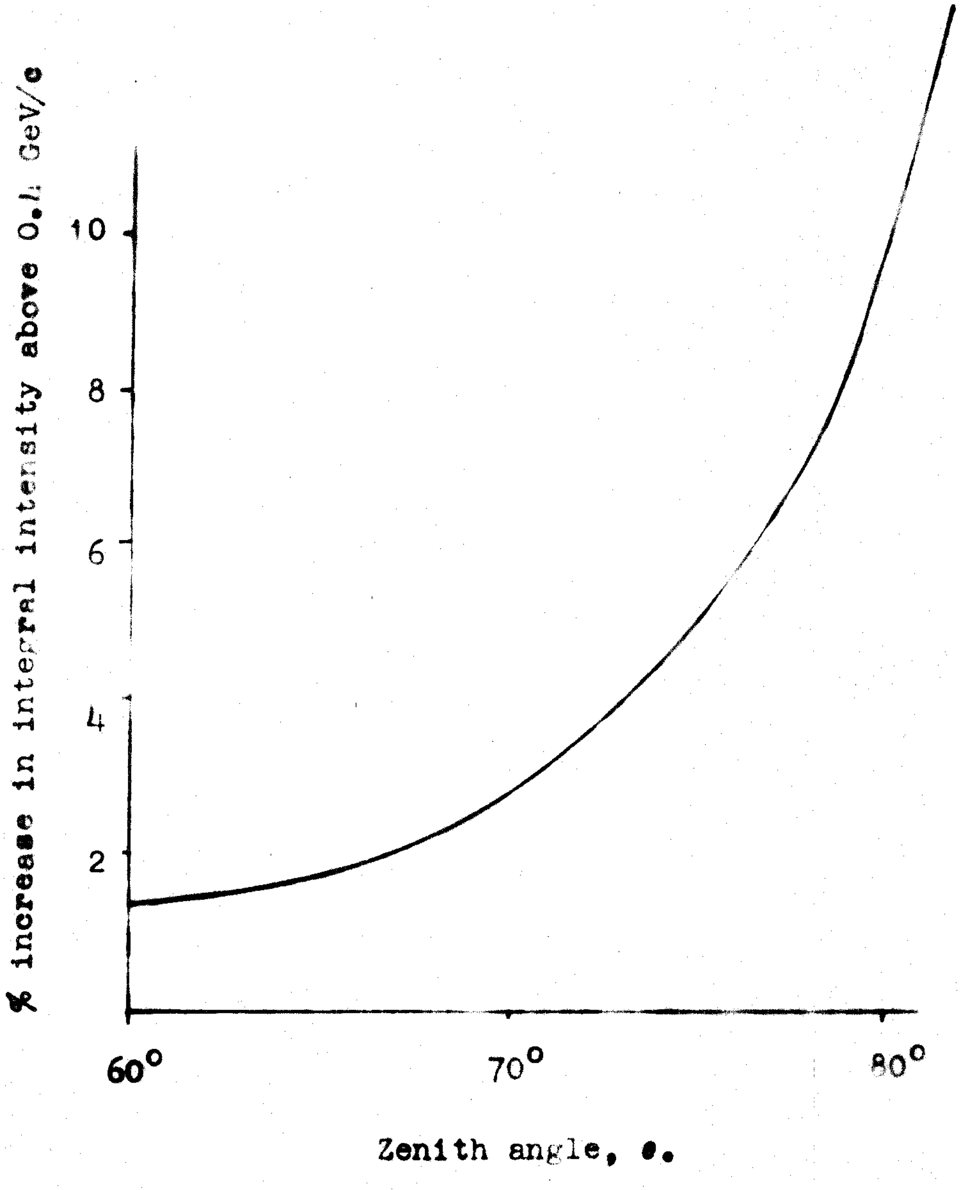

Figure 6.7 : The scattering correction.

Table 6.6 : Intensities at great depths by various authors.

Barton, (1961)

Depth	Relative Intensity	Intensity†
0	1	7.54×10^{-3}
1660	$2.95 \pm 0.4 \times 10^{-5}$	2.22×10^{-7}
3280	$1.0 \pm 0.3 \times 10^{-6}$	7.54×10^{-9}
5650	$< 2.2 \times 10^{-7}$	$< 1.65 \times 10^{-9}$

Miyake et al, (1962)

Depth	Intensity†
790	2.0×10^{-8}*
1783	1.35×10^{-7}
3340	9.5×10^{-9}
4200	2.35×10^{-9}
6380‡	1.30×10^{-10}

Bollinger, (1951)

	Intensity ($cm^{-2} sec^{-1} st^{-1}$)	No. of counts	Zenith angle	Effective Depth	Energy (GeV)	Corrn. factor	Corrected Intensity†
I	5.56×10^{-8}	79	48½	2773	1500	1.46	3.82×10^{-8}
	6.88×10^{-8}	97½	42⅞	2507	1200	1.33	5.18×10^{-8}
	8.6×10^{-8}	122	37¾	2322	1060	1.25	6.90×10^{-8}
	1.14×10^{-7}	162	31¾	2162	930	1.17	9.8×10^{-8}
	1.23×10^{-7}	176	26	2046	850	1.10	1.12×10^{-7}
	1.52×10^{-7}	217	16¾	1920	780	1.02	1.48×10^{-7}
II	4.84×10^{-8}	39	55⅞	2668	1300	1.71	2.84×10^{-8}
	7.45×10^{-8}	60	50¾	2369	1100	1.52	4.87×10^{-8}
	1.11×10^{-7}	89	45	2119	900	1.36	8.1×10^{-8}
	1.57×10^{-7}	127	39½	1945	780	1.28	1.22×10^{-7}
	2.11×10^{-7}	169	32¾	1784	680	1.17	1.80×10^{-7}
	2.61×10^{-7}	210	20	1597	580	1.06	2.47×10^{-7}

* normalised to best estimate of depth intensity data of figure 6.4 at this depth.

‡ private communication, May 1962.

† $cm^{-2} . sec^{-1} st^{-1}$

The measured intensities for depths below 2000 m.w.e. are compared with the predicted values in figure 6.8. The upper full curve is the best estimate of the depth intensity variations from the measured data. The lower full curve is the predicted intensity calculated from the sea-level integral spectrum of μ-mesons and the mean range-energy relation as before. The conclusions to be drawn from the comparison of these two full curves will be deferred until after the next section where the effect of fluctuations in the average rate of energy loss is considered. For the present however, it can be seen from figure 6.8 that there are again quite wide limits in the variation of the measured intensities obtained by different authors.

6.6 The Effect of Straggling on Range

The average rate of energy loss by μ-mesons has been considered in sections 6.31-6.34. At high energies the terms involving bremsstrahlung and nuclear losses are a large fraction of the total energy loss. The probabilities for fractional energy loss, v, considered in the above sections have shown that for bremsstrahlung, (equation 6.15a), and nuclear interactions, (equation 6.17), alone, the probability of a fractional energy loss v is approximately

$$f(E,v) \propto \frac{1}{v}$$

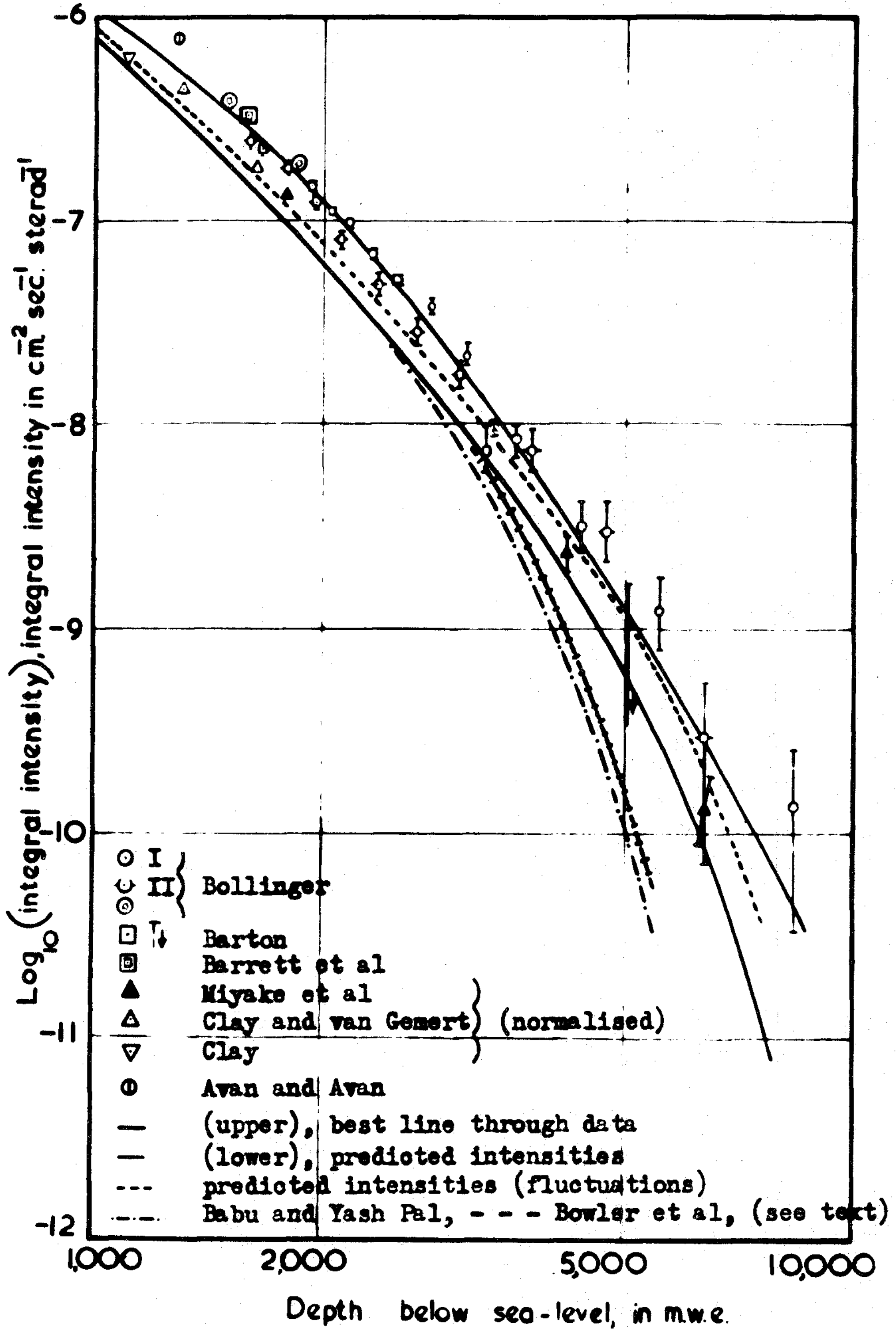

Figure 6.8 : The comparison of the measured intensities with the predicted values at depths below 2000 m.w.e.

and that the other forms of energy loss fall off more rapidly.

The energy loss process can thus no longer be considered as a continuous process at high energies, since a μ-meson may lose a very large fraction of its energy in one collision. It is because of the possible large energy losses in single collisions that the range of μ-mesons of a given energy will not be constant. The situation will be analogous to the so-called straggling process observed in β-ray absorption. The straggling process has the effect of increasing the intensity of particles predicted at great depths using the average rate of energy loss and the mean range energy relation, because some of the particles at low energies where the intensity is greater, will have energy losses less than the average value and so will be able to survive to greater depths.

Bollinger, (1951), has performed a Monte Carlo calculation to evaluate the magnitude of this effect for the absorption of μ-mesons underground. He concluded that the effect was small, and corresponded to $\sim$ 10% increase in intensity, but, however, the calculation was a numerical one based on only 100 particles.

Mando and Sona, (1953), have considered the problem theoretically, by solution of the diffusion equation through the earth. However it was carried out only approximately using first order terms and collision and bremsstrahlung losses only, and the increase in intensity was found to be, only ~ 2%.

Rozental and Strel'tsov, (1959), have made a similar theoretical treatment, for different sea-level spectra and photo-nuclear cross-sections. Their results are given in table 6.7. These authors have used similar cross-sections for the various energy-loss processes to those used in sections 6.3.3-6.34, so their results could be directly applied to the present work. It can be seen that the value of the ratio by which the predicted intensity, I_m, which is obtained by using the mean range-energy relation, figure 6.3, should be increased, I_s/I_m, increases with increasing σ_w, γ, E and depth. However it appears that the correction factors have been evaluated at underground energies of about 3000 GeV, or sea-level energies of about 3500 GeV, at the shallowest depth for which the factors were calculated. Thus this work cannot be directly applied to the present problem.

The Monte Carlo calculations carried out by Bollinger to find the survival probability of μ-mesons of different energies to given depths have recently been repeated by Palmer (1962, p.c.) following a similar method to that adopted by Bollinger but with greater statistical accuracy. Palmer has determined the survival probability for 1000 particles (~ 3% accuracy) using a computer. The probability

Table 6.7 : The Correction factors derived by Rozental' and Stel'tsov.

$E = 3000$ GeV, $\sigma_w = 10^{-28}$ cm^{-2}/nucleon.

Depth (m.w.e.)	1350	2700	4580	γ, integral
Correction factor	1.1	1.25	1.5	2
	1.3	1.9	2.9	3

$E = 3000$ GeV, $\sigma_w = 5 \times 10^{-28}$ cm^{-2}/nucleon.

Depth (m.w.e.)	1350	2700	4500	
Correction factor	1.15	1.35	1.7	2
	1.5	2.2	4.8	3

E is the energy of the μ-meson at the stated depth.

γ is the slope of the integral μ-meson spectrum at sea-level.

The correction factor, I_s/I_m, is the factor by which the predicted intensity using the average rate of energy loss should be multiplied to obtain the resulting intensity corrected for fluctuations in energy loss.

Table 6.8 : The ratio I_s/I_m calculated by Palmer, (1962, p.c.).

Depth	1000	2000	3000	5000	7500
I_s/I_m	1.10	1.21	1.32	1.86	3.10

of a fractional energy loss, v, has been calculated by taking approximate forms for the average rate of energy loss calculated by the author and given in table 6.2,

$$-\frac{dE}{dx}_{\text{pair}} \simeq 1.6 \times 10^{-6} E \text{ MeV/gm.cm}^{-2} \qquad 6.27$$

$$-\frac{dE}{dx}_{\text{brems}} = 1.8 \times 10^{-6} E \text{ MeV/gm.cm}^{-2} \qquad 6.28$$

$$-\frac{dE}{dx}_{\text{nuclear}} \simeq 1.7 \times 10^{-6} E \text{ MeV/gm.cm}^{-2} \qquad 6.29$$

The error introduced by these approximate forms is not greater than ±3%. The average rate of energy loss for collision processes follows closely the value given by equation 6.9. Using the integral spectrum of figure 6.1 extrapolated to high energies assuming a constant exponent, $\gamma = 2.64$, for the differential π-meson production spectrum, the ratio by which the intensity is increased when fluctuations in energy loss are allowed for, over the intensity calculated assuming a mean range for the μ-mesons, I_s/I_m, has been calculated by Palmer for various depths and is given in table 6.8. In order to obtain the correct predicted values of intensity at the depths given in the table, the predicted intensity values given in figures 6.4 and 6.8, which have been calculated assuming a mean range for μ-mesons, must be multiplied by these ratios. The predicted intensities corrected for the effect of fluctuations in the average rate of energy loss, are shown in figures 6.4 and 6.8 as the "dashed" lines.

It is concluded from table 6.8, and figures 6.4 and 6.8, that the effect of fluctuations in energy loss is extremely important, and that the correction to be applied for this effect increases with increasing values of the slope of the sea-level integral μ-meson spectrum and increasing average rate of energy loss. The comparison of the corrected predicted intensities with the best estimate of the measured intensities underground will now be considered.

6.7 Conclusions

The intensity measurements made at sea-level may be subject to bias effects because of the selection methods used in the collection of data, Chapter 3. The measured integral μ-meson spectrum at sea-level refers essentially to single particles. These particles at high μ-meson energies, $\sim 10^{12}$ eV, are parts of the observed extensive air showers, E.A.S., which at sea-level contain mostly electrons, together with a small percentage of μ-mesons. At low energies, the electron component is rapidly absorbed before it reaches sea-level. Thus the bias effects due to particles which accompany the μ-mesons will increase with energy. Barrett et al have found that practically all E.A.S., having more than 500 electrons at sea-level, contain a μ-meson of energy ($E \sim 10^{12}$ eV) sufficient to penetrate to 1600 m.w.e., and that individual μ-mesons occur within ~ 10 m of the core of a shower. With the present apparatus it is clear that if a density of associated particles greater than about 1 m^{-2} occurs, then this type of event will not be accepted for measurement. The bias effect can be evaluated for μ-mesons and electrons from the lateral distribution curves given by Fukui et al, (1960). Using these curves it is found that the density of electrons is greater than 1 m^{-2} over a radius of 1.5 m for a shower containing 10^3 electrons at sea-level. The density of μ-mesons is almost independent of the position from the core of the shower up to radii of 10 m, and the total number of μ-mesons associated with the core of the shower is ~ 3, in good agreement with the values given by Barrett et al. Thus the μ-mesons which are associated with an electron density > 1 m^{-2} within 1.5 m of a shower axis will be lost from the present measurement, but these do not account for more than 5% on average of the total numbers. It is therefore concluded that the E.A.S. bias effect is small.

Before any conclusions can be drawn from the very important measurements on intensities at great depths, in order to obtain information on the energy spectrum of μ-mesons at sea-level at energies above 10^{12} eV, the validity of the best estimate of the rate of energy loss derived in this chapter must be confirmed. The integral spectrum of μ-mesons at sea-level is well known up to energies of about 1000 GeV. Comparison of the predicted intensities corrected for the effect of fluctuations, with the best estimate of the underground intensities is given in figure 6.4. It can be seen that there is good agreement of the best estimate of the measured intensities with the predicted intensities in the region 100 - 1000 m.w.e. and also between 1000 and 2000 m.w.e. with the predicted intensities corrected for the effect of fluctuations in energy loss, "dashed line". In particular, the normalised intensities, which cover a wide range of depths, show excellent agreement with the predicted intensities over a wide range of depths and especially in the region 1000 - 2000 m.w.e., thus lending support to the validity of the form of the energy loss adopted as the best estimate. It is unfortunate that there are no absolute measurements of intensity underground, which extend over a wide range of depths. It is therefore concluded that the average rate of energy loss derived in this chapter and shown in figure 6.2 is an accurate representation of the energy loss and that the effect of fluctuations in the rate of energy loss is important in arriving at this conclusion.

At depths greater than 2000 m.w.e., the average rate of energy loss which has been verified at shallower depths (and hence lower energies) is extrapolated to obtain the mean range for μ-mesons of higher energy. Since the relevant corrections which apply at high energies (such as for atomic screening) have been included in the derivation of the rate of loss of energy, the use of this relation is considered to be justified. In order to continue the comparison carried out in figure 6.4 for depths up to 2000 m.w.e., the predicted intensities at depths greater than 2000 m.w.e. have again been found using the extrapolated sea-level integral μ-meson spectrum, figure 6.1 and the extrapolated mean range-energy relation, corrected as before for the effect of fluctuations, table 6.8. The predicted intensities found in this way are shown in figure 6.8, the "dashed line". Although the difference between the predicted and best estimate of the measured intensities found in figure 6.4, is again apparent, the normalised intensities in figure 6.8 (see table 6.6) of Miyake et al are in excellent agreement with the predicted intensities. The normalisation of the data of these authors at 790 m.w.e. is unaffected by the form of the rate of energy loss adopted. It would be of great interest if the very precise measurements carried out by these authors could be determined as absolute intensities, instead of rates, which have subsequently to be normalised. It is therefore concluded that there is some evidence for the extrapolated form of the present sea-level integral spectrum, that is with a constant differential exponent of the π-meson production spectrum having $\gamma = 2.64$, which is in disagreement with the results of Fujimoto et al, (1960) and Duthie et al, (1961), and Bowler et al, (1962) (see section 8.2). Also shown in figure 6.8 are the intensities derived from the integral sea-level μ-meson spectra of Duthie et al, and Babu and Yash Pal, (1962). The work of Duthie et al and Bowler etal on γ-ray cascades has been used to find a π^0-meson production spectrum which has subsequently been used to predict the μ-meson spectrum at sea-level at energies above 300 GeV. It can be seen, figure 6.8, that this leads to intensities at depths below 2000 m.w.e. which are much less than those predicted by the present work. The sea-level spectrum derived by Bowler et al has a greater slope than that found from the authors work above 300 GeV, so that the corrections to be applied for the effect of fluctuations in energy loss will be greater. This also applies to the other intensity curve shown in figure 6.8, derived from the theoretical work of Babu and Yash Pal, (1962), which, briefly, assumes that a hyperon source gives rise to μ-mesons at high energies. This work is further considered in chapter 9. The corrections to be applied to these two curves (having greater slopes) for the effect of fluctuations in energy loss are not available but would be unlikely to be of such value as to give agreement with the best estimate of the measured intensities. The only way in which these curves can be accommodated into the present picture, is by reducing the rate of energy loss of μ-mesons, which would suggest that one or more of the theoretical estimates of the cross-sections for the various energy loss processes might be in error and need revision. It is therefore concluded that although there is some indication for the form of the energy loss derived in this chapter, giving rise to good agreement of the intensities derived from the extrapolated form of the integral spectrum assuming constant γ, modification to the rate of energy loss, and hence the theoretical cross-section for energy loss by the different processes, would be necessary if the sea-level spectrum of Bowler et al was to give good agreement with the measured intensities underground.

Chapter 7

The Measured Charge Ratio of μ-mesons at Sea-Level

7.1 Introduction

The measurement of the charge ratio of μ-mesons at sea-level is of particular interest at the present time, because of the recently proposed theory of Peters (1962), that some μ-mesons at high energy, and in particular energies covered by the present work, are produced via hyperon decay. Since there are no other measurements of the charge ratio above 100 GeV/c, the present work provides an important test of this theory and the need for a complete knowledge of the technical factors affecting the accuracy of the determination of the ratio is vital.

Although the charge of μ-mesons is easily identified by the magnetic deflection, many forms of bias can arise from the use of magnetic spectrographs. The types of bias can be grouped into two forms: geometric bias and time dependent magnetic bias. Geometric bias is inherent in the construction of the spectrograph and involves asymmetries in the alignment or acceptance geometry of the instrument. The time dependent magnetic bias depends more on the variation of the magnitude of the deflecting field with time and the relative times for which data are collected on each field direction, and the efficiency of the Geiger counter telescope during these times.

It is fortunate that most geometric, time dependent and magnetic bias can be reduced to effects which have negligible effect on the final result by frequent reversal of the magnetic field. The charge ratio of μ-mesons, defined in section 2.5, then involves only the elementary summation of numbers of positively charged, and negatively charged μ-mesons falling in various deflection cells. The only systematic corrections which need to be applied are those for the momentum selector, (section 5.5), and errors in track location, (sections 5.9, and 5.10).

The basic data will now be considered in the light of the bias effects and systematic corrections will be applied to obtain the positive to negative ratio of μ-mesons.

7.2 The Bias Effects

7.2.1 The Geometric Bias Effects

The causes which can give rise to these effects will arise from errors in the acceptance geometry of the Geiger counters, and in the measurement and alignment geometry of the flash-tube system. Since these effects are of different magnitudes, the first involving dimensions of the magnitude of the horizontal Geiger counter separations (3.8 cm) and the second involving dimensions of the magnitude of the accuracy of alignment of the flash-tube system (0.04 cm), they will be easy to differentiate between.

The basic data are shown in table 7.1. All the data are statistically independent and are uncorrected for systematic effects introduced by the selector and meas-

Table 7.1 : Basic Data for the Positive-Negative Ratio, $\frac{N(+)}{N(-)}$

Deflection Cell, cm	Positive Field, H_+	$\frac{N_{H_+}(+)}{N_{H_+}(-)}$	Negative Field, H_-	$\frac{N_{H_-}(+)}{N_{H_-}(-)}$	Fixed Geometry $\frac{N_{H_+}(+)}{N_{H_-}(-)}$	 $\frac{N_{H_-}(+)}{N_{H_+}(-)}$
0.02 -0.06	2+ 3-		3+ 0-		$\to \infty$	1.0
0.06 -0.10	6+ 2-		2+ 2-		3.0	1.0
0.10 -0.18	15+ 14-		7+ 3-		5.0	0.5
0.18 -0.26	17+ 20-		20+ 13-		1.3	1.0
0.26 -0.34	23+ 22-		38+ 12-		1.9	1.7
0.34 -0.42	32+ 36-		41+ 22-		1.5	1.14
0.42 -0.50	29+ 35-		55+ 21-		1.4	1.6
0.50 -1.30	676+ 598-		729+ 502-		1.35	1.22
1.30 -2.50	1321+ 943-		1204+ 1093-		1.21	1.28
2.50 -4.10	1371+ 778-		982+ 1135-		1.21	1.26
4.10 -6.50	964+ 376-		472+ 782-		1.23	1.25
					Negative Deflection	Positive Deflection

urement errors. Geometric bias effects will be indicated by considering the ratio

$$\frac{N_{\mu^+}}{N_{\mu^-}} = \frac{N(+)}{N(-)}$$

for a given algebraic deflection, and then comparing the two possible ratios obtained.

The cells with larger deflection (projection measurements) give ratios in good agreement with each other indicating no serious geometric defects in the assumed Geiger counter acceptance geometry. The track simulator measurements, bearing in mind the statistical accuracy, do not indicate any errors in measurement or assumed geometry (Δ_0). The symmetry in the distribution of ϕ, figure 5.12 also adds confidence to the accuracy of the geometry.

7.2.2 The Time-dependent Magnetic Bias

This problem has been considered in section 5.2. Frequent reversal of magnetic field reduces this effect to a minimum.

7.3 The Correction for Momentum Selector Asymmetry

This has been evaluated in section 5.5 and is shown in figures 5.5a and 5.5b. In order to equalise the relative acceptance of positive and negative particles, the factors in these figures are applied to reduce the numbers of positive particles on positive field, and the numbers of negative particles on negative field. Since the factors are only appreciable compared with statistical errors for the projector data, the adjustment is only carried out on this data. This is justified since the correction, although by factors of up to 2, in fact turns out to be only a first order one, in that it is applied to the numerator and denominator of the final positive-negative ratio.

The ratio K, calculated from these corrected numbers of particles is given in table 7.2, where there is seen to be good agreement between the two sets of data, indicating that the correct magnitude of the momentum selector asymmetry has been evaluated.

The final numbers of positive and negative particles are shown in Table 7.3.

7.4 The Final Corrected Positive-Negative Ratio

In order to obtain better statistical accuracy at high momenta, the track simulator data of table 7.1 have been grouped to give larger cells, table 7.3. Also shown in this table are data which have been subjected to the rejection criterion of section 5.10 and Appendix 4.

The median momenta of the cells have been calculated from the best-fit deflection spectrum and correspond to the median momenta of each deflection cell. The errors are statistical only. If the positive-negative ratio is given by

$$K = \frac{N(\mu^+)}{N(\mu^-)} = \frac{N(+)}{N(-)}$$

then the error in K is

Table 7.2 : Basic data corrected for momentum selector asymmetry.

Deflection Cell, cm.	Momentum Selector Asymmetry	Corrected $\frac{N_{H^+}(+)}{N_{H^+}(-)}$	Corrected $\frac{N_{H^-}(+)}{N_{H^-}(-)}$
0.02 -0.18	1		
0.18 -0.34	1.007		
0.34 -0.50	1.022		
0.50 -1.30	1.05	$\frac{645+}{598-} = 1.07$	$\frac{729+}{478-} = 1.52$
1.30 -2.50	1.13	$\frac{1169+}{943-} = 1.240$	$\frac{1204+}{967-} = 1.245$
2.50 -4.10	1.37	$\frac{1001+}{778-} = 1.287$	$\frac{982+}{829-} = 1.185$
4.10 -6.50	2.08	$\frac{463+}{376-} = 1.231$	$\frac{472+}{376-} = 1.255$

Table 7.3 : The Final Corrected Positive-Negative Ratio

Deflection cell, cm	Positive Particles	Negative Particles	Momentum Corresponding to median deflection (Gev)	K	After Corr. for noise	After corr. for sea-level protons	Error* δK
			TRACK SIMULATOR (AFTER REJECTION)				
0.02 -0.06	3	2					
0.06 -0.10	5 } 20	1 } 15	240	1.33	1.41	1.40	± 0.45
0.10 -0.18	12	12					
			TRACK SIMULATOR (NO REJECTION)				
0.02 -0.18	35	24	240	1.46	1.62	1.61	± 0.38
0.18 -0.34	98	67	120	1.46		1.45	± 0.23
0.34 -0.50	157	114	77	1.38		1.37	± 0.16
			PROJECTION MEASUREMENTS				
0.50 -1.30	1374	1076	35	1.276		1.268	± 0.051
1.30 -2.50	2373	1910	17.5	1.242		1.233	± 0.037
2.50 -4.10	1983	1607	10.4	1.234		1.223	± 0.038
4.10 -6.50	935	752	6.7	1.243		1.229	± 0.049

* Based on numbers of particles before correction for momentum selector assymmetry.

The Positive-Negative Ratio using the Geiger counters alone

9.6	1.2193	±0.019
4.0	1.244	±0.010
1.98	1.208	±0.010
0.96	1.185	±0.010
0.47	1.626	±0.021

$$\delta K = \pm K \sqrt{N(+)^{-1} + N(-)^{-1}}$$

Only the particles in the cell of smallest deflection of the track simulator measurements will be subject to correction for errors in track location. This correction has been evaluated by taking different known constant positive-negative ratios for these cells derived from deflection spectra with positive and negative deflections and then applying errors of track location to each sign of deflection to find the resultant positive-negative ratio which would be measured. This method of correction is uncertain to the extent that the form of variation of K with momentum is unknown, it being arbitrarily assumed constant in this range. The final justification is whether the corrected value of K is in good agreement with the value expected by extrapolation from the close region where the correction has not been applied. Using the value for the error in track location given by equation 5.11, which refers to track simulator measurements not subject to rejection criteria, then the apparent ratio indicates a true one 11% higher, whereas for the track simulator data, which have been subjected to rejection, the apparent ratio increases by 6%. The corrected ratios are given in table 7.3. It can be seen from this table that the measured positive-negative ratio decreases as momentum increases, passing through a minimum in the region of 10 GeV/c and then increasing again at higher momenta. Although the track simulator data subject to rejection have a lower value of K, it is not different by a statistically significant amount. In fact, as it is based on a more accurate method of measurement it will refer to a slightly higher median momentum.

7.5 The Comparison with Other Work

The data from the present work are shown in figure 7.1 where they are compared with the data obtained using the Geiger counters. Over the common region there is good agreement. It is possible to draw a continuous curve through the flash-tube data not subject to rejection criteria but in the lower momentum region, greater weight has been attached to the Geiger counter data for the best estimate line because of their greater statistical accuracy. Similarly the track simulator data which have been subjected to rejection criteria will be more accurate since they are based on a more accurate measurement technique. The upper and lower limits of K have been estimated in order to compare its magnitude and accuracy with other work. This is done in figure 7.2.

It can be seen that the present work is in good agreement with the work of Owen and Wilson, (1951), Pine et al, (1959) and Filosofo et al, (1954), the data of all of these workers exhibit a decrease in K from its expected maximum value, section 2.5, at about 5 GeV/c, and the data

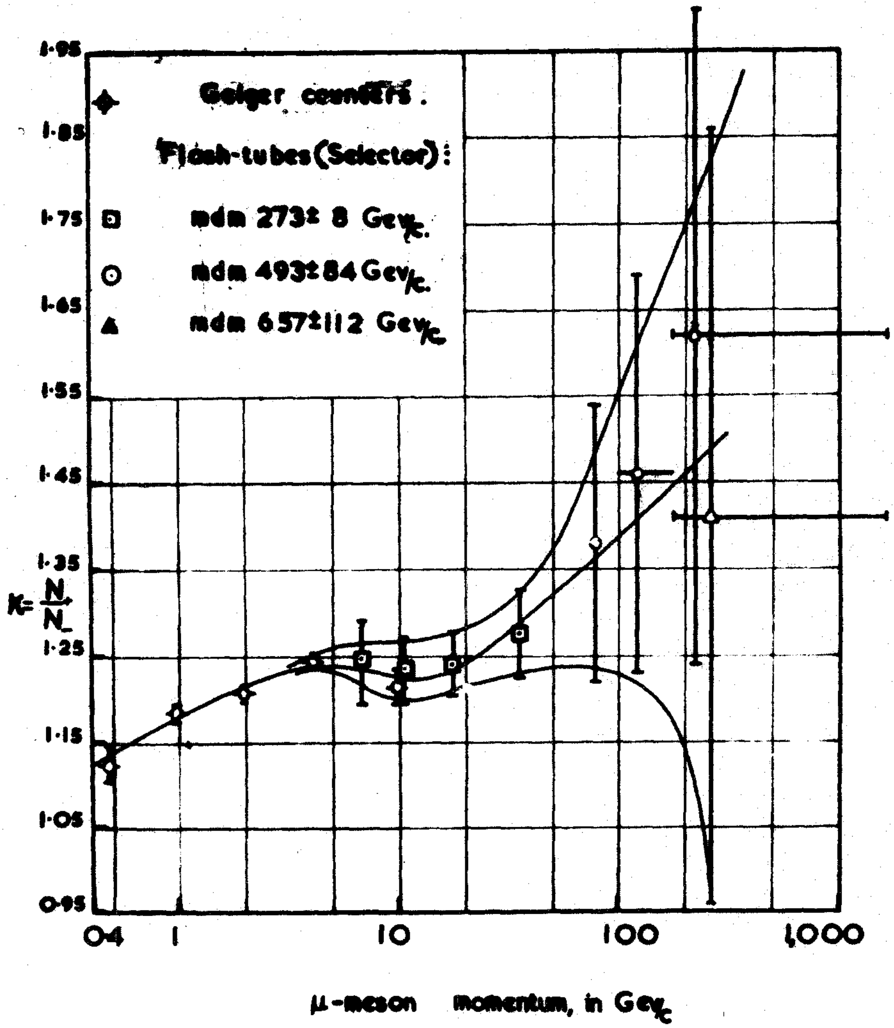

Figure 7.1 : The measured positive-negative ratio.

of these workers are not inconsistent with a minimum in the region of 10 GeV/c. Of these data, only that of Pine et al extends to momenta above 50 GeV/c. The ratio at highest momenta, 50 GeV/c, calculated by Pine et al, has been calculated from a cell which is free from particles of opposite sign due to contribution from errors in track location. Of the data of other workers shown in figure 7.2, that of Holmes et al, (1961b), has been considered before in chapter 5 where it is compared with the μ-meson spectrum from the present work. It was shown in figure 5.16 that there are differences between the μ-meson spectrum of the present work and that of Holmes et al. The values of K deduced by Holmes et al show a marked tendency to values higher than deduced from the present work. In particular the high values of K given by the Geiger counter work might indicate some form of instrumental bias. Holmes et al have also estimated the effect of errors of track location on their highest momentum cell, of mean momentum 98 GeV/c. Because this cell is so large, 0-0.5 cm deflection, the effect is negligible compared to the statistical error. Holmes et al plot their values of K at the mean momentum of each cell.

Recently measurements have been made by Kamiya et al, (1962), using a rotatable magnetic telescope with neon hodoscopes. Their results shown in figure 7.2 are seen to be in good agreement with the present work up to 60 GeV/c.

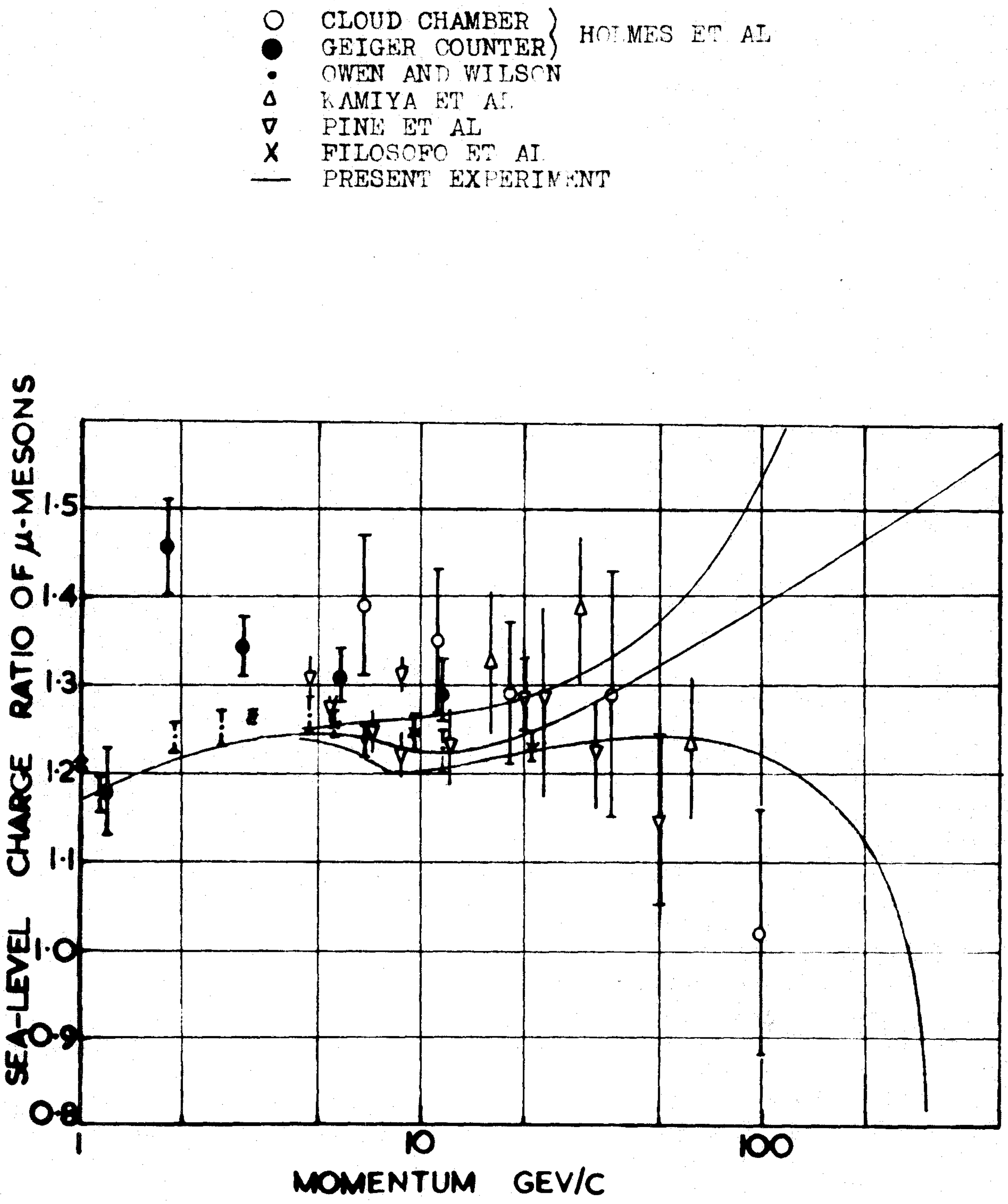

Figure 7.2 : The comparison of the limits and best estimate of the positive-negative ratio of the present work, with the results of other workers.

7.6 Conclusions

There is thus no work which is inconsistent with the present work in the range 5-50 GeV/c. Above 50 GeV/c the work of Pine et al, and Holmes et al is in disagreement with the present work but the work of Kamiya et al at 66 GeV/c, although 10% lower than the present work, is not significantly different from the present work.

The present work indicates a decrease in K to a minimum value at about 10 GeV/c, after which there is an increase in K. Thus K is always positive.

Any theoretical treatment will have to predict such an increase in K. The recent theories of Peters, (1962), and Babu and Yash Pal, (1962), already considered in chapter 6, indicate a negative excess of μ-mesons at sea-level. There is thus no evidence from the present work to suggest this and it will be further considered in chapter 9.

Chapter 8

The Energy Spectrum of Charged π-mesons at Production in the Atmosphere

8.1 Introduction

The energy spectrum of charged π-mesons at production in the atmosphere is of great interest. It has been shown that this spectrum can be derived in a simple way from the μ-meson spectrum at sea level if assumptions are made as to the mode of propagation of the components through the atmosphere (Appendix 3). Pine et al, (1959), have shown that the differential π-meson energy spectrum at production can be represented by

$$F(E) = 0.156E^{-2.64} \text{ cm}^{-2}\text{sec}^{-1}\text{st}^{-1} \text{ (GeV)}^{-1} \qquad 8.1$$

over the μ-meson energy range 10-200 GeV.

In this chapter each measured point on the μ-meson sea-level differential momentum spectrum has been carried through the analysis to give the corresponding point on the π-meson production spectrum, which can then be compared with other estimates of the production spectrum derived from other methods.

The slope of the differential spectrum of μ-mesons at sea-level and at production, and π-mesons at production, are derived and compared.

Using the latest spectrum of the primary cosmic radiation, which is now well known, an expression has been derived for the π-meson production spectrum using the Fermi model for the production of π-mesons, following an original treatment which has been developed by the present author. This expression can thus be compared with the derived spectrum and used to study the properties of the primary nuclear interactions under various assumptions.

8.2 The π-meson Production Spectrum Derived from the Measured Data

The use of a proposed π-meson production spectrum (with one variable, the exponent, γ) to derive a momentum spectrum at sea-level, is a convenient way to present the measured data for the purpose of comparison and application of the various correction factors (e.g. for uncertainty in track location, etc.).

The various steps in the calculation of the μ-meson sea-level comparison spectrum, outlined in Appendix 3, depend on certain simplifying assumptions. It has been shown by Allen and Apostolakis, (1961), that these simplfying assumptions do not introduce appreciable errors ($\lesssim$5%) into the predicted sea-level spectrum. The assumptions have been applied to the measured points on the sea-level μ-meson spectrum which have been carried through the analysis, point by point, to derive the corresponding π-meson production spectrum. It has been assumed that all the μ-mesons are derived from π-mesons which are produced at a unique height. The μ-mesons however, on production, lose energy in their path to sea-level. This energy loss will vary with energy as does their survival probability, since at lower energies a large fraction will decay. It is also assumed that the π-mesons on decay, give rise to μ-mesons of unique energy. With these assumptions, the π-meson production spectrum, derived from the measured μ-meson sea-level spectrum, is shown in figure 8.1.

The measured points are in good agreement with the proposed π-meson production spectrum at momenta above 20 GeV/c. Below this momentum, there is good agreement with the π-meson production spectrum derived from the Geiger counter data, Gardener et al, (1962). The cell width correction, important at low energies, where the energy interval at sea-level corresponds to a greater interval at the level of production, is negligible here. The π-meson production spectrum at low energies, has been derived from the sea-level Geiger counter data using a more accurate model for μ-meson propagation in the atmosphere than that assumed for the present work. Thus the two models show no appreciable difference in the common energy range.

A more accurate model for π-meson propagation has also been considered by Allen and Apostolakis, (1961). These authors find that the π-meson intensity at production can be represented by an expression of the form

$$F(E) = I_0 E^{-\gamma} \qquad 8.2$$

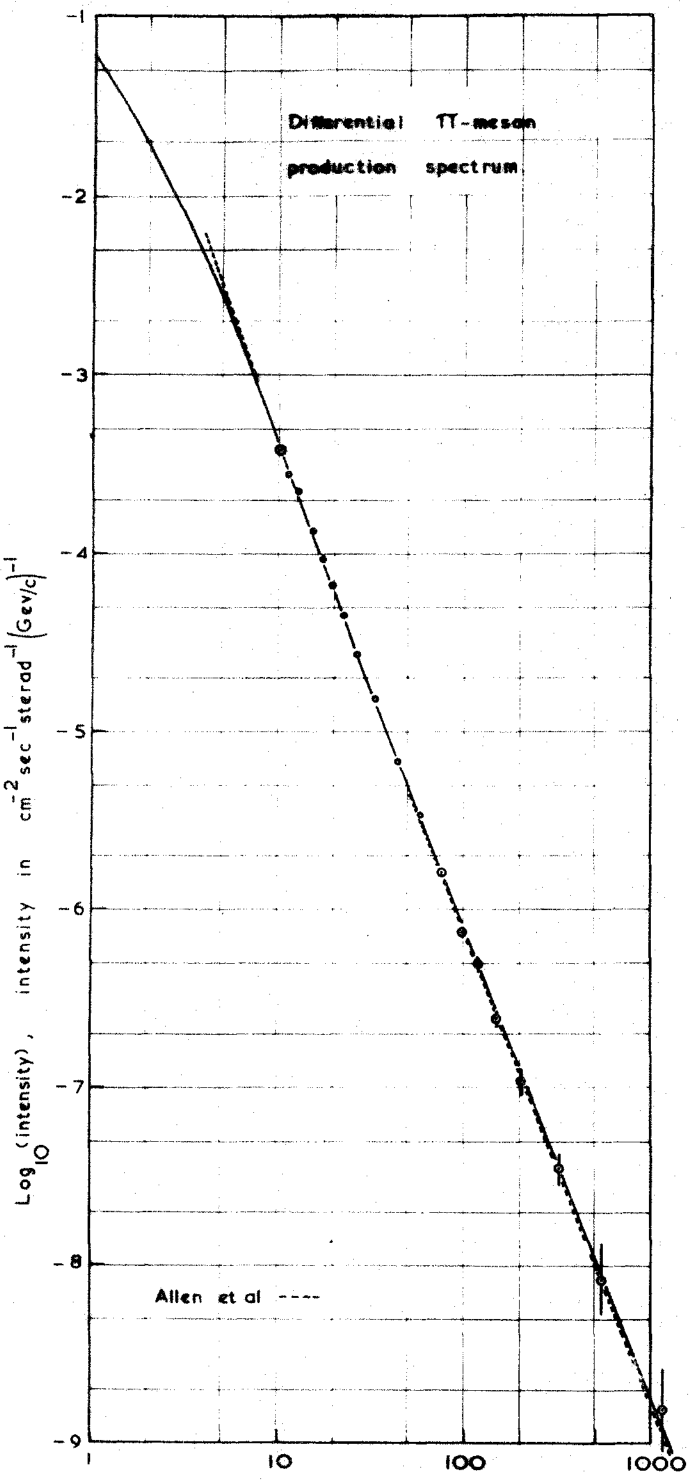

Figure 8.1 : The differential π-meson production spectrum derived from the sea-level results (where no errors are shown the radius of the circles gives the errors).

where $I_o = a - b \log_{10} E$ and $\gamma = c - d\ (1 - b \log_{10} E)^{-1}$ and E is the π-meson energy in GeV and the intensity is in units of $cm^{-2} sec^{-1} st^{-1} (GeV)^{-1}$.

The values of a, b, c, d deduced from the preliminary sea-level spectrum using the flash-tubes, Ashton et al, (1960), were $a = 0.425$, $b = 0.125$, $c = 3.92$, $d = 0.944$. In order to apply this result to the present work, the intensities derived from equation 8.2, using these values, have been decreased by a factor by which the predicted μ-meson spectrum of the present work is less than that predicted in the preliminary work - the correction calculated at a particular μ-meson momentum and applied to the π-meson spectrum at the appropriate π-meson momentum. It is estimated that the π-meson production spectrum from the corrected expression of Allen and Apostolakis is in good agreement with the present work over the entire momentum range.

The slopes of the various spectra are of particular interest. These have been calculated at the various stages of propagation in the atmosphere and are shown in figure 8.2. The slope of the differential μ-meson spectrum is seen to increase rapidly and tends to a constant value of -3.64 at energies >1000 GeV. The slope of the μ-meson spectrum at production is seen to increase from a nearly constant value of -2.64 at low energies to a similar constant value of -3.64 at high energies, as in the μ-meson

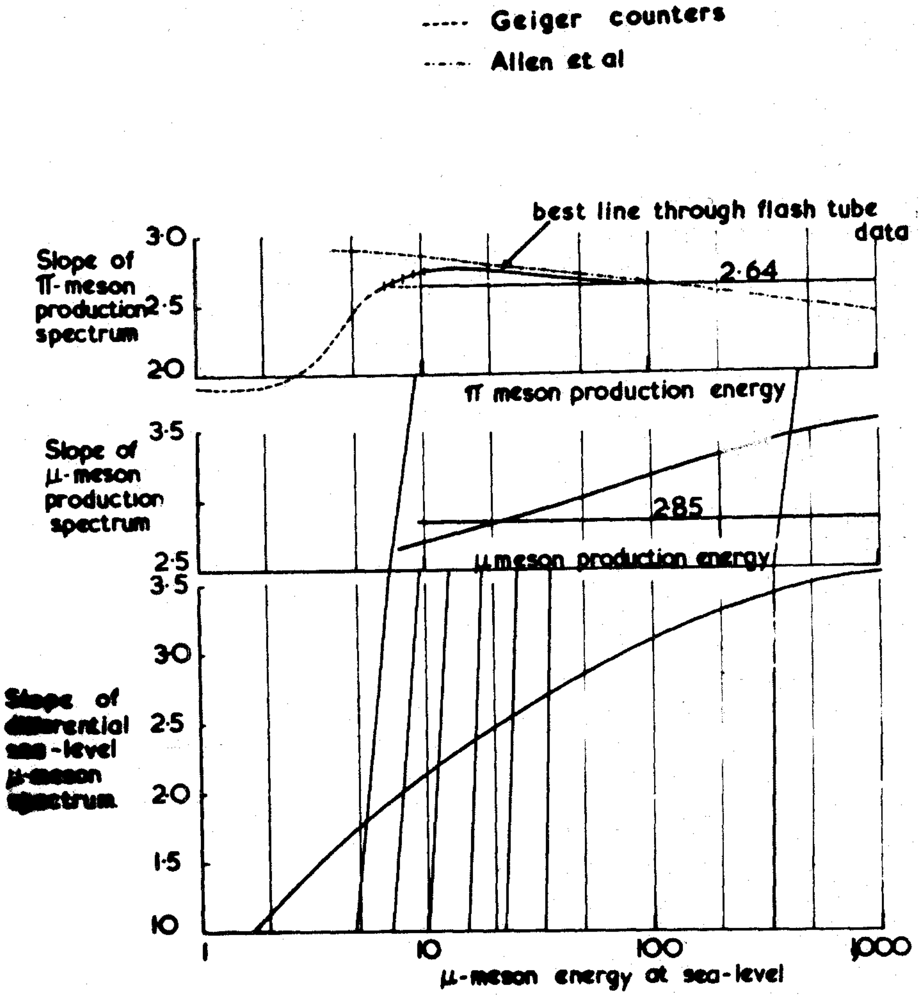

Figure 8.2 : The slopes of the various differential spectra derived from the sea-level results.

spectrum. This is well understood in terms of the absence of a fraction of μ-mesons at high energies due to the interaction of the π-mesons before they can decay. The constant value of -2.85 taken by Holmes et al, (1961b), and Rodgers, (1957), as the exponent of the μ-meson production spectrum giving best fit to their data is seen to be a good approximation over the range of energy where the greatest weight is attached to their data, i.e. up to 100 GeV. The best slope of the π-meson production spectrum derived from the measured data is compared with the best fit value of -2.64. There is good agreement above 40 GeV with the assumed value of -2.64, which gives the best fit over the μ-meson range 10.1 - 333 GeV/c, and which is a good average value for that derived by the method of Allen et al. Their value of γ however is coupled to another variable, I_0, and the value of γ shown in figure 8.2 was derived from the preliminary data as mentioned earlier. Gardener et al, (1962), also adopt a similar representation. At lower energy, 10-40 GeV, the measured slope of the π-meson production spectrum seems to be slightly in excess of the assumed value of 2.64 although the absolute intensity is in good agreement with that derived from the Geiger counter data at sea-level. The slope in this region is, however, in good agreement with the value of obtained by Allen et al.

It is therefore concluded that the measured μ-meson spectrum at sea-level is in good agreement with it having a source of π-mesons only, and intensity at production given by

$$F(E\ ) = 0.16\ E_{\pi}^{-2.64}\ \mathrm{cm}^{-2}\mathrm{sec}^{-1}\mathrm{st}^{-1}(\mathrm{GeV})^{-1} \qquad 8.2a$$

for $10 \leqslant E_{\pi} \leqslant 1000$ GeV, where E_{π} is in GeV, over the whole range covered by the present work, and in good agreement with the π-meson production spectrum deduced by Pine et al.

It is relevant here to compare the value of the exponent of the differential π-meson production spectrum with the values determined by other workers using different methods. The value of the exponent derived by Fujimoto et al, (1959), for neutral π-mesons, with $200 \leqslant E_{\pi} \leqslant 1000$ GeV, at mountain altitudes, is -2.8 ± 0.2. The Bristol group, Duthie et al, (1961), Bowler et al, (1962), also for neutral π-mesons, find an exponent of -3.3 for $400 \leqslant E_{\pi} \leqslant 1500$ GeV, and -3.8 for $E_{\pi} > 1500$ GeV, but conclude that a value -3.5 ± 0.2 would cover the whole range of their measurements. Thus the present work cannot be regarded as being inconsistent with these results since they refer to higher energies.

The theoretical derivation of an expression for F(E) will now be considered.

8.3 The Theoretical π-meson Production Spectrum

An expression for the π-meson production spectrum may be derived theoretically if certain simplifying assumptions are made, concerning the nature of the interactions of the primary particles which give rise to the π-mesons.

It is assumed that the differential spectrum of primary particles can be represented by

$$N(E_p) = A\, E_p^{-s} \qquad 8.3$$

The values of A and s have been taken from the spectrum given by Rossi, (1960), (1962),

$$N(>E_p) = 2.5\, E_p^{-1.6}\ \mathrm{cm}^{-2}\mathrm{sec}^{-1}\mathrm{st}^{-1} \qquad 8.4$$

$$\text{or} \quad N(E_p) = 4.0\, E_p^{-2.6}\ \mathrm{cm}^{-2}\mathrm{sec}^{-1}\mathrm{st}^{-1}(\mathrm{GeV})^{-1} \qquad 8.5$$

for $5.10^{11} \lesssim E_p \lesssim 1.5.10^{14}$ eV, which corresponds to the approximate limits of μ-meson energy, (5-500 GeV), covered by the present work, and further considered in section 8.5.

The number of particles produced in the interaction of a primary particle, henceforward assumed to be a proton, has been measured as a function of the primary particle energy by many workers. Perkins, (1960) and Sitte, (1961), have summarised the results. The measured ratio of charged π-mesons to uncharged π-mesons is not inconsistent with the principle of charge independence. The numbers of charged mesons produced in an interaction increases slowly with energy. It has been shown by other workers that in a collision, the primary particle collides with only one target nucleon in the target nucleus at the primary energies covered by the present work. Large fluctuations are possible in the numbers of π-mesons produced for a given primary energy, figure 8.3 (after Perkins, (1960)). However the mean multiplicity, $n_s(E_p)$ increases only slowly with primary energy. Observations of the multiplicity from interactions in light target materials, Fretter et al, (1960, 1960a), indicate lower multiplicity than from interactions in heavy elements. Also, the multiplicity at low primary energies, such as is obtained in the beams of proton synchrotrons, indicates low multiplicities.

Several models of meson production have been proposed. Over the range of primary energies considered in the present work, the Fermi model of meson production has been applied with considerable success to many problems. Thus in the present range, the number of charged mesons $n_s(E_p)$ will be assumed to be given by

$$n_s(E_p) = 3\,E_p^{\frac{1}{4}} \qquad (E_p \text{ in Gev}) \tag{8.6}$$

The total number of π-mesons produced is

$$n_T(E_p) = \frac{3}{2}\,n_s(E_p) = B\,E_p^{\alpha} \tag{8.7}$$

where $B = 4.5$ and $\alpha = \frac{1}{4}$. This expression is shown in figure 8.3. The value of B is realistic at the primary energies considered although at lower energies a smaller value is indicated. If any major differences are indicated between the predicted and measured π-meson production spectra, then the differences can be investigated by the relaxation of the values of B and α.

With these two basic assumptions, the production of

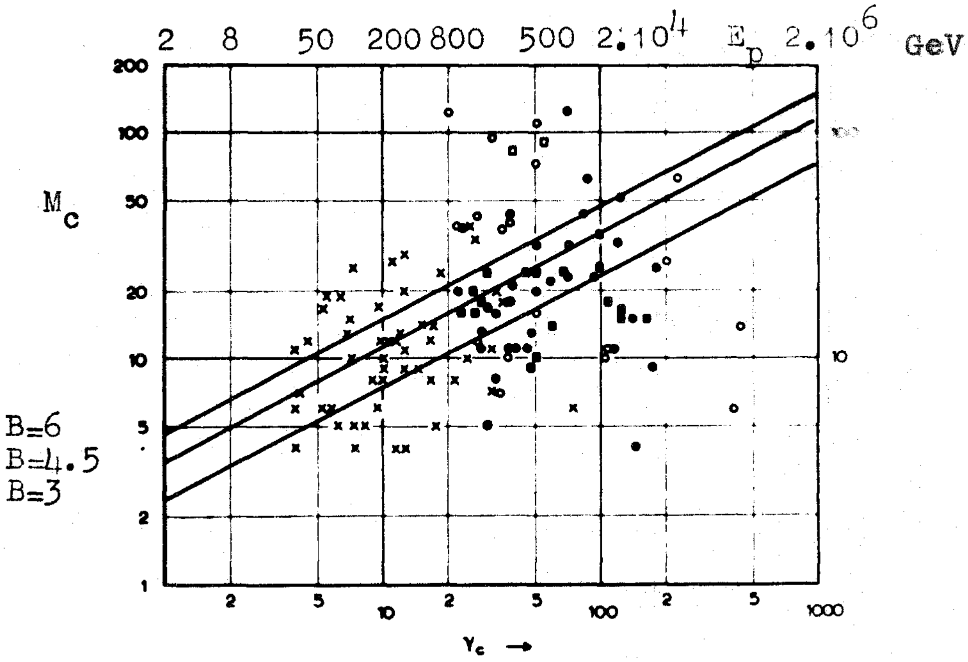

The distribution of multiplicity, n_s, as a function of the primary energy in the CM system, γ_c. The primary energy in the laboratory frame is approximately $2\gamma_c^2$ GeV/nucleon. The data are taken from Table V.

- ● proton primaries, interactions in emulsion.
- ○ α-primaries, interactions in emulsion.
- ■ proton primaries, interactions in brass sheets.
- □ α-primaries, interactions in brass sheets. (Kaplon and Ritson [1952].)
- × Secondary jets (Bristol events only).

Figure 8.3 : The measured multiplicities (after Perkins, (1960))

π-mesons can be considered in various approximations. Firstly, the π-mesons can be considered as being produced with equal energies in the L-system, and secondly with equal energies in the C-system. The variations on these two models are considered in Appendix 6, A6.1-3.

It is concluded that the π-meson production spectrum in the L-system can be expressed by

$$F(E_\pi) = \frac{A}{1-\alpha}\, \beta^{\frac{2-s}{1-\alpha}}\, k^{-\left(\frac{1+\alpha-s}{1-\alpha}\right)}\, E_\pi^{\frac{2\alpha-s}{1-\alpha}} \,.\, I \qquad 8.8$$

where $I = \frac{2^{\beta'}}{\beta'+1}$ for an isotropic distribution of π-mesons in the C-system and $I = 2^{\beta'-1}$ for a forward-backward (f-b) peaked distribution of π-mesons in the C-system.

So far it has been assumed that the primary particle makes only one collision. The factor k, the loss factor, is the total fraction of the primary energy available for π-meson production and for a single collision corresponds to the π-meson inelasticity, K_π. Comparison of the measured interaction and absorption lengths of protons, indicates that on the average they make about two energetic collisions before they lose most of their energy. The effect of more than one collision per primary proton is considered in Appendix 6 also (section A6.4). The theoretical π-meson intensity at production is seen to be reduced. This is accounted for by remembering that a proton undergoing more than one collision will produce fewer π-mesons in each collision than in one collision in which all the available primary energy is dissipated as π-mesons and the mean energy will consequently be lower. The resultant intensity of π-mesons at production due to more than one collision of the primary proton is given by

$$F'(E_\pi) = F_1(E_\pi) + F_2(E_\pi) + F_3(E_\pi) + \cdots\cdots \qquad 8.9$$

$$= 0.435\,\Pi_1(E_\pi) \qquad 8.10$$

Equation 8.10 is consistent with the measured result that the interaction length ($\sim$70 gm.cm^{-2}) is about half the absorption length ($\sim$120 gm.cm^{-2}). The comparison with the measured π-meson production spectrum will now be considered.

8.4 The Comparison of the Theoretical and Measured π-meson Production Spectra

The π-meson production spectrum, equation 8.2a, can be compared with the theoretical one deduced under the various simplifying assumptions of the previous section.

The exponent of the energy term in the theoretical production spectrum of equation 8.8 is of particular interest in that it involves only two variables, α and s. Equating the theoretical exponent to the measured value of -2.64, then

$$-2.64 = \frac{2\alpha - s}{1-\alpha} \qquad 8.11$$

If s = 2.6 (equation 8.5), then $\alpha = 0.06$. Alternatively if $\alpha = 0.25$ (equation 8.6), then $s = 2.48$. Thus there is an indication that smaller values of α and s than those assumed, while still satisfying equation 8.11, might be indicated from the present work. This is quite possible since other meson theories, such as the Heisenberg theory, would predict smaller values of α. Also the present work is weighted to smaller values of s than the mean value assumed, because of the form of the sea-level μ-meson spectrum. However, for the present comparison, the values of $s = 2.6$ and α based on the Fermi model for π-meson production, will be used and this leads to a value of -2.80 for the exponent of the π-meson production spectrum which can hardly be regarded as being in disagreement with the experimental result.

The constant factor, 0.16, in the measured π-meson production spectrum can be compared with the predicted value. This has been done in table 8.1 for $\alpha = 0.25$, $s = 2.6$ and $B = 4.5$, and also for two other values of B in order to investigate the dependence of the π-meson production spectrum on the multiplicity. From the comparison, the value of the total fraction of energy available for π-meson production, k_{π}, has been derived using the multiple collision model for each of the three values derived for the integral, I, (for $B = 6$) and for the isotropic and f-b distributions for $B = 4.5$ and $B = 3$.

Table 8.1 : Comparison of the theoretical and measured coefficients in the π-meson production spectrum.

Variables $\alpha = 0.25$ $s = 2.6$

Multiple collisions

$B = 6 : k_\pi^{1.8} .\ 0.86 \times 0.435 = 0.16$

I	k_π, loss factor	$K_\pi = \frac{k_\pi}{2}$, the inelasticity
1	0.62	0.31
1.24	0.55	0.28
1.74	0.46	0.23

$B = 4.5 : k_\pi^{1.8} .\ 1.07 \times 0.435 = 0.16$

I	k_π	$K_\pi = \frac{k_\pi}{2}$, the inelasticity
1.24	0.49	0.25
1.74	0.40	0.20

$B = 3 : k_\pi^{1.8} .\ 1.48 \times 0.435 = 0.16$

I	k_π	$K_\pi = \frac{k_\pi}{2}$, the inelasticity
1.24	0.41	0.21
1.74	0.34	0.17

It can be seen that k_π, and therefore the inelasticity $K_\pi = \frac{k_\pi}{2}$, increases as the multiplicity coefficient, B, increases. The direction of emission of π-mesons in the C-system, as described by the integral I, has been shown by other authors to be related to the energy of the primary particle; thus as the primary energy increases and the emission of π-mesons becomes more peaked in the f-b direction in the C-system, the inelasticity, K_π, as derived in table 8.1, is seen to decrease.

The values of inelasticity, K_π, derived from the present work are compared with values obtained using more direct methods in figure 8.4. The limits of the values of inelasticity are shown for the cases $B = 6$ and $B = 3$ at the limits of primary energy, E_p, corresponding to the present work (section 8.5). Remembering the energy dependence of the emission assymmetry of π-mesons, then it is deduced that the shaded portions of the limits indicated will be the values most likely to occur in the interactions. Thus K_π falls from about 0.28 at $E_p \sim 5 \times 10^{11}$ eV ($B = 6$) to about 0.17 at $\sim 1.5 \times 10^{14}$ eV ($B = 3$). The lower value of K_π is in good agreement with the measured values reviewed by Perkins above primary energies of 2×10^{12} eV, but at lower primary energies there appears to be a difference. Most of the measured values of K_π in this region refer to π-meson-nucleon collisions where a selection criterion which biasses the value of K_π to

ISOTROPIC F-B

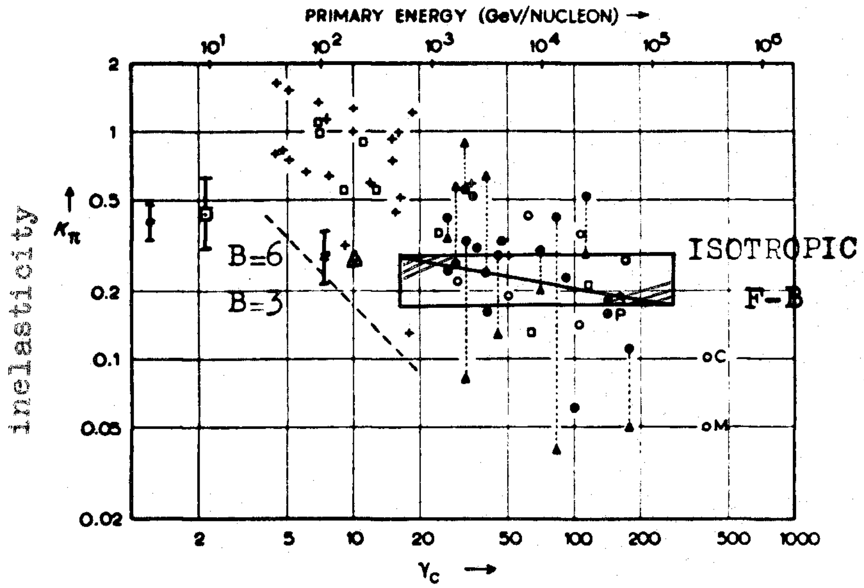

The estimated values of the fraction of the total available energy which is radiated as pions, K_π, as a function of γ_c, and the primary energy. The estimate of K_π was in most cases based on the measurement of the angular distribution of the shower particles, in jets produced by primary protons (●), primary α-particles (○), by secondary charged particles (·) and by secondary neutral particles (□). Estimates based on measurements of the associated soft component are shown thus: ▲. The vertical dotted lines indicate where K_π has been calculated by both methods. The points with letters attached indicate events in which it was possible to carry out a rather complete analysis, and for which the errors in K_π are believed to be small.

S — Chicago S-star (2 + 15p) (Schein *et al.* [1955])
P — Bristol P20 (0 + 4p) (Edwards *et al.* [1958])
M — Minnesota event (1 + 6α) (Fowler *et al* [1957])
C — Warsaw event (0 + 14α) (Ciok *et al.* [1957]).

The diagonal broken line on the left-hand side of the diagram indicates the rough limits on K_π imposed by the selection criterion that $n_s \geq 4$. For further details, see text. (after Perkins, (1960))

● Daniel et al, (1960)
□ Bogachev et al, (1960)
× Fretter et al, (1960)
▲ Grigorov et al, (1958)
▭ The limits derived from the present model

Figure 8.4 : The Comparison of the limits of the derived inelasticity for the present model with the values obtained by other workers using more direct methods.

higher values. Other values of inelasticity have been added to Perkins' review and there is good agreement, in particular, with the inelasticity value deduced by Fretter et al, (1960), for interactions of high energy primaries in carbon. Bearing in mind the approximation of s, and hence A, over the large energy range, then there is good agreement over the whole energy range of the present work. It is therefore concluded that the best estimate of the inelasticity, K_π, falls from 0.25 at $\sim 5 \times 10^{11}$ eV to 0.20 at $\sim 1.5 \times 10^{14}$ eV for B = 4.5.

8.5 The Relation Between the Average μ-meson Sea-Level Energy and the Primary Energy

The best estimate of the inelasticity obtained in the previous section can be used to calculate the relation between the average μ-meson energy at sea-level and the average energy of the primary particle which produced it. Since at the high primary energies covered by the present work, there will be a greater tendency for μ-meson emission in the forward-backward direction, a value for the inelasticity, $K_\pi = 0.20$, will be assumed. If it is further assumed that the π-mesons produced in the interaction and emitted in the forward direction in the C-system carry away most of the energy then

$$\frac{n_T(E_p)}{2} \cdot E_\pi = K_\pi \cdot E_p \qquad 8.12$$

where E_π is the mean energy of the emitted π-mesons, and E_p the primary energy, both in the L-system. From equation 8.7 and 8.12

$$E_p = \left(\frac{B}{2K_\pi}\right)^{\frac{1}{1-\alpha}} E_\pi^{\frac{1}{1-\alpha}}$$

Using the value $K_\pi = 0.20$ for $B = 4.5$ and $\alpha = 0.25$ and also the relation between the average μ-meson energy produced from a π-meson of energy E_π, then

$$E_p = \left(\frac{B}{2 \cdot K_\pi \cdot 0.76}\right)^{4/3} \left(E_\mu + E_i\right)^{4/3}$$

$$= 36 \left(E_\mu + E_i\right)^{4/3} \qquad 8.13$$

where E_μ is the sea-level μ-meson energy and E_i its ionisation loss in the atmosphere. Hence a 5 GeV μ-meson at sea-level is produced from a primary having energy $\sim 5 \times 10^{11}$ eV, and a 500 GeV μ-meson from a primary having energy $\sim 1.5 \times 10^{14}$ eV.

8.6 Conclusions

The method by which the π-meson production spectrum is derived is well understood. Of the parameters involved in the construction of a model for meson production, there are many which are not well known. It is known that there are large fluctuations in the fraction of the primary energy dissipated in the production of mesons in high energy interactions. The Fermi model for meson production assumed in the present work, although not allowing for the large fluctuations involved in the numbers of mesons produced gives a good representation of the mean numbers of mesons produced but however does not allow for the decrease in the inelasticity. The Heisenberg model, however, allows for both large fluctuations and a decrease in the inelasticity, but would predict too few mesons produced at the higher primary energies.

Thus within the framework of the assumptions of the present work and the values assumed for the various parameters, it is concluded that the process of π-meson production is consistent on the Fermi model with the sea-level measurements on cosmic rays and with the various parameters deduced by other authors.

Chapter 9

The Theoretical Charge Ratio of μ-mesons at Sea-Level

9.1 Introduction

The positive excess of μ-mesons at sea-level is ascribed to the charge exchange reactions of the primary protons.

Attempts have been made by several authors to derive the charge ratio of μ-mesons at sea-level. Of those authors who have derived the form of the variation of the charge ratio with energy, the results of Yeivin, (1955), and Cini and Wataghin, (1950), have been most successful. They predicted that the charge ratio would decrease with increasing μ-meson energy but the absolute value predicted was always lower and certainly in disagreement with the measured values. These authors therefore resorted to normalisation in the region where the experimental measurements were most accurate.

Pine et al, (1959), have carried out a similar analysis using the measured positive excess, to study the primary interactions. They have estimated the effective multiplicity of π-mesons produced in the primary interactions to be 1.8 from protons of energy 600 GeV, which is much less than that predicted on the Fermi model of π-meson production. It has been noted in figure 8.3 that the number of charged π-mesons produced in an interaction fluctuates widely from one interaction to another. Thus the value of 1.8 found by

Pine et al is a weighted average value which is representative of the variable conditions of the primary interactions due to the possible fluctuations. Thus because of the greater frequency of the lower energy primary protons a greater statistical weight will be given to those fluctuations which result in π-mesons being produced from primaries whose energy is lower than the average value for such a process. From equation A6.1 it will be seen that this corresponds to interactions where $n_{\pi}(E_p)$ is low and K is high.

An original treatment of the derivation of the positive-negative ratio has been developed by the present author. The transference of the positive charge to the π-mesons in the primary interactions, and its dilution by second and subsequent generations of π-mesons, will now be considered, with regard to the effect of fluctuations. Finally the effect of fluctuations on the π-meson production spectrum will be considered.

9.2 The Theoretical Positive-Negative Ratio of π-mesons at Production

At the primary energies covered by the present work, the primary interaction has been shown by several authors to be between the primary proton and a single nucleon in the nucleus. Thus the reactions which can take place are

			charge excess	
$p+p \rightarrow$	$p+p$	$+ n_T(E_p)$:	0	9.1
$\rightarrow$	$p+n$	"	+1	9.2
$\rightarrow$	$n+p$	"	+1	9.3
$\rightarrow$	$n+n$	"	+2	9.4
$p+n \rightarrow$	$p+n$	"	0	9.5
$\rightarrow$	$n+n$	"	+1	9.6
$\rightarrow$	$n+p$	"	0	9.7
$\rightarrow$	$p+p$	"	-1	9.8

The average primary interaction thus leads to the transference of charge of a $+\frac{1}{2}$ to the first generation of charged π-mesons produced. If there are M_c charged π-mesons produced, M_c^+ of which are positive and M_c^- of which are negative then the positive-negative ratio in the primary interaction is

$$R_1(M_c) = \frac{M_c^+ + \frac{1}{2}}{M_c^-}$$

$$= \frac{2M_c + 1}{2M_c - 1} \qquad 9.9$$

The secondary protons and neutrons which still have appreciable energy will not produce a further charge excess of π-mesons in further interactions since the protons and neutrons occur in equal numbers. Thus

$$R_i(M_c) = 1 \quad \text{for } i = 2, 3, \ldots \qquad 9.10$$

It has been assumed that all the primaries are protons. In fact a large proportion, about 10% of the primary radiation, is composed of Helium nuclei. Since these have equal numbers of neutrons and protons they will not contribute to the positive excess. The proportion of neutral primary radiation is negligible, Bowler et al, (1962), Kraushaar et al, (1962).

The secondary protons and neutrons will have the effect of diluting the positive excess of first generation π-mesons when they produce further π-mesons. At low primary energies where the multiplicity of π-mesons produced is lower, the effect of μ-meson decay will prevent some of the first generation μ-mesons from reaching sea-level and the effect of the second generation π-mesons produced nearer sea-level will be increased. At high energies, the second and higher generation π-mesons, which are produced lower in the atmosphere will interact rather than decay because of the greater density of matter in the region where they are produced and their diluting effect on the positive excess of first generation π-mesons will be decreased.

The effect of fluctuations in the numbers of π-mesons produced is considered in Appendix 7 using the measured distribution of multiplicities of figure 8.3. Thus the charged π-mesons produced in an interaction with average energy in the interval dE_π at E_π will have maximum and minimum multiplicities respectively, given by A7.9, and A7.10,

$$(M_c)_{max} = 28.5\, E_\pi^{\frac{\alpha}{1-\alpha}} \qquad 9.11$$

$$(M_c)_{min} = 0.86\, E_\pi^{\frac{\alpha}{1-\alpha}} \qquad 9.12$$

The multiplicity spectrum of charged π-mesons is derived from equation A7.15,

$$N(M_c) = N\left(n_T(E_p)\right) \frac{d\, n_T(E_p)}{d\, M_c}$$

$$= \frac{3}{2} \cdot \frac{A}{K_\pi (1-\alpha) \log j^{2/1-\alpha}} \cdot E_p^{-s} \qquad 9.13$$

$$= \left(\frac{3}{2}\right)^{1-s} \cdot K_\pi^{-(1-s)} \frac{A}{(1-\alpha)\log j^{(2/1-\alpha)}} \cdot E_\pi^{-s} \cdot (M_c)^{-s} \qquad 9.13a$$

Equation 9.13 shows the multiplicity dependence on the spectrum of the primary particles discussed in section 9.1.

The positive-negative ratio of π-mesons will then be given by equation A7.16.

The theoretical positive-negative ratio of μ-mesons, derived from equation A7.16, will now be considered and compared with the measured positive-negative ratio.

9.3 The Comparison of the Theoretical and Experimental Positive-Negative Ratios of μ-mesons at Sea-Level.

The derivation of the μ-meson positive-negative ratio from equation A7.16 involves the correction of each of the terms in the equation A7.17 for the effect of μ-meson decay and π-meson interaction. The effect of each of these phenomena on the sea-level positive-negative ratio was considered in section 9.2 in a qualitative manner. If the first generation π-mesons are considered to be produced at an atmospheric depth of 70 $gm.cm^{-2}$, the second generation π-mesons at 140 $gm.cm^{-2}$ etc. then the corrections to be applied to each of the terms in equation A7.16 will be different for each generation and π-meson energy. A further more accurate evaluation of the positive-negative ratio would be obtained by relaxation of the unique levels of production and substitution of incremental production levels.

However, for the purposes of comparison of the theoretical and experimental values of the positive-negative ratio, it is considered sufficient to ascribe limits to the theoretical values of the positive-negative ratio, because of the large errors involved, especially at the higher μ-meson energies of the experimental work.

At high energies where the probability of π-meson interaction is becoming increasingly important, the upper limit of the theoretical positive-negative ratio can be found by the effect of the first generation π-mesons only, since π-mesons produced low in the atmosphere will have a high probability of removal by interaction. Thus the upper limit is given by

$$\bar{R}_1(E_\pi) = \frac{\int_{(M_c)_{min}}^{(M_c)_{max}} R_1(M_c)\, N_1(M_c)\, dM_c}{\int_{(M_c)_{min}}^{(M_c)_{max}} N_1(M_c)\, dM_c} \qquad 9.14$$

The π-meson energies have been converted to μ-meson energies assuming each μ-meson to have 0.76 the energy of its parent π-meson and to have an energy loss from a height of 100 $gm.cm^{-2}$ to sea-level, which is given by the value calculated by Sternheimer, (1959), figure A3.1, A3.2.

The μ-meson positive-negative ratio, $\bar{R}_1$, calculated from equation 9.14 with these assumptions, is shown in figure 9.1. Also shown is $R_1(M_c)$, the positive-negative ratio derived from equations A7.11 and 9.9, which neglect the effect of fluctuations in the multiplicity of π-mesons produced in interactions.

At the lower energies of the present work the positive-negative ratio of the first generation of π-mesons is diluted by the production of equal numbers of positive and negative π-mesons nearer sea-level. Thus the positive negative ratio, $\bar{R}_{\Sigma i}$, calculated from equation A7.17 will be a better estimate at lower π-meson energies.

In the range of μ-meson energies covered by the experimental results on the positive-negative ratio, 5-250 GeV, there will be a transition from the theoretical value given by $\bar{R}_{\Sigma i}$ at low energy ($\sim$5 GeV) to the value given by $\bar{R}_1$ at high energy ($\sim$250 GeV), shown by the

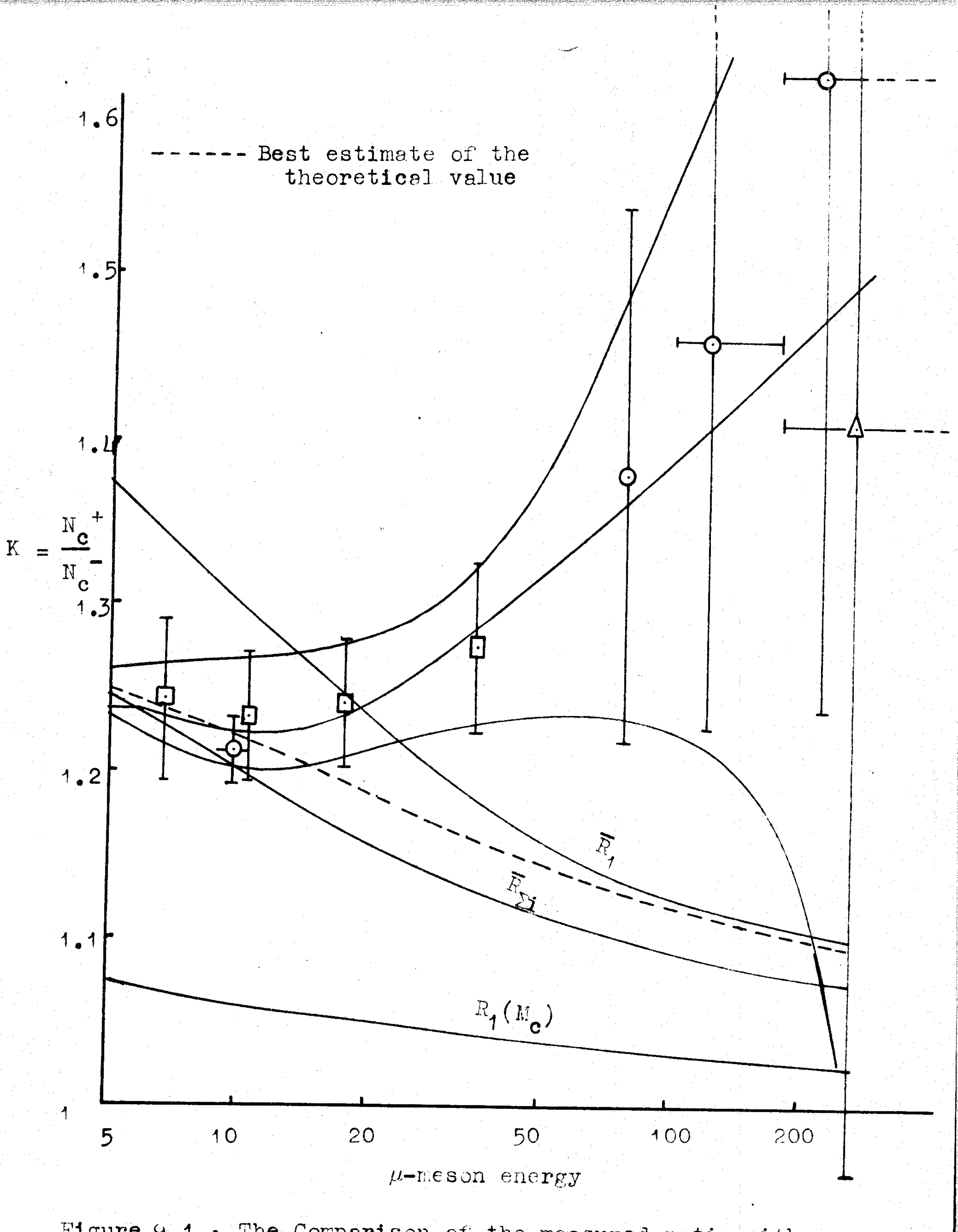

Figure 9.1 . The Comparison of the measured ratio with the best theoretical estimate.

dotted line in figure 9.1, which is considered to be the best estimate of the ratio. At still lower energies the positive-negative ratio falls after passing through a maximum value at about 4 GeV, due to the increasing effect of μ-e decay.

The measured values of the positive-negative ratio are also shown in figure 9.1 where they can be compared with the best estimate of the positive-negative ratio from the theoretical work. In the low energy region, 5-10 GeV, where the measured data have greatest statistical accuracy, there is good agreement with the absolute value of the positive-negative ratio from the theoretical work. Above 10 GeV, where the measured μ-meson positive-negative ratio begins to increase again, there is an increasing divergence between the measured and predicted values, although the measured data at the highest energy is not significantly different from the predicted value, due to its large statistical error.

There is thus a significant difference between the measured positive-negative ratio of μ-mesons at sea-level above 10 GeV and the value predicted assuming that the μ-mesons are all derived from π-mesons.

9.4 The Effect of Fluctuations on the π-meson Production Spectrum

The analysis carried out in chapter 8 assumed that the π-mesons produced in an interaction involving a nucleon of given energy always had the same multiplicity.

Using the multiplicity spectrum derived in A7.2, the π-meson production spectrum has been derived in A7.4. It is seen that the expression is identical, except for the square brackets, to that derived in chapter 8, (e.g. equation A6.5, when corrected to apply to charged particles only). Inserting the values $s = 2.6$, $\alpha = \frac{1}{4}$, $j = 3$ the expression in the square brackets reduces to 1.14. The effect on the values of k_π deduced in table 8.1 is small. For the value of B used in the model for the positive-negative ratio in 9.2 and 9.3, $B = 4.5$, then the values of k_π in the multiple collision model become

I	k_π(neglecting fluctuations)	k_π(corrected for fluctuations)
1.24	0.49	0.45
1.74	0.40	0.37

It is thus seen that the effect of fluctuations on the analysis of chapter 8 is small.

As $j \rightarrow 1$ in equation A7.18, the effect of fluctuations in the multiplicity of π-mesons produced, is reduced and equation A7.18 reduces to equation A6.5, which refers to all π-mesons produced.

9.5 Conclusions

The measured positive-negative ratio of μ-mesons at sea-level derived in chapter 7 has been corrected for all known bias effects. The measured data are consistent within themselves and are in good agreement with the Geiger counter data over the common energy region. Above 10 GeV the positive-negative ratio of the measured data increases continuously up to the maximum energy of 240 GeV. The measured positive-negative ratio of the present work is in good agreement with the values obtained by all other workers apart from the points at highest energy given by Holmes et al (at 100 GeV) and Pine et al (at 50 GeV). There is some indication that the measured positive-negative ratio deduced by other workers also increases, apart from the two cases mentioned above.

The predicted positive-negative ratio from the work of this chapter, which assumes that all the μ-mesons at sea-level are derived from π-mesons, is in disagreement with all the measured data in the range 10-50 GeV apart from the two cases mentioned above, although the absolute predicted values are in excellent agreement with the measured values between 5 and 10 GeV. It is concluded therefore that either particles other than π-mesons are playing an important role at these energies or that there is some change in the character of the interactions.

Significant changes in the positive-negative ratio are predicted by the hyperon model of Peters, (1962). Assuming that a hyperon in many cases carries away most of the energy of the primary, instead of the proton and neutron assumed in the present work, Babu and Yash Pal (1962), have derived the energy spectrum of μ-mesons at sea-level arising from the π-mesons which are the decay products of the hyperons. These authors have also shown that this leads to an excess of particles of negative charge at high energies (e.g. $N_c^+/N_c^- = 0.56$ at 100 GeV). Although the hyperon theory in its present form seems to show promise of explaining many of the features of high energy nuclear physics, it is inconsistent with the positive-negative ratio which is greater than one at least up to several hundreds of GeV. Further, Akashi et al, (1962) have found disagreement with the expected number of delayed π^0-mesons in close proximity to the primary nuclear interactions.

If the hyperon model is correct there will also be an effect on the sea-level μ-meson spectrum but the μ-mesons which arise from a hyperon source do not begin to have comparable intensity to the μ-mesons from the π-meson source below a μ-meson energy of 1000 GeV. It is thus possible that the present experiment would not detect any increase in the sea-level μ-meson intensity due to a source other than the π-meson source assumed for the purpose of comparison in the present work.

The hyperon theory of Peters assumes that all four hyperons of strangeness -1 are produced in equal proportions and because of the decay schemes the hyperons give rise to a negative excess of μ-mesons at sea-level. The negative excess is thus due to the postulation of strangeness -1 hyperons in the primary and subsequent interactions and this itself is based on the observation at low energies using the CERN proton beam that more K-mesons of positive strangeness (K^+, +1) are produced than with negative strangeness (K^-, -1).

A point of interest in the present discussion has been put forward by Babu and Yash Pal who have suggested that since the primary cosmic radiation is predominantly positively charged, it is likely that Σ^+ may be produced more frequently than the other hyperons, which would lead to a reduction of the calculated negative excess of μ-mesons at sea-level, and might possibly explain the observed result.

It is thus concluded that although hyperon effects will not greatly increase the intensity of μ-mesons at sea-level below about 1000 GeV μ-meson energy, there would be a pronounced effect on the positive-negative ratio. The predicted negative excess has not been found but the increase in the ratio found experimentally could be explained by a modified model in which the production of Σ^+-hyperons greatly exceeds that of Σ^--hyperons.

Chapter 10

Conclusions

It has been shown that the application of flash-tubes to a magnetic spectrograph has resulted in a reliable instrument having a high rate of collection of data and high accuracy of momentum determination.

The momentum spectrum and charge-ratio of μ-mesons have been measured to higher momenta than hitherto. It is concluded that if the μ-mesons at sea-level are derived solely from π-mesons then the differential spectrum of the π-mesons at production can be represented by

$$N(E) = 0.156\ E^{-2.64}\ \mathrm{cm}^{-2}\mathrm{sec}^{-1}\mathrm{st}^{-1}(\mathrm{GeV})^{-1}$$

The sea-level integral μ-meson spectrum has been compared with the integral intensities of particles able to penetrate to various underground depths. This has been done by assuming a relation for the average rate of energy loss in rock, which although giving a rate of energy loss greater than that assumed by other workers, is considered by the author to be the best theoretical estimate at the present time. This relation, together with the integral spectrum of the present work, leads to intensities underground which are less than the measured ones. It has been shown that the effect of fluctuations in energy loss accounts for much of the deficiency, but modification of the assumed theoretical cross-sections is not discounted.

An expression for the π-meson production spectrum has been derived from the measured primary spectrum and a simple model for the nucleon cascade through the atmosphere. It has been assumed that the total number of π-mesons produced in the collision of a primary of energy E_p is $n_T(E_p) \doteq 4.5\ E_p^{\frac{1}{4}}$ and the predicted π-meson production spectrum has been derived as a function of the inelasticity of the interactions (the inelasticity is defined as the fraction of available energy appearing as π-mesons in the interaction). Comparison with the "measured" π-meson production spectrum shows that the inelasticity of the interactions decreases as the primary energy increases. Thus at a primary energy of $\sim 5 \times 10^{11}$ eV, the derived inelasticity is 0.25, whilst at higher primary energies, $\sim 1.5 \times 10^{14}$ eV, the inelasticity is 0.20. It is concluded that there is excellent agreement with the measured values of inelasticity by other workers using more direct methods.

The charge ratio of μ-mesons at sea-level has been measured. It is concluded that at low energies 5 - 10 GeV there is good agreement with the values of the positive-negative ratio measured by other workers. Above 10 GeV there is some uncertainty because of the wide variation of the results of other workers, which have been made with instruments having lower momentum resolution and because of the lower statistical accuracy of their results. It is concluded that the present results indicate a continuous increase in the positive-negative ratio with increasing momentum, but a slow decrease at high momenta cannot be ruled out.

The cascade model referred to earlier has been used to predict the positive-negative ratio of π-mesons and it has been shown that fluctuations in the numbers of π-mesons produced in an interaction have an important effect on the results. An estimate of the positive-negative ratio has been made under the usual assumptions that the μ-mesons are all derived from π-mesons. It is concluded that there is excellent agreement of the absolute value of the predicted positive-negative ratio and the measured results of the present work in the range of μ-meson energy 5 - 10 GeV. At higher energies, however, there is an increasing difference, with the predicted ratio falling and the measured ratio rising.

It seems likely, therefore, that the increase in the ratio at high energies arises from the generation in the primary interactions of particles other than π-mesons. It has recently been suggested by Peters, (1962), that hyperons play an important role at high energies. In the form developed by Peters the "hyperon model" predicts that the positive excess of μ-mesons at sea-level should go negative at high energy. This is just the opposite of what has been found experimentally. Of the possible explanations, the most likely one would appear to be that Σ^+-hyperons are produced and carry off most of the primary energy, with greater frequency than the other hyperons do at the energies concerned.

Acknowledgments

The author wishes to thank Professor G.D. Rochester, F.R.S., for the provision of the facilities which have made this work possible and for his interest at all times.

It is with gratitude that the author acknowledges the guidance of Dr. A.W. Wolfendale in this work.

Members of the Cosmic Ray Magnet Group are thanked for their individual contributions to the spectrograph and help given by discussions on various aspects of the work. In particular Mr. G. Brooke is thanked for his skilled assistance in the initial measurement of the films and the subsequent reduction on the computer and Mr. N. Palmer for making available the underground calculations. Many other colleagues and members of the Staff of the Physics Department have given help and the author is grateful to them.

The technical staff of the Physics Department, in particular Mr. W. Threadgill, Mr. D. Jobling, Mr. M. Crossland and Mr. K. Tindale, are thanked for their willing help.

Miss P. Hall has helped considerably with this thesis and her patient assistance is acknowledged with thanks.

Finally, the Department of Scientific and Industrial Research is thanked for financial support in the award of a Studentship and Fellowship while this work has been carried out.

References

Akashi, M., et al (Cooperative Japanese Emulsion Group), 1962, J. Phys. Soc., Japan, 17, Int.Conf. on Cosmic Rays and the Earth Storm, III, 427.

Allen, J.E., and Apostolakis, A.J., 1961, Proc. Roy. Soc., A265, 117.

Allkofer, O.C., 1959, Atomkernenergie, 10, 389.
1960, Zeits f. Phys., 158, 274.

Apostolakis, A.J., and Macpherson, I., 1957a, Proc. Phys. Soc., A70, 146
1957b, Proc. Phys. Soc., A70, 154.

Ashton, F., Kisdnasamy, S., and Wolfendale, A.W., 1958, Nuovo Cim., 8, 615.

Ashton, F., Nash, W.F., and Wolfendale, A.W., 1959, Proc. Roy Soc., A253, 163.

Ashton, F., Brooke, G., Gardener, M., Hayman, P.J., Jones, D.G., Kisdnasamy, S., Lloyd, J.L., Taylor, F.E., West, R.H., and Wolfendale, A.W., 1960, Nature, London, 185, 364.

Ashton, F., 1961, Proc. Phys. Soc., 77, 587.

Avan, L., and Avan, M., 1955, Compt. Rend., 241, 1122.

Avan, L., and Avan, M., 1957, C.R. Acad. Sci., Paris, 244, 450.

Babu, P. and Yash Pal, 1962, J. Phys. Soc., Japan, 17, Int. Conf. on Cosmic Rays and the Earth Storm, III, 322.

Barrett, P.H., Bollinger, L.M., Cocconi, G., Eisenberg, Y., and Greisen, K., 1952, Rev. Mod. Phys, 24, 133.

Barton, J.C., 1961, Phil. Mag., 6, 1271.

Bethe, H.A., 1930, Ann. Phys., Lpz., 5, 325.

1932, Z. Phys., 76, 293.

Bethe, H.A., and Heitler, W., 1934, Proc. Roy. Soc., A146, 83.

Bhabha, H.J., 1935, Proc. Phys. Soc., A152, 559.

Bhabha, H.J., 1938, Proc. Roy. Soc., 164, 257.

Block, M.M., King, D.T. and Wada, W.W., 1954, Phys. Rev., 96, 1627.

Bogachev, N.P. Buniatov, S.A., Merekov, U.O., Sidorov, V.M., Yarba, V.A., 1960, J.E.T.P., 34(4), 1346.

Bohr, N., 1948, Det. Kgl. Dans. Vid. Sels., 18, 8.

Bollinger, L.M., 1951, Ph.D. Thesis (Cornell, New York, U.S.A.).

Bowler, M., Duthie, J., Fowler, P., Kaddoura, A., Perkins, D., Pinkau, K., and Wolter, W., 1962, J. Phys. Soc., Japan, 17, Int. Conf. on Cosmic Rays and the Earth Storm, III, 424.

Brooke, G., Hayman, P.J., Taylor, F.E. and Wolfendale A.W., 1962a, J. Phys. Soc., Japan, 17, Int. Conf. on Cosmic Rays and the Earth Storm, III, 311.

Brooke, G., Gardener, M., Lloyd, J.L., Kisdnasamy, S., and Wolfendale, A.W., 1962b, Proc. Phys. Soc., in the press.

Bull, R.M., Coates, D.W., Nash, W.F., and Rastin, B.C., 1962, Suppl. Nuovo Cim., 23, 28-51.

Caro, D.E., Parry, J.K., and Rathgeber, H.D., 1951, Aust.J.Sci. Res. A4, 16.

Christy, R.F., and Kusaka, S., 1941, Phys. Rev., 59, 414.

Cini, M., and Wataghin, G., 1950, Nuovo Cim., 7, 135.

Clay, J., 1939, Rev. Mod. Phys., 11, 128.

Clay, J., and Van Gemert, A., 1939, Physica, 6, 497.

Coates, D.W., 1961, Ph.D. Thesis (Nottingham).

Conversi, M., and Gozzini, A., 1955, Nuovo Cim., 2, 189.

Cousins, J.E., 1960, Ph.D. Thesis (Nottingham).

Coxell, H., and Wolfendale, A.W., 1960, Proc. Phys. Soc., 75, 378.

Daniel, R.R., Kameswar Rao, N., Malhotra, P,K., and Tsuzuki, B.Y., 1960, Nuovo Cim., 7, 1.

Davies, H., Bethe, H.A., and Maximon, L.C., 1954, Phys. Rev., 93, 788.

Driggers, F.E., 1952, Phys. Rev., 87, 1080.

Duthie, J.G., Fisher, C.M., Fowler, P.H., Kaddoura, A., Perkins, D.H., and Pinkau, K., 1961, Phil. Mag., 6, 89, and 113.

Ehmert, A., 1937, Zeits. f. Phys., 106, 751.

Fermi, E., 1939, Phys. Rev., 56, 1242.

Filosofo, I., Pohl, E., and Pohl-Rueling, J., 1954, Nuovo Cim., 12, 809.

Fretter, W.B., and Hansen, L.F., 1960, I.U.P.A.P., Cosmic Ray Conference, Moscow, I, 136.

Fretter, W.B., and Hansen, L.F., 1960a, Phys. Rev., 118, 812.

Fujimoto, Y., Hasegawa, S., Kazimo, M., Nishimura, J., Niu, K., and Ogita, M., 1960, I.U.P.A.P., Cosmic Ray Conference, Moscow, 1, 41.

Fukui, Hasegawa, Matano, Muira, Oda, Suga, Tanahashi and Tanaka, 1960, I.U.P.A.P., Cosmic Ray Conference, Moscow, II, 30.

Gaebler, J.F., Hazen, W.E., and Hendel, A.Z., 1961, Nuovo Cim., 19, 265.

Gardener, M., Kisdnasamy, S., Rössle, E., and Wolfendale A.W., 1957, Proc. Phys. Soc., B, 70, 687.

Gardener, M., Jones, D.G., Taylor, F.E., and Wolfendale A.W., 1962, Proc. Phys. Soc., in the press.

George, E.P. and Evans, J., 1950, Proc. Phys. Soc., A63, 1248.

George, E.P., 1952, P.C.R.P., I, 409.

George, E.P., 1956, Proc. Phys. Soc., A69, 428.

Glaser, D.A., Hamermesh, B., and Safanov, G., 1950, Phys. Rev., 80, 625.

Grigorov, N.L., Shestoperov, V.Ia., Soniniakov, V.A., Podgurskaia, 1958, J.E.T.P., 33(6), 848.

Halpern, O., and Hall, H., 1940, Phys. Rev., 57, 459.

1948, Phys. Rev., 73, 477.

Hayman, P.J., and Wolfendale, A.W., 1962, Proc. Phys. Soc., in the press.

Hayman, P.J., and Wolfendale, A.W., 1962a, Nature, London, in the press.

Hayakawa, S., and Tomanaga, S., 1949, Prog. in Theor. Phys. 4, 496.

Hirokawa, S., Komori, S.H., and Ogawa, S., 1956, Nuovo Cim., 4, 736.

Holmes, J.E.R., Owen, B.G., Rodgers, A.L., and Wilson, J.G., 1956, Report on Conference on recent developments in cloud chamber and associated techniques (London, Univ. Coll.), 177.

Holmes, J.E.R., Owen, B.G., and Rodgers, A.L., 1961a, Proc. Phys. Soc., 78, 496. 1961b, Proc. Phys. Soc., 78, 505.

Hyams, B.D., Mylroi, M.G., Owen, B.G., and Wilson, J.G., 1950, Proc. Phys. Soc., A63, 1053.

Jahnke, E., and Emde, F., 1945, Tables of Functions (New York : Dover Pub.), p24.

Jakeman, D., 1956, Canad. J. Phys., 34, 432.

Jones, D.G., 1961, Ph.D. Thesis (Durham).

Jones, D.G., Taylor, F.E., and Wolfendale, A.W., 1962, Proc. Phys. Soc., in the press.

Kamiya, Y., Sagisaka, S., Ueno, H., Kato, S., Sekido, Y., 1962, J. Phys. Soc., Japan, 17, Int. Conf. on Cosmic Rays and the Earth Storm, III, 315.

Kessler, D., and Kessler, P., 1956, Nuovo Cim., 4, 601.
1956, Comp. Rend., 242, 3045.

Kessler, P., 1959, Compt. Rend., 249, 1471.

Kisdnasamy, 1958, Ph.D. Thesis (Durham).

Kraashaar, W.C., and Clark, G.W., 1962, J. Phys. Soc., Japan, 17, Int. Conf. on Cosmic Rays and the Earth Storm, III, 1.

Lloyd, J.L., and Wolfendale, A.W., 1959, Proc. Phys. Soc., 73, 178.

Mando, M., and Ronchi, L., 1952, Nuovo Cim., 9, 517.

Mando, M., and Sona, P.G., 1953, Nuovo Cim., 9, 1275.

Marshak, R.E., 1952, Meson Physics (New York : Dover Pub., 1958).

Massey, H.S.W., and Corben, H.C., 1939, Canb. Phil. Soc., 35, 463.

Meyer, M.A., Wolfendale, A.W., Hughes, E.B., Marsden, P.L., 1962, J. Phys. Soc., Japan, 17, Int. Conf. on Cosmic Rays and the Earth Storm, III, 342.

Miesowicz, M., and Massalski, J.M., 1950, Acta Phys. Polon., 10, 274.

Miyake, S., Narasimham, V.S., and Ramanamurthy, P.V., 1962, J. Phys. Soc., Japan, 17, Int. Conf. on Cosmic Rays and the Earth Storm, III, 318.

Miyazaki, 1949, Phys. Rev., 76, 1733.

Murota, T., Ueda, A., Tanaka, H., 1956, Prog. in Theor. Phys., 16, 482.

Mylroi, M.G., and Wilson, J.G., 1951, Proc. Phys. Soc., A64, 404.

Owen, B.G., and Wilson, J.G., 1951, Proc. Phys. Soc., A64, 417. 1955, Proc. Phys. Soc., A68, 409.

Ozaki, S., 1962, J. Phys. Soc., Japan, 17, Int. Conf. on Cosmic Rays and the Earth Storm, III, 330.

Pak, W., Ozaki, S., Roe, B.P., and Greisen, K., 1961, Phys. Rev., 121, 905.

Peaslee, D.C., 1952, Nuovo Cim., 9, 56.

Perkins, D.H., 1960, P.E.P.C.R.P., 5, 259.

Peters, B., 1962, Nuovo Cim., 23, 88.

Pine, J., Davison, R.J., and Greisen, K., 1959, Nuovo Cim., 14, 1181.

Pine, J., Davison, R.J., and Greisen, K., 1960, I.U.P.A.P. Cosmic Ray Conference, Moscow, I, 295.

Randall, C.A., and Hazen, W.E., 1950, Phys. Rev., 81, 144.

Racah, G., 1937, Nuovo Cim., 14, 93.

Regener, H.V., 1951, Phys. Rev., 84, 161.

Rodgers, A.L., 1957, Ph.D. Thesis (Manchester).

Roe, B.P., and Ozaki, S., 1959, Phys. Rev., 116, 1022.

Rossi, B., 1948, Rev. Mod. Phys., 20, 537.

Rossi, B., 1952, High Energy Particles (New York : Prentice-Hall).

Rossi, B., 1960, I.U.P.A.P., Cosmic Ray Conf. Moscow, II, 18

1962, preprint 1962.

Rozental and Strel'tsov, 1958, J.E.T.P., 35, 1440.

Sitte, K., 1961, Hand. der Phys., XLVI/I, 157.

Smith, J.A., and Duller, N.M., 1959, Journ. Geophys. Res., 64, 2297.

Sreekantan, B.V., and Naranan, S., 1952, Proc. Ind. Acad. Sci., 36, 97.

Sreekantan, B.V., Naranan, S., and Ramanamurthy, P.V., 1956, Proc. Ind. Acad. Sci., 43, 113.

Sternheimer, R.M., 1952, Phys. Rev., 88, 851.

1959, Phys. Rev., 115, 137.

Walker, W.D., 1953, Phys. Rev., 90, 234.

Wick, G.C., 1941, Ric. Scient., 12, 858.

1943, Nuovo Cim., 1, 302.

Wilson, V.C., 1938, Phys. Rev., 53, 337.

Yeivin, Y., 1955, Nuovo Cim., 2, 658.

York, C.M., 1952, Phys. Rev., 85, 998.

Appendix 1. The Incoherence of Particle Trajectories

The derivation of the dependence of the incoherence of the trajectory of a particle due to the errors in the estimation of deflection and the geometry of, and scattering in, the spectrograph will be considered theoretically.

a) Scattering

The r.m.s. projected angle of scattering $\langle\phi\rangle$ of a particle of momentum p, passing through the spectrograph is given by

$$\langle\phi\rangle = \frac{1}{\sqrt{2}} \sum \frac{K t^{\frac{1}{2}}}{p\beta} \qquad \text{A1.1}$$

where K = 0.22 MeV and t is measured in radiation lengths. The sum is taken over all the material in the flash-tube arrays B, C and the Geiger counters G_B, C_G, G_C. Dividing $\langle\phi\rangle$ by equation 2.2, then

$$K' = \frac{\langle\phi\rangle}{\theta} = \frac{1}{\sqrt{2}} \cdot \frac{\sum K t^{\frac{1}{2}}}{300 \int H \, dl} \cdot \frac{1}{\beta} \qquad \text{A1.2}$$

Inserting the measured values for the quantities in A1.2, then

$$K' = 0.054 \qquad \text{A1.3}$$

for μ-mesons with $\beta \to 1$ i.e. $p \gtrsim 0.5$ GeV/c. Thus the defelction of each particle has an uncertainty of standard deviation 5.4% due to multiple scattering. The effect of this on any determination of the momentum spectrum of μ-mesons at sea-level, would be to smooth out any fine structure that may occur.

b) Location Accuracy of the Flash-tubes

The magnitude of this quantity has not been investigated theoretically under the conditions of the parameters used in the spectrograph. Hence it is derived under experimental conditions in the next section.

c) Relation Between Scattering Error, Location Error and Magnetic Deflection

The magnitude of the two effects described in a, and b above can be determined under the actual experimental conditions. In deriving the trajectory of a particle, uncertainties due to the scattering and location of the trajectory arise. If the estimated positions at the 4 flash-tube measuring levels are projected to intersect the level M, figure A1.1, where magnetic deflection is assumed to take place, then the discrepancy due to the incoherence can be explained and used to estimate the contributions of scattering, checking a, above, and to estimate the locational error under experimental conditions.

Scattering

In figure A1.1a it is assumed that all the scattering in the Geiger counters and flash-tubes at a given measuring level can be concentrated at one horizontal plane. Contributions to the difference B'C' will arise from scattering taking place at B and C. If the discrepancy is due entirely to scattering then

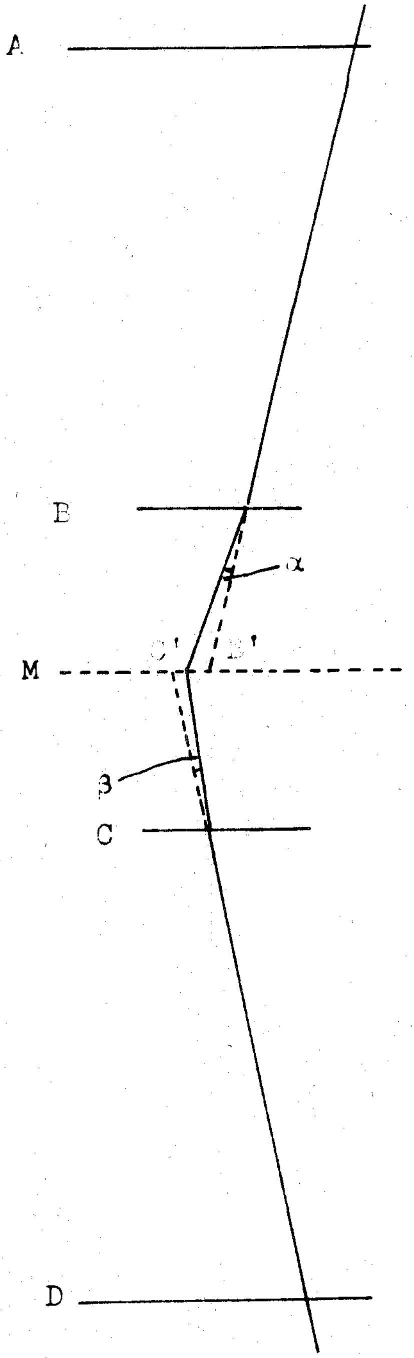

Scattering

Figure A1.1a

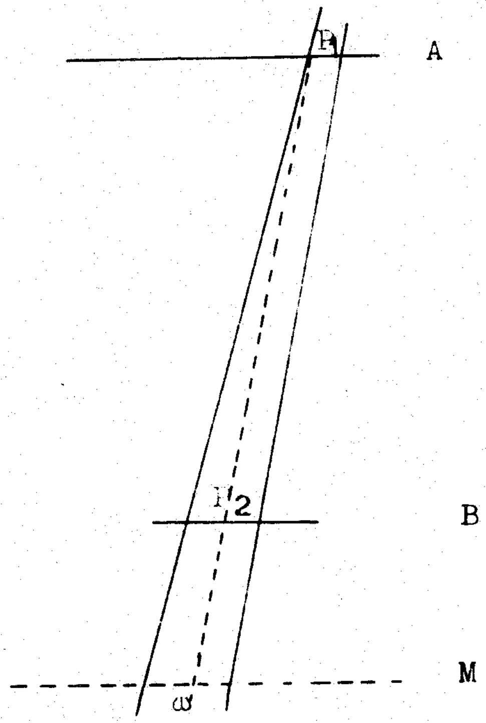

Location error

Figure A1.1b

$$B'C' = z(\alpha + \beta)$$

If the total r.m.s. separation due to scattering is $\langle \delta s \rangle$ then

$$\langle \delta_s \rangle^2 = 2 z_1^2 \langle \alpha \rangle^2 \qquad \text{where } \langle \alpha \rangle^2 = \langle \beta \rangle^2$$

If K is the ratio of scattering deflection to magnetic deflection

$$K = \frac{\langle \phi \rangle}{\theta} = \frac{\sqrt{2}\langle \alpha \rangle}{\theta}$$

Hence from equation 2.2a

$$\delta_s = K \cdot \frac{\Delta}{y} \cdot z_1$$

Location

There is also a contribution to B'C' due to error in location of particle trajectory. If δ_ℓ is the total error due to location at all the 4 flash-tube measuring levels A, B, C, D, then

$$\delta_\ell = \gamma_a \delta_a$$

where δ_a is the error at each level and γ_a is a geometrical constant. Since the geometry is symmetrical, consider one half A, B, see figure A1.1b. Errors p_1 and p_s occur in the trajectory at A and B and result in an error w at the level M. Then

$$\begin{aligned} w &= (p_2 - p_1)\left(\frac{z_1 + y}{y}\right) + p_1 \\ &= p_1\left(\frac{-z_1}{y}\right) + p_2\left(\frac{z_1 + y}{y}\right) \\ \langle w \rangle^2 &= \left(\frac{z_1}{y}\right)^2 p_1^2 + \left(\frac{z_1 + y}{y}\right)^2 p_2^2 \end{aligned}$$

Now δ_ℓ = r.m.s. error at M due to location for both halves. Hence

$$\delta_\ell^2 = 2\langle w\rangle^2 \quad \text{and} \quad p_1^2 = p_2^2 = \delta_a^2$$

$$\delta_\ell^2 = 2\left[\left(\frac{z}{y}\right)^2 + \left(\frac{z+y}{y}\right)^2\right]\delta_a^2 = \gamma_a^2\,\delta_a^2$$

Total

The total r.m.s. value of B'C', ϕ, is given by

$$\begin{aligned}\phi^2 &= \delta_s^2 + \delta_\ell^2 \\ &= \left(\frac{z}{y}\right)^2 K^2\Delta^2 + 2\left[\left(\frac{z}{y}\right)^2 + \left(\frac{z+y}{y}\right)^2\right]\delta_a^2\end{aligned}$$

Inserting the values used for y and z ($\frac{y_1+y_4}{2}$ and $\frac{y_2+y_3}{2}$ in table 3.1).

$$\phi^2 = 0.108\,k^2\Delta^2 + 3.748\,\delta_a^2 \qquad \text{A1.4}$$

In practice a mean value of ϕ^2 is observed, $(\bar{\phi})^2$ over a range of $(\Delta)^2$.

Appendix 2. The Derivation of the Correction Factors for Errors in Track Location

The r.m.s. standard deviation of the total uncertainty in particle trajectory location, equation 5.3, is derived from a quantity which is well represented by a Gaussian distribution, figure 5.7. Thus the requirement for the measured deflection spectra that $N(\Delta) = 0$ when $\Delta = 0$ (i.e. as $p \to \infty$) will no longer hold. The expected distribution in $N(\Delta)$ will now be derived. Let the total uncertainty in track location, or "noise", δ_T be represented by a Gaussian distribution

$$\frac{1}{\delta_T\sqrt{2\pi}} \exp - \frac{\Delta^2}{2\delta_T^2}$$

Then, in figure A2.1, the number of particles with true deflection Δ_i, but having deflection Δ due to "noise" is

$$K\Delta_i \frac{1}{\delta_T\sqrt{2\pi}} \exp - \frac{(\Delta_i - \Delta)^2}{2\delta_T^2}$$

The total number at Δ for $\Delta_i = 0$ to ∞ is

$$\int_0^\infty \frac{K}{\delta_T\sqrt{2\pi}} \cdot \Delta_i \exp - \frac{(\Delta_i - \Delta)^2}{2\delta_T^2} \, d\Delta_i$$

Let $y = \Delta_i - \Delta$, $dy = d\Delta_i$, then

Total number at Δ is

$$\frac{K}{\delta_T\sqrt{2\pi}} \int_{-\Delta}^{\infty} (y+\Delta) \exp - \frac{y^2}{2\delta_T^2} \, dy$$

$$= K\Delta\left(\frac{1}{2} + \operatorname{erf}\Delta\right) + \frac{K}{\sqrt{2\pi}} \cdot \delta_T \exp - \frac{\Delta^2}{2\delta_T^2} \qquad \text{A2.1}$$

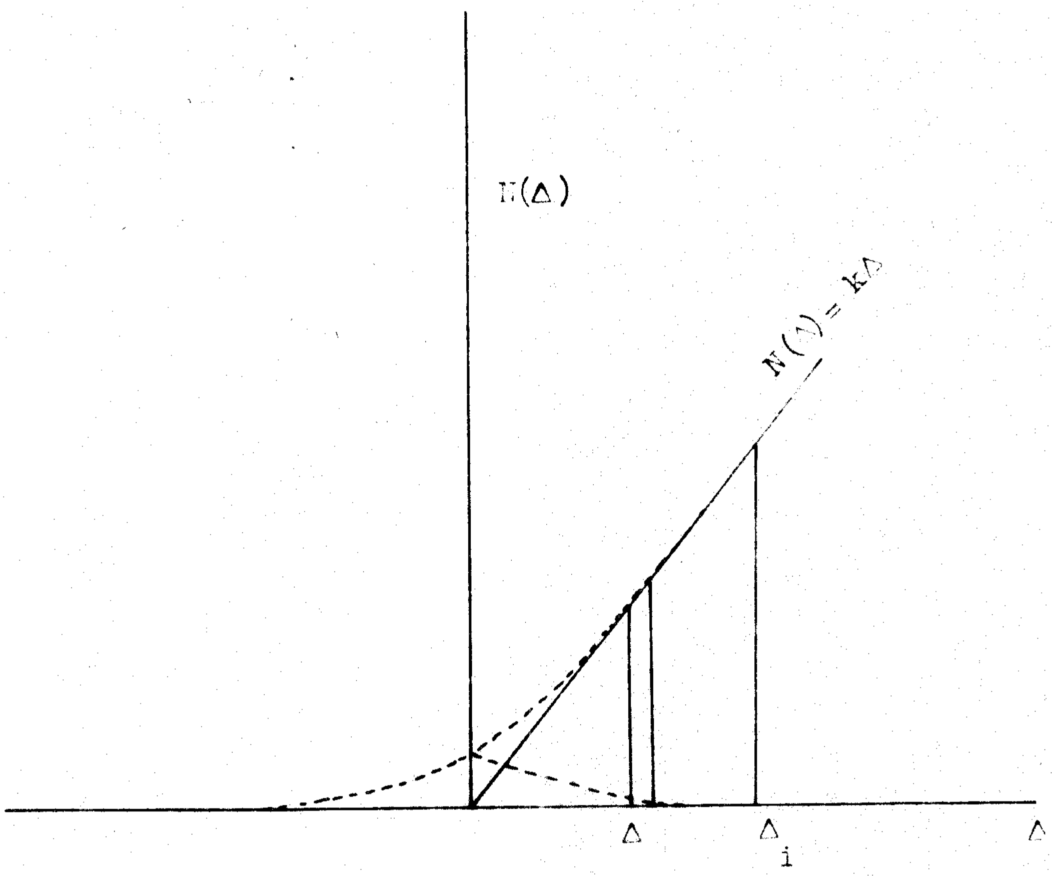

Figure A2.1 : The effect of errors in track location on the deflection spectrum.

where $$\mathrm{erf}\,\Delta = \frac{1}{\delta_T\sqrt{2\pi}}\int_{-\Delta}^{0} \exp - \frac{y^2}{2\delta_T^2}\,dy$$

The contribution at $-\Delta$ for Δ_i from 0 to ∞ can be similarly found. Letting $z = \Delta_i + \Delta$ the total number at $-\Delta$ is

$$\frac{K}{\delta_T\sqrt{2\pi}}\int_{\Delta}^{\infty}(z-\Delta)\exp - \frac{z^2}{2\delta_T^2}\,dz$$

$$= K\Delta\left(\mathrm{erf}\,\Delta - \frac{1}{2}\right) + \frac{K}{\sqrt{2\pi}}\cdot\delta_T \exp - \frac{\Delta^2}{2\delta_T^2} \qquad \text{A2.2}$$

The total contribution from $\Delta = -\Delta_i$ to $\Delta = \infty$ is obtained by the summation of equations A2.1, and A2.2, and is

$$N'(\Delta) = K\Delta\left[E_2\,\frac{\Delta}{\delta_T\sqrt{2}} + \frac{2\delta_T}{\Delta}\cdot\frac{1}{\sqrt{2\pi}}\cdot\exp - \frac{\Delta^2}{2\delta_T^2}\right]$$

where $E_2(\Delta) = \frac{2}{\sqrt{\pi}}\int_0^{\Delta}\exp - t^2 . dt$ (Jahnke and Emde, 1945).

The factor, R, by which the true intensity is increased by noise is thus,

$$R = \frac{N'(\Delta)}{N(\Delta)} = \frac{N'(\Delta)}{K\Delta}$$

$$= E_2\,\frac{\Delta}{\delta_T\sqrt{2}} + \frac{2\delta_T}{\Delta}\cdot\frac{1}{\sqrt{2\pi}}\cdot\exp - \frac{\Delta^2}{2\delta_T^2}$$

and the correction factor to be applied to the measured intensities is R^{-1}.

The correction has been derived for a deflection spectrum approximated by the expression $N(\Delta) = K(\Delta)$, where K is a constant. In fact this expression corresponds to a momentum spectrum falling off as p^{-3}, in good approximation to the measured result.

Appendix 3. The Sea-level μ-meson Differential Spectrum Above 10 GeV/c.

The form of the spectrum is derived from analysis due to Barrett et al, (1952). The primary radiation assumed to be mostly protons is absorbed at the top of the atmosphere exponentially with a mean free path λ_p. Considering then a depth x gm.cm^{-2} below the top of the atmosphere, let $d\Pi(E')$ be the increase in the number of π-mesons of energy E' in depth dx gm.cm^{-2}, then

$$\frac{d\Pi(E')}{dx} = F(E')\exp-\left(\frac{x}{\lambda_p}\right)\cdot\frac{1}{\lambda_p} - \frac{\Pi(E')}{\lambda_\pi} - \frac{\Pi(E')\, m_\pi c}{p'\rho c\tau_0} \qquad \text{A3.1}$$

Where $F(E')$ is the differential spectrum of π-mesons at production and λ_π is the absorption mean free path of π-mesons.

The first term on the right in A3.1 accounts for the exponential attenuation of the primary radiation. Of the $\Pi(E')$ π-mesons produced in x, a fraction $\frac{dx}{\lambda_\pi}$ will be lost by interaction, second term, and there is a certain probability depending on their momentum, p' and position, that some will have been lost by decay, third term, where m_π is the mass of the π-meson, ρ, the density of air, and τ_0 the mean lifetime of π-mesons at rest.

At these energies $E' \simeq p'c$ and, in the vertical direction,

$$\rho = \frac{x}{h_0}$$

where $h_0 = 6.46 \times 10^5$ cm. The equation can then be re-written

$$\frac{d\Pi(E')}{dx} = F(E')\exp -\frac{x}{\lambda_p}\cdot\frac{1}{\lambda_p} - \Pi(E')\left\{\frac{1}{\lambda_\pi} + \frac{B'}{E'x}\right\}$$

where $B' = \frac{m_\pi c^2 h_0}{c\tau_0} = 117.4$ GeV and taking the usual values for the other quantities. The solution of A3.1 can be written,

$$\Pi(E',x) = F(E')\exp -\frac{x}{\lambda}\cdot\frac{x}{\lambda}\left\{1 + \frac{B'}{E'}\right\}^{-1} \qquad \text{A3.2}$$

in the special case where $\lambda_p = \lambda_\pi = \lambda$

From equation A3.2 the number of μ-mesons, M(E), produced by π-μ decay at a given depth, x_0' can be calculated,

$$M(E) = \frac{1}{r}\int_0^{x_0}\frac{m_\pi c^2}{E'\rho c\tau_0}\,\pi(E')\,dx = \frac{B'}{rE'}\int_0^{x_0}\Pi(E')\frac{dx}{x} = \frac{B}{rE}\int_0^{x_0}\Pi(E')\frac{dx}{x} \qquad \text{A3.3}$$

where B = B'r = 89.26 GeV and $r = \frac{m_\mu}{m_\pi}$, m_μ is the mass of the μ-meson.

The μ-mesons of energy E, equation A3.3 come from π-mesons having a small range of energy

$$\Delta U_\mu = 2p_\mu' p_\pi \qquad \text{(units of } \mu\text{-meson rest mass)}$$

where p_μ' is the momentum of the μ-meson in the rest system of the decaying π-meson, of momentum p_π. The probability of emission at a given angle $F(U_\mu)$ is independent of angle

$$F(U_\mu) = (2p_\mu' p_\pi)^{-1}$$

so that the spectrum is flat. The mean energy of emission of the μ-meson, $\bar{E}_\mu$ is given by

$$\bar{E}_\mu = \frac{E_\pi r}{2}\left(r + \frac{1}{r}\right), \quad r = \frac{m_\mu}{m_\pi} = 0.76$$

$$= E_\pi . r . 1.04 \qquad \text{A3.4}$$

At high energies the μ-meson has a maximum energy

$$(E_\mu)_{max} \sim E_\pi$$

whilst the lower limit it

$$(E_\mu)_{min} \sim E_\pi . r^2$$

Previous workers, Barrett et al, (1952), Pine et al, (1959), have assumed $\bar{E}_\mu = rE_\pi$ $(E = rE')$ in good approximation to A3.4 and this value will be used in order that direct comparison of the present work with other work can be carried out.

Assuming again that $\lambda_p = \lambda_\pi$, then A3.3 has an exact solution when $x_o \rightarrow \infty$

$$M(E) = \frac{F(E/r)}{r} . \left(1 + \frac{E}{B}\right)^{-1} \qquad \text{A3.5}$$

Hence the probability of π-meson interaction can be expressed as

$$I(E) = \left(1 + \frac{E}{B}\right)^{-1} \qquad \text{A3.6}$$

It is assumed that $F(E/r)$ has the form $A(E')^{-\gamma}$ where A is that value given by Pine et al, (1959)

$$A = 0.156 \qquad \text{A3.7}$$

There is a certain probability that the μ-mesons, once formed, will decay. Assuming that the μ-mesons are all produced at the 100 $gm.cm^{-2}$ level in the atmosphere, then the probability of a μ-meson reaching sea-level with energy, E_s, is given, following Owen and Wilson, (1955), by

$$D\left(E_s\right) = \left(\frac{t_0}{t}\left(1+\frac{E_i}{E_s}\right) - \frac{E_i}{E_s}\right)^{-\epsilon} \qquad \text{A3.8}$$

where $\epsilon = \frac{h m_\mu c}{c\tau(E_s+E_i)}$; h is the scale height of the atmosphere and E_i is the energy loss of μ-mesons in the atmosphere. The energy loss of μ-mesons in air has been given by Sternheimer, (1959), figure A3.1a, and the value of E_i as a function of E_s is given in figure A3.1b. The quantities t_o, t, are the total mass thickness and thickness from the 100 gm.cm^{-2} level, respectively, to sea-level.

The theoretical expected spectrum can now be written

$$M(p_s)\,dp_s = \frac{18{\cdot}2}{(0{\cdot}76)^{-\gamma}}\left(p_s+p_i\right)^{-\gamma}\left(89{\cdot}26+p_s+p_i\right)^{-1}\left\{10\left(1+\frac{p_i}{p_s}\right)-\frac{p_i}{p_s}\right\}^{\frac{1{\cdot}114}{p_s+p_i}} dp_s \qquad \text{A3.9}$$

$$M(p_s) = A'.\,F(p_s, p_i).\,I(p_s, p_i).\,D(p_s, p_i) \qquad \text{A3.10}$$

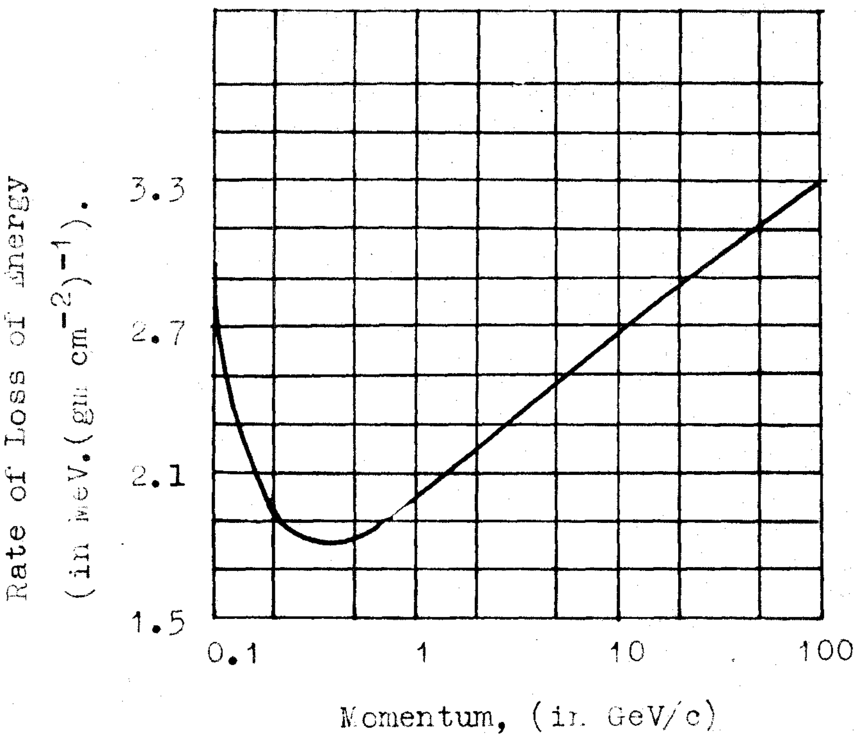

Figure A3.1a : The average rate of energy loss of μ-mesons in air, (after Sternheimer, 1959)).

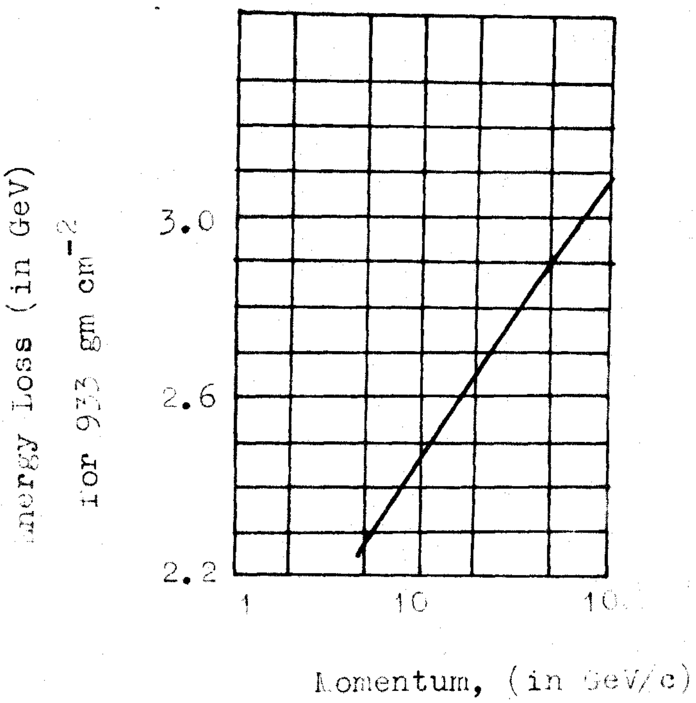

Figure A3.1b : The energy lost in the atmosphere from the 100 gm. cm^{-2} level.

Appendix 4. The Ultimate Accuracy of Track Location

The possibility of increasing the accuracy of particle trajectory location has been investigated. It can be seen that the distribution in ϕ in figure 5.12 is not quite Gaussian, because of the "tail". In order to increase the accuracy of particle trajectory location which is derived from the frequency distribution of ϕ, it is necessary to remove this tail, and find the resulting factor by which the accuracy is increased.

This was done by using 50 "pseudo particles" to simulate the passage of particles through the spectrograph, on the Track Simulator. An angle was chosen and the cursor of the Track Simulator, section 3.5.3, was set at some random position. In order to determine whether the "tubes" intersected by the track so defined would flash or not, a simple Monte Carlo spinning wheel was constructed. Using the internal (absolute) efficiency, η_A, of the flash-tubes (section 3.2.2) calculated from the particles in table 5.7 with deflection less than 0.26 cm, a probability function of flashing was drawn for each layer of the arrays ABCD. The experimentally observed and the expected average values of η_A are shown in figure A4.1. The expected average value of η_A was calculated from the characteristics of the flash-tubes. For a time delay of 10 μsec and rise time of pulse of 0.5 μsec, this is 85%, Coxell et al, (1960).

Typical error $e = \sqrt{\frac{\eta_a (1-\eta_a)}{N}}$

$\eta_a = 90\%$ [illegible] e $\pm 3\%$

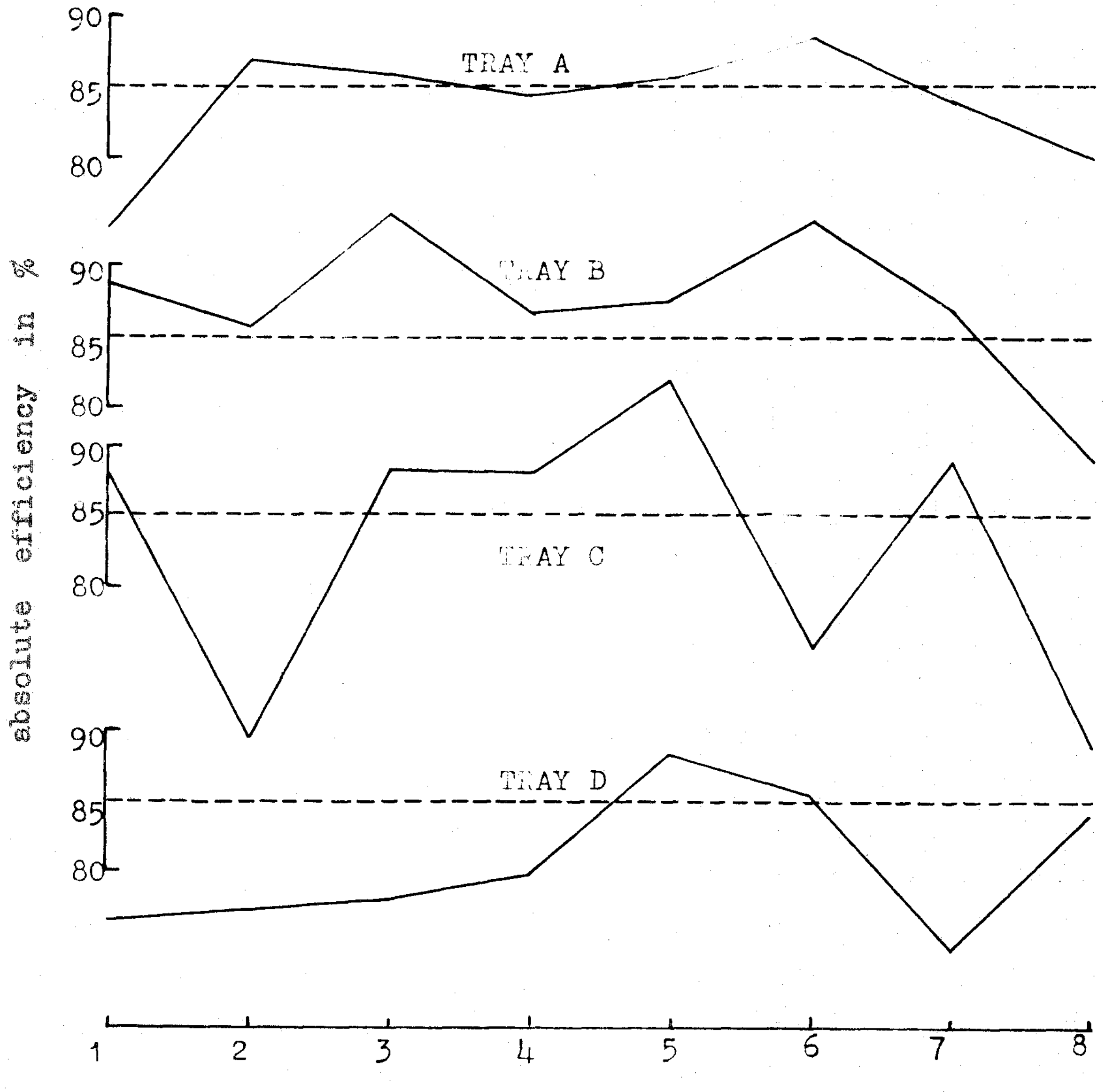

Figure A4.1 : The measured absolute efficiencies of the flash-tube for the present work.

Using the spinning wheel it was then decided whether or not the particular flash-tube intersected had flashed or not. When this had been done for layers, which had flashed in each array, the limits over which the cursor could be moved were determined, consistent with the criteria previously adopted for measurement. The mean of the two limits was calculated and also the value of the difference from the true position. The "deflection" Δ, and value of ϕ were obtained by drawing the particles on a scale diagram of the spectrograph.

The distribution in ϕ was found to have a median value, figure A4.2a, of

$$(\phi)_{med} = 0.064 \pm 0.018 \text{ cm}$$

compared with the measured median value of 0.066 ± 0.01 cm (equation 5.9). The frequency distribution of Δ is shown in figure A4.2b, which has a median value of

$$\Delta_{med} = 0.064 \text{ cm}$$

If those particles with $\phi \geqslant (\phi)_{med}$ are rejected, then the median value of Δ is reduced to

$$(\Delta_{med})_{rej} = 0.048 \text{ cm}$$

Ideally, if there were no errors in measurement of particle track position, all the values of Δ would be zero. Thus the accuracy with which Δ is determined is increased by

$$\Delta_{med} \Big/ (\Delta_{med})_{rej} = 1.33 \qquad \text{A4.1}$$

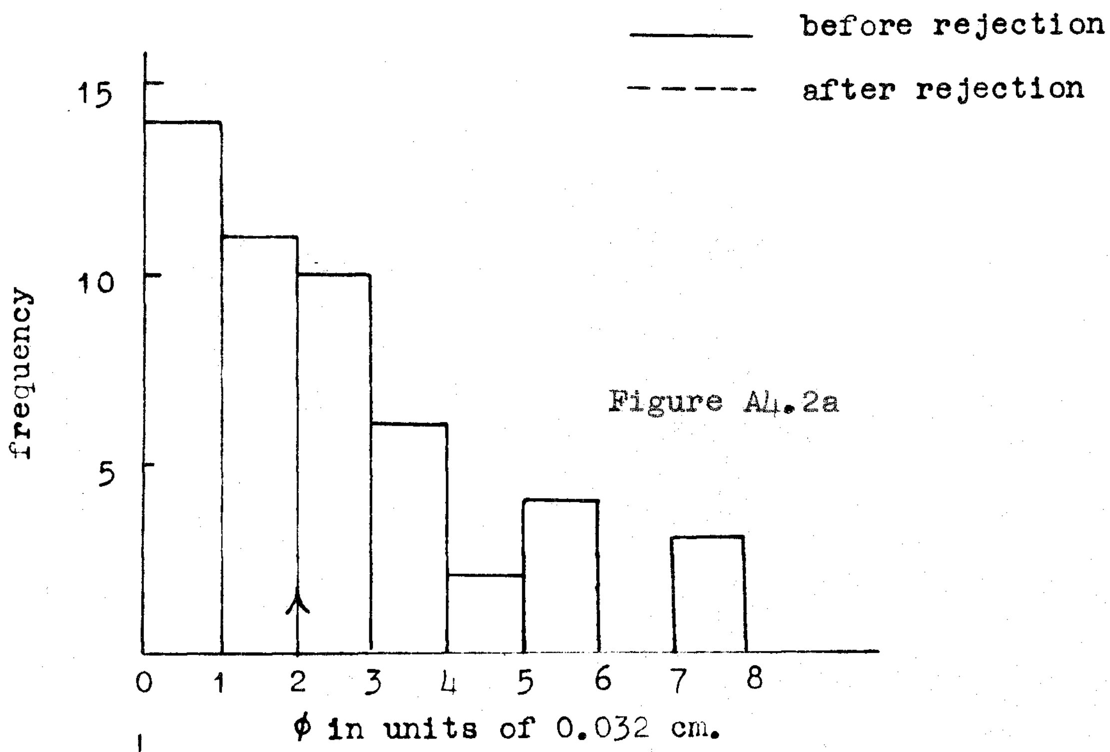

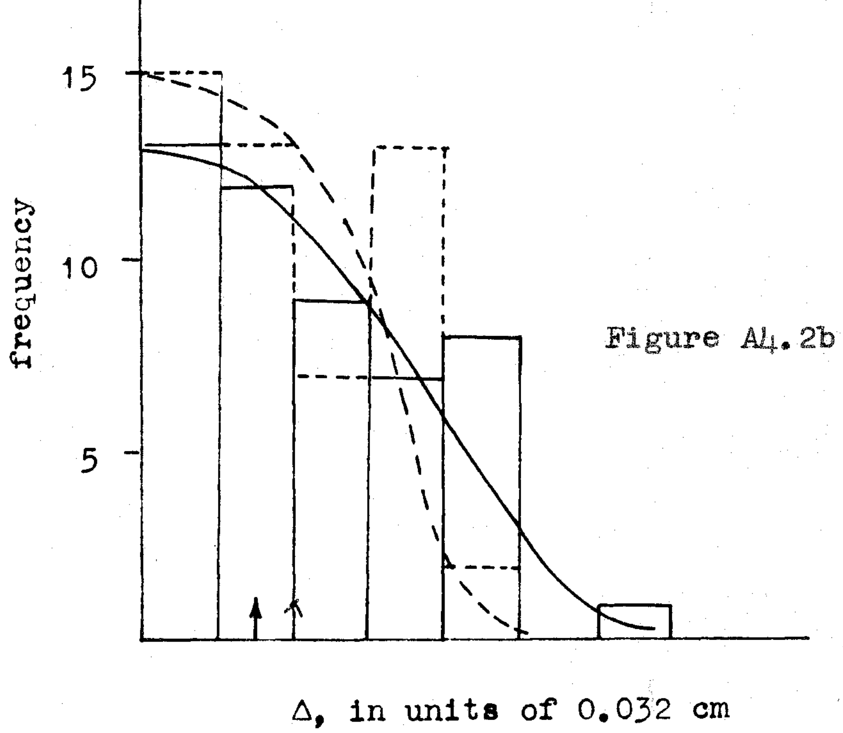

Figure A4.2a : The distribution of ϕ for the simulated particles.

Figure A4.2b : The distribution of Δ for the simulated particles.

The method used to simulate the passage of particles does not take into account the variation of absolute efficiency with radius of the flash-tube. In order to take this into account, the absolute efficiencies, figure A4.1, were put into 4 groups with mean efficiencies of 100%, 87%, 69%, and 52%, table A4.1.

The two groups with efficiencies of 69% and 52% were assumed to have this low efficiency because of electrical (geometric) or optical defects in the pulsing or recording systems, and the efficiency at the centre of the tube was proportionally lower, and not 100% as in the other two groups. The absolute efficiency of these 4 groups is shown in figure A4.3.

The trajectories of ten particles were simulated in the way previously adopted. The probability of flashing of flash-tubes intersected by the randomly chosen "true" trajectory was determined by measuring the distance of the "track" from the edge of the tube.

The frequency distribution of ϕ was compared with the previously found distribution but no difference, within the statistical accuracy of the data, could be found. The effect of taking the radius of the flash-tube into account when enumerating the efficiency, is small, and with the present arrangement is probably overshadowed by the inherent inefficiency of some of the layers of flash-tubes.

Table A4.1

Mean efficiency of layer	layer
100	B_3, B_6; C_5
87	A_{2-7}; B_1, B_2, B_4, B_5, B_7; C_1, C_3, C_4, C_7; D_5, D_6, D_8
69	A_1, A_8; B_8; C_6; D_{1-4}, D_7
52	C_2, C_8

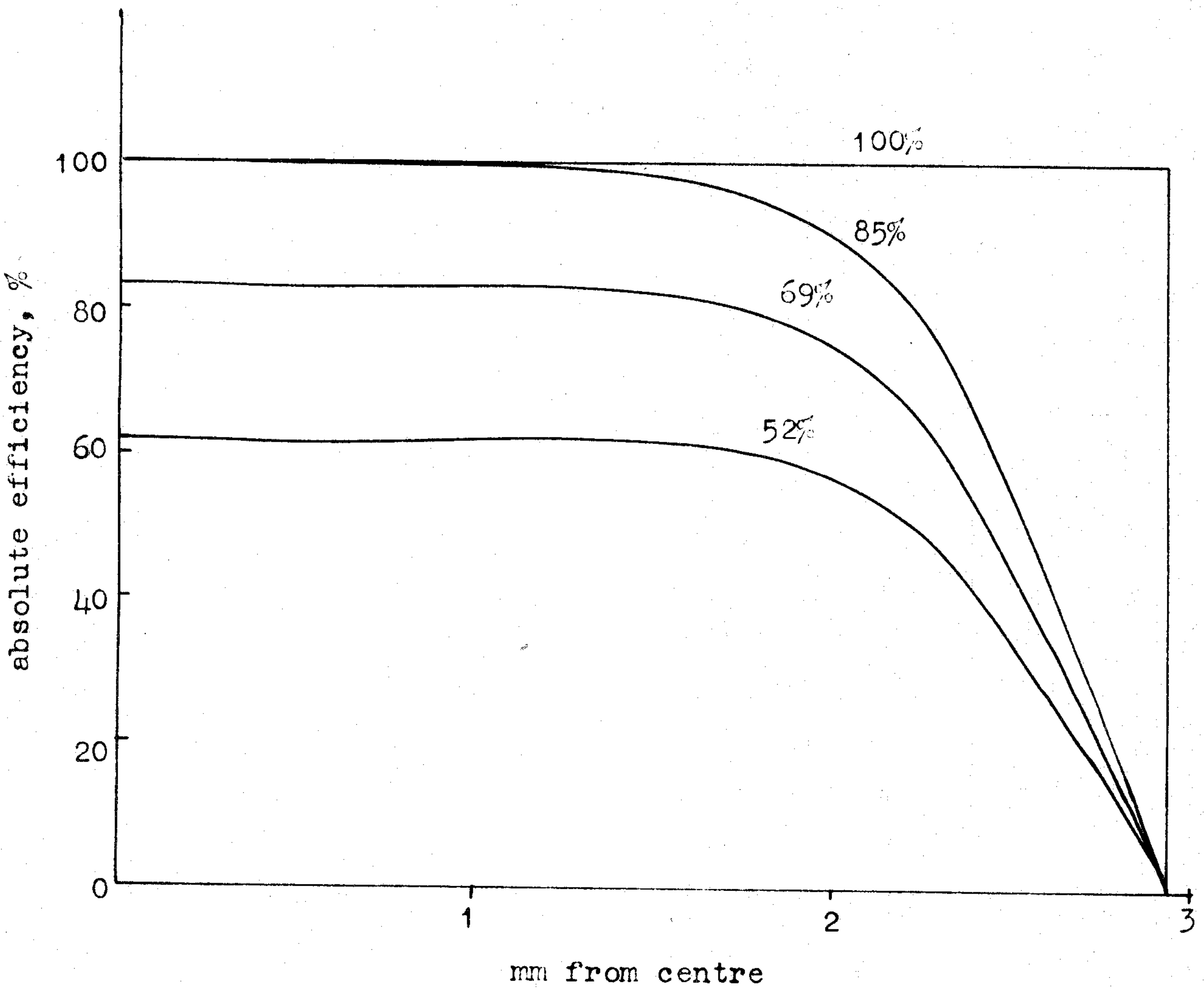

Figure A4.3 : The variation of the absolute efficiency of the flash-tubes with radius.

It has been pointed out, Bull et al, (1962) and Wolfendale, that the enforced association of the two halves of the trajectory, e.g. AX and YD, figure 3.12, demanding that ϕ should be zero, should produce a more accurate determination of Δ.

This was investigated using the original 50 "particles" mentioned in this Appendix. The trajectories were constructed by drawing, in the manner mentioned previously. A point was chosen in XY such that the ratio in which XY was intersected when the two halves of the trajectory were associated, was proportional to the values of the difference between the mean and true positions at B and C, since these have by far the largest effect on the value of ϕ. The best estimate of the trajectory was then determined by making the fractional distances of new intersections from the true position at A, B, C, D equal. The median value of the frequency distribution of Δ was found as before, and has the value

$$\Delta'_{\text{med}} = 0.060 \text{ cm}$$

which is some 7% smaller than the previous value. This is in good agreement with the results of Coates, (1961), and Bull et al who found a similar improvement.

The conclusions to be drawn from this analysis are that the accuracy of location of trajectories can only be increased by a factor 1.33 by the present method of analysis.

If however the distribution in ϕ was greatly different from a Gaussian then it is obvious that a large gain in accuracy of trajectory location could be effected by rejecting particles in the "tail" without an exhorbitant decrease in statistical accuracy.

Appendix 5.

Table A5.1

The Best Estimate of the Differential Intensity of Near-vertical Cosmic Ray Muons as a Function of Momentum over the Complete Range 0.4-1000 GeV/c.

Momentum (GeV/c)	Differential Intensity $cm^{-2}sec^{-1}sterad^{-1}(GeV/c)^{-1}$	Exponent of differential spectrum, γ_μ
0.4	2.58×10^{-3}	-0.44
0.5	2.85×10^{-3}	-0.16
0.7	2.80×10^{-3}	+0.22
1.0	*2.45×10^{-3}	+0.56
1.5	1.93×10^{-3}	+0.90
2.0	1.48×10^{-3}	+1.14
3.0	8.73×10^{-4}	+1.42
5.0	3.79×10^{-4}	+1.76
7.0	2.0×10^{-4}	+1.96
10.0	1.02×10^{-4}	+2.14
15	4.16×10^{-5}	+2.35
20	2.04×10^{-5}	+2.48
30	7.20×10^{-6}	+2.65
50	1.77×10^{-6}	+2.85
70	6.60×10^{-7}	+2.98
100	2.25×10^{-7}	+3.10
150	6.28×10^{-8}	+3.22
200	2.40×10^{-8}	+3.30
300	6.10×10^{-9}	+3.38
500	1.20×10^{-9}	+3.47
700	3.50×10^{-10}	+3.51
1000	9.70×10^{-11}	+3.55

* Normalised to the intensity given by Rossi, (1948)

Table A5.2 The Best Estimate of the Integral Intensity of Near-vertical Cosmic Ray muons as a Function of Momentum Over the Complete range 0.4-1000 GeV/c.

Momentum (GeV/c)	Integral Intensity $cm^{-2}sec^{-1}sterad^{-1}$	As percentage above 0.4 GeV/c
0.4	7.54×10^{-3}	100
0.5	7.25×10^{-3}	96.15
0.7	6.72×10^{-3}	89.12
1.0	5.90×10^{-3}	78.25
1.5	4.84×10^{-3}	64.19
2.0	4.00×10^{-3}	53.05
3.0	2.87×10^{-3}	38.06
5.0	1.71×10^{-3}	22.68
7.0	1.14×10^{-3}	15.12
10	7.00×10^{-4}	9.28
15	3.83×10^{-4}	5.08
20	2.40×10^{-4}	3.18
30	1.18×10^{-4}	1.56
50	4.37×10^{-5}	6.03×10^{-1}
70	2.20×10^{-5}	2.97×10^{-1}
100	1.01×10^{-5}	1.34×10^{-1}
150	4.08×10^{-6}	5.41×10^{-2}
200	2.14×10^{-6}	2.84×10^{-2}
300	8.10×10^{-7}	1.07×10^{-2}
500	2.22×10^{-7}	2.94×10^{-3}
700	9.40×10^{-8}	1.25×10^{-3}
1000	3.78×10^{-8}	5.01×10^{-4}

Appendix 6. The Derivation of the Theoretical π-meson Production Spectrum

6.1 π-mesons Produced with Equal Energies in the L-system

In this model it is assumed that the primary, of kinetic energy E_p makes one collision, in which it loses a fraction K of its energy (i.e. K is the total fraction of energy going into π-meson production). Then if K E_p is the energy available for the production of $n_T(E_p)$ π-mesons each of energy E_π

$$K E_p = n_T(E_p) . E_\pi \qquad \text{A6.1}$$

From equation 8.7

$$E_\pi = \frac{K}{B} E_p^{\,1-\alpha} \qquad \text{A6.2}$$

In order to conserve energy in the interaction it is required that

$$K . E_p . N(E_p) \, dE_p = N_1(E_\pi) . E_\pi \, dE_\pi \qquad \text{A6.3}$$

In this case the production spectra of π-mesons is

$$F(E) = N_1(E_\pi) = N(E_p) . \frac{E_p}{E_\pi} . \frac{dE_p}{dE_\pi} \qquad \text{A6.4}$$

$$= \frac{A}{1-\alpha} . B^{\left(\frac{2-S}{1-\alpha}\right)} . K^{-\left(\frac{1+\alpha-S}{1-\alpha}\right)} . E_\pi^{\left(\frac{2\alpha-S}{1-\alpha}\right)} \qquad \text{A6.5}$$

from equation 8.3. Inserting the numerical values of A and B and a factor $\frac{2}{3}$ to allow for charged π-mesons only, then the production spectra of charged π-mesons is

$$F(E) = 1{\cdot}07 . K^{-\left(\frac{1+\alpha-S}{1-\alpha}\right)} . E_\pi^{\left(\frac{2\alpha-S}{1-\alpha}\right)} \qquad \text{A6.6}$$

It is further assumed that all the π-mesons are emitted in the forward direction. This can only be obtained by emission in the C-system in a direction perpendicular to the line of approach of the interacting centres.

6.2 π-mesons Produced with Equal Energies in the C-system

The treatment in this section follows a similar method proposed by Yeivin, (private communication).

In this model it is assumed that the primary of kinetic energy W_p in the C-system, makes one collision in which it loses a fraction K of its energy (i.e. K is again the total fraction of energy going into π-meson production). The energy available for π-meson production will now be K W_p and if $n_T(W_p)$ is the number of π-mesons produced, each of energy W_π in the C-system, then

$$K\, W_p = n_T(W_p) .\, W_\pi \qquad \text{A6.7}$$

The multiplicity relation of equation 8.7 can be expressed in the C-system as

$$n_T(W_p) = a\, W_p^{2\alpha} \qquad \text{A6.8}$$

using the extreme relativistic transformation, $E_p = \frac{\gamma_c^2}{2} = \frac{W_p^2}{2M_c^2}$, where γ_c is the Lorentz factor of the C-system M_c^2 is the proton rest energy, and $a = B(2\, M_c^2)^{-\alpha}$.

The mean π-meson energy in the C-system is then

$$W_\pi = \frac{K W_p}{n_T(W_p)} = \frac{K}{a} W_p^{(1-2\alpha)} \qquad \text{A6.9}$$

The π-mesons are now allowed to be emitted in the C-system at various angles, θ, with the line joining the colliding nuclei. There is not now a unique relation between the π-meson energy in the C-system and L-system, but the π-meson L-system energy is determined by its C-system direction,

$$E_\pi = \frac{W_p W_\pi}{2Mc^2}(1+w) \qquad \text{A6.10}$$

where $w = \cos\theta$, or

$$(2Mc^2)^\alpha E_\pi = \frac{K}{a}(1+w)\, E_p^{(1-\alpha)} \qquad \text{A6.11}$$

It is required to find the average properties of the collision - different collisions will produce different distributions of π-mesons in the C-system. If the function $R(E_\pi, E_p)$ is the π-meson production spectrum describing the average result of collisions of primaries of energy E_p, then the multiplicity, or average total number of π-mesons produced per collision is

$$n_r(E_p) = \int R(E_\pi, E_p)\, dE_\pi \qquad \text{A6.12}$$

This expression describes the collision for a given E_p; for different values of E_p, the numbers of primaries with energy E_p is described by equation 8.3, $N(E_p) = A\,E_p^{-s}$ so that the spectrum of π-mesons from the first collision will be a function of $N(E_p)$ and $R(E_\pi, E_p)$. The propagation of this π-meson spectrum in the atmosphere has been considered in Appendix 3. The diffusion equation,

equation A3.1 will now be

$$\frac{d\Pi_1(E',x)}{dx} = \frac{1}{\lambda_p}\int R(E_\pi,E_p)N(E_p,x)\,dE_p - \Pi_1(E',x)\left\{\frac{1}{\lambda_\pi}+\frac{m_\pi c}{p'\rho c\tau_0}\right\} \qquad \text{A6.13}$$

where $E' = E_\pi = p'c$.

Since the probability of survival to depth x for a primary is e^{-x/λ_p}, the probability of just one collision is $\frac{x}{\lambda_p}\, e^{-x/\lambda_p}$. The dependence of the spectra in this diffusion equation on x is then

$$\left.\begin{aligned} N(E_p,x) &= N(E_p)\,e^{-x/\lambda_p} \\ \Pi_1(E_\pi,x) &= \Pi_1(E_\pi)\,x\,e^{-x/\lambda_p}\cdot\frac{1}{\lambda_p} \end{aligned}\right\} \qquad \text{A6.14}$$

The solution of A6.13 is then ($\lambda_p = \lambda_\pi = \lambda$)

$$\Pi_1(E,x) = \frac{\frac{x}{\lambda}\, e^{-\frac{x}{\lambda}}}{1+\frac{B'}{E_\pi}}\int R(E_\pi,E_p)\,.\,N(E_p)\,dE_p \qquad \text{A6.15}$$

or $$F(E) = \Pi_1(E_\pi) = \int R(E_\pi,E_p)\,dE_\pi\,.\,N(E_p)\,.\,\frac{dE_p}{dE_\pi} \qquad \text{A6.16}$$

In order to evaluate the average value of the integral in equation A6.16, we have to introduce an expression for the π-meson angular distribution on production, f(w), where

$$\int f(w)\,dw = 1$$

and

$$n_T(E_p) = \int n_T\{E_p(E_\pi,w)\}\,f(w)\,dw \qquad \text{A6.17}$$

From A6.12, A6.16 and A6.17

$$F(E) = \Pi_1(E_\pi) = \int n_T\{E_p(E_\pi,w)\}f(w)\,dw\,.\,N\{E_p(E_\pi,w)\}\frac{dE_p}{dE_\pi} \qquad \text{A6.18}$$

$$F(E) = A\left(2Mc^2\right)^{\alpha}\int E_p^{\alpha-s} \cdot \frac{dE_p}{dE_\pi} \cdot f(w)\,dw \qquad \text{A6.19}$$

$$= \frac{A}{1-\alpha}\,\beta^{\left(\frac{2-s}{1-\alpha}\right)}\,K^{-\left(\frac{1+\alpha-s}{1-\alpha}\right)}\,E_\pi^{\left(\frac{2\alpha-s}{1-\alpha}\right)} \cdot I \qquad \text{A6.20}$$

where $I = \int (1+w)^{-\left(\frac{1+\alpha-s}{1-\alpha}\right)} f(w)\,dw$ A6.21

Thus the expression is the same as in the first model, except for the extra factor I, which expresses the angular emission of π-mesons in the C-system.

In both of these models it is assumed that the inelasticity is independent of the primary energy, and in this section it is further assumed that the angular distribution is independent of E_p. Further, because of fluctuations in the numbers of particles produced, the inelasticity relevant to the present work is the average value. Evaluation of the integral I will now be considered in two special cases.

6.3 Evaluation of I

Consideration of the integral when w = 1, i.e. $\theta = 90°$ leads to the solution arrived at in the first model. Emission at right angles to the collision axis, in the C-system is the only way in which π-mesons can be produced with equal energies in the L-system.

In a summary of the angular distribution of secondary particles, Sitte, (1961), has concluded that for the lower primary energies (i.e. $E_p \lesssim 10^{11}$ eV) the emission of particles is very nearly isotropic in the C-system, whilst at moderately high energies, $10^{12} \lesssim E_p \lesssim 10^{12}$ eV there is a tendency for preferential emission in the forward and backward directions in the C-system. At higher primary energies there is an indication of bias against emission in the direction perpendicular to the collision axis.

Evaluation of the integral I in the extreme cases of isotropic distribution and, forward-backward (f-b) distribution in the C-system has been considered by Yeivin (p.c.). Yeivin considers that distributions peaked in the f-b direction may be approximated by

$$f(w) = \frac{\gamma+1}{2}|w|^{\gamma} \qquad \text{A6.22}$$

where $\frac{1}{2}(\gamma+1)$ conserves normalisation. The integral I then becomes

$$I(\beta',\gamma) = \frac{\gamma+1}{2}\int_{-1}^{+1}(1+w)^{\beta'}|w|^{\gamma}\,dw = \frac{\gamma+1}{2}\int_{0}^{1}\left[x^{\beta'}(1-x)^{\gamma} + (1+x)^{\beta'}x^{\gamma}\right]dx$$

$$= \frac{\frac{1}{2}}{\frac{\beta'+\gamma+1}{\beta'}} + \frac{\gamma+1}{2}\sum_{n}\frac{\left|{\beta' \atop n}\right|}{n+\gamma+1} \qquad \text{where } \beta' = -\left(\frac{1+\alpha-S}{1-\alpha}\right)$$

Isotropic distribution in the C-system

This will occur for $\gamma = 0$ and $f_i = f(w) = \frac{1}{2}$, and so

$$I_i = \frac{1}{2}\int_{-1}^{1}(1+w)^{\beta'}\,dw = \frac{2^{\beta'}}{\beta'+1} \qquad \text{A6.23}$$

The f-b distribution in the C-system

Using the delta functions $f_q = f(w) = \frac{1}{2}\left[\delta(-1) + \delta(+1)\right]$

$$I_a = 2^{\beta'-1} \qquad \text{A6.24}$$

A6.4 The Effect of Multiple Collisions on F(E)

In this section the value of $\beta' = \frac{1+\alpha-s}{1-\alpha}$ will be evaluated for $s = 2.6$ and $\alpha = \frac{1}{4}$.

If the primary particle is allowed to lose half of its energy in the first collision, then $K_\pi = K = \frac{k_\pi}{2}$ where K_π is now the inelasticity per interaction or "inelasticity", and k_π is the total fraction of the primary energy transferred and used in π-meson production. The first generation π-meson production spectrum is then

$$F_1(E_\pi) = \frac{A}{1-\alpha}\, B^{\left(\frac{2-s}{1-\alpha}\right)} \left(\frac{k_\pi}{2}\right)^{-\left(\frac{1+\alpha-s}{1-\alpha}\right)} E_\pi^{\left(\frac{2\alpha-s}{1-\alpha}\right)} .\, I \qquad \text{A6.25}$$

$$= 2^{\left(\frac{1+\alpha-s}{1-\alpha}\right)} \pi_1(E_\pi) \qquad \text{from A6.20} \qquad \text{A6.26}$$

$$= 0.29\, .\, \pi_1(E_\pi)$$

The primary particle carries on with energy $E_s = \frac{E_p}{2}$ and the spectrum of primary particles after their first collision will be

$$N(E_s) = N(E_p)\,\frac{dE_p}{dE_s}$$

$$= A\,(2E_s)^{-s} .\, 2$$

$$= A'\,E_s^{-s} \qquad \text{A6.27}$$

where $A' \simeq A2^{1-s}$.

If the primary particle in the second collision loses $\frac{E_s}{2} = \frac{E_p}{4}$, then $K_{\pi} = k_{\pi/2}$ and the second generation spectrum of π-mesons is

$$F_2(E_\pi) = 2^{1-s} \cdot \Pi_1(E_\pi) \cdot 2^{\left(\frac{1+\alpha-s}{1-\alpha}\right)} \qquad \text{A6.28}$$

$$= 0{\cdot}10 \; \Pi_1(E_\pi)$$

Similarly $$F_3(E_\pi) = 2^{2(1-s)} \cdot \Pi_1(E_\pi) \cdot 2^{\left(\frac{1+\alpha-s}{1-\alpha}\right)} \qquad \text{A6.29}$$

The π-meson production spectrum is then

$$\begin{aligned} F'(E_\pi) &= \sum_{i=1}^{\infty} F_i(E_\pi) \\ &= \left[1 + 2^{t} + 2^{2t} \text{----}\right] \Pi_1(E_\pi) \cdot 2^{\left(\frac{1+\alpha-s}{1-\alpha}\right)} \quad \text{where } t = 1-s \\ &= 0{\cdot}435 \, \Pi_1(E_\pi) \qquad \text{A6.30} \end{aligned}$$

Certain approximations have been made in the above considerations. The treatment in the two previous cases does not include the fact that the inelasticity, K_π, varies with E_p or that for low energies, a larger fraction of the transferred energy goes into π-meson production. There is some experimental indication also that at the primary energies considered here, the loss of a half of the primary energy is an overestimate, and that a more accurate value would be 0.4.

The summation to ∞ in equation A6.30 is justified when it is remembered that the interaction length for protons in air is ~ 70 gm.cm^{-2} and that a primary proton, if it could survive with sufficient energy, would make ~ 14 collisions before reaching sea-level.

Appendix 7. The Effect of Fluctuations in π-meson Production.

7.1 The Effect of Fluctuations

The measured multiplicities of charged π-mesons, M_c, show a wide distribution for a given primary energy E_p. The best line through the data can be represented on the Fermi model of π-meson production by equation 8.6, and the total number produced by equation 8.7,

$$n_T(E_p) = BE_p^{\alpha} \qquad \text{A7.1}$$

where $B = 4.5$ and $\alpha = \frac{1}{4}$.

On the $\log M_c$ - $\log E_p$ plot of figure 8.3 the frequency distribution of $\log M_c$ for a given $\log E_p$ can be considered constant for values of M_c in the range

$$M_c/j \lesssim M_c \lesssim jM_c \qquad \text{A7.2}$$

where $j = 3$. Thus the probability of $\log M_c$ occurring is constant in these limits,

$$P(\log M_c) = \text{constant} \qquad \text{A7.3}$$

The differential probability, $f(M_c)$, of a multiplicity M_c occurring can then be represented by

$$f(M_c)dM_c = P(\log M_c).d(\log M_c) \qquad \text{A7.4}$$

Normalisation requires that

$$\int_{(M_c)_{min}}^{(M_c)_{max}} f(M_c).dM_c = 1$$

giving

$$f(M_c) = \left(M_c.\log\frac{(M_c)_{max}}{(M_c)_{min}}\right)^{-1} \qquad \text{A7.5}$$

The values of M_c at the limits are obtained from the energy balance in the primary interaction, since

$$E_\pi \cdot \frac{n_T(E_p)}{2} = \frac{k_\pi}{2} \cdot E_p \qquad \text{A7.6}$$

where k_π is the loss factor in Appendix 6, ($K_\pi = \frac{k_\pi}{2}$ is the inelasticity) and E_π is the mean energy of each of the $n_T(E_p)$ π-mesons produced. The π-mesons are assumed in this model to be all produced with equal energy. It is further assumed that in the simple model to be used to derive the μ-meson positive excess that the particles are emitted in a forward-backward direction in the C-system. Those π-mesons emitted backwards in the C-system will have low energy in the L-system and the μ-mesons from the decay of the π-mesons will also have low energy. Thus most of the energy transferred by the primary will be concentrated in the forward directed π-mesons (in the C-system).

The value of $(M_c)_{max}$ can then be derived from $(n_T(E_p))_{max}$

$$(n_T(E_p))_{max} = j \cdot n_T(E_p) = j B E_p^{\alpha}$$

$$(M_c)_{max} = \frac{2}{3} (jB)^{\frac{1}{1-\alpha}} \left(\frac{E_\pi}{k_\pi}\right)^{\frac{\alpha}{1-\alpha}} \qquad \text{A7.7}$$

$$(M_c)_{min} = \frac{2}{3} \left(\frac{B}{j}\right)^{\frac{1}{1-\alpha}} \left(\frac{E_\pi}{k_\pi}\right)^{\frac{\alpha}{1-\alpha}} \qquad \text{A7.8}$$

The value of M_c is given from equations A7.7, A7.8 with $j = 1$. Inserting the values for B and k_π (4.5 and 0.40 respectively) then

$$(M_c)_{max} = 28.5\ E^{\frac{1}{3}} \qquad \text{A7.9}$$

$$(M_c)_{min} = 0.86\ E^{\frac{1}{3}} \qquad \text{A7.10}$$

$$(M_c) = 6{\cdot}6\ E^{\frac{1}{3}} \qquad \text{A7.11}$$

7.2 The Multiplicity Spectrum of π-mesons

The number of interactions taking place in which $n_T(E_p)$ π-mesons of energy E_π are produced, in the interval dE_π, at E_π, is

$$N\left(n_T(E_p)\right) dE_\pi = f\left(n_T(E_p)\right) N(E_p)\, dE_p \qquad \text{A7.12}$$

where $f\left(n_T(E_p)\right) = \frac{1}{n_T(E_p)}\left(\log \gamma^{\frac{2}{1-\alpha}}\right)^{-1}$ from A7.5

Then

$$N\left(n_T(E_p)\right) dE_\pi = \left(\log \gamma^{\frac{2}{1-\alpha}}\right)^{-1} \cdot \frac{A E_p^{-s}\, dE_p}{n_T(E_p)} \qquad \text{A7.13}$$

From A7.1 and A7.6

$$dE_\pi = \frac{k_\pi(1-\alpha)}{n_T(E_p)} \cdot dE_p \qquad \text{A7.14}$$

so that

$$N\left(n_T(E_p)\right) dE_\pi = \frac{A}{k_\pi(1-\alpha)\log \gamma^{\frac{2}{1-\alpha}}} \cdot E_p^{-s}\, dE_\pi \qquad \text{A7.15}$$

or

$$N(M_c) = \left(\frac{3}{2}\right)^{1-s} \cdot \left(k_\pi\right)^{-(1-s)} \cdot \frac{A}{(1-\alpha)\log \gamma^{\frac{2}{1-\alpha}}} \cdot E_\pi^{-s} (M_c)^{-s}$$

7.3 The Effect of Fluctuations on the Positive-negative Ratio of π-mesons

If $R_i(M_c)$ is the positive-negative ratio for π-mesons, of energy E_π, in the i-th generation, then the weighted (or effective) mean is

$$\bar{R}_{\Sigma i}(E_\pi) = \frac{\int_{(M_c)_{min}}^{(M_c)_{max}} N_i(M_c) R_i(M_c)\, dM_c}{\int_{(M_c)_{min}}^{(M_c)_{max}} N_i(M_c)\, dM_c} \qquad \text{A7.16}$$

where the $R_i(M_c)$ are given by equations 9.9, 9.10.

Using the multiple collision model of A6.4, then the successive contributions to $\bar{R}_{\Sigma i}(E\ )$ are

$$\bar{R}_{\Sigma i}(E_\pi) = \frac{\int N_1(M_c)R_1(M_c)\,dM_c + 2^{(1-s)}\int N_1(M_c)\,dM_c + 2^{2(1-s)}\int N_1(M_c)\,dM_c \cdots\cdots}{(1+2^{1-s}+2^{2(1-s)}+\cdots\cdots)\int N_1(M_c)\,dM_c} \qquad \text{A7.17}$$

7.4 The Effect of Fluctuations in Multiplicity on the π-meson Production Spectrum

The charged π-mesons of energy E_π will be derived from all values of M_c between the limits of equations A7.9, A7.10,

$$N(E_\pi) = \int_{(M_c)_{min}}^{(M_c)_{max}} N(M_c).M_c.dM_c$$

$$\simeq \left[\frac{j^{\frac{2-s}{1-\alpha}} - j^{-\left(\frac{2-s}{1-\alpha}\right)}}{(2-s)\log j^{\frac{2}{1-\alpha}}}\right]\frac{2}{3}\cdot\frac{A}{1-\alpha}\cdot E_\pi^{\left(\frac{2\alpha-s}{1-\alpha}\right)}\cdot k_\pi^{-\left(\frac{1+\alpha-s}{1-\alpha}\right)}\,\beta^{\left(\frac{2-s}{1-\alpha}\right)} \qquad \text{A7.18}$$